

**Generation of induced pluripotent stem cells and their
differentiation into microglia for the analysis of Alzheimer's
disease.**

Dissertation

zur Erlangung des
Doktorgrades der Naturwissenschaften
(Dr. rer. nat.)

der

Naturwissenschaftlichen Fakultät I
– Biowissenschaften –

der Martin-Luther-Universität
Halle-Wittenberg,

vorgelegt

von Herrn Toni Ehrhardt

geb. am 21.10.1987 in Ilmenau

Gutachter:

Prof. Dr. Guido Posern

Prof. Dr. Thomas Groth

Prof. Dr. Winfried Neuhaus (AIT Wien)

Datum der Verteidigung:

24.01.2022

ACKNOWLEDGEMENT

I would like to express my great appreciation to Prof. Dr. Dan Rujescu for the opportunity to work at the University Clinic and Outpatient Clinic Polyclinic for Psychiatry, Psychotherapy, and Psychosomatics, for his patience guidance, enthusiastic encouragement, and useful criticism regarding my work.

Great acknowledgement is given to Dr. Matthias Jung and Dr. Annette Hartmann for their continuous support and their valuable and constructive suggestions. Further I would like to thank PD Dr. Ina Giegling and Bettina Konte for their generous support during the past years. Special thanks go to Prof. Dr. Guido Posern, for supervising me and for offering his helpful advice throughout the project.

I would also like to thank all current and former members of the junior research group of Dr. Matthias Jung under the leadership of Prof. Dr. Rujescu. They all created a friendly, pleasant, inspiring, and motivating working atmosphere. I am especially grateful for the help of Dr. Matthias Jung, Carla Hartmann, Bernadette Harwardt, Jana Hirschfeld, and Katja Junghans. Special thanks go to PD Dr. Dagmar Riemann, Dr. Alexander Navarrete-Santos, Dr. Chiara Massa, Dr. Matt Fuszard, Dr. Alessandro Ori and Dr. Kaya Bork for their excellent support in experimental design, instrument use, and method establishment.

Special gratitude is expressed to the group of Prof. Dr. Kielstein and the staff of the Institute of Anatomy and Cell Biology. Prof. Dr. Anne Navarrete-Santos, Dr. Dagmar Quandt, Dr. Nora Raulien, Dr. Maria Schindler, Dr. Julia Spielmann, Dr. Albrecht Klemenz, Dr. Tim Hohmann and Dr. Juliane-Susanne Jung, who supported me with their constant advice. For excellent technical support I would like to thank Christine Fröhlich, Sabine Schrötter, Michaela Kirstein, Susann Möschter, Franziska Knöfel, Hans-Joachim Heine, Elisabeth George, Evelyn Axmann and Patrizia Zwarg. I would like to thank them especially for creating a nice, friendly, and enjoyable time. I am very thankful towards Prof. Dr. Simm, Prof. Rüdiger Horstkorte and Prof. Dr. Regine Heller who accepted me into the Research Training Group GRK 2155 ProMoAge. Furthermore, I would like to express my gratitude to the MLU Halle, the University Clinic and Outpatient Clinic for Psychiatry, Psychotherapy, and Psychosomatics, and the Wilhelm Roux Program for their financial support.

My heartfelt gratitude and appreciation go to my son and my parents. I would foremost like to thank my mother and my friends, who have always supported me and given me strength and motivation to complete this work.

LIST OF FIGURES

Figure 1: Amyloid cascade hypothesis in AD.	1
Figure 2: Enzymatic process of the amyloid-precursor protein.	2
Figure 3: Apolipoprotein E isoforms	5
Figure 4: Microglial ITIM – ITAM cascade signaling.	16
Figure 5: SNP genotyping plot and mass spectra of rs3826656 in CD33.	33
Figure 6: Flow cytometry analysis of CD33-dependent phagocytosis.	34
Figure 7: Transcript analysis of CD33-dependent phagocytosis.	35
Figure 8: Morphology and alkaline phosphatase staining of iPSCs.	36
Figure 9: Verification of pluripotency-related genes in generated iPSCs.	36
Figure 10: Shotgun proteome analysis.	37
Figure 11: Transcript analysis of spontaneous differentiation.	38
Figure 12: Differentiation of MGLCs via hematopoietic progenitors.	39
Figure 13: Cell morphology images during differentiation into MGLCs.	40
Figure 14: Evaluation of microglia marker expression.	41
Figure 15: Immunofluorescence analysis of MGLCs.	42
Figure 16: Flow cytometry analysis of microglial surface markers on MGLCs.	43
Figure 17: Properties of MGLCs.	43
Figure 18: Motility of MGLCs determined by time-lapse microscopy.	44
Figure 19: Dynamic processes determined by time-lapse microscopy in MGLCs.	45
Figure 20: Telomere length analysis in MGLCs.	46
Figure 21: Multiplex cytokine assay analysis of MGLCs.	47
Figure 22: Evaluation of CX3CR1 in MGLCs.	48
Figure 23: Explorative analysis of proteomic data.	49
Figure 24: Comparative protein content analysis of microglia-like cells.	51
Figure 25: Gene ontogolgy of biological processes.	52
Figure 26: Altered biological processes in LOAD-specific MGLCs.	53
Figure 27: Overview of the thesis work packages.	79

LIST OF TABLES

Table 1: List of LOAD-related genotyped SNPs.	32
Table 2: List for patient / donor information	35

LIST OF ABBREVIATIONS

Abbreviation	Explanation
APC	allophycocyanin
AD	Alzheimer's disease
ADNI	Alzheimer's Disease neuroimaging initiative
APP	amyloid precursor protein
ANOVA	analysis of variance
A β	beta-amyloid
CNS	central nervous system
CSF	cerebrospinal fluid
Da	Dalton
DNA	deoxyribonucleic acid
DD	differential diagnosis
EOAD	early-onset AD
E	embryonic day
ESCs	embryonic stem cells
FAD	familial AD
FITC	fluorescein isothiocyanate
GERAD1	genetic and environmental risk in Alzheimer's Disease consortium 1
GWAS	genome-wide association studies
HPLC	high performance liquid chromatography
HEK	human embryonic kidney
IF	immunofluorescence
ITAM	immunoreceptor tyrosine-based activation motif
ITIM	immunoreceptor tyrosine-based inhibition motif
iPSC	induced pluripotent stem cells
IL	interleukin
IAA	iodoacetamide
LOAD	late-onset AD
LPS	lipopolysaccharides
B-LCL	B-lymphoblastoid cell lines
m/z	mass-to-charge ratio
MALDI-TOF	matrix-assisted laser desorption ionization-time of flight mass
mRNA	messenger ribonucleic acid
miRNA	micro ribonucleic acid
MGDM	microglial differentiation medium
MGLC	microglia-like cell
MIPS	monoisotopic precursor selection
OR	odds ratio
PFA	paraformaldehyde
PBMC	peripheral blood mononuclear cell
PE	phycoerythrin
PSEN1	presenilin 1
PSEN2	presenilin 2
A β pE3-42	pyroglutamate-modified A β
STRING	search tool for the retrieval of interacting genes/proteins
SAP	shrimp alkaline phosphatase
SNP	single nucleotide polymorphism
MS/MS	tandem mass spectrometry
UPLC	ultra performance liquid chromatography
PCR	polymerase chain reaction
PFA	paraformaldehyde
PBS	phosphate-buffered saline

ABSTRACT

Alzheimer's disease (AD) is the most common cause of dementia in the elderly. Accumulation of intercellular β -Amyloid (A β) plaques and intracellular neurofibrillary tangles are two hallmarks of AD that may drive neuronal death and the corresponding dramatic loss of cognitive abilities. A complex interaction between genetic and environmental factors contributes to molecular processes that drive AD. Microglial-mediated processes are key determinants to the accumulation of A β deposits in AD, playing roles in amyloid degradation, and initiation and growth of plaques. Environmental and genetic factors contribute to the risk for AD, but the underlying disease mechanisms are poorly understood. In recent years, genome-wide association studies (GWAS) allowed the identification of DNA variations associated with an elevated risk for AD. Thereby, several AD susceptibility genes including CD33 and TREM2 point towards the immune system as a player in onset, progression, and treatment of AD. To further examine this hypothesis, we generated patient-specific induced pluripotent stem cell lines (iPSC) for the generation of microglia in vitro enabling the functional characterization of disease-associated DNA variants in microglia genes. Furthermore, potentially functional SNP variants in CD33, MSA4, EPHA1, CD2AP, and TREM2 were genotyped in late-onset AD (LOAD) patients. This study generated iPSCs from patients carrying one of these genetic predispositions. Control iPSCs were generated from healthy donors. Based thereon, pluripotency was verified by alkaline phosphatase staining, the expression of pluripotency markers, as well as differentiation into derivatives of the three germ layers. The expression of pluripotency marker genes was successfully induced as shown by RNA expression and proteome profile analyses. Additionally, cells were also screened for the most efficient induction of neural cell fates including glia cell fates. Further, we established a completely new four-step protocol for the generation of late-onset AD LOAD-specific microglia-like cells (MGLCs) from hematopoietic progenitor cells, enabling the focused analysis of functional alterations in LOAD. The protocol was characterized by morphology, FACS, IF, and RNA expression analysis of hematopoietic lineage and crucial microglia markers. Furthermore, cytokine release, phagocytosis, and ramification of AD-MGLCs was compared to healthy controls to determine functional differences. Finally, proteome analysis of patient specific MGLCs was performed to characterize the proteomic changes in LOAD in more detail and provide new functional relevant molecular insights. The proteome results confirmed that the immune system is altered in LOAD, which was already hypothesized in the literature by previous GWAS data. Proteome results also suggest involvement in endocytosis, and lipid processing, which is linked to the immune system. Moreover, subsequent analysis of the significant identified proteins in LOAD MGLCs revealed a strong alteration in actin cytoskeleton remodeling. Thereby, the cytoskeleton organization crucially influences most of the microglial function, as verified by subsequent functional tests including motility, cytokine release, and cell activation. In summary, the here established LOAD-specific iPSC lines represent a powerful tool for the analysis of molecular and cellular disease mechanisms. Furthermore, combination of the iPSC technology, with the here established microglia differentiation protocol provide a promising tool to characterize known disease mechanisms more precisely.

ZUSAMMENFASSUNG

Die Alzheimer-Krankheit (AD) ist die häufigste Ursache für Demenz bei älteren Menschen. Interzelluläre Plaques aus β -Amyloid (A β) und intrazellulärer Neurofibrillen sind zwei Kennzeichen der AD, die mit Verlust von Neuronen und dem entsprechend dramatischen Verlust kognitiver Fähigkeiten einhergeht. AD hat verschiedene Ursachen, die in einem komplexen Zusammenspiel von genetischen Faktoren und Umweltfaktoren wirken. Mikroglia sind involviert in die Schlüsselprozesse für die Akkumulation von A β . Sie steuern Amyloid-Abbau und das Wachstum von Plaques. Obwohl bekannt ist, dass Umwelteinflüsse und genetische Faktoren das Risiko für AD erhöhen, ist wenig über die grundlegenden Krankheitsursachen bekannt. Jedoch wurden in den vergangenen Jahren in genomweiten Assoziationsstudien (GWAS) DNA-Variationen identifiziert, die mit einem erhöhten Risiko für die AD assoziiert sind. Darunter sind DNA-Variationen in CD33 und TREM2, die nahe legen, dass das Immunsystem beim Ausbruch, dem Fortschreiten und der Behandlung der AD eine wichtige Rolle spielt. Um diese Hypothese weiter zu untersuchen, wurden in dieser Arbeit induzierte pluripotente Stammzelllinien (iPSC) aus Patienten generiert, um die Funktion der DNA-Variationen besser zu verstehen. Zunächst wurde die DNA von Patienten genotypisiert. Nur DNA-Variationen in CD33, MSA4, EPHA1, CD2AP und TREM2, die nach Literaturangaben zu einer funktionellen Änderung auf der DNA führen, wurden untersucht. Träger von DNA-Variationen wurden für die Herstellung von iPSC ausgewählt. Auch von gesunden Spendern wurden iPSC als Kontrollen hergestellt. Die Pluripotenz generierter iPSC wurde durch Färbung der alkalischen Phosphatase und Differenzierung in die drei Keimblätter nachgewiesen und sowohl durch Transkriptanalysen als auch eine Proteomanalyse bestätigt. Die effiziente Induktion von neuronalen Vorläufern wurde ebenfalls demonstriert. Weiterhin etablierte diese Arbeit ein völlig neues Vier-Stufen-Protokoll für die Generierung von Mikroglia-ähnlichen Zellen (MGLCs), die über hämatopoetische Vorläuferzellen generiert werden. Die so erhaltenen MGLC sind für die späte nicht-familiäre Form der AD besonders relevant. Das Protokoll wurde intensiv über die Morphologie, FACS, IF-Analysen sowie die Transkriptanalysen charakterisiert und die Entwicklung hämatopoetischer Vorläufer bestätigt. Mikroglia-Marker wurden in MGLC nachgewiesen. Weiterhin wurde die Zytokinfreisetzung, die Phagozytose und die Verästelung von AD-spezifischen MGLC untersucht, um funktionelle Unterschiede im Vergleich zu gesunden Kontrollen zu finden. Eine Proteomanalyse brachte neue Erkenntnisse zu relevanten molekularen Mechanismen. Die erhaltenen Daten bestätigen, die aus den Daten der GWAS abgeleiteten Hypothese zur Beteiligung des Immunsystems an der AD. Die gefundenen Signalwege regulieren Endozytose, Lipidverarbeitung sowie den Umbau des Zytoskeletts. Das Zytoskelett reguliert maßgeblich die Funktionalität der Mikroglia. Die Ergebnisse konnten mit funktionellen Analysen wie der Motilität, Zytokinfreisetzung und Zellaktivierung bestätigt werden. Zusammenfassend lässt sich sagen, dass die hier etablierten LOAD-spezifischen iPSC-Linien ein leistungsfähiges Werkzeug für die Analyse von molekularen und zellulären Krankheitsmechanismen darstellen. Darüber hinaus bietet die Kombination der iPSC-Technologie mit dem hier etablierten Mikroglia-Differenzierungsprotokoll ein vielversprechendes Werkzeug, um bekannte Krankheitsmechanismen genauer zu untersuchen.

Table of Content

ACKNOWLEDGEMENT	I
LIST OF FIGURES	II
LIST OF TABLES	II
LIST OF ABBREVIATIONS	III
ABSTRACT	IV
ZUSAMMENFASSUNG	V
Table of Content	VI
1 Introduction	1
1.1 Alzheimer's Disease	1
1.1.1 Neuropathology of AD	2
1.1.2 EOAD	3
1.1.3 LOAD	3
1.1.3.1 Genome-Wide Association Studies in LOAD	3
1.1.3.2 APOE Function in the CNS and its Role in LOAD	4
1.2 Induced Pluripotent Stem Cells (iPSC)	6
1.2.1 Reprogramming Stem Cells	6
1.2.2 Characteristics of iPSCs	7
1.2.3 In vitro iPSCs for Modelling LOAD	8
1.3 Microglia	9
1.3.1 Microglia Origin and Development	10
1.3.2 Microglia Mediated Pathology	11
1.3.2.1 Microglia Phenotypes in AD	11
1.3.2.2 Mechanisms of Microglia Activation	12
1.3.2.3 Immune Receptors in Health and Disease State	13
1.3.3 CD33 Molecule	14
1.3.3.1 CD33 Molecule in LOAD	14
1.3.3.2 CD33 and TREM2	15
1.4 Aims of the Study	17
2 Materials and Methods	18
2.1 Ethical Considerations and Patient Classification	18
2.2 Cell Culture	18
2.2.1 Culture of Human iPSCs	18
2.2.2 Culture of primary cells and cell lines	18
2.2.2.1 Human Embryonic Kidney cells	18
2.2.2.2 Mouse Embryonic Fibroblasts (MEFs)	19
2.2.2.3 Human Primary Microglia	19
2.2.2.4 Culture and Isolation of Primary Monocytes	19
2.2.3 Generation and Culture of B-LCLs	19

2.2.4	Generation of iPSCs	20
2.2.5	Spontaneous Differentiation of iPSCs	21
2.2.6	Manufacture of Microglia-Like Cells	21
2.3	Analysis of mRNA and Protein Expression	22
2.3.1	RNA Isolation and Reverse Transcription	22
2.3.2	Semi-Quantitative Polymerase Chain Reaction (PCR)	22
2.3.3	Quantitative Real Time PCR (qRT PCR)	22
2.3.4	Telomere Length Analysis	23
2.3.5	Immunofluorescence (IF) Analysis	23
2.3.6	Flow cytometry	23
2.4	Histology	23
2.4.1	Alkaline Phosphatase Staining	23
2.4.2	Wright-Giemsa Staining	24
2.5	Microglia Physiology and Morphology	24
2.5.1	Electrophysiology	24
2.5.2	Time-Lapse Microscopy	24
2.5.3	Phagocytosis Assay	25
2.5.3.1	Analysis using Fluorescence-Labeled Latex Beads	25
2.5.3.2	Analysis Using <i>Escherichia coli</i> K-12-Strain BioPartikel	25
2.5.3.3	CD33-Dependent Phagocytosis	25
2.5.4	Multiplex Cytokine Assay	26
2.5.4.1	Principle of Analysis	26
2.5.4.2	Cytokine Determination	26
2.6	Mass Spectrometry	26
2.6.1	iPlex Assay and the MassArray System	27
2.6.1.1	Performing PCR Amplification	27
2.6.1.2	Performing Shrimp Alkaline Phosphatase Treatment	27
2.6.1.3	Performing and Desalting the iPlex Extension Reaction	27
2.6.1.4	MassARRAY-System	27
2.6.2	Quantitative Proteomic Analysis with SYNAPT	28
2.6.2.1	Protein Isolation, Digestion, and Clean Up	28
2.6.2.2	Label-Free Data Analysis	28
2.6.3	Quantitative Proteomic Analysis by Orbitrap Fusion Lumos	29
2.6.3.1	Protein Extraction, Digestion, and Clean Up	29
2.6.3.2	Data Acquisition for Label-Free Analysis	30
2.6.3.3	Data Processing	30
3	Results	32
3.1	Genotyping of B-LCLs and search for AD-associated DNA risk variants	32
3.2	CD33-dependent phagocytosis	34
3.3	Generation of LOAD-specific iPSCs	35
3.3.1	Verification of pluripotency by alkaline phosphatase staining	36
3.3.2	Verification of pluripotency by transcript analysis	36

3.3.3	Proteome analysis of iPSCs and their donor cells _____	37
3.3.4	Verification of SNP genotype pattern in iPSCs _____	38
3.3.5	Verification of pluripotency by differentiation into derivatives of three germ layers _____	38
3.4	Generation of human iPSC derived MGLCs via hematopoietic progenitors _____	39
3.4.1	Characterization of developing monocyte lineage MGLCs _____	39
3.4.1.1	Morphology and histological staining _____	39
3.4.1.2	Transcript Analysis _____	40
3.4.1.1	Immunofluorescence analysis _____	41
3.4.1.2	Flow cytometry _____	42
3.4.1.3	Electrophysiology and Cytokine Analysis _____	43
3.4.2	Functional Analysis of Immune Plasticity in MGLCs from LOAD Patients _____	44
3.4.2.1	Time-Lapse Microscopy for Analyzing Motility _____	44
3.4.2.2	Measurement of Ramification and Activation _____	45
3.4.2.3	Telomere Length Analysis _____	45
3.4.2.4	Cytokine Analysis _____	46
3.5	Proteome Analysis of MGLCs _____	47
3.5.1	Flow cytometry to Verify the Culture Purity _____	48
3.5.2	Raw data Analysis and Hierarchical Clustering _____	48
3.5.3	Non-Hypothesis-Driven Analysis _____	50
3.5.4	Altered Cytoskeleton Organization in LOAD MGLCs _____	52
4	Discussion _____	54
4.1	Genotyping of LOAD-Associated DNA Risk Variants in B-LCLs _____	54
4.2	CD33-Dependent Phagocytosis _____	58
4.3	Generation of AD-Specific iPSCs _____	61
4.3.1	Verification of Pluripotency Markers _____	61
4.3.2	Proteome Analysis of iPSCs and their Corresponding donors _____	62
4.3.3	Verification of pluripotency by differentiation into derivatives of three germ layers _____	64
4.4	Generation of Human iPSC-Derived MGLCs _____	64
4.4.1	Characterization of Developing Monocyte Lineage MGLCs _____	66
4.4.2	Functional Analysis of Immune Plasticity in LOAD MGLCs _____	68
4.5	Proteome Analysis of MGLCs _____	72
4.5.1	Non-Hypothesis-Driven Analysis _____	73
4.5.2	Focused Analysis Revealed by Cytoskeleton Organization in LOAD _____	74
5	References _____	81
6	APPENDIX _____	IX
7	CURRICULUM VITAE _____	XVI
	EIDESSTATTLICHE ERKLÄRUNG _____	XVII

1 Introduction

1.1 Alzheimer's Disease

Alzheimer's disease (AD) is the most common cause of dementia in the elderly population with estimated 50-75% of all dementia cases¹. Changes in AD pathophysiology occur years before the onset of the first clinical symptoms². After the age of 65, the prevalence and incidence of AD doubles in five-year age increments³. The disease is named after the physician Alois Alzheimer, who first described it in 1906 after he noticed characteristic changes in the brain of a deceased patient⁴. Due to the increasing ageing of the population, it is predicted that by 2050 about a quarter of the population will be over 65 years of age⁵, which is associated with an increasing number of AD cases. Accumulation of extracellular beta-amyloid (A β) plaques and intracellular neurofibrillary tangles are two hallmarks of AD that may drive neuronal death and the corresponding dramatic loss of cognitive abilities (**Fig. 1 A-B**). The two hallmarks are found in both early-onset AD (EOAD) and late-onset AD (LOAD) shown in figure 1 A.

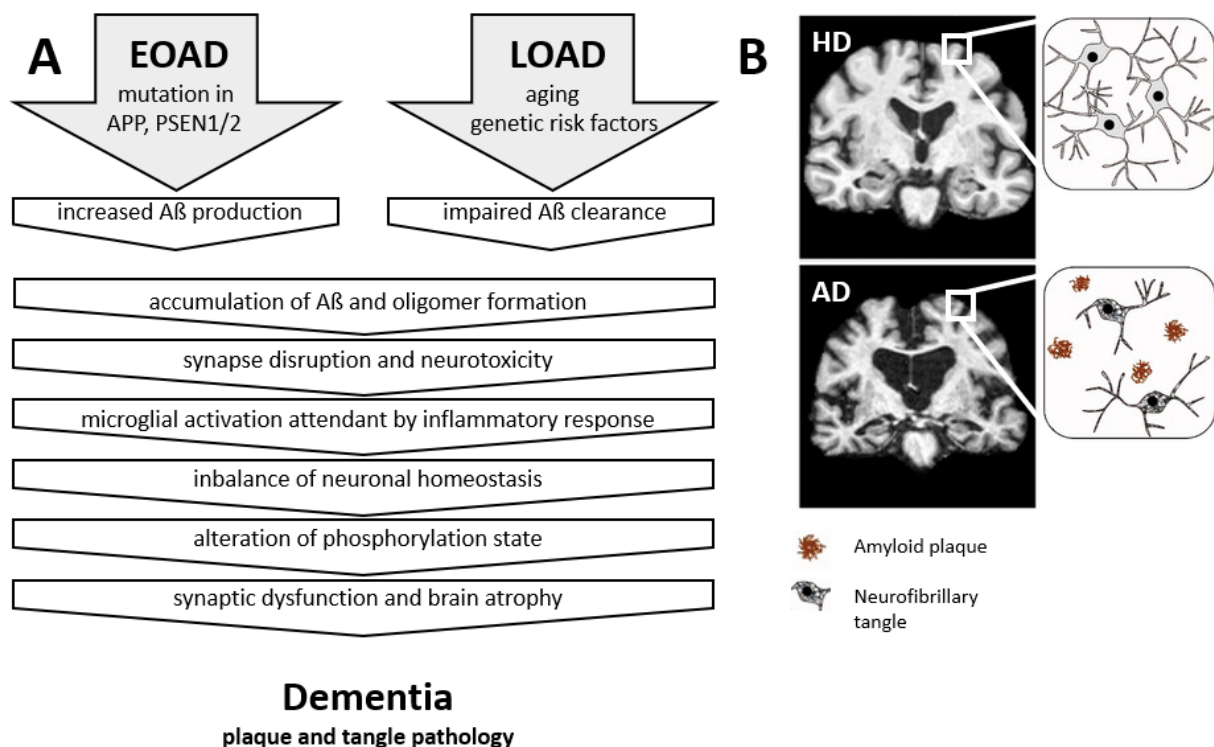


Figure 1: Amyloid cascade hypothesis in AD.

According to Selkoe and Hardy⁶ modified figure the altered A β metabolism is illustrated in EOAD and LOAD. (A) Synaptic changes, inflammation, oxidative stress, and tau phosphorylation are consequences of increased concentrations of soluble A β . In the early stage of this cascade, A β was shown to impair synaptic function. Further processes lead to neuronal dysfunction, cell death and dementia with plaque and tangle pathologies. (B) Illustration of a healthy control (HD) brain compared to AD⁷. Brain AD shows massive atrophy, thinning of the cortex and larger ventricles compared to the healthy brain. Extracellular amyloid plaques and intracellular accumulation of neurofibrillary tangle are the main pathologies of AD.

A complex interaction between genetic and environmental factors contributes to molecular processes that drive AD⁸. However, the molecular and cellular pathways causative for the disease are poorly understood, which prevents the development of efficient therapies.

1.1.1 Neuropathology of AD

Up to ten years before the first clinical symptoms appear, plaques form in the brain, which are composed of incorrectly folded A β peptides. In addition to the accumulation of extracellular A β , there is an intracellular accumulation of hyperphosphorylated tau protein⁹. The cytoskeleton, which consists partly of microtubules, has the function of structural integrity, and thus determines the neuronal morphology. Microtubule-associated proteins, such as the tau protein, serve to maintain the composition and stability of the microtubules¹⁰. Hyperphosphorylation of paired helical tau filaments leads to functional loss, which prevents it from further interacting with the microtubules¹¹. A β aggregates are generated by enzymatic cleavage of the amyloid precursor protein (APP) and are further processed by either non-amyloidogenic or amyloidogenic pathways. In the physiological non-amyloidogenic pathways, the α -secretase cleaves APP and leads to a fragment of 83 amino acids. In a second step, the generated fragment is further cleaved by the γ -secretase to a three amino acid-sized peptide, P3 (A $\beta_{17-40/42}$) and the A β precursor protein intracellular domain. In case of the amyloidogenic pathway, the β -secretase cleaves APP at the N-terminus, resulting in the fragment C99, which is subsequently cleaved by the γ -secretase¹² (**Fig. 2**). In 1991 Braak described a classification of AD stages. To establish the stages, the accumulation and anatomical localization of the protein's tau and A β were assessed. In contrast to A β , tau revealed a consistent increase in accumulation and with increasing severity of AD, anatomical localization assigned to the stages was affected.

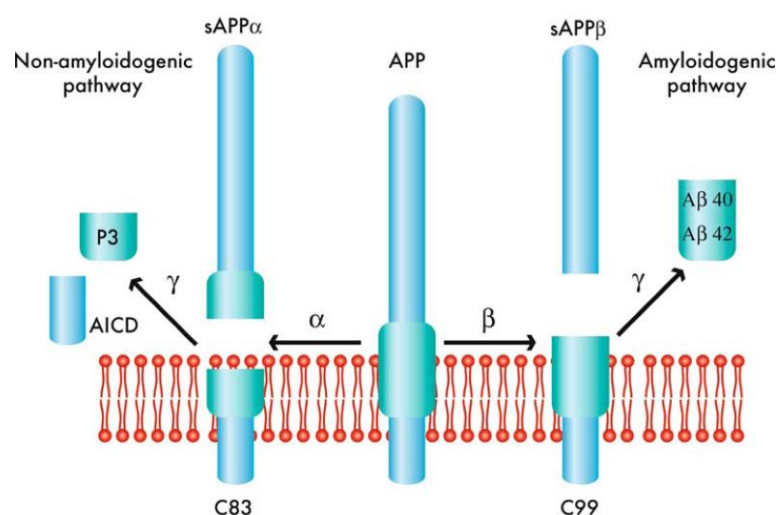


Figure 2: Enzymatic process of the amyloid-precursor protein.

The figure from Shepherd et al. shows different forms of APP cleavage¹³. APP cleavage by α -secretase followed by processing of soluble APP α (sAPP α) by γ -secretase produces the peptide p3 and the amyloid intracellular domain (AICD), which illustrates the non-amyloidogenic way. Cleavage by β -secretase followed of soluble APP β (sAPP β) by γ -secretase demonstrates the amyloidogenic way and generated A β peptide in the two forms of A β 40 and A β 42.

The Braak stages I and II are classified as mild, mainly restricted to the transentorhinal region of the brain, in stages III and IV, the limbic regions of the hippocampus are affected. In Braak stages V and VI, neocortex involvement occurs¹⁴.

1.1.2 EOAD

AD is the most common form of dementia that usually occurs in people over the age of 65, but up to 5% show EOAD before the age of 65. AD occurs predominantly sporadically, but can also be caused by autosomal dominant familial AD genetic defects in mainly the three genes APP, presenilin 1 and 2 (PSEN1 and PSEN2)¹⁵. Together, over 200 mutations have been described for the three genes, of which PSEN1 accounts for the majority of autosomal-dominant with 173 cases¹⁶. EOAD is most common in early-stage dementia, along with other forms such as, vascular dementia, frontotemporal dementia, drug-related diseases and autoimmune or infectious causes¹⁷. EOAD, in comparison to LOAD, is characterized by an increased accumulation of neuritic plaques and neurofibrillary tangles with the consequent loss of synapses in the frontal and parietal lobes. Furthermore, the two forms of AD differ in the localization of the atrophy occurring during the disease. While EOAD affects the neocortical area, LOAD causes increased atrophy of the hippocampus¹⁸.

1.1.3 LOAD

LOAD currently accounts for over 90% of described AD cases. By the age of 65 and older, more than 13% are already affected by AD, which rises to 30-50% in people older than 80 years. LOAD is up to 80% hereditary^{19,20}. LOAD occurs predominantly sporadically and is a complex multifactorial disease. Sporadic AD is not a monogenic defect and is thought to be caused by a number of genetic susceptibilities and environmental factors. One of the first and strongest susceptibility marker is a DNA variation in the gene apolipoprotein E (APOE) named the APOE4 allele²⁰. APOE4 is linked to the metabolism of A β , because it promotes A β aggregation and causes the erroneous release of A β ²¹.

1.1.3.1 Genome-Wide Association Studies in LOAD

Genome-wide association studies (GWAS) are a well-established and effective method for identifying genetic loci associated with a disease. GWAS involve the analysis of at hundreds or thousands of variants across the genome in large cohorts of individuals, divided into control and patient groups, to identify variants associated with the trait in question. Thus, GWAS offer the possibility to study diseases using genetic variants in order to achieve a better understanding of the underlying mechanism²². Until 2009, only one gene variant, APOE4, had been identified as a known risk factor^{9,23} in AD. In 2009, Lambert and co-authors published a two-step GWAS analysis performed on AD patients and controls. In addition to the two newly discovered susceptibility sites, clusterin (CLU) and complement C3b/C4b receptor 1 (CR1), they additionally found evidence of an association of phosphatidylinositol binding clathrin assembly protein (PICALM)

with AD in the first stage of the meta-analysis⁹. A collaborative consortium from Europe and the US performed a GWAS on 19,000 individuals with AD and controls in 2009, identifying the loci *CLU* and *PICALM* that are significantly associated with AD. Furthermore, the two genes bridging integrator 1 (*BIN1*) and DAB adaptor protein 1 (*DAB1*) were observed to be associated with AD²⁴. In 2010, a three-step GWAS meta-analysis was conducted with 35,000 individuals (8000 AD cases) to identify further associations with LOAD. For the loci *BIN1*, *CLU*, and *PICALM* significant associations with LOAD were identified²⁵. A combined GWAS analysis from four AD consortia - Genetic and Environmental Risk in Alzheimer's Disease Consortium 1 (*GERAD1*), Translational Genomics Research Institute (*TGEN1*), Alzheimer's Disease Neuroimaging Initiative (*ADNI*) and European Alzheimer's Disease Initiative 1 (*EADI1*) identified under the participation Prof. Rujescu's group the susceptibility loci ATP binding cassette subfamily A member 7 (*ABCA7*), encoding membrane spanning 4A (*MS4A*), CD2-associated protein (*CD2AP*), CD33 molecule (*CD33*, *SIGLEC3*), and encoding ephrin receptor A1 (*EPHA1*) in the year 2011 and verified also previously described loci²³. In addition to the nine genetic susceptibility factors already described, a further GWAS analysis in 2013 observed five newly associated loci: major histocompatibility complex, class II, DR β 1 and 5 (*HLA-DRB1*, *HLA-DRB5*), protein tyrosine kinase 2 β (*PTK2B*), sortilin-related receptor 1 (*SORL1*), solute carrier family 24 member 4- Ras and Rab interactor 3 (*SLC24A4*, *RIN3*), and desmoglein-2 (*DSG2*). Within a combined analysis another seven loci were found: CUGBP Elav-like family member 1 (*CELF1*), inositol polyphosphate-5-phosphatase (*INPP5D*), fermitin family member 2 (*FERMT2*), zinc finger, CW type with PWWP domain 1 (*ZCWPW1*), myocyte enhancer factor 2 (*MEF2C*), NME/NM23 family member 8 (*NME8*), and Cas scaffolding protein family member 4 (*CASS4*)²⁶. Genome sequencing techniques revealed in 2013 triggering receptor expressed on myeloid cells 2 (*TREM2*) as a susceptibility locus²⁷. *TREM2* variant was discovered with the participation of the working group of Prof. Rujescu. Another new and rare mutation was identified in the unc-5 netrin receptor C gene (*UNC5C*) one year later²⁸. Most of the genes identified by GWAS that are associated with AD can be classified into three superordinate signaling pathways. Susceptibility loci in *CLU*, *CR1*, *ABCA7*, *CD33*, *TREM2*, *MS4A*, *HLA-DRB1*, *HLA-DRB5*, *INPP5D*, and *EPHA1* show that the immune system plays a major role in AD. Susceptibility loci in *PICALM*, *SORL1*, *BIN1*, *CD33*, and *CD2AP* cover genes that regulate cell membrane processes including endocytosis. Susceptibility loci in *APOE*, *SORL1*, *DSG2*, *CLU*, and *ABCA7* target genes involved in cell's lipid metabolism^{23,29}.

1.1.3.2 APOE Function in the CNS and its Role in LOAD

APOE has been associated with sporadic AD in the age of 40-90 as a major risk factor, irrespective of gender and across all ethnicities. GWAS revealed differences between the populations. *APOE4* indicated a weaker association with AD among African Americans (4/4, odds ratio (OR) 5.7) and Hispanics (4/4, OR 2.2), while it was more strongly associated with AD among Japanese (4/4, OR 33.1) and Europeans (4/4, OR 12.5)³⁰. The OR is a calculated value that expresses the relationship between a suspected risk factor and a particular disease. It is defined by the ratio of the number of

diseased individuals with a risk factor / without a risk factor to those who are non-affected with a risk factor / without a risk factor³¹. The APOE protein belongs to the structural proteins in the phospholipid outer shell of lipoproteins. The transport of triglycerides and cholesterol in the blood is mediated by lipoproteins. In the brain, APOE is functionally involved in neurite growth, the regeneration of axons, and myelination of axons. The 34 kDa glycoprotein is synthesized and secreted mainly by astrocytes, but also by microglia and neurons after injuries³².

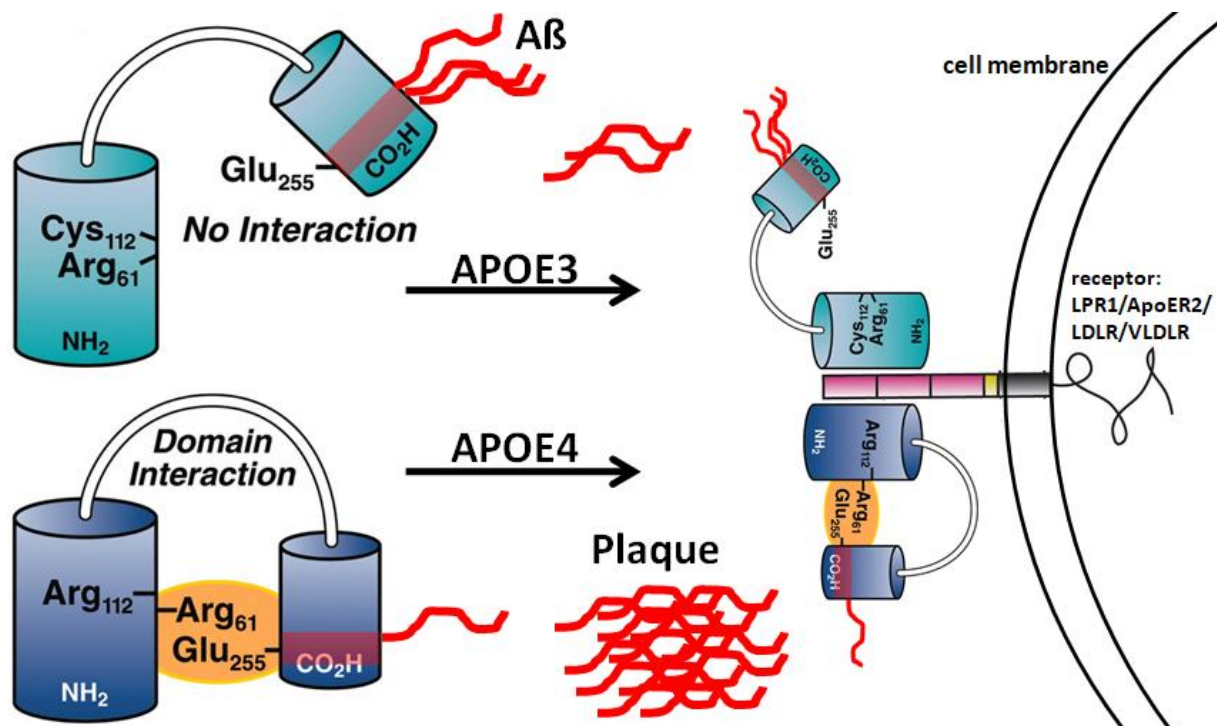


Figure 3: Apolipoprotein E isoforms

Arg-61 in the N-terminal domain of APOE4 interacts with Glu-255 in the C-terminal domain. In APOE3, this interaction is absent, resulting in a higher affinity to Aβ. APOE binds to its receptors via the N-terminal domain. The C-terminal domain harbors the binding site for Aβ. APOE4 leads to increased Aβ deposition supporting the accumulation of Aβ in plaques. Figure was adapted from Mahley R.W. et al³³. LPR1, low density lipoprotein receptor-related protein 1; ApoER2, apolipoprotein E receptor 2; LDLR, low density lipoprotein receptor; VLDLR, very low density lipoprotein receptor.

APOE is the only serum apolipoprotein present in the cerebrospinal fluid (CSF). Accordingly, it plays a crucial role in the central nervous system in lipid transport. For lipid transport, APOE proteins are loaded with essential lipids to supply neurons and glial cells by binding to endocytic APOE receptors on their surfaces³⁴. APOE is encoded on chromosome 19 and carries two single nucleotide polymorphisms (SNPs) that lead to three different isoforms: APOE2 (cys112, cys158), APOE3 (cys112, arg158) and APOE4 (arg112, arg158)³⁵. The SNPs belonging to the three different isoforms are rs429358 and rs7412³⁶. In Europeans, there are different frequencies for the different isoforms APOE2 (8.0%), APOE3 (80.0%), and APOE4 (12.0%). In AD patients, the frequency of the APOE4 is dramatically increased up to 40.0%³⁷. Even though the three isoforms of APOE differ only by one or two amino acids, the related structural changes are strongly impact APOE functions. APOE3 and APOE4 only differ in one amino acid (**Fig. 3**), which is very close to a domain responsible for initialization of lipid binding³⁸. The third isoform APOE2 accounts to a

lower amount in AD patients suggesting that there is a protective effect for AD³⁹. A β metabolism is depends on the APOE protein, especially in A β deposition and senile plaque formation (**Fig. 3**), and cerebral amyloid angiopathy, which are considered major hallmarks of amyloid pathology in AD brains⁴⁰. In line with this is the fact that APOE4 carriers (AD patients and cognitively normal individuals), are more prone to have a greater A β plaque load⁴¹. Specifically, APOE contributes to A β pathology by enhancing the A β load by controlling A β oligomerization, aggregation, and receptor-mediated clearance. In case of a dysfunction of one of those processes, the A β load is increased resulting in a faster plaque formation and aggregation. In contrast to APOE3, APOE4 directly interacts with A β resulting in an increase of A β fibrillisation²¹. In addition, impaired A β clearance also leads to A β accumulation in brain parenchyma, which enhances the accumulation of A β oligomers and amyloid plaques⁴².

1.2 Induced Pluripotent Stem Cells (iPSC)

1.2.1 Reprogramming Stem Cells

In 2006, a Japanese research group succeeded in generating induced pluripotent stem cells (iPSCs) from mouse fibroblast cells using a retroviral transduction with four transcription factors: Octamer-binding transcription factor 4 (OCT4, POU5F1), SRY-box transcription factor 2 (SOX2), MYC proto-oncogene, bHLH transcription factor (MYC), and krueppel-like factor 4 (Klf4)⁴³. One year later it was shown that human fibroblasts can also be reprogrammed into iPSCs using the factors OCT4, SOX2, Nanog homeobox (NANOG), and lin-28 homolog A (LIN28A). The obtained iPSCs share almost all properties with human embryonic stem cells (ESCs). Pluripotency means that they have the potential to develop into all cell types of the human body and can divide infinitely. Since the proto-oncogene MYC appears to pose a risk of tumor formation, the factors NANOG and LIN28A were used as a replacement for KLF4 and MYC to reprogram human fibroblasts⁴⁴. It is important to note that the use of retroviral and lentiviral systems increases the risk of mutations, as it can lead to genomic integration of transgenes⁴⁵. An excision of the exogenous transgenes is possible by using LoxP (locus of X-over P1) elements and Cre recombinase for transgene removal after lentiviral reprogramming⁴⁶. Lentiviruses have the capability to infect both dividing and non-dividing cells. They also extend the tropism of the virus through alternative envelope proteins and they induce an efficient and stable expression of the target genes, which together enables lentiviral transduction of many cells⁴⁷. In fact, it has been shown that both the transcriptomic profiles and the epigenetic signature of non-integrating iPSCs are more similar to ESCs than cells generated by integrating methods^{48,49}. Accordingly, non-integrating methods very developed using episomal plasmids, non-integrating viral vectors, mRNAs, miRNAs, proteins, small molecules⁴⁹, and transposons⁵⁰. There are advantages and disadvantages of each reprogramming method. The selection of an appropriate method depends on many factors including the number cells available for reprogramming, the cell type or the source tissue, the expected reprogramming efficiency, expected footprints⁵¹. The efficiency of the most

commonly used non-integrating reprogramming methods is different with highest efficiency for mRNA-based reprogramming (2.1%) and low efficiencies for Sendai virus-based vectors (0.077%) and episomal plasmids (0.013%)⁵². In contrast, lentiviral reprogramming shows higher efficiencies (0.27%). However, the success rate of the individual reprogramming strategies between different laboratories, obtained as well, showed that the mRNA-based method is the most unreliable with 27%, in contrast to the Sendai virus-based method with 94%, the method with episomal plasmids with 93% and reprogramming using lentiviruses with 100%⁵². For the generation of patient-specific iPSCs, there are two common somatic donor cell types representing fibroblasts^{53,54} and hematopoietic progenitor cells carrying the antigen CD34 molecule (CD34) obtained from peripheral blood⁵⁵. Other methods for other somatic cells have been developed such as umbilical cord blood^{56,57}, neural stem cells⁵⁸, dental bulb cells⁵⁹, epidermal keratinocytes⁶⁰, urine cells⁶¹, adipose-derived stem cells⁶², and umbilical cord endothelial cells⁶³. In mice, iPSCs were also generated from bone marrow⁶⁴, stomach, and liver cells⁶⁵. B-lymphoblastoid cell lines (B-LCL) have been used sporadically, but they are stable, easy to cultivate, and easily accessible, making them a well suited starting material for the generation of patient-specific iPSCs⁶⁶.

1.2.2 Characteristics of iPSCs

Stem cells are primitive cells that can be divided into five groups according to their differentiation potential⁶⁷. The cells have the ability to develop into identical stem cells on the one hand or to specify themselves into somatic cells on the other hand. Due to a high expression of the protein telomerase, stem cells become senescent to a lower extent and are capable to undergo a certain number of divisions depending on the potency of stem cells. Totipotent (omnipotent) cells are zygotes, which are capable to build the whole organism. Pluripotent stem cells (iPSCs, and ESCs) have the potential to develop into all cells of the human body, whereas the potency of multipotent stem cells (adult stem cells) is much more restricted to cells of a certain tissue or organ⁶⁸. The differentiation potential for oligopotent stem cells is even more restricted to a few different cell types and unipotent stem cells are restricted to one cell type⁶⁷. A major advantage of iPSCs is that they offer the possibility of autologous transplantation in regenerative medicine, while allogeneic cell transplantation with ESCs requires the administration of immunosuppressive drugs to suppress an immune response⁶⁹. Obtaining donor material from human beings to produce iPSCs is much less disputed in comparison to obtaining in vitro fertilized eggs for the generation of human ESCs^{51,70}. Likewise, ESCs and iPSCs are used for the generation of different cell types for modelling of diseases, but iPSCs can be used to generate cells in a patient-specific manner. Patient-specific in vitro cultures can be used for cell- and disease-specific drug screenings or to investigate genetic variations (mutations, SNPs). Patient-specific in vitro cultures provide a tool for elucidating underlying mechanisms of diseases that are difficult to study⁷¹. Most established drugs on the market have been developed by drug screening in animal models. The disadvantage of animal models is that the pathophysiology of diseases is most often not fully understood due to species differences. Application of the iPSC technology allows to extend drug screenings for diseases where the underlying mechanisms are not yet understood^{72,73}. These can now be used not only for drug

screening, but also for modeling diseases⁷⁴⁻⁷⁶, cell replacement therapies^{77,78}, and gene therapies⁷⁹. In addition, iPSCs are able to develop three-dimensional organoid cultures. These more complex iPSC-based organoid cultures represent a physiological interface between human cell culture and animal models⁸⁰. Organoids have already been successfully produced for the brain. The morphology of the brain organoids as well as biological functions such as cell-cell and cell-matrix interactions has been demonstrated in an approximately physiological way. In addition to the production of three-dimensional cultures of the brain, organoids of the liver and lung are most important for translational medicine, as these organs are crucial for late stage drug screenings⁸¹.

1.2.3 In vitro iPSCs for Modelling LOAD

Disease-specific iPSC models are used to investigate the course of diseases and the function of substances in the human body. These disease models are also able to depict the development and course of specific diseases and the underlying molecular processes. The use of iPSCs has enormous advantages regarding the creation of disease models. Due to the manufacturing process of iPSCs using somatic donor cells, the high demand for pluripotent cells for such models can be met more easily and specifically than is possible with human ESCs. In addition, iPSCs can be used to create patient-specific models for the mimicking disease progression. The individual effect of certain therapies on the patient can be reproduced using tissue models if these are derived from personalized iPSCs. Patient-specific iPSC models were already generated and have been used in different diseases models, such as cancer, neurodegenerative diseases or heart disease⁸². Especially, for neuropsychiatric diseases, iPSCs hold a great promise because the access to the affected brain cells in human beings is limited. Patient-specific iPSC models were shown to reproduce disease-related phenotypes in vitro⁷¹. However, there is a problematic patient stratification in clinical studies due to the lack of established phenotypic and genetic AD markers. Similar to AD models using zebrafish and rodents, human iPSCs offer the possibility to study both EOAD and LOAD⁸³. There is a broad set of different AD mutations that could be analyzed in iPSCs representing a major advantage to study AD subtypes. Thus, iPSCs are a powerful human screening tool. Although mouse models offered the basis for elucidating AD pathomechanisms over the last decades, they lack mimicking certain human-specific aspects of the AD pathophysiology. Most mouse models carry mutations known from EOAD in PSEN1, PSEN2 and APP. However, mutations in these genes are almost indispensable for onset of LOAD⁷⁴.

Human iPSCs overcome this obstacle as they can be generated from donor material of both familial and sporadic AD patients carrying related mutations. Once generated and cultured, iPSCs can differentiate into certain cell types and grow into a three-dimensional culture. Those cultures can be differentiated into neural cells carrying distinct AD-associated genotypes and assayed in vitro. Although iPSCs are a cellular system, they mimic specific AD pathomechanisms including A β peptide production, amyloid plaques, tau pathology, synaptic dysfunction, immune activation, genomic instability, and aberrant endosome trafficking⁸⁴. However, an important disadvantage of iPSCs is the partial lack of maturity because age-related epigenetic marks are erased during reprogramming⁸⁵. This is also the case for neuronal cultures differentiated from iPSCs as the

obtained differentiated neurons are characterized by a fetal, immature phenotype without traces of maturity signatures of their source cells⁸⁶. Nevertheless, although iPSCs lack the above mentioned maturity signatures, certain phenotypic characteristics of LOAD can be observed⁸⁷. Moreover, the iPSC technology offers the possibility of gene engineering of the cellular ontogeny of interest. By gene correction of these iPSCs, mainly via clustered regularly interspaced short palindromic repeats endonuclease cas9 (CRISPR cas9), isogenic controls can be obtained and compared to the non-corrected ones showing disease phenotypes. While this approach is an important step to gain insights into AD pathomechanisms, the interpretation of the obtained data must be considered with care. Apart from the isogenic control approach in AD, iPSCs can also be generated from both LOAD and EOAD patients and compared to those of healthy control subjects. An example of such an approach was recently described for the manipulation of APOE⁸⁸. Microglia are of great importance in the development and progression of AD. Modelling of AD in microglia using iPSC technology enables a better understanding of the underlying disease mechanisms related to the risk factors identified by GWAS such as APOE, TREM2, CD33, CR1, and MS4A. Recently, it has become possible to differentiate mature and functional microglia-like cells (MGLCs) comparable with primary cells. Based on the model using iPSC-derived MGLCs, it should be possible in the future to gain new insights into AD⁸⁹.

1.3 Microglia

The central nervous system (CNS) is composed of nerve cells (neurons) and a special connective tissue, the glial cells. These glial cells make up almost half the volume of the entire CNS and account for about 90% of its cells⁹⁰, with microglia accounting for about 10%⁹¹. Microglia are immunocompetent myeloid cells that play an important role in the maintenance of the brain. Robertson was the first, who described these cells and named them mesoglia cells⁹². Initially, the cells were described as rod cells by Franz Nissl⁹³ or as granular cells by Alois Alzheimer⁹⁴, who noticed that they accumulate near inflammation-induced lesions in the CNS. As immune cells of the brain, microglia exist mainly in a dormant stage and continuously monitor their cellular environment⁹⁵. As soon as an injury or infection by bacteria occurs in the CNS, microglia are activated. When activated, microglia play a crucial role in the removal of debris through their phagocytosis function⁹⁶. Based on the major histocompatibility complex (MHC) class II, microglia can additionally present the antigens on their surface to other immune cells, such as T cells⁹⁷. Activated microglia have neuroprotective functions in which microglia produce anti-inflammatory factors to provide trophic support to neurons when they get damaged⁹⁶. In addition, microglia have a fundamental function in controlling neuronal proliferation, differentiation, and the formation of synaptic connections. Thus, microglia are involved in the development of neural networks and are able to recognize and take away malformed neurons⁹⁸. Microglia possess receptors for neurotransmitters such as adenosine triphosphate (ATP) and glutamate, which enables the cells to be regulated and activated. Together with the complement proteins complement component 1q and complement component 3 on the surface of the microglia, they play a crucial role in synaptic

development and synaptic pruning⁹⁹. Microglia highly express the enzyme nicotinamide adenine dinucleotide phosphate oxidase, which enables them to produce extracellular reactive oxygen species. This oxygen species can induce long-term synaptic depression and may be involved in the regulation of synaptic activity¹⁰⁰.

1.3.1 Microglia Origin and Development

The exact origin of the microglia has not yet been fully clarified. However, three hypotheses are described in the different studies so far. According to the first hypothesis, microglia are formed during embryonic development from erythromyeloid progenitor cells or primitive macrophages of the yolk sac before peripheral hematopoiesis occurs. A second hypothesis describes how circulating monocytes migrate into the already developed brain, where they take on an amoeba-like form of microglia, which then develop into branched microglia¹⁰¹. Furthermore, there is a third and rarer hypothesis, whereby microglia develop from infiltrated pericytes¹⁰². The development of microglia according to the second hypothesis provide the basis for the iPSC-based differentiation model described in this thesis and will now be described in detail. Gastrulation describes a stage of embryogenesis in which the hypoblast layer at the end organizes itself into a trilaminar structure corresponding to the three germ layers. The germ layer that is decisive for the nervous system is the ectoderm, providing the basis for the development of both the skin and the neuroectoderm¹⁰³. Microglia arise from the peripheral mesodermal tissue. In early mesodermal differentiation, stem cells positive for KIT proto-oncogene, receptor tyrosine kinase (KIT, alias c-kit) develop into both erythroid and myeloid precursor cells in the yolk sac. In this way they can develop into microglia and macrophages¹⁰⁴. Hemangioblast cells are formed in the posterior primitive streak during embryogenesis and migrate into the yolk sac, forming islands of blood at embryonic day (E) 6.5-7.0. Later in development, primitive erythroblasts and primitive macrophages are formed at a stage of E7.0-7.5 and primitive macrophages at a stage of E8.5-9.0. At the beginning of the circulation, the primitive macrophages leave the yolk sac and spread into the developing brain at E10.5 to form microglia¹⁰⁵. Microglia development begins when precursor cells migrate into the yolk sac. For the controlled differentiation of microglia, some key factors are required. Runt-related transcription factor 1 (RUNX1) plays a key role in this process by binding directly to enhancer elements of several genes that are crucial for hematopoietic development¹⁰⁶. Transcription factor Spi-1 proto-oncogene (SPI1, alias PU.1) is a key transcription factor in microglial development, which is bound by the enhancer of RUNX, thereby modulating its expression throughout development towards mature microglia^{104,106}. The expression of the receptor for colony stimulating factor receptor (MCSF-R) is additionally regulated by RUNX1¹⁰⁷. Initial RUNX1 positive cells are observed at E6.5-7.5. RUNX1 is responsible for the differentiation of stem cells into myeloid and erythroid precursors of hematopoietic origin¹⁰⁸. Except for lesions, in which microglia proliferate strongly and are amoeboid, RUNX1 is not further expressed in adult ramified microglia. This indicates an involvement of RUNX1 in microglial activation¹⁰⁹. Another important transcription factor is PU.1, which is continuously activated in quiescent and activated microglia and is a major regulator of myeloid differentiation during embryonic development. PU.1 is essential for the

maturation of myeloid precursors in the yolk sac and the expression of terminal myeloid markers such as MCSF-R, integrin subunit alpha M (CD11B), integrin subunit beta 2 (CD18), and Fc fragment of IgG receptor Ib (CD64)¹¹⁰. Via MCSF, PU.1 can be activated and thus stimulate enhanced myeloid differentiation of hematopoietic stem cells¹¹¹. The control of PU.1 expression has an impact on function in adult microglia by regulating phagocytosis¹¹². Another key regulator of myeloid lineage cells is MCSF-R. The two natural ligands MCSF and interleukin 34 (IL34) regulate the proliferation, differentiation, and survival of macrophages and microglia¹¹³. Interferon regulatory factor 8 (IRF-8) is involved as a transcription factor in the development of the immune system by playing a key role in differentiation into phagocytic myeloid progenitor cells. IRF-8 is also involved in maintaining homeostasis and regulating the activation of microglia. In embryonic development, the expression of IRF-8 is significantly higher than in adult microglia. IRF-8 also plays a crucial role in the development of microglia¹⁰⁴. During development in yolk sac progenitors, IRF-8 is decisive for the induction of EGF-like module-containing mucin-like hormone receptor-like 1 (F4/80) and C-X3-C motif chemokine receptor 1 (CX3CR1)¹¹³. For the development of myeloid progenitor cells, which do not migrate from yolk sac directly into the CNS, but differentiate towards monocytes, the two factors cytokine thrombopoietin (TPO) and fms related tyrosine kinase 3 (FLT3) are additionally required in later embryonic development¹¹⁴. Adult microglia are able to maintain their CNS population by self-renewal, with peripheral blood cells contributing marginally. Monocytes are slightly separated from microglia in terms of development and function^{113,115}. Under certain conditions, monocytes are able to migrate into the brain parenchyma and differentiate into microglia, which integrate into the network of the resident microglia population¹¹⁶. Inflammation can be a major trigger, in which bone marrow derived precursor cells and monocytes can migrate the blood-brain barrier to enter the CNS¹¹³. Furthermore, it could be demonstrated in a mouse model that peripheral monocytes are recruited into the CNS even in neurodegenerative diseases such as Parkinson's disease and AD. These myeloid or bone marrow derived MGLCs differentiate locally and are found in case of AD near A β plaques¹¹⁷.

1.3.2 Microglia Mediated Pathology

1.3.2.1 Microglia Phenotypes in AD

Recent studies highlighted the pivotal role of neuroinflammation, especially of microglia in AD, as there is emerging evidence of microglia surrounding A β plaques¹¹⁸. Resident ramified microglia are highly ramified. During activation by A β plaques, the morphology of microglia is rapidly changing to amoeboid and highly motile cells, which accumulate close to A β plaques^{119,120}. The resident ramified cells change to amoeboid. Further, the number of microglia increases during AD progression due to proliferation of brain-derived microglia and the migration of bone marrow derived progenitor cells and circulating monocytes via the plexus choroideus¹¹³. Large GWAS revealed several SNPs in genes encoding for microglia proteins involved primarily in processes as phagocytosis and cytokine production. These microglia proteins are encoded by genes as TREM2,

CD33, inositol polyphosphate-5-phosphatase D (INPP5D alias SHIP1), and APOE. A special role is attributed to the TREM2-associated protein TYRO protein tyrosine kinase-binding protein (TYROBP) which was found to be involved in LOAD postmortem brain tissue¹²¹. However, it is difficult to distinguish which microglia functions are the result of AD and which are just age-related, although there seems to be a clear association with LOAD. Current works described alterations in the genes TREM2 and CD33, which show that there is a clear link between microglia and AD pathophysiology. Apart from that, it was shown that A β deposits are linked with activated microglia, as well as induce the secretion of proinflammatory cytokines, chemokines, ROS, and acute phase proteins. Interestingly, fibrillar forms of A β can also trigger the secretion of the same proinflammatory cytokines, including interleukin 1 beta (IL1 β), interleukin 6 (IL6), tumor necrosis factor alpha (TNF α), transforming growth factor beta 1 (TGFB1 aka TGF β), and other proinflammatory proteins, as well as the formation of ROS. Nevertheless, A β fibrils were associated with NLR family pyrin domain containing 3 (NLRP3) inflammasome activity, which is involved in AD pathogenesis and disease progression¹²². However, the exact pathomechanisms of microglia in LOAD remains to be elucidated.

1.3.2.2 Mechanisms of Microglia Activation

Microglia activation takes place in several activation stages. In the early stage of activation there is an increased proliferation. At the stage of homeostasis, the cells respond immediately to the slightest changes in the environment, which initiates the activation. At the same time, the phenotype changes, in which the branched, resting microglia transform into round cell morphology and upregulate activation markers such as C3 and MHC class I and II antigens¹²³. Among the proteins of the complement system, there are expression changes in proteins involved in cell adhesion, cytoskeletal remodeling, cell-cell interaction, membrane transport, chemokine signaling, and intracellular degradation pathways. Furthermore, immediately after the detection of a lesion, the nuclear factor NF-kappa-B (NFkB1 alias NF- κ B) is formed, which co-regulates the migration with the involvement of integrins such as integrin alpha-L (ITGAL). Thus, NF- κ B is of crucial importance in the activation and motility of microglia by regulating gene expression¹²⁴. Signaling molecules such as IL1 β , IL6, TNF α , and TGF β are responsible for the activation of the microglia as occurs after injury¹²⁵. However, the strongest mitogens are macrophage MCSF and granulocyte-macrophage colony-stimulating factor (GMCSF), which is secreted by activated astrocytes¹²⁶. Microglia may directly regulate synaptic activity, enabling them to play a role in neuronal plasticity. The perception of released ATP/ADP and adenosine or concentration changes of neurotransmitters, especially glutamate, activates the cells⁹⁹. Glutamate acts as a second messenger regulating mitogen-activated protein kinases (MAPKs), phosphatidylinositol-3-kinase/Akt (PI3K/Akt), NF- κ B, phospholipase C (PLC) and calcium/calmodulin signaling activity¹²⁷. Brain-derived neurotrophic factor (BDNF) can be released via activation of the protein kinase C (PKC) signaling pathway and intracellular release of calcium¹²⁸. The ATP signals are detected by P2Y purinoceptor 12 (P2Y12), causing the microglia to move rapidly towards the region of injury or inflammation. Binding to the P2Y12 receptor initiates mainly the PLC and PI3K

signaling pathways and appears to play a role in the migration¹²⁹. Adenosine receptors counteract this signal. Activation of microglia via ATP and glutamate also regulates the production of TNF α , IL1 β , BDNF, prostaglandin E2 (PGE2), and ROS¹³⁰. Conversely, TNF α is released by low glutamate levels, which binds postsynaptically to tumor necrosis factor receptor 1 (TNFR1), thereby increasing neuronal activity by increasing the expression of glutamate receptors¹³¹. The activity and protein expression of glutamate receptors can likewise be influenced by IL1 β ¹³². Morphological changes and the release of second messenger have an enormous influence on the movement behavior of the microglia. This behavior can be regulated by cell-cell contact as well as by released substances. The activated microglia cell moves very quickly to the dying cell due to the released substances¹³³. Another mechanism that plays an important role in the activation of microglia is the regulation of ion channels. Potassium and chloride channels are involved in the alteration of cell shape and volume, which is controlled by the membrane potential. Thus, these channels are required in the biological processes of intracellular calcium turnover, cytoskeletal rearrangement, and the cell cycle, which in turn are crucial for morphology, proliferation, migration, and motility. Additionally, potassium concentration regulation is involved in the maturation of IL1 β in the cytosol by activating the cascade of caspase-1¹³⁴. Potassium efflux activation and P2Y12 receptor activation are closely related¹³⁵.

1.3.2.3 Immune Receptors in Health and Disease State

Microglia play a central role in the progression of AD as immune cells by phagocytizing A β and releasing proinflammatory cytokines. In the case of activation of microglia, as occurs by A β , a variety of immune receptors are expressed, which are required for recognition, internalization and clearance¹³⁶. Microglia surrounded by A β plaques reveal a change in the expression of scavenger receptors. This group is capable of binding both pathogens and endogenous substances. Class A scavenger receptors bind and internalize lipids¹³⁷, while class B receptors, such as platelet glycoprotein 4 (CD36), are additionally involved in the phagocytosis of pathogens. CD36 also appears to be closely related to toll-like receptors (TLR) by forming a heterodimeric complex with TLR-4 and TLR-6 by binding to A β ¹³⁸. As an important microglial marker, CD68 in turn belongs to the group of scavenger receptors and is classified in class D. The expression of macrophage marker (CD68) increases significantly after activation of microglia¹³⁹. TLRs are among the most prominent receptors that microglia need to recognize signals from the immune system. For AD, TLR4 and TLR2 receptors have been identified as particularly important. Monocyte differentiation antigen CD14 (CD14) provides a co-receptor for the two TLRs and is involved in the clearance of A β and together they increase the phagocytosis rate¹¹⁸. TLR responses are regulated by binding of TREM2 to TYROBP¹⁴⁰ (see 1.3.3.2). Nucleotide-binding oligomerization domain-like receptors (NOD-like receptors) are another pattern-recognition receptor besides TLRs involved in the immune response and immune homeostasis. Activated NOD-like receptors are associated with TLRs and appear to be involved in the clearance of A β and IL1 β maturation (see 1.3.2.1). Inflammasome formation, signal transduction, transcriptional activation and autophagy are further functions of NOD-like receptors that play a role in the progression of AD^{122,141}. Furthermore, the chemokine receptor

CX3CR1, is of major importance in the progression of AD by paracrine signal transmission between neurons and microglia. In contrast to the previously mentioned receptors, the clearance of A β is increased with reduced expression of CX3CR1¹⁴². In the brain, besides neurons and astrocytes, microglia are the cells that express glucagon-like peptide 1 (GLP-1) and the corresponding G protein-coupled receptor, GLP-1 receptor (GLP-1R). Both GLP-1 and GLP-1R are downregulated when microglia are activated. Furthermore, GLP-1R is enabled to regulate proinflammatory cytokines with the support of exendin-4¹⁴³. GLP-1 regulation has also been related to impaired A β clearance in AD¹⁴⁴. As already mentioned in the chapter 1.3.2.2, the purine receptor P2Y12 is involved in the immune response via signals such as ATP and ion channels. Together with Fc receptors, P2Y12 is involved in the phagocytosis complex and may play a role in plaque clearance. Microglia express activating and inhibiting Fc receptors, providing a regulatory function for phagocytosis and the release of cytokines¹⁴⁵.

1.3.3 CD33 Molecule

CD33 is a 67 kDa transmembrane protein that belongs to the siglecs. CD33 is expressed on hematopoietic and phagocytic cells, such as macrophages, monocytes, dendritic cells and microglia cells¹⁴⁶. It is composed of an extracellular sialic acid binding N-terminal V-set immunoglobulin domain and a variable C2-set Ig domain. A transmembrane domain connects the extracellular part with the cytoplasmic region, which is mostly formed by two immunoreceptor tyrosine-based inhibition motifs (ITIMs)¹⁴⁷. Human CD33 binds preferentially to alpha-2,6-bound sialic acid and is different from CD33 in mice^{148,149}. CD33 of the mouse has a different intracellular composition of the motifs. Instead of one ITIM domain and one ITIM-like domain as in humans, the mouse has one ITIM and two Atypical ITIM domains¹⁴⁸. The binding of the sialic acid and CD33 is based on a positively charged conserved arginine residue in the active site of CD33 and the sialic acid which is attached to glycoconjugates. This binding leads to a salt bridge, which enables a stable interaction¹⁴⁹. Switching on the ITIM domains leads to phosphorylation, which in turn leads to the recruitment of SH2 domains containing tyrosine phosphatases 1 and 2 (PTPN6 alias SHP1 and SHP2 alias PTPN11) and SH2-domain-containing effector molecules. CD33 is an inhibitory receptor that plays a role in the regulation of innate immunity¹⁴⁷.

1.3.3.1 CD33 Molecule in LOAD

CD33 is one of the risk factors for LOAD identified by GWAS and replicated in various genetic and ethnic group analyses^{19,23,26,150,151}. In the brain, CD33 is a myeloid immune receptor expressed exclusively on microglia. In patients suffering from AD, an increased expression of the surface marker has been observed, which probably inhibits phagocytosis and the associated A β clearance¹⁵². So far there is no evidence that CD33 behaves differently with age¹⁵³. The process of alternative splicing of exon 2 seems to regulate CD33 surface expression. Exon 2 encodes the Ig-V set domain, which is responsible for the binding of sialic acid, which leads to the activation of the receptor¹⁵². So far, sialic acid is the only known ligand for CD33, implying its functional importance¹⁵⁴. One AD susceptibility SNP, rs3865444, is located 373 base pairs upstream in the promoter region of

CD33 and is directly involved in the splicing of exon 2. An increased expression of the full-length CD33 isoform was associated with the C allele of SNP rs3865444. The truncated form of CD33 lacking exon 2 shows no changes¹⁵². The SNP rs2455069 also causes truncated CD33 by an amino acid exchange Arg69Gly at the 168th base of exon 2 and is associated with AD^{155,156}. The two SNP rs2455069 and rs3865444 are in linkage disequilibrium¹⁵⁷. A further SNP associated with LOAD in CD33 is located 1722 base pairs upstream of the coding region. This SNP, rs3826656, is associated with increased expression of CD33¹⁵⁸. Less frequently mentioned variants, such as rs1354106¹⁵⁹, rs1803254¹⁶⁰, rs201074739¹⁶¹, rs34813869¹⁶², rs35112940¹⁶³, rs73932888 and rs8112072¹⁶⁰ are associated with AD or mild cognitive impairment but have not been further investigated.

1.3.3.2 CD33 and TREM2

TREM2 is a transmembrane glycoprotein consisting of an extracellular V-set immunoglobulin-like domain that binds to the adapter receptor, such as TYROBP, via a charged lysine residue in the transmembrane domain. Intracellularly, it has a short cytoplasmic tail¹⁶⁴. Microglia express TREM2 very strongly on their surface and several GWAS have identified it as a very strong AD risk factor besides APOE4¹⁶⁵. The extracellular domains are responsible for ligand recognition and subsequent binding, while the intracellular motifs of the receptors transmit the signals as an immunological response. An activation of the signaling cascade is induced by immunoreceptor tyrosine-based activation motif (ITAM) domains, while the ITIM domain has an inhibitory effect. ITAM-domain activated pathways are evolutionarily highly conserved processes involved in a complicated intracellular signaling cascade that leads to immune responses such as phagocytosis and cytokine release¹⁶⁶. The activation of intracellular ITAM domains, such as TYROBP or Fc-receptors, occurs via charged amino acids in a transmembrane domain of immune receptors like TREM2. After binding of a ligand to the receptor, the recruitment of the Src-kinase family (SKF) members leads to phosphorylation of the tyrosine residues of the ITAM domain. The phosphorylated domain serves as an adapter for the Src homology 2 (SH2) of the spleen associated tyrosine kinase (SYK) protein kinase, thereby initiating the activating signaling pathway¹⁶⁷. To activate the signaling pathways, SYK recruits growth factors such as growth factor receptor binding protein 2 (GRB2). Phosphorylation of GRB2 activates the signaling pathways PI3K and extracellular signal-regulated kinase (ERK). These pathways regulate calcium and the activation of NF- κ B leads to the release of pro-inflammatory cytokines and chemokines¹⁶⁶. As a counter-regulation to the activating ITAM domain, the ITIM domain has an inhibiting function (**Fig. 4**).

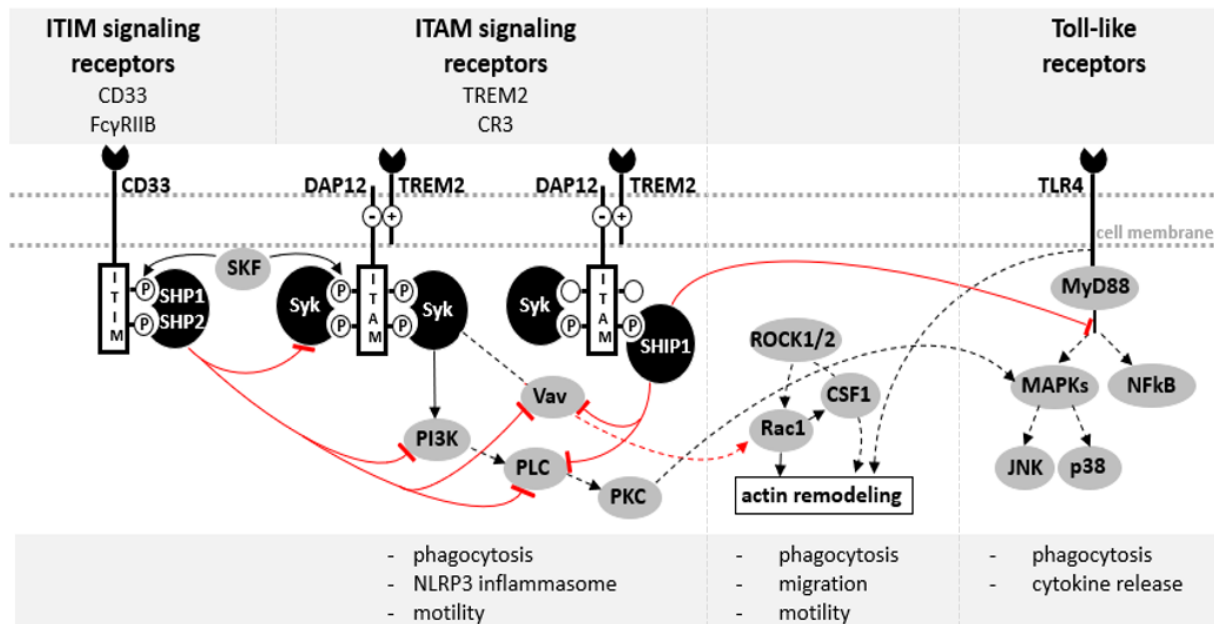


Figure 4: Microglial ITIM – ITAM cascade signaling.

ITAM-containing adapter receptors, such as TYROBP (alias DAP12), interact with the activating receptors, such as TREM2 and CR3, via charged amino acids (-/+) of the transmembrane domain. By binding ligands, SKF phosphorylate the ITAM and ITIM domain at the tyrosine residues. SyK protein kinases bind to phosphorylated ITAMs and activate the signal cascade. Inhibitory receptors with ITIM domain, such as CD33 and low affinity immunoglobulin gamma Fc region receptor II-b (FcγRIIB), recruit SHP1/2, which can suppress the signals of the activating receptors containing ITAM domains via phosphatase activity¹⁶⁸. SHP1 activation leads to dephosphorylation of Rho-family guanine-nucleotide exchange factor Vav (Vav) and the downstream Rac1¹⁶⁹. Cofilin 1 (CSF1) is one of the key proteins for actin remodeling whose phosphorylation status is regulated by rho-associated protein kinase (ROCK) and Rac family small GTPase 1 (RAC1) among others¹⁷⁰. Inhibition by SHP1/2 blocks SyK-signaling. Additional inhibition is caused by monolateral SYK ITAM ligand binding and recruitment of SHIP1 to the ITAM domain of DAP12. This results in downstream inhibition of PI3K, PLC- γ , MAPK and NF- κ B and inhibition of TLR-associated myeloid differentiation primary response protein MyD88 (MyD88), which limits the TLR-induced pro-inflammatory cytokine response¹⁷¹. Resulting biological processes such as cytokine release and actin cytoskeleton remodelling are inhibited by activated ITIM domains, thereby blocking JNK, p38, PLC and PKC. Altered phagocytosis, motility and migration are consequences of the modulation of the actin cytoskeleton. The figure is modified according to Linnartz et. al¹⁶⁸.

Inhibitor receptors with ITIM domains, such as CD33, suppress the activation signals of the ITAMs after ligand binding. Inhibition is achieved by recruiting SHIP1, SHP1 and SHP2, which in turn can modulate the function of different signaling pathways^{172,173}. After activation of the ITIM cascade by SHP1 and 2, these phosphatases directly remove phosphate groups from substrate proteins that ITAM-induced activation requires, resulting in inhibitory biological functions such as cell adhesion, endocytosis, and cytokine release¹⁶⁸. An additional calcium-dependent inhibition of the downstream pathways MAPK, RAS, and ERK is induced by the recruitment and activation of SHIP1¹⁷⁴ (**Fig. 4**). A partial dephosphorylation of the ITAM domain induces a recruitment of SHIP1 and an associated actin depolarization. SHIP1 recruited at ITAM has an inhibitory effect on TLR signaling (**Fig. 4**), especially TLR4, by dephosphorylation of the signal intermediates¹⁷¹. By binding highly sialylated proteins and lipids such as CLU, APOE, and gangliosides, which are abundant in AD plaques, an inhibitory signaling cascade could be mediated¹⁷². The clearance of microglia-mediated phagocytosis could be disturbed by this inhibitory effect.

1.4 Aims of the Study

The establishment of patient-specific iPSCs and the development of a microglia differentiation protocol to analyze LOAD is the overall goal of this work. Combining LOAD-specific iPSC lines and their differentiation into microglia allows the analysis patient-and diseases-specific aspects of LOAD. For this purpose, B-LCLs of both LOAD patients and matched controls need to be genotyped for certain LOAD-associated DNA risk variants. Further, B-LCLs of patients carrying risk variants and controls without risk variants need to be reprogrammed to patient-specific iPSCs and differentiated into microglia. Therefore, a microglia differentiation protocol needs to be established. There is a need to characterize the established protocol for the generation of MGLCs and to perform functional analysis of obtained MGLCs from LOAD patients and matched controls. Together, there are the following aims:

- I) the generation of LOAD-specific iPSC lines**

- II) the establishment of a new differentiation protocol generating MGLCs from iPSCs**

- III) the functional analysis of LOAD-specific MGLCs in comparison to matched controls**

2 Materials and Methods

2.1 Ethical Considerations and Patient Classification

The ethical approval for the use of the donor material was obtained from the Ethics Committee of the Ludwig Maximilian University Munich. Dementia was diagnosed in patients according to criteria proposed by the diagnostic and statistical manual of mental disorders (DSM-IV). According to the Mini Mental Status Examination, family history was evaluated to exclude subjects with a known psychiatric history. In addition, all subjects were over 60 years old. In order to assess cognitive performance, the Wechsler Adult Intelligence Scale, Revision 1991 was applied. For genotyping, chip technology and imputation were used.

2.2 Cell Culture

2.2.1 Culture of Human iPSCs

WAI001-B (also known as iPS-DF19-9-7T) and WAI004-B (also known as IPS(IMR90)-4 or WISCi004-B) were obtained from the Wisconsin International Cell Bank (WiCell Research Institute, USA). MLUi007-J, MLUi007-H, MLUi008-B, MLUi009-A, and MLUi010-B were generated in this thesis by reprogramming of B-LCLs. Therefore, a recently published protocol¹⁷⁵ was modified by the treatment with 1.0 μ M BIX-01294 (histone-lysine methyltransferase) and 0.04 μ M RG-108 (DNA methyltransferase inhibitor; both from Merck, Germany). Cells were grown in at 37.0°C in a humidified environment of 5.0% O₂, 5.0% CO₂, and 90.0% N₂ (hypoxia). Cells were cultured in mTeSRTM1 (Stemcell Technologies, Germany) supplemented with 1.0% 10000 U/10000 μ g penicillin/streptomycin (Thermo Fisher Scientific, Germany) on MatrigelTM (VWR, Germany) using 0.5 mg in 6.0 ml KnockoutTM-DMEM (Thermo Fisher Scientific, Germany) for coating of one 6-well plate.

2.2.2 Culture of primary cells and cell lines

2.2.2.1 Human Embryonic Kidney cells

Human embryonic kidney (HEK293T, ATCC® CRL-11268TM) cell line was obtained from the American Type Culture Collection (ATCC, Germany). The cells were cultured in DMEM (Thermo Fisher Scientific, Germany) supplemented with 2.0 mM L-glutamine, 1.0% 10000 U/10000 μ g penicillin/streptomycin, and 10.0% fetal bovine serum (FBS) (Biochrom, Germany) (HEK-medium). HEK293T cells were seeded in a cell concentration between 6 and 7 x 10⁴ cells/cm² and passaged at 80-90% confluence by exposing cells to 0.25% trypsin / 0.53 mM ethylenediaminetetraacetic acid (EDTA) solution (Thermo Fisher Scientific, Germany) for about 3.0 min and rinsing once in HEK cell medium. Finally, the cell suspension was centrifuged at 100 g

for 5.0 min and the cell pellet reconstituted in HEK cell medium. Sub cultivation ratio was 1:6 to 1:10 weekly and the medium renewal was every two to three days.

2.2.2.2 Mouse Embryonic Fibroblasts (MEFs)

MEFs were isolated from CF-1 (Crl:CF1, Charles River, USA) mice and cultivated in DMEM (Thermo Fisher Scientific, Germany) supplemented with 0.1 mM beta-mercaptoethanol (Merk Millipore, Germany), 1.0% 10000 U/10000 µg penicillin/streptomycin, 1.0% non-essential amino acids (NEAA), and 10.0% FBS (Biochrom, Germany). MEFs were seeded in a range of 3 to 5 x 10⁵ cells/cm² and passaged at 80-90% confluence by exposing cells to 0.25% trypsin/0.53 mM EDTA solution (Thermo Fisher Scientific, Germany) for about 3.0 min and rinsing in MEF medium. Finally, the cell suspension was centrifuged at 100 g for 5.0 min and the reconstituted cells were shuttled in a 0.1% gelatin coated 6-well.

2.2.2.3 Human Primary Microglia

Human primary microglia (Pelo Biotech, Germany) were cultured under normoxic conditions onto 0.1% gelatin-coated 6-well plates in microglial differentiation medium (MGDM, without growth factors) containing Neurobasal™ medium supplemented with 20.0 µl/ml B27™ supplement, 10.0 µl/ml N2 supplement, 2.0 mM glutamine, 1.0% 10000 U/10000 µg penicillin/ streptomycin (all from Thermo Fisher Scientific, Germany), 1.0 mg/ml lipoic acid, 0.2 µl/ml lactic acid (85% syrup), 2.0 mg/ml lipidated bovine serum albumin, 1.0 mg/ml L-ascorbic acid (all from Merck, Germany), 10.0 ng/ml biotin, 1.0 mM sodium pyrovat (both from PanReac Applichem, Germany), and 50.0 mM NaCl (Carl Roth, Germany) as recently described¹⁷⁶. The cells were passaged once a week by exposing cells to 0.25% trypsin/0.53 mM EDTA solution (Thermo Fisher Scientific, Germany) for about 5 min and rinsing in MGDM medium.

2.2.2.4 Culture and Isolation of Primary Monocytes

Primary monocytes were isolated from healthy blood donors obtained from the transfusion medicine department of the University Hospital in Halle according the protocol previously described¹⁷⁷. The Transfusion Medicine Department has complied with the Transfusion Law during collection, storage, and processing. The obtained cells were cultured in X-Vivo 15 Serum-free Hematopoietic Cell Medium (Lonza, Sweden) supplemented with 1.0% sodium pyruvate, 2.0 mM glutamine, 1.0% 10000 U/10000 µg penicillin/ streptomycin (all from Thermo Fisher Scientific, Germany). All cells were grown in at 37.0°C in a humidified environment of 20.0% O₂ and 5.0% CO₂ under normoxic oxygen conditions.

2.2.3 Generation and Culture of B-LCLs

Initially, 7.0 ml blood was mixed with 10.0 ml RPMI 1640 medium (Biochrom, Germany) supplemented with 1.0 mM sodium pyrovate (Applichem, Germany) and 0.1 mg/ml Gentamycin (Biochrom, Germany). Gently layer the blood on the top of 4.0 ml of Ficoll Paque Plus (Sigma-Aldrich, Germany). Centrifuge the tubes for 40.0 min at 1400 rpm in room temperature in

a swing-out bucket. Aspirate the whitely buffy coat formed in the interphase between ficoll and medium. Peripheral blood mononuclear cells (PBMCs) from the buffy coat are washed twice with 30.0 ml RPMI 1640 medium (Biochrom, Germany) (centrifugation at 1400 rpm for 5.0 min), supplemented with 1.0 mM sodium pyruvate (Applichem, Germany), 10.0% fetal bovine serum (Biochrom, Germany), 1.0 µg/ml phytohemagglutinin-L (PHA-L) (Merk-Millipore, Germany), and 0.1 mg/ml gentamycin (Biochrom, Germany) and resuspend in 5.0 ml of the previously used medium in 25 cm² suspension flask (TIP, Switzerland). Afterwards, 2.0 ml of Epstein-Barr-virus (EBV) supernatant was added to the cells. Medium was changed once every week.

2.2.4 Generation of iPSCs

Human iPSCs were derived from BLCLs of controls (MLUi009-A, and MLUi010-B) and LOAD patients MLUi007-J, MLUi007-H, MLUi008-B). B-LCLs were maintained in RPMI 1640 (Thermo Fisher Scientific, Germany) supplemented with 15.0% FBS, and 2.0 mM L-glutamine and cultured at 37.0°C and 5.0% CO₂ in a humidified incubator. BLCLs were reprogrammed into virus-free iPSC lines with the Neon Transfection System (Thermo Fisher Scientific, Germany) using 1.5 µg of each episomal plasmid (Addgene) expressing 7 factors: OCT4, SOX2, KLF4, MYC, LIN28, SV40 large T antigen (SV40LT), and cellular tumor antigen p53 (p53) shRNA (pEP4 E02S ET2K, pCXLE-hOCT3/4-shp53-F, pCXLE-hUL, and pCXLE-hSK). BLCLs (0.5 x 10⁶ cells per nucleofection) were collected, centrifuged at 1000 rpm for 5.0 minutes, re-suspended in 100.0 µl R Buffer of the NEON Transfection System, and nucleofected using the B3 program (2000 V, 15 ms, 2 Pulse). These nucleofected cells were plated on MEF (3 x 10⁵ cells per well of a 6-well plate) pre-coated by 0.1% gelatin. Fibroblasts were already inactivated with a final concentration of 10.0 µg/ml mitomycin C (Applichem, Germany). All cultures were maintained at hypoxic (5.0% O₂, 5.0% CO₂, 90.0% N₂) conditions during the reprogramming process. Reprogramming media contained DMEM/nutrient mixture F12 (Biochrom, Germany), 1.0% non-essential amino acids (NEAA) (Thermo Fisher Scientific, Germany), 1.0% GlutaMax (Thermo Fisher Scientific, Germany), 1.0% N2 (Thermo Fisher Scientific, Germany), 2.0% B27-Supplement without vitamin A (Thermo Fisher Scientific, Germany), 1.0% 10000 U/10000 µg penicillin/streptomycin (Thermo Fisher Scientific, Germany), 0.1 µM β-mercaptoethanol (MerkMillipore, Germany), 100.0 ng/ml basic fibroblast growth factor (bFGF), 0.5 ng/ml human leukemia inhibitory factor (hLIF) (both from Peprotech, Germany), 0.5 µM MEK/ERK pathway inhibitor (PD0325901), 3.0 µM WNT pathway activator (CHIR99021) (both from Stemcell Technologies, Germany), 10.0 µM Protein kinase inhibitor (HA-100), and 0.5 µM Activin/NODAL/TGF-β pathway inhibitor (A-83-01) (both from Santa Cruz, Germany). The cells were maintained in Reprogramming media for next 20 d with fresh media replenishment every other day. A successful transfection produces iPSC colonies between the MEF feeder, which can be passaged manually, transferred onto 6-well plates coated with MatrigelTM (VWR, Germany), and maintained in mTeSRTM1 medium (Stemcell Technologies, Germany). The iPSC clones were further expanded and scaled up for further analysis.

2.2.5 Spontaneous Differentiation of iPSCs

Human iPSCs were cultivated in a medium for spontaneous differentiation for ten days after reaching a confluence of about 70-80%. The medium is composed of DMEM/nutrient mixture F12 (Biochrom, Germany), 1.0% NEAA (Thermo Fisher Scientific, Germany), 1.0% GlutaMax (Thermo Fisher Scientific, Germany), 1.0% 10000 U/10000 µg penicillin/streptomycin, 20.0% embryonic stem cell qualified FBS (both from Thermo Fisher Scientific, Germany), 0.1 µM beta-mercaptoethanol (Merk Millipore, Germany). After three days, five and ten samples were collected for RNA isolation. The medium was changed every other day.

2.2.6 Manufacture of Microglia-Like Cells

Human iPSCs were cultured to a confluence of about 70-80% and subsequently treated with 80.0 ng/ml bone morphogenetic protein 4 (BMP4) in mTeSRTM1 under hypoxic conditions to differentiate MGLCs via hematopoietic precursor cells. At the second day of differentiation, HA-100, an inhibitor for protein kinases (Santa Cruz, Germany), was added to the medium. After four days of differentiation into the mesodermal germ layer, the cells were further cultured in StemProTM-34 SFM (Thermo Fisher Scientific, Germany) supplemented 20.0 ng/ml fibroblast growth factor 2 (FGF2), 100.0 ng/ml stem cell factor (SCF also known as KITLG) and 80.0 ng/ml vascular endothelial growth factor A (VEGFA). On day six, the composition of the medium was changed, and the cells were further cultured in Stem ProTM 34 SFM supplemented with 60.0 ng/ml SCF, 50.0 ng/ml FMS-like tyrosine kinase-3 ligand (FLT3L), 60.0 ng/ml interleukin 3 (IL3), 50.0 ng/ml MCSF, and 5.0 ng/ml TPO. Hypoxia was discontinued at day nine and normoxia was used for further differentiation. Two days after switching to normoxic conditions, the cells were detached with TrypLETM (Thermo Fisher Scientific, Germany), transferred to 0.1% gelatin-coated 6-well plates, and cultured with StemProTM-34 SFM supplemented by 50.0 ng/ml MCSF, 50.0 ng/ml FLT3L, and 20.0 ng/ml GMCSF (all from Peprotech, Germany). Detached cells from the supernatant were collected with consumed media, centrifuged, and seeded again with fresh media. Between day 24-25, the detached hematopoietic precursor cells of the supernatant were transferred to one well of a 0.1% gelatin-coated 6-well plate and cultured with MGDM containing NeurobasalTM supplemented by 20.0 µl/ml B27-Supplement, 10.0 µl/ml N2 supplement, 2.0 mM glutamine, 1.0% 10 000 U/10 000 µg penicillin/streptomycin (all from Thermo Fisher Scientific, Germany), 1.0 mg/ml lipoic acid, 0.2 µl/ml lactic acid (85% syrup), 2.0 mg/ml lipidated bovine serum albumin, 1.0 mg/ml L-ascorbic acid (all from Merck, Germany), 10.0 ng/ml biotin, 1.0 mM sodium pyrovate (both from Pancreac Applichem, Germany), 10.0 ng/ml MCSF, 10.0 ng/ml IL34 (both from Peprotech, Germany), and 50.0 mM NaCl (Carl Roth, Germany) under hypoxic conditions. After one day of cultivation under hypoxic conditions, cells were further cultured under normoxic conditions with fresh MGDM as recently described¹⁷⁶. MGLCs were obtained at day 40.

2.3 Analysis of mRNA and Protein Expression

2.3.1 RNA Isolation and Reverse Transcription

RNA isolation and desoxyribonuclease treatment were performed according to the manufacturer's protocol using the RNeasyTM Mini Kit (Qiagen, Germany). Reverse transcription of RNA into complementary DNA was performed using reverse transcription reaction mix (20.0 μ l) containing 0.5 μ l ribonuclease inhibitor, 1.0 μ l 200 U/ μ l Revert AidTM M-MuLV Reverse Transcriptase, 4.0 μ l 5x buffer, 2.0 μ l 10.0 mM deoxyribonucleotides (dNTPs), 1.0 μ l 20.0 pmol/ μ l Oligo (dt)18 primer (all from Thermo Fisher Scientific, Germany) and 11.5 μ l ribonuclease-free water including 2.0 μ g RNA. The approach was incubated at 65.0°C for 5.0 min, 42.0°C for 60.0 min and 70.0°C for 10.0 min.

2.3.2 Semi-Quantitative Polymerase Chain Reaction (PCR)

For the semi-quantitative PCR reaction mix, a master mix of 25.0 μ l was prepared, consisting of 2.5 μ l 10x buffer-BD, 2.0 μ l 25.0 mM MgCl₂, 2.0 μ l 2.5 mM dNTPs, 0.25 μ l 5 U/ μ l FirepolTM DNA polymerase (all from Solis Biodyne, Estonia), 1.0 μ l 10.0 pmol/ μ l forward and reverse primer (Biomers, Germany), and RNase-free water including template DNA. The cycler program used for PCR was composed as follows: 95.0°C for 5.0 min; 30-40 cycles of denaturation at 95.0°C for 45.0 s, annealing at 57.0°C for 1.0 min, and extension at 72.0°C for 45.0 s; final extension at 72.0°C for 10.0 min. The amplified products were separated in 1.5-2.0 % agarose gels with 0.5 μ g/ml ethidium bromide. The separation of the agarose gels was performed at 100 V for about 30-40 min in a buffer solution with trisbase, acetic acid, and EDTA. Visualization of the amplicons was performed with ultraviolet light. Glyceraldehyde 3-phosphate dehydrogenase (GAPDH) was used as endogenous control. Primer used for analysis are listed in **Supplement 3**.

2.3.3 Quantitative Real Time PCR (qRT PCR)

iQTM 5 Multicolor Real-Time PCR Detection System (Biorad, Germany) was used to perform qRT PCR. Reaction plates and the sealing films were obtained from Biorad. The 20.0 μ l master mix used included 4.0 μ l 5x EvagreenTM reagent (Jena Bioscience, Germany), 10.0 pmol of each primer (Biomers, Germany), ribonuclease-free water, and 1.0 μ l template DNA. The used program with the conditions for the thermal cycler was composed as follows: 95.0°C for 90.0 s, followed by 40 cycles with 10.0 s denaturation at 95.0°C, 10.0 s annealing at 60.0°C, and 25.0 s extensions at 72.0°C including melting curve analysis. All qRT PCR reactions were performed in triplicates and calculated using the comparative cycle threshold method for comparison of a target gene with 60 S ribosomal protein L32 (RPL32) using the formula $2^{-\Delta\Delta CT}$. Primers are published or have been designed for this thesis using the online tool Primer3Plus (<http://www.bioinformatics.nl>) and listed in **Supplement 3**.

2.3.4 Telomere Length Analysis

A monochromatic multiplex qRT PCR was used to measure the telomere / single copy gene (T / S) ratio to analyze telomere length as previously described¹⁷⁸. Genomic DNA was extracted using the DNeasy™ Blood and Tissue Kit (Qiagen, Germany) according to the manufacturer's instructions. As described above, the multiplex qRT PCR was performed with the CFX Connect™ Real-Time Detection System (Biorad, Germany). Primers were applied with different concentration (900 nM final concentration telomere primer: 500 nM final concentration reference primer for albumin). 20 ng genomic DNA were used as template. Mean and standard derivation (SD) for measurements of one group were obtained from technical replicates (triplicates) and biological replicates (two iPSC lines). GraphPad, Prism 6.01 was used for statistical analysis (**Supplement 7**) including variance (one-way ANOVA) and post-hoc tests (Tukey's multiple comparisons (GraphPad Software Incorporation, USA)).

2.3.5 Immunofluorescence (IF) Analysis

Cells that were grown on 0.1 % gelatin-coated glass cover slips, washed three times with PBS, and fixed for 15.0 min at room temperature in 4.0% paraformaldehyde (Pancreac Applichem, Germany). Fixed cells were incubated with PBS containing 0.1% Triton™ X-100 (Merck, Germany) and 1.0% horse serum (Thermo Fisher Scientific, Germany) for 30 min. Overnight, the cells were incubated with primary antibodies at 4.0°C, washed in PBS, and incubated with secondary antibodies at room temperature for 2 h (**Supplement 4**). After further washing steps with PBS, 5.0 µg/ml Hoechst 33342™ (Thermo Fisher Scientific, Germany) were used for DNA staining. Samples were mounted using the Dako™ fluorescence mounting medium (Agilent Technologies, Germany).

2.3.6 Flow cytometry

A Navios flow cytometer (Beckman Coulter, Germany) was used for flow cytometry of cells using the following antibodies: FITC anti human CD11b, FITC anti human CD14 (both Beckman Coulter, Germany), PE-Cy7 anti human CD33, PE-Cy7 anti human CD11c, PE anti-human CX3C chemokine receptor 1 (CX3CR1) (all Biolegend, Germany), and APC-Vio770 anti human Receptor-type tyrosine-protein phosphatase C (CD45; Miltenyi Biotech, Germany) (**Supplement S5**). To exclude dead cells, the cells were stained with propidium iodide.

2.4 Histology

2.4.1 Alkaline Phosphatase Staining

Alkaline Phosphatase staining was performed using the Alkaline Phosphatase Staining Kit (System Biosciences, USA) according to the manufacturer's instructions.

2.4.2 Wright-Giemsa Staining

With the Aerospray™ pro series slide staining centrifuge (Kreienbaum Neoscience, Germany) the cells were centrifuged on slides, fixed with ethanol, and stained with a modified May-Gruenwald Giemsa staining solution (Merck-Millipore, Germany) including eosin and thiazine.

2.5 Microglia Physiology and Morphology

2.5.1 Electrophysiology

As recently described, perforated whole cell patch clamp technique was applied at room temperature with 240.0 µg/ml amphotericin B in patch pipette solution¹⁷⁹. Cells were grown on 0.1% gelatine-coated glass cover slips and placed in a recording chamber mounted on an Axiovert 25 microscope (Carl Zeiss, Germany). An Axopatch 1D amplifier and pCLAMP 6 software (MDS Analytical Technologies, USA) were used to create the recordings. Corresponding membrane potentials were measured in zero current clamp mode. Patch pipettes were drawn from borosilicate glass capillaries and had resistances of 6-10 MΩ. The patch pipette solution was composed of 110.0 mM KCl, 10.0 mM NaCl, 0.5 mM CaCl₂, 1.0 mM MgCl₂, 5.0 mM EGTA, and 10.0 mM 2-(4-(2-Hydroxyethyl)-1-piperazinyl) ethane sulfonic acid (HEPES) with a pH of 7.2 adjusted with KOH (all from Carl Roth, Germany). Extracellular Na⁺ solution composed of 145.0 mM NaCl, 5.0 mM KCl, 2.0 mM CaCl₂, 1.0 mM MgCl₂, 5.6 mM glucose, and 10.0 mM HEPES with pH 7.4 adjusted with NaOH (all from Carl Roth, Germany) permanently perfused the cells on glass cover slips.

2.5.2 Time-Lapse Microscopy

For the measurement of motility, time-lapse microscopy was performed as recently described¹⁸⁰ using a DMi8 microscope (Leica, Germany) at 37.0°C 5.0% CO₂. Cells were seeded on 0.1% gelatin-coated 6-well plates 20 h prior to initiation of exposure. A distinct MATLAB script (Mathworks, USA) was used to evaluate the motility and the degree of ramification by measuring the ramification index (RI) through the convex hull and the circumference of cells¹⁸¹. Convex shape and perimeter, two different methods to determine the ramification index RI on respectively defined characteristics, are form factors that describe the morphological differences between the geometric pattern of a cell and a circle. RI is calculated as the ratio between the area A of the circle with a perimeter equal to the outline of the cell and the area U of the perimeter of the corresponding cell (perimeter method) defined as: $RI = 4 * \pi * (A / U^2)$. Furthermore, RI is used to investigate the convex shape was calculated by the ratio between the area A and the area V, the area of a polygonal object defined by the most prominent protrusions of the cell, defined as the polygonal object: $RI = A / V$. RI close to 1 would correspond to a circular cell, while values less than 1 correlate with branching.

2.5.3 Phagocytosis Assay

2.5.3.1 Analysis using Fluorescence-Labeled Latex Beads

1×10^6 cells were treated with $3.0 \mu\text{M}$ hydrocortisone (Rotexmedica, Germany) and $100.0 \mu\text{g/ml}$ lipopolysaccharides from *Escherichia coli* O111:B4 (LPS, Merck, Germany) for 24 h. For analyzing phagocytosis, cells were incubated for 1.0 h with Fluoresbrite™ YG Microspheres $1.00 \mu\text{m}$ (Polyscience, USA) according to manufacturer's instructions with a bead to cell ratio of 1 : 300. Subsequently, cells were stained with propidium iodide to exclude dead cells and analyzed using a Navios flow cytometer (Beckman Coulter, Germany). To quantify phagocytosis, the total amount of engulfed beads was calculated. For this purpose, four gates were set to discriminate cells with different amounts of internalized beads. The gate number was multiplied by the detected cell amount in each gate to obtain the total number of internalized beads.

2.5.3.2 Analysis Using *Escherichia coli* K-12-Strain BioPartikel

For analyzing receptor-mediated phagocytosis, 6×10^4 cells were incubated with $100.0 \mu\text{g/ml}$ *Escherichia coli* K-12 strain BioParticles™ conjugated with Alexa Fluor™ 488 (Thermo Fischer Scientific, Germany) for 1.0 h at 37.0°C and incubated on ice as a control. Then, cells were washed, incubated for 2 min on ice with 1:10 trypan blue solution to quench extracellular fluorescence, and analyzed using a Navios flow cytometer (Beckman Coulter, Germany).

2.5.3.3 CD33-Dependent Phagocytosis

Monocytes were thawed and seeded at a density of 1×10^6 cells onto a non-treated 6-well-plate (Eppendorf, Germany) in X-VIVO15 medium (Lonza, Sweden) supplemented with 1.0% sodium pyruvate, 2.0 mM glutamine, 1.0% 10000 U/10000 μg penicillin/ streptomycin (all from Thermo Fisher Scientific, Germany). After 2.0 h of incubation, cells were treated for 4.0 h with 10.0 mM sialic acid and stimulated for 12.0 h with $100.0 \mu\text{g/ml}$ LPS. N-acetylneuraminic acid (Neu5Ac alias NANA) was used as sialic acid for the experiments. The inhibitor for protein kinases HA-100 (Santa Cruz, Germany) was added in a concentration of $10.0 \mu\text{g/ml}$ simultaneously to stimulation with LPS whereas the monoclonal mouse IgM antibody specific for human CD33 (Abcepta, San Diego) was added 30.0 minutes before the end of the stimulation. For analyzing phagocytosis, Fluoresbrite™ YG Microspheres $1.00 \mu\text{m}$ (Polyscience, USA) were directly added to the monocytes at 300 beads per cell for 1.0 h. Subsequently, cells were stained with propidium iodide to exclude dead cells and analyzed using a Navios flow cytometer (Beckman Coulter, Germany). A total of twelve gates were set to discriminate cells with different numbers of internalized beads. In order to obtain the total bead number, the gate number was multiplied by the detected cell number in each gate and the individual values were added together. Statistical analysis was performed by using unpaired t test with Welch's correction ($n = 3$). Statistics and visualizations were performed using GraphPad Prism 6.01 (GraphPad Software Incorporation, USA).

2.5.4 Multiplex Cytokine Assay

2.5.4.1 Principle of Analysis

Multiplex technology is a method that enables the simultaneous measurement of numerous parameters from very small sample volumes. The principle is based on the use of fluorescence-coded polystyrene microparticles coupled with antibodies against the cytokines to be measured. Antibodies bind to the cytokines in the sample. Biotinylated detection antibodies directed against the cytokines of interests are added to form antibody-antigen sandwiches. Phycoerythrin (PE) conjugated streptavidin is added and binds to the biotinylated detection antibodies. The signals obtained by PE were then measured using the Bio-Plex 200 system (BioRad, Germany). The measurement is based on the principle of flow cytometry, in which the particles pass two laser beams through a measuring cuvette. The detector for the red laser detects the individual colors of the microparticles, which can thus be assigned to a defined group of cytokines. In parallel, a green laser simultaneously detects the fluorescence of the PE-coupled streptavidin and quantifies the bound cytokines for each microparticle.

2.5.4.2 Cytokine Determination

The Bio-Plex™ Precision Pro™ Human Cytokine Assay (BioRad, Germany) was used for the measurement of interleukins. The magnetic bead-based assays allowed an accurate measurement of low levels of ten human cytokines (IL1 β , IL2, IL4, IL5, IL6, IL10, IL12 (p70), IL13, IFN γ , TNF α). To increase the cytokine release, 10.0% FBS (Biochrom, Germany) was added to the medium. The supernatant of primary microglia as well as the generated MGLCs were analyzed both stimulated and unstimulated. For stimulation, the cells were treated for 24.0 h with 5.0 μ M recombinantly produced A β pE3-42 kindly provided by Dr. Holger Cynis at Fraunhofer Institute for Cell Therapy and Immunology in Halle (Saale), Germany. A β is added to the medium pre-diluted in 0.1 M NaOH (Carl Roth, Germany). Therefore, the non-stimulated cells are treated the same way using 0.1 M NaOH without A β . The samples were incubated with microparticles in a 96-well plate and subsequently washed three times to remove unbound cytokines. Afterwards, biotinylated secondary antibodies were added followed by further washing steps with PBS. Finally, microparticles were tagged with PE-coupled streptavidin. Standard curves for each cytokine were generated for sample analysis. The implementation was carried out according to the manufacturer's protocol. Bio-Plex™ Manager software 6.0 was used to calculate the standard curves of the individual cytokines. These standard curves were used to calculate the amount of cytokines.

2.6 Mass Spectrometry

This work used mass spectrometry (i) for the genotyping of samples for LOAD associated SNPs, (ii) to generate a proteome profile of iPSCs and somatic donors, (iii) to generate a proteome profile of iPSC derived MGLCs. For genotyping, a PCR-based iPlex MS technique was used. A UPLC

SYNAPT was used to measure the proteome profiles of the iPSCs and an Orbitrap Fusion Lumos was used to measure the proteome profiles of iPSC derived MGLCs.

2.6.1 iPlex Assay and the MassArray System

2.6.1.1 Performing PCR Amplification

The PCR cocktail was prepared in a 1.5 ml microcentrifuge tube on ice and contained 0.8 μ l Nuclease-free water, 2.0 μ l 5 ng/ μ l genomic DNA, 0.5 μ l 10x PCR buffer, 0.4 μ l 25 mM MgCl₂, 0.1 μ l 25 mM dNTP mix, 1.0 μ l 500 μ M PCR primer mix (**Supplement 1**), and 0.2 μ l 5 U/ μ l PCR enzyme (all from Agena Bioscience, USA). PCR reaction were performed using the following cycle parameters: initial denaturation at 95.0°C for 2.0 min, 45 cycles denaturation at 95.0°C for 30.0 s, annealing at 56.0°C for 30 s, elongation at 72.0°C for 1 min and final extension at 72.0°C for 5.0 min. Agena Bioscience's online tool, the Assay Design Suite (ADS) (AgenaCx.com), was used for primer design.

2.6.1.2 Performing Shrimp Alkaline Phosphatase Treatment

The shrimp alkaline phosphatase (SAP) cocktail was prepared a 1.5 ml microcentrifuge tube on ice and contained 1.53 μ l HPLC-grade water, 0.17 μ l 10X SAP Buffer, and 0.30 μ l SAP 1.7 U/ μ l Enzyme (all from Agena Bioscience, USA). Apply 2.0 μ l of SAP cocktail into each well and centrifuge 5.0 s with 3200 x g. Thermocycler was performed by using the following conditions: 37.0°C for 40.0 min followed by an 85.0°C step for 5.0 min.

2.6.1.3 Performing and Desalting the iPlex Extension Reaction

The iPlex extension cocktail was prepared a 1.5 ml microcentrifuge tube on ice and contained 0.62 μ l HPLC-grade water, 0.20 μ l 10X iPlex Buffer Plus, 0.20 μ l 10X iPlex Termination Mix, 0.94 μ l 10.0 μ M Extend Primer Mix (**Supplement 2**), and 0.04 μ l 32 U/ μ l iPlex Pro Enzyme (all from Agena Bioscience, USA). Dispense 2.0 μ l of extension cocktail into each well and centrifuge 5.0 s with 3200 x g. Thermocycler was performed by using the following conditions: initial denaturation at 95.0°C for 30.0 s; 40 cycles at 95.0°C for 5.0 s, 52.0°C for 5.0 s, and 80.0°C for 5.0 s; final extension at 72.0°C for 3.0 min. Desalting process of iPlex extension reaction product was performed by following the guideline manuscript from Agena Bioscience.

2.6.1.4 MassARRAY-System

After the desalting reaction, 12.0 nl of extension products were spotted on a 96-well chips SpectroCHIP II using the RS1000 Nanodispenser (Sequenom, USA). Then the CHIP was placed in the Mass Analyzer 4 matrix-assisted laser desorption ionization time-of-flight (MALDI-TOF) mass spectrometer (MS) (Sequenom, USA), where each spot with DNA is shot with a laser under vacuum according to the MALDI-TOF method. Desorption and ionization source in the MALDI mass spectrometry application is a laser beam. Once the sample molecules are vaporized and ionized, they are electrostatically transferred to a TOF-MS where they are detected individually.

Based on the initial molecular weight of the extend primer, the mass spectrometry system detects which terminator was added and the software assigns a call for each SNP. Data processing and analysis was performed by Mass ARRAY Typer Analyzer v3.3 (Sequenom, USA).

2.6.2 Quantitative Proteomic Analysis with SYNAPT

2.6.2.1 Protein Isolation, Digestion, and Clean Up

Cells were harvested, washed with PBS, lysed in 100.0 μ l cold radioimmunoprecipitation assay (RIPA), and sonicated thrice for 1 min with a break of 1.0 min. RIPA buffer contained 150.0 mM NaCl, 50.0 mM triethylammoniumbicarbonate, 1.0% sodium dodecyl sulfate, 0.5% deoxycholic acid (all from Carl Roth, Germany), protease inhibitor cocktail, and phosphatase inhibitor cocktail (both from Merck, Germany). Obtained lysates were treated thrice by denaturation at 95.0°C for 10.0 min and freezing at -80.0°C for 10.0 min. Afterwards, lysates were sonicated again thrice for 1.0 min with a break of 1.0 min. Lysates were centrifuged at 1000 x g for 5.0 min and the supernatants were incubated for 15.0 min at 95.0°C with 20.0 mM dithiothreitol (DTT) (Thermo Fisher Scientific, Germany). Alkylation of lysates was achieved by treatment with 200 mM iodoacetamide (IAA) (Merck, Germany) for 30.0 min at room temperature in the dark. To purify proteins and to remove salts, lysates were precipitated by adding four volumes ice cold acetone, vortexed, and incubated at 4.0°C for 18.0 h. The lysate was centrifuged at 15000 x g for 10.0 min at 4.0°C. The supernatant was carefully collected and washed twice with ice cold acetone / water (4:1) by centrifugation with 15000 x g for 10.0 min at 4.0°C. The precipitated proteins were centrifuged for 15.0 min at room temperature and dissolved in 25.0 μ M ammonium bicarbonate (Merck, Germany). Protein concentration was measured using a BioDrop™ μ LITE (Thermo Fischer Scientific, Germany) and 50.0 μ g of protein were subsequently digested with trypsin (1 : 100; Promega, Germany) at 37.0°C for 18.0 h. Obtained peptides were cleaned using Pierce™ Peptide Desalting Spin Columns (Fisher Scientific, Germany) according to the manufacturer's instructions, dried at room temperature and dissolved in 20.0 μ l 0.1% formic acid (Merck, Germany).

2.6.2.2 Label-Free Data Analysis

Samples were analyzed by a coupled liquid chromatography / mass spectrometry system using a nanoAcquity UPLC™ and a SYNAPT™ G2-Si HDMS™ (both Waters, Germany). We performed three technical replicates. For separation, 400.0 ng of peptides were trapped on an Acquity UPLC M-Class C18 Trap Columns (180.0 μ m x 2.0 cm) and separated on an Acquity UPLC M-Class C18 Analytical Columns (75.0 μ m x 25.0 cm; both from Waters, Germany). Ionization was performed with a Zspray NanoLockSpray™ source (Waters, Germany) with the following parameters: emitter tip voltage of 2.8 kV, solvent gradient according to ¹⁸² over a 90.0 min gradient with a constant flow rate of 300.0 nl/min. Data acquisition was done according to the UDMS^E principle outlined in¹⁸². Raw data files were then processed using Protein Lynx Global Server™ 3.0.1 (Waters, Germany). Protein identification was done by searching of processed data against the complete proteome set

of *Homo sapiens* from Uniprot (accessed 2018-09-01) with a fixed modification of carbamidomethylated cysteines, variable modifications of oxidized methionines, and phosphorylated serines, threonines and tyrosines. The results file databases were then accessed using the ISOQuant software¹⁸³, whereby each technical replicate injection were assimilated and each precursor was identified in each run and compared throughout all runs for accurate label-free quantification between all samples.

2.6.3 Quantitative Proteomic Analysis by Orbitrap Fusion Lumos

2.6.3.1 Protein Extraction, Digestion, and Clean Up

Samples were processed for quantitative mass spectrometry analysis as described in¹⁸⁴. According to the cell number obtained from the pelleted cells, a volume of lysis buffer (2.0% SDS, 100.0 mM HEPES, pH8, 50.0 mM DTT) was added. Samples were lysed with sonication (10 cycles, 60.0 s on / 30.0 s off, high energy, 20.0°C) in a Bioruptor Plus (Diagenode, Germany), heated at 95.0 °C for 10.0 min, and afterwards sonicated again. Lysates were centrifuged at 20800 x g for 5.0 min at room temperature, and the supernatant transferred to a new tube for alkylation (15.0 mM IAA, 30.0 min, room temperature, in the dark). Proteins were precipitated overnight at 20.0°C after addition of a 4-fold volume of ice-cold acetone. The following day, the samples were centrifuged at 20800 x g for 30.0 min at 4.0°C and the supernatant was carefully removed. Pellets were washed twice with 1.0 ml ice-cold 80.0% (v/v) acetone in water and centrifuged at 20800 x g at 4.0°C. Pellets were allowed to air-dry before addition of 50-100 µl of digestion buffer (1.0 M guanidine hydrochloride, 100.0 mM HEPES, pH=8). Samples were resuspended with sonication (see above), lysyl endopeptidase (LysC) (Wako, UK) was added at 1 : 100 (w/w) enzyme-protein value and digestion proceeded for 4.0 h at 37.0°C with shaking (1000 rpm for 1.0 h, then 650 rpm). Samples were then diluted 1:1 with distilled water and trypsin (Promega, Germany) added at the same enzyme to protein ratio. Samples were further digested overnight at 37.0°C with shaking at 650 rpm. Afterwards the digests were acidified by the addition of trifluoroacetic acid (TFA) (Merk, Germany) to a final concentration of 2.0% (v/v) and then desalted with Waters OasisTM HLB µElution Plate 30 µm (Waters Corporation, USA) in the presence of a slow vacuum. In this process, the columns were conditioned with 3 x 100 µl solvent B of 80.0% (v/v) acetonitrile (Merk, Germany) solution containing 0.05% (v/v) formic acid (Merk, Germany) and equilibrated with 3 x 100 µl solvent A containing 0.05% (v/v) formic acid in distilled water. The samples were loaded, washed three times with 100.0 µl solvent A, and then eluted into 200.0 µl tubes with 50.0 µl solvent B. The eluates were dried down with the speed vacuum centrifuge and dissolved at a concentration of 1.0 µg/µl in reconstitution buffer with 5.0% (v/v) acetonitrile and 0.1% (v/v) formic acid in distilled water. Reconstituted peptides were either analyzed directly for label-free analysis or stored at -20.0°C.

2.6.3.2 Data Acquisition for Label-Free Analysis

Peptides were separated using the nanoAcquity UPLC system (Waters Corporation, USA) fitted with a trapping (nanoAcquity Symmetry C₁₈, 5 µm, 180 µm x 20 mm) and an analytical column (nanoAcquity BEH C₁₈, 1.7 µm, 75 µm x 250 mm). The outlet of the analytical column was coupled directly to an Orbitrap Fusion Lumos using the Proxeon Nanospray electrospray ionization source (both from Thermo Fisher Scientific, Germany). Solvent A was water, 0.1% (v/v) formic acid and solvent B was acetonitrile, 0.1% (v/v) formic acid. The samples (500 ng) were loaded with a constant flow of solvent A at 5.0 µl/min onto the trapping column. Trapping time was 6 min. Peptides were eluted via the analytical column with a constant flow of 0.3 µl/min. During the elution step, the percentage of solvent B increased in a linear fashion from 3.0% to 25.0% in 30.0 min, then increased to 32.0% in five more min and finally to 50.0% in a further 0.1 min. Total runtime was 60.0 min. The peptides were introduced into the mass spectrometer via a Pico-Tip Emitter (360 µm OD x 20 µm ID, 10 µm tip) (New Objective, USA) and a spray voltage of 2.2 kV was applied. The capillary temperature was set at 300.0°C was set to 30.0%. Full scan MS spectra with mass range 375-1500 mass-to-charge (*m/z*) ratio were acquired in profile mode for the Orbitrap with resolution of 120000 frequently reported in full width at half maximum (FWHM). The filling time was set at maximum of 50 ms with limitation of 2×10^5 ions. The Top Speed method was employed to take the maximum number of precursor ions (with an intensity threshold of 5×10^3) from the full scan MS for fragmentation using higher-energy collisional dissociation (HCD) of 30.0% and quadrupole isolation (1.4 Da window) and measurement in the ion trap, with a cycle time of 3.0 s. The monoisotopic precursor selection (MIPS) peptide algorithm was employed but with relaxed restrictions when too few precursors meeting the criteria were found. The fragmentation was performed after accumulation of 2×10^3 ions or after filling time of 300 ms for each precursor ion (whichever occurred first). MS/MS data were acquired in centroid mode, with the Rapid scan rate and a fixed first mass of 120 mass-to-charge ratio (*m/z*). Only multiply charged (2^+ - 7^+) precursor ions were selected for MS/MS. Dynamic exclusion was employed with maximum retention period of 60.0 s and relative mass window of 10 ppm. Isotopes were excluded. Additionally, only one data dependent scan was performed per precursor (only the most intense charge state selected). Ions were injected for all available parallelizable time. In order to improve the mass accuracy, a lock mass correction using a background ion (*m/z* 445.12003) was applied. For data acquisition and processing of the raw data, Xcalibur 4.0 (Thermo Fisher Scientific, Germany) was employed.

2.6.3.3 Data Processing

For data acquisition the MaxQuant software (version 1.5.3.28, MPI of biochemistry, Germany) was used. The data were searched against a human database (Swiss-Prot entries of the Uniprot KB database release 2016_01, 20198 entries) with a list of common contaminants appended. The data were searched with the following modifications: Carbamidomethyl (C) (fixed) and Oxidation (M) and Acetyl (Protein N-term) (variable). The mass error tolerance for the full scan MS spectra was set at 20 ppm and for the MS/MS spectra at 0.5 Da. A maximum of two missed cleavages were

allowed. For quantitative analysis, iBAQ values¹⁸⁵ from the MaxQuant output were used. Only protein groups identified by at least two unique peptides were retained. To reduce technical variation, data were \log_2 transformed and median-centered. For bioinformatic analysis as well as visualization, GraphPad Prism 6.01 (GraphPad Software Incorporation, USA) and the open-source software Perseus (version 1.6.2.3, MPI of biochemistry, Germany) was used, which is part of MaxQuant (Team, R Development Core, 2008). Venn-diagrams were generated with the online tool VENNY 2.1.

3 Results

To improve our understanding of LOAD, iPSCs from LOAD patients were generated and applied for functional analysis. Therefore, a microglia differentiation model was established.

3.1 Genotyping of B-LCLs and search for AD-associated DNA risk variants

Genotyping of LOAD-associated risk variants was performed in B-LCLs from 16 clinically characterized LOAD patients and 26 healthy controls available in Dan Rujescu's lab (**Tab. 1**).

Table 1: List of LOAD-related genotyped SNPs

Presented are the LOAD-associated SNPs with susceptible locus and associated risk alleles in red for LOAD patients (LCL007, LCL008) and healthy controls in green (LCL009, LCL010). Homozygous and heterozygous risk alleles are underlined and marked in gray.

SNP	A1/A2	Frequency	Gene	AA Change	LCL007	LCL008	LCL009	LCL010
rs7412*	C/T	0.072 / 0.928	APOE	R176C	CC	CC	CC	CC
rs429358*	T/C	0.816 / 0.184	APOE	C130R	<u>CC</u>	<u>CT</u>	TT	TT
rs1354106	T/G	0.662 / 0.338	CD33	intron	TT	TT	<u>GG</u>	<u>GG</u>
rs138197061	InDel	Del = 0.067	CD33	intron	Ins	Ins	n.d.	n.d.
rs1399839	T/G	0.541 / 0.459	CD33	intron	AA	AA	<u>AG</u>	AA
rs1803254	G/C	0.924 / 0.076	CD33	3'UTR	GG	GG	<u>CG</u>	<u>CG</u>
rs201074739	InDel	Del = 0.006	CD33	G156 Fs	Ins	Ins	n.d.	n.d.
rs2455069	A/G	0.552 / 0.448	CD33	R69G	AA	<u>GG</u>	AA	AA
rs34813869	A/G	0.664 / 0.336	CD33	intron	AA	AA	<u>GG</u>	<u>GG</u>
rs35112940	G/A	0.788 / 0.212	CD33	G304R	GG	GG	GG	GG
rs3826656	A/G	0.780 / 0.220	CD33	intron	<u>GG</u>	AA	AA	AA
rs3865444	T/G	0.310 / 0.690	CD33	5'UTR	<u>CC</u>	<u>CC</u>	AA	AA
rs73932888	T/C	0.979 / 0.021	CD33	inton	TT	TT	n.d.	n.d.
rs8112072	A/G	0.971 / 0.029	CD33	intron	AA	AA	n.d.	n.d.
rs11767557	T/C	0.782 / 0.218	EPHA1	intron	TT	TT	<u>CT</u>	TT
rs11771145	G/A	0.637 / 0.363	EPHA1	intron	<u>AA</u>	<u>GA</u>	GG	<u>AG</u>
rs4938933	T/C	0.596 / 0.404	MS4A4E	Spl.Ac.	<u>TC</u>	<u>CC</u>	<u>CT</u>	TT
rs610932	G/T	0.564 / 0.436	MS4A6A	3'UTR	<u>GT</u>	<u>TT</u>	<u>GT</u>	GG
rs9349407	G/C	0.749 / 0.251	CD2AP	intron	<u>GC</u>	GG	<u>GC</u>	<u>GC</u>
rs104894002	C/T	0.999 / 0.001	TREM2	Q33X	GG	GG	GG	GG
rs201258663	G/A	0.999 / 0.001	TREM2	T66M	GG	GG	GG	GG
rs142232675	C/T	0.997 / 0.003	TREM2	D87N	CC	CC	CC	CC
rs149622783	C/T	0.999 / 0.001	TREM2	R136Q	CC	CC	CC	CC
rs2234256	A/G	0.944 / 0.056	TREM2	L211P	AA	AA	AA	AA
rs2234258	C/T	0.986 / 0.014	TREM2	W191X	CC	CC	CC	CC
rs28937876	A/C	n.f.p.	TREM2	K186N	CC	CC	CC	CC
rs104894001	C/T	0.999 / 0.001	TREM2	W44X	CC	CC	CC	CC
rs121908402	A/C	0.999 / 0.001	TREM2	V126G	AA	AA	AA	AA
rs79011726	C/T	0.999 / 0.001	TREM2	E151K	CC	CC	CC	CC
rs200820365	T/A	0.999 / 0.001	TREM2	S183C	TT	TT	TT	TT

Allele frequencies were obtained from the NCBI online database. Fs = Frameshift; UTR = Untranslated Region; UpVar = Upstream Variation; Spl.Ac. = Splice Acceptor; A1 = Allel1/A2 = Allel2 (risk allele), InDel = insertion and deletion, n.d. = not determined, ins = insertion, Del = deletion, n.f.p. = no frequency provided. *Genotypes were already known.

LOAD-specific B-LCLs (LCL007, LCL008) and healthy control B-LCLs (LCL009, LCL010) are shown in **Table 1** because they were applied for the generation of iPSCs. The selection of DNA risk variants was based on previous studies from our lab demonstrating that the majority of susceptibility variants are located in loci harboring genes regulating the innate immune system as introduced earlier. The present study successfully genotyped 30 SNPs in CD33, TREM2, CD2AP, EPHA1, MS4A4E, MS4A6A, TREM2, and APOE in B-LCLs of 16 LOAD patients and in the 26 healthy controls. The genotyping approach covered twelve LOAD-associated DNA risk variants in CD33. As an antagonist of CD33, TREM2 was analyzed by eleven risk variants. SNPs are located in functional DNA regions or lead to an amino acid change (**Tab. 1**).

This study found risk variants in the CD33 (rs138197061 [Del], rs2455069 [G], rs3826656 [G], rs3865444 [C]), EPHA1 (rs11771145 [A]), MS4A4E (rs4938933 [T]), MS4A6A (rs610932 [G]), and CD2AP (rs9349407 [C]) in LOAD patients (**Tab. 1**). LOAD patients carried rs3826656 and rs3865444 representing risk alleles that have been most often described in the literature.

In healthy controls, genotypes for CD33, EPHA1, MS4A, and CD2AP were obtained from a SNP chip data set, which was available in the lab. In LOAD patients, genotypes were determined by genotyping, which was performed in the present study. In LCL009 and LCL010 a few SNPs were not determined (n.d.) because they were not present on the analyzed SNP chip data set.

Results were plotted in a cluster plot with the corresponding mass spectra for the respective genotypes. Cluster plot and corresponding mass spectra for genotyping of rs3826656 are shown in **Figure 5 B-D**.

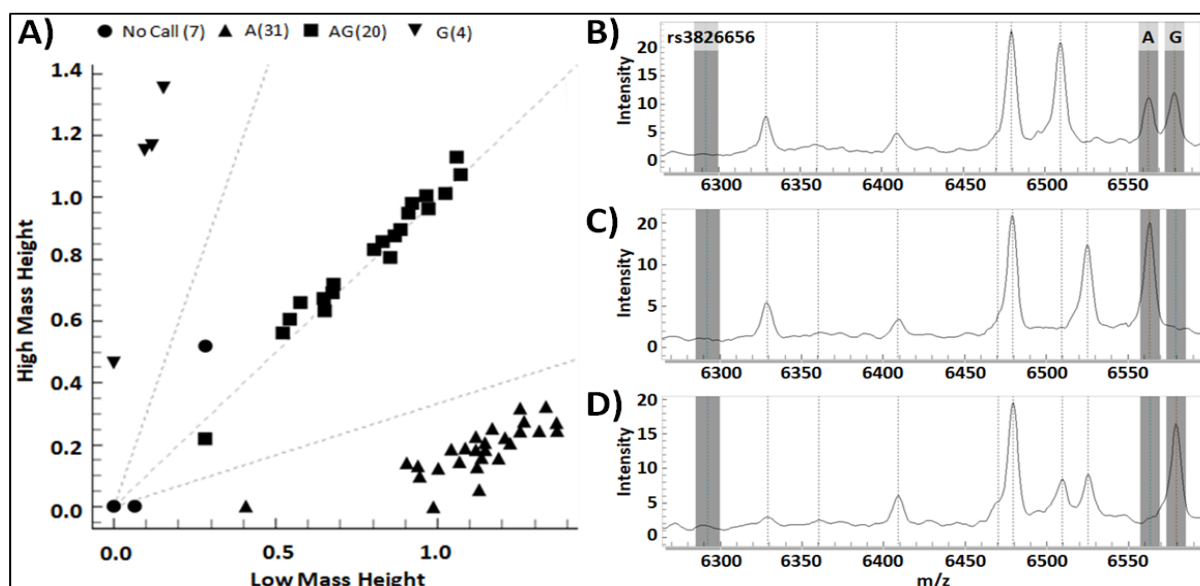


Figure 5: SNP genotyping plot and mass spectra of rs3826656 in CD33.

(A) The cluster plot displays the SNP genotypes for rs3826656 of 42 samples assayed. (B-D) Diagrams show MALDI-TOF mass spectra obtained from genotyping of bi-allelic SNPs. Primer extension reactions of a multiplex reaction are shown for rs3826656 [A / G] in CD33. (B; identified as a square in A) Heterozygous rs3826656 [A / G]. (C; identified as a pyramid in A) Homozygous rs3826656 [A]. (D; identified as an inverted pyramid in A) Homozygous rs3826656 [G]. No Call indicates the failed measurements.

3.2 CD33-dependent phagocytosis

To prove activation of phagocytosis via CD33, a simple cell culture model using human primary monocytes was applied. The molecular machinery regulating phagocytosis in microglia and monocytes are very similar. Monocytes were isolated from healthy patients and used for the analysis of phagocytosis. Monocytes were treated with sialic acid, LPS, and CD33 antibodies. Afterwards, phagocytosis of latex beads was measured by flow cytometry. The sialic acid treatment was suitable to activate CD33 by binding with sialic acid, which led to the down regulation of phagocytosis (**Fig. 6**). LPS stimulated phagocytosis of latex beads. CD33 antibodies blocked CD33 signaling without modifying phagocytosis. Sialic acid treatment counteracted LPS treatment and reduced induction of phagocytosis. Blocked CD33 signaling by an antibody against CD33 combined with LPS treatment strongly increased phagocytosis. Treatment with the protein kinase inhibitor HA-100 targeting several protein kinases, including protein kinase C regulating the phosphorylation of CD33, served as a control. Inhibition of protein kinases strongly decreased phagocytosis.

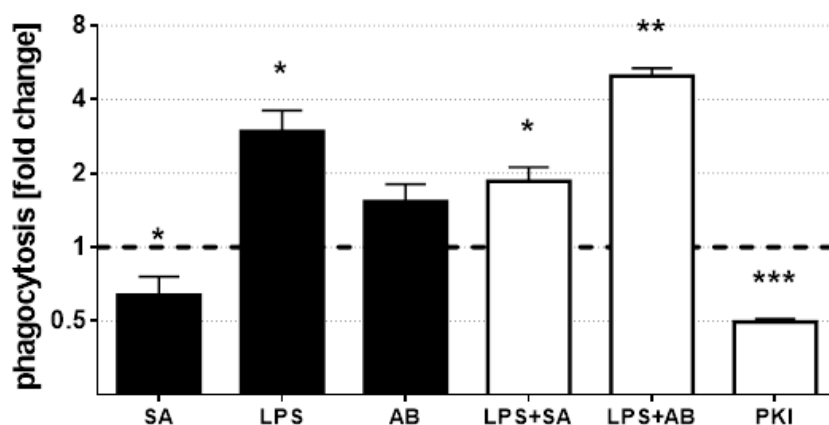


Figure 6: Flow cytometry analysis of CD33-dependent phagocytosis.

Primary Monocytes treated with sialic acids (SA), lipopolysaccharides (LPS), and CD33 antibodies (AB) revealed a CD33-dependent phagocytosis (black bars). Untreated control is set 1 (dotted line at 1). The white bars represent the controls used for monocyte treatment. SA decreased LPS-induced phagocytosis whereas AB further induced LPS-mediated phagocytosis. Treatment with the protein kinase inhibitor (PKI) HA-100 reduced phagocytosis. Error bars represent SD (** $p \leq 0.001$; ** $p \leq 0.01$; * $p \leq 0.05$).

To prove the induction of pro-inflammatory cytokines via CD33 activation, a gene expression analysis was performed. Again, monocytes were applied for treatment with sialic acids, LPS, and CD33 antibodies. Combined treatment with sialic acids and LPS served as a control. Both, sialic acids and CD33 antibodies slightly increased transcription of IL1 β , IL6, and Phosphatase and tensin homolog (PTEN), but differences were not significant (**Fig. 7**). Stimulation with LPS significantly increased the transcription of IL1 β , IL6, and PTEN. In contrast to interleukins, the PTEN mRNA level further increased with the combined treatment with sialic acids and LPS (**Fig. 7 C**).

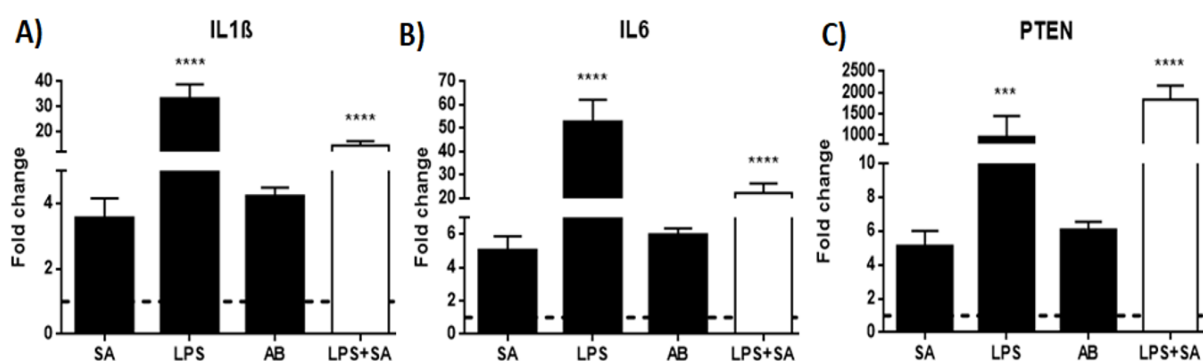


Figure 7: Transcript analysis of CD33-dependent phagocytosis.

(A) Interleukin 1 beta (IL1β), (B) interleukin 6 (IL6) and (C) Phosphatase and tensin homologue (PTEN) were investigated by qRT PCR in primary monocytes after treatment from with sialic acids (SA), lipopolysaccharid (LPS), and CD33 antibodies (AB). Treatment with LPS and SA serves as a control. Results are shown as a fold change compared to the untreated controls (dotted line at 1). One-Way ANOVA with Bonferroni's multiple comparisons test were used for statistics (n = 3; **** p ≤ 0.0001; *** p ≤ 0.001).

3.3 Generation of LOAD-specific iPSCs

In the present study, iPSCs were generated from B-LCLs obtained from two LOAD patients (LCL007 and LCL008) and two healthy controls (LCL009 and LCL010) (TAB 2). B-LCLs from healthy control patients were selected according to defined matching criteria including age, sex, and the presence of homozygous APOE3.

B-LCLs were reprogrammed using non-viral and non-integrative vectors for the forced expression of reprogramming factors. Characterization of iPSC clones revealed a set of four iPSC lines suitable for microglia differentiation. LOAD-specific iPSC lines are MLUi007-H and MLUi008-B. Healthy control iPSC lines are MLUi009-A and MLUi010-B.

Table 2: List for patient / donor information

Information about ethnicity, sex, and course of LOAD and corresponding data from healthy controls.

	LOAD patient 007	LOAD patient 008	healthy control 009	healthy control 010
AD symptoms	yes, according to DSM-IV	yes, according to DSM-IV	no	no
age	79	76	64	64
sex	female	female	female	female
ethnicity	caucasian	caucasian	caucasian	caucasian
diagnosis	mild-grade dementia syndrome, AD, DD fronto-temporal dementia	mild-grade dementia syndrome, AD, DD cerebral microangiopathy	suffer from psychiatric or neurological diseases and CNS damage were excluded.	suffer from psychiatric or neurological diseases and CNS damage were excluded.
diabetes	no	Typ 2 diabetes	no	no
APOE	44	34	33	33
Number of iPSC clones	6	9	3	1
iPSC clone used for the generation of microglia	MLUi007-H, MLUi007-J	MLUi008-B	MLUi009-A	MLUi010-B

APOE44 represents the homozygous presence of the APOE4 allele; APOE33 represents the homozygous presence of APOE3 allele, and APOE34 represents heterozygous presence of APOE3 and APOE4; DD: differential diagnosis.

3.3.1 Verification of pluripotency by alkaline phosphatase staining

First colonies appeared approximately between day 30-60. Colonies representing independent iPSC lines were picked and passaged. Alkaline phosphatase staining of colonies from all clones was performed between the first and the third passage on MEFs assuring simple and rapid detection of pluripotency (**Fig. 8**). Afterwards, cells were adapted to MEF-independent culture conditions.

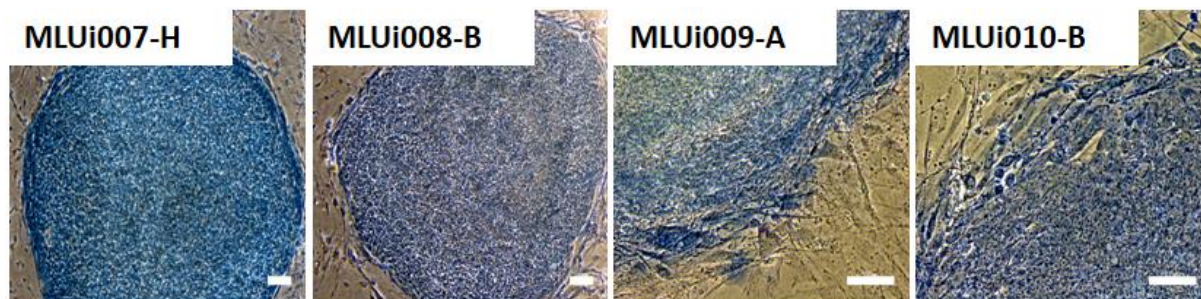


Figure 8: Morphology and alkaline phosphatase staining of iPSCs.

Colonies show tightly packed cells with cobblestone morphology and a high nucleus-cytoplasm ratio. MLUi007-H, MLUi008-B, MLUi009-A, and MLUi010-B are shown because these cell lines were applied for microglia differentiation. Surrounding MEFs do not appear in blue because of absent alkaline phosphatases. Scale bar 100 μ m.

3.3.2 Verification of pluripotency by transcript analysis

To further characterize the pluripotency of the generated iPSC lines, the transcription of pluripotency-related genes was investigated including CDH1, DPPA2, KLF4, LIN28A, MYC, NANOG, OCT4, REST, and SOX2 (**Fig. 9**). GAPDH was used as loading control. Because B-LCLs were used as starting material for the reprogramming, B cell marker genes including GRP183, FCRLA, and BTLA were analyzed. Pluripotency-related genes were verified in MLUi007-J, MLUi008-B, MLUi009-A, and MLUi010-B together with colleagues.

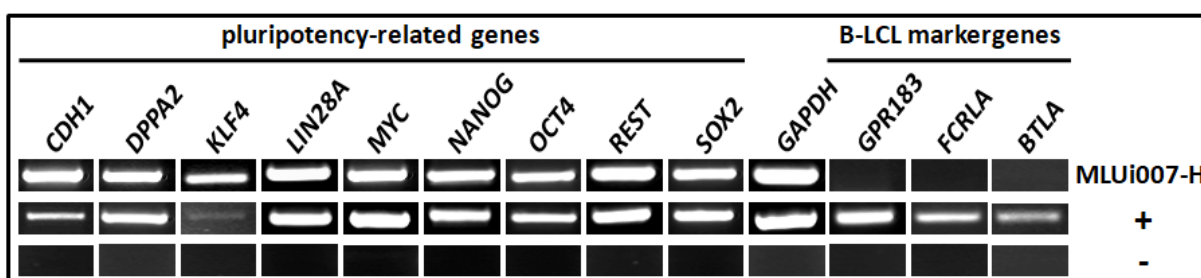


Figure 9: Verification of pluripotency-related genes in generated iPSCs.

Representative gel documentation of the transcript analysis from LOAD-specific MLUi007-H. WAI001-B iPSCs served as a positive control for pluripotency-related genes (+). B-LCL line LCL009 was used as a positive control for the B-LCL marker genes. A non-template control serves as negative control (-). GAPDH was used as a loading control.

3.3.3 Proteome analysis of iPSCs and their donor cells

The present study shows a proteome analysis of successfully generated iPSCs (MLUi007, MLUi008, MLUi009, MLUi010) and their donor B-LCLs (LCL007, LCL008, LCL009, LCL010). Using a shotgun proteomics approach, we identified 1970 proteins in total. According to a filtering process, filter rows based on valid values obtained 1568 proteins. Hierarchical cluster analysis of the B-LCLs and iPSCs was performed to measure the similarities and differences. For multi-sample test comparison of proteins and determination of significant differences in protein abundances, ANOVA with Kruskal Wallis statistics were applied with a threshold p-value of 0.05 and S0 of 0. For the visualization of the hierarchical clustering, the values were normalized by using the Z-Score. In order to determine the degree of relationship, a hierarchical clustering of the 75 proteins identified as significant by ANOVA was carried out (**Fig. 10 A**). Successfully generated iPSCs were compared to WAI001-B and WAI004-B iPSCs representing gold standard cell lines for analyzing pluripotency. The hierarchical cluster consists of two super ordinate groups. Group one consists of four B-LCLs. Healthy controls (LCL009, LCL010) and LOAD-specific B-LCLs (LCL007, LCL008) cluster together. In the second group are five iPSC lines generated in this study and two reference iPSC lines.

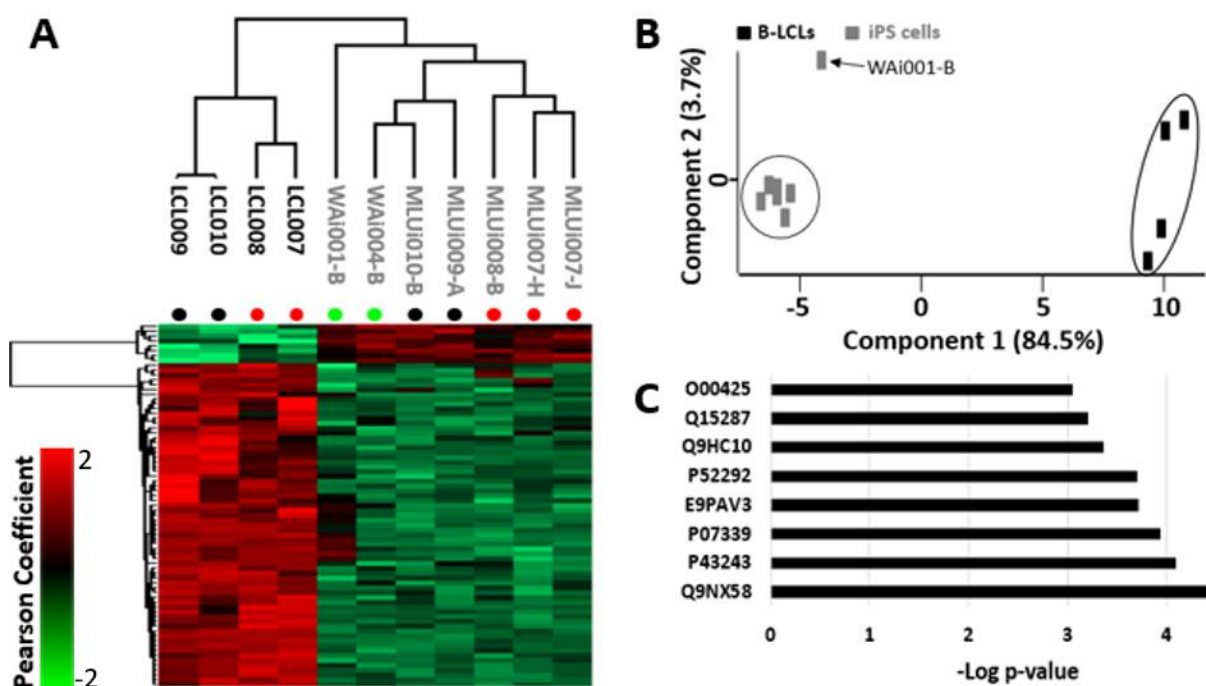


Figure 10: Shotgun proteome analysis.

(A) Hierarchical clustering of iPSC lines and their corresponding donor B-LCLs. Successfully reprogrammed iPSC lines were quite similar to reference iPSCs and very different from donor B-LCLs. Pearson correlation coefficients are shown in green and red. Dendrogram visualizes similarities and differences of groups. (B) Principal component analysis (PCA) shows clustering of B-LCLs in large distance to iPSCs. (C) For the eight significantly upregulated proteins analyzed in the iPSCs, their corresponding p-values are displayed. Abbreviations: **O00425**, Insulin-like growth factor 2 mRNA-binding protein 3; **Q15287**, RNA-binding protein with serine-rich domain 1; **Q9HC10**, Otoferlin; **P52292**, Importin subunit alpha-1; **E9PAV3**, Nascent polypeptide-associated complex subunit alpha, muscle-specific form; **P07339**, Cathepsin D; **P43243**, Matrin-3; **Q9NX58**, Cell growth-regulating nucleolar protein.

Two of the LOAD iPSCs (MLUi007-H, MLUi007-J) clustered together because they were generated from one donor indicating a high similarity. Additionally, the second LOAD iPSC line (MLUi008-B) is in this branch of the cluster. In another cluster the healthy control MLUi010-B is highly similar to the reference iPSC line WAi004-B and is located together with the second healthy control MLUi009-A on the same branch. Compared to the other six iPSC lines, the second reference stem cell line (WAi001-B) is different and forms a separate branch (**Fig. 10 A**). A PCA of the data was performed to get an overview of the obtained group profiles. The results indicate that the profiles of the B-LCLs differ significantly from those of the iPSCs (**Fig. 10 B**). The analysis of the obtained 75 significantly regulated proteins revealed that eight of these proteins upregulated in iPSCs in comparison to B-LCLs (**Fig. 10 C**).

3.3.4 Verification of SNP genotype pattern in iPSCs

Genotyping of iPSCs was performed according to the previous genotyping approach in B-LCLs to verify the same SNP genotype pattern (**Tab. 1**). LOAD MLUi007-J and MLUi008-B iPSCs carried the same SNP genotype pattern as their corresponding donor B-LCLs LCL007 and LCL008. Healthy control iPSCs carried the same SNP genotype pattern as their corresponding B-LCLs LCL009 and LCL010.

3.3.5 Verification of pluripotency by differentiation into derivatives of three germ layers

A key property of pluripotent iPSCs is their ability to develop into derivatives of the three germ layers. To demonstrate this ability, the cell line MLUi007-H was treated with fetal calf serum for spontaneous differentiation. Markers of ectoderm (PAX6, MSI1, SHH), mesoderm (TBXT, PRRX1, MEOX1), and endoderm (CXCR4, FOXA2, SOX17) were analyzed at day three, five, and ten. Due to the spontaneous nature of this process, all markers instead of FOXA2 were detected in differentiated cells from MLUi007-H iPSCs at least at one time point (**Fig. 11**). Spontaneous differentiation of MLUi007-J, MLUi008-B, MLUi009-A, and MLUi010-B into three germ layers was verified together with colleagues.

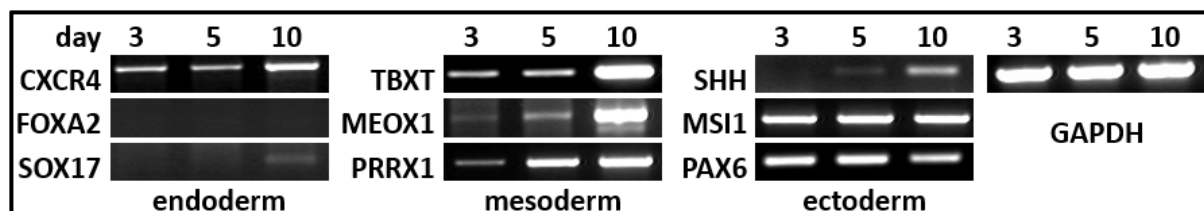


Figure 11: Transcript analysis of spontaneous differentiation.

Representative gel documentation of transcript analysis. LOAD-specific MLUi007-H was analyzed at day three, five, and ten. All markers instead of FOXA2 were found in differentiated cells verifying the potential to develop into the derivatives of the three germ layers. GAPDH served as a loading control.

3.4 Generation of human iPSC derived MGLCs via hematopoietic progenitors

MGLCs were generated via hematopoietic progenitors from human iPSCs using a completely new differentiation protocol. During an initial induction phase over four days, iPSCs differentiated into early mesodermal precursor cells representing primitive streak-like cells. These adherent myeloid lineage precursors differentiated towards monocyte lineage cells that finally detached not later than 24 days after start of differentiation and subsequently grew in suspension. Suspension cells were collected from the supernatant and transferred to gelatin-coated cell culture dishes containing MGDM and cultured until day 40. Terminal differentiated MGLCs were stable for about 2 weeks. The protocol demonstrates an efficient and robust production of microglial progenitor cells. Progenitor cells were continuously produced for up to four weeks starting from day 24 and added to a pool of progenitors until medium was changed to terminal differentiation (Fig. 12).

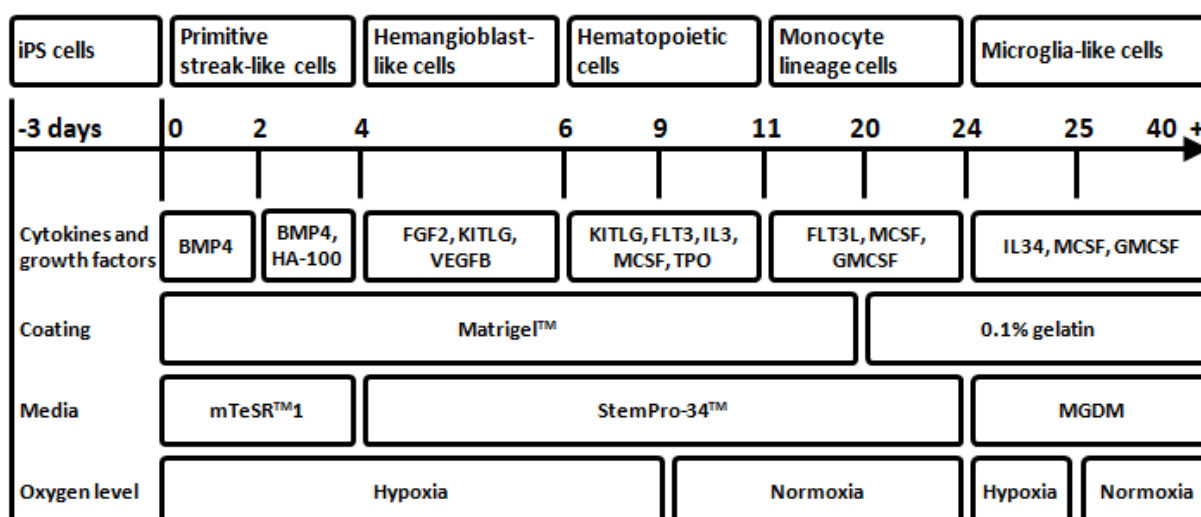


Figure 12: Differentiation of MGLCs via hematopoietic progenitors.

The scheme shows developmental stages for the differentiation of iPSCs into MGLCs. For the different developmental stages, specific media, growth factors and cytokines, matrix, and oxygen levels were provided.

3.4.1 Characterization of developing monocyte lineage MGLCs

To investigate the properties of the generated MGLCs, this study used morphological observation studies, histological staining, transcript analyses, immunofluorescence analysis, flow cytometry, and patch-clamp analysis.

3.4.1.1 Morphology and histological staining

The morphology was observed in different developmental stages during differentiation of MLU009-A iPSC into MGLCs. The histological characterization by Wright-Giemsa staining showed strong macroscopic similarities between primary monocytes isolated from fresh blood and

differentiated intermediate monocyte-like cells representing progenitors for the generation of MGLCs (**Fig. 13 B**).

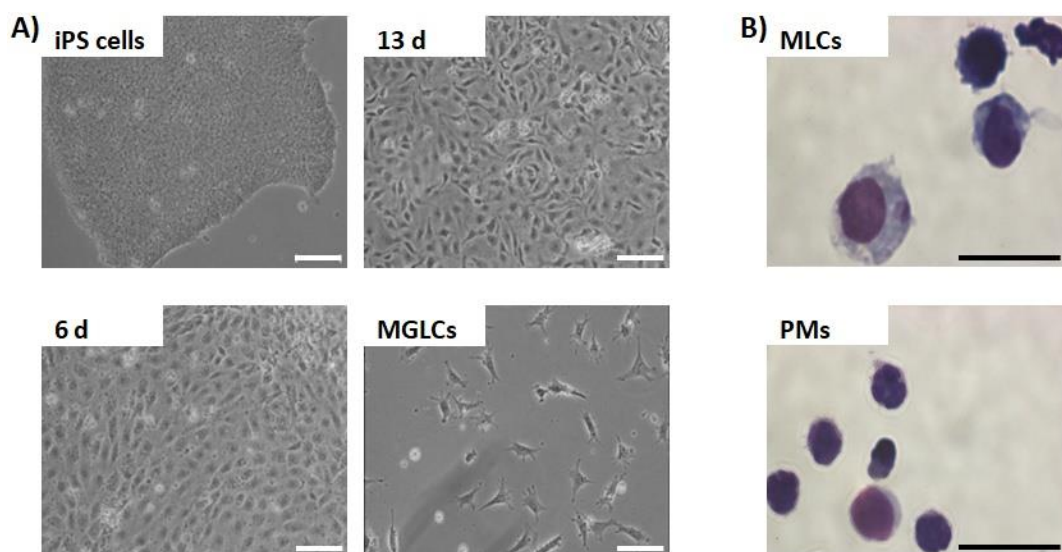


Figure 13: Cell morphology images during differentiation into MGLCs.

Morphology during differentiation of MLUi009-A iPSC into MGLCs are presented at different developmental stages: **(A)** Undifferentiated iPSC colonies on day 0, hemangioblast-like cells on day 6, the formation of hematopoietic progenitor cells on day 13, and mature MGLCs. **(B)** Monocyte-like cells (MLCs) develop during differentiation and histological staining of MLCs and primary monocytes (PMs) revealed comparable results. PMs and MLCs were analyzed by Wright-Giemsa staining. Scale bar 50 μm .

3.4.1.2 Transcript Analysis

Transcript analysis showed that MLUi010-B -derived MGLCs express crucial myeloid markers (AIF1, CD68, SPI1) as well as the markers involved in phagocytosis (TREM2, CD33, TYROBP) (**Fig. 14 A**). Quantitative transcript analysis by qRT PCR revealed less expression of the genes MER proto-oncogene, tyrosine kinase (MERTK), complement C1q A chain (C1QA), vitamin K-dependent protein S (PROS1), and growth arrest specific 6 (GAS6) in monocytes compared to primary microglia and differentiated MGLCs (**Fig. 14 B**). Gene expression was quite similar between differentiated MGLCs and primary microglia.

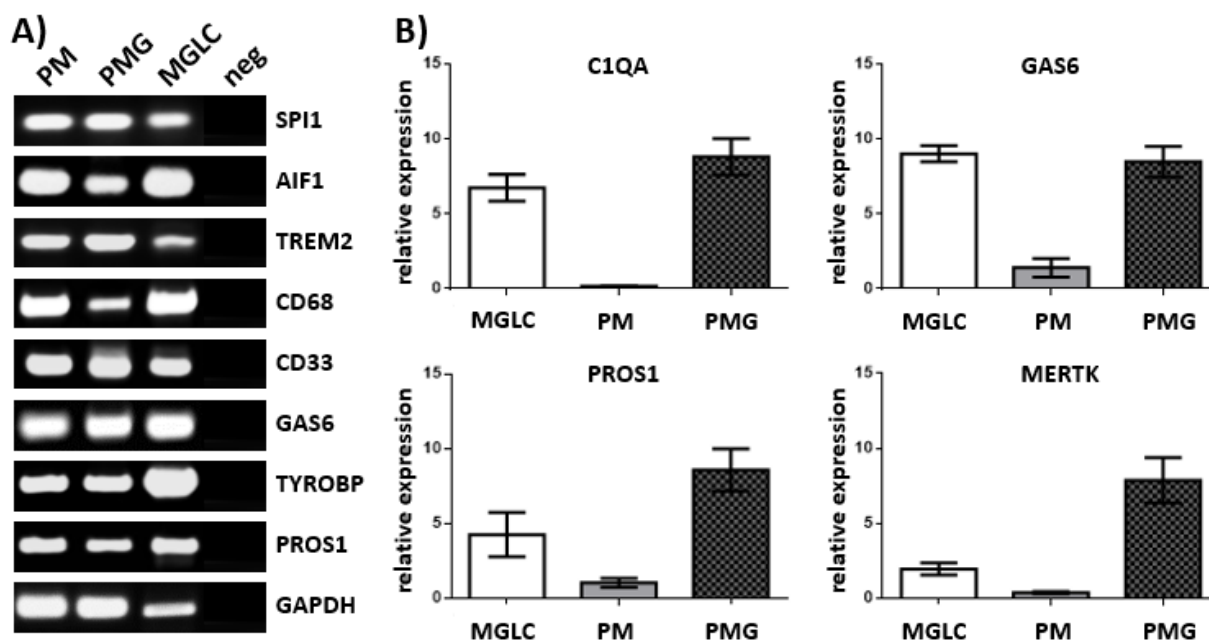


Figure 14: Evaluation of microglia marker expression.

(A) Gel documentation of transcript analysis. Crucial microglial markers (AIF1, CD68, SPI1) and myeloid markers (TREM2, CD33, TYROBP) involved in the process of phagocytosis are present in MLU010-B-derived MGLCs. Primary monocytes and primary microglia served as a positive control. GAPDH served as a loading control. The negative control (neg) is a no template control. (B) qRT-PCR of four genes (Gas6, PROS1, MERTK, C1QA) used to distinguish microglial cells from monocytes and macrophages. GAPDH was used for normalization. **Abbreviations:** PM, primary monocytes; PMG, primary microglia; MGLC, microglia-like cells.

3.4.1.1 Immunofluorescence analysis

In order to provide evidence for the translation and expression of functional proteins in addition to the transcription, two different methods were used. First, immunofluorescence analysis was used to visualize proteins on the cell surface, in the cytoplasm, and in the nucleus. Second, results were confirmed, and proteins were quantified by flow cytometry.

For immunofluorescence analysis, MGLCs derived from MLU009-A, and MLU010-B seeded on cover slips and cells were fixed at day 40 for staining with primary antibodies against tubulin beta 3 class III (TUBB3), protein tyrosine phosphatase, receptor type C (PTPRC), ITGAM, CD68, CD33, TREM2, PU.1, and AIF1 as microglia markers. Primary antibodies were detected with fluorescence-labeled secondary antibodies. Staining is shown in **Figure 15**. In addition to data obtained from transcript analysis for crucial microglia markers, the protein expressions of these markers were verified in differentiated MGLCs.

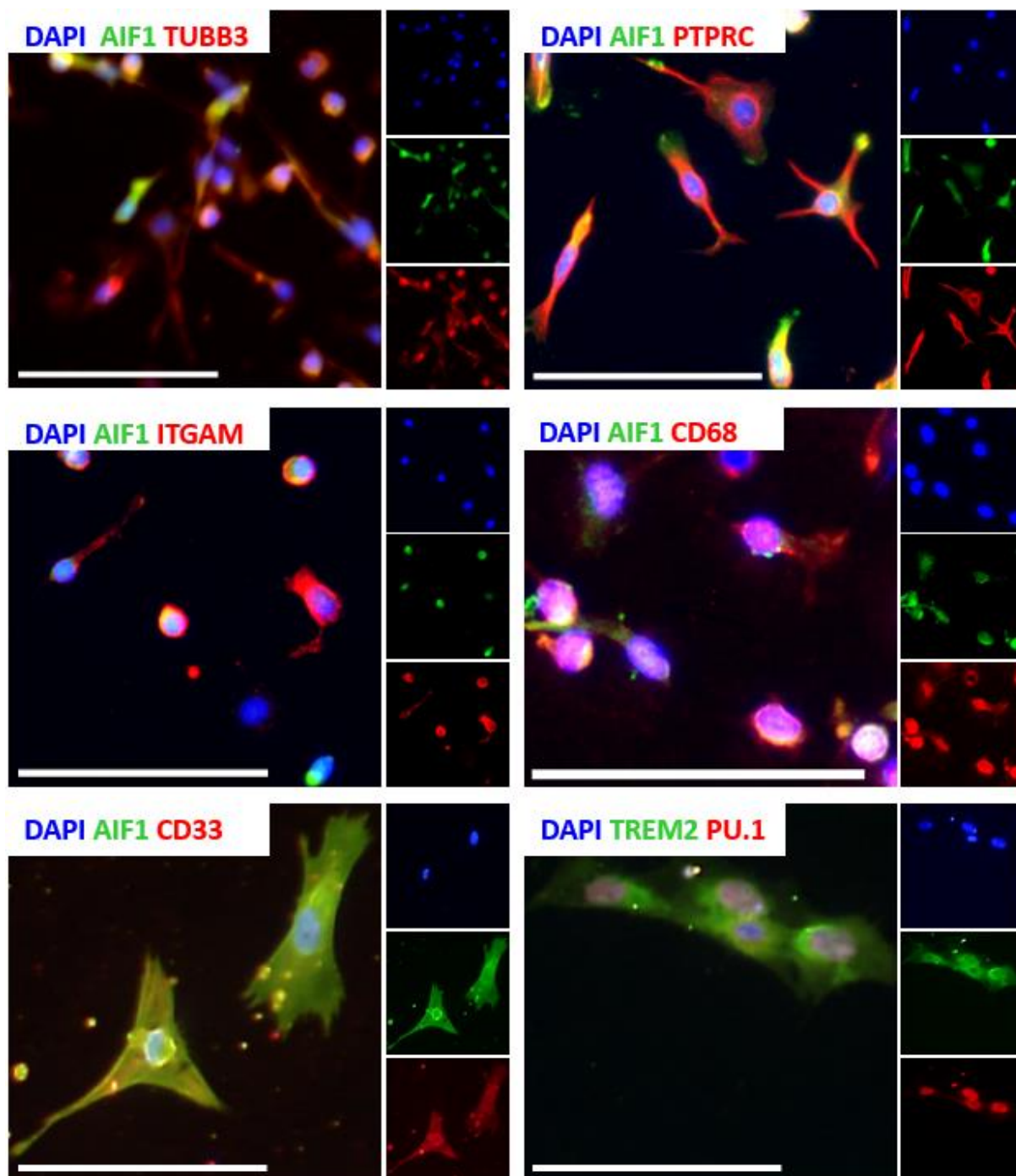


Figure 15: Immunofluorescence analysis of MGLCs

MGLCs derived from MLUi008-B were stained with antibodies against TUBB3, PTPRC, ITGAM, CD68, CD33, TREM2, PU.1, and AIF1. Cell nuclei were labelled with Hoechst 33342TM. A Biozero 9000 fluorescence microscope (Keyence) was used for epifluorescence microscopy. Scale bar: 100 μ m.

3.4.1.2 Flow cytometry

In **Figure 16**, the expression of surface proteins of MLUi009-A derived MGLCs at day 40 is determined by flow cytometry. MGLCs expressed microglial surface molecules CD11b, CD11c, CD14, CD40, CD45, and CD33. Among the different experiments, a differentiation efficiency of about 70% was achieved shortly after transfer to the MGD medium on day 25.

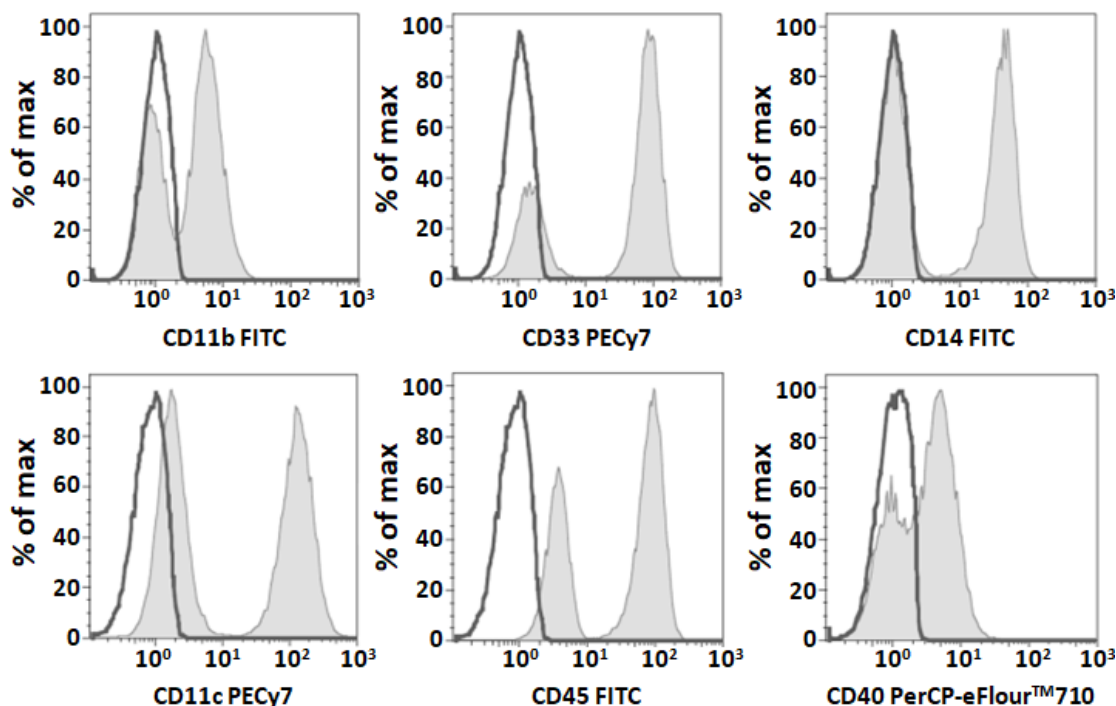


Figure 16: Flow cytometry analysis of microglial surface markers on MGLCs.

MGLCs derived from MLUi009-A were stained for the microglial markers CD11b, CD11c, CD33, CD45, CD14, and CD40 (gray pattern) on day 25. The respective isotype controls are shown (black line). Representative histograms of one representative differentiation from $n = 8$ experiments.

3.4.1.3 Electrophysiology and Cytokine Analysis

The membrane potential and the ability to produce interleukins were measured in MGLCs derived from MLUi010-B iPSCs. **Figure 17 A** shows the mRNA expressions of the interleukins 1 β , 6, 8, 10 and TNF α for undifferentiated stem cells and for the differentiated MGLCs. The patch clamp technique was used to measure the resting membrane potential in differentiated cells. MGLCs showed a resting membrane potential of about -60 mV and depolarized in response to KCL (**Fig. 17 B**). The resting membrane potential is the membrane potential of excitable MGLCs.

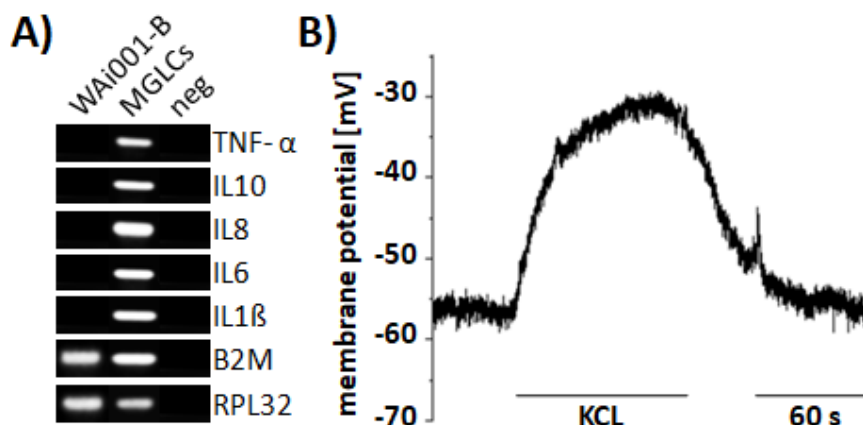


Figure 17: Properties of MGLCs.

(A) Transcript analysis of MLUi010-B-derived MGLCs for the expression of the interleukins 1 β , 6, 8, 10 and TNF α . RPL32 and beta-2-microglobulin (B2M) were used as loading controls. The negative control (neg) is a no template control. In Figure (B) the resting membrane potential (RMP) is displayed. Original recording of depolarization (D) by 25mM external KCl (RMP of $-49,5 \pm 3,7$ mV, D of $24,5 \pm 1,4$ mV). Figure shows one representative recording from $n = 6$ experiments.

3.4.1.4 Phagocytosis analysis

For the investigation of LOAD-dependent phagocytosis, MGLCs were generated from patients and healthy controls and analyzed by flow cytometry. For the analysis of phagocytosis, two different approaches were used. First, cells were fed with fluorescence-labeled latex beads to study the feeding behavior of MGLCs from LOAD patients compared to healthy controls (**Supplement 6 A**). Phagocytosis of untreated MGLCs and after LPS treatment of 4 h is higher in healthy control cells than in LOAD cells. 24 h after LPS treatment, LOAD cells show increased phagocytosis compared to the healthy controls. In a second approach, the differentiated cells were fed with *Escherichia coli* K-12 strain BioParticles™ to measure receptor-dependent phagocytosis on MGLCs of healthy controls (**Supplement 6 B**). Internalization of *Escherichia coli* K-12 strain BioParticles™ was shown to be a stable method for measuring phagocytosis. Based on a healthy control it could be shown that the generated MGLCs are functionally able to phagocyte the particles. Furthermore, phagocytosis could be increased by both LPS and hydrocortisone. An ice control was carried along in order to exclude unspecific side reactions such as sticking of the particles to the receptors.

3.4.2 Functional Analysis of Immune Plasticity in MGLCs from LOAD Patients

3.4.2.1 Time-Lapse Microscopy for Analyzing Motility

The morphology of microglia is very dynamic and depends on external stimuli, injuries, or inflammations. By perceiving the microenvironment, microglia can change from a resting phase to an amoeboid phase to adjust their speed. Due to their homeostasis, microglia are present in different activation stages and consequently move at various speeds. Therefore, this study analyzed the motility of MGLCs for over 12 h using time-lapse microscopy. The evaluation showed a significantly increased speed of LOAD-specific MGLCs compared to the speed of healthy control MGLCs (**Fig. 18**).

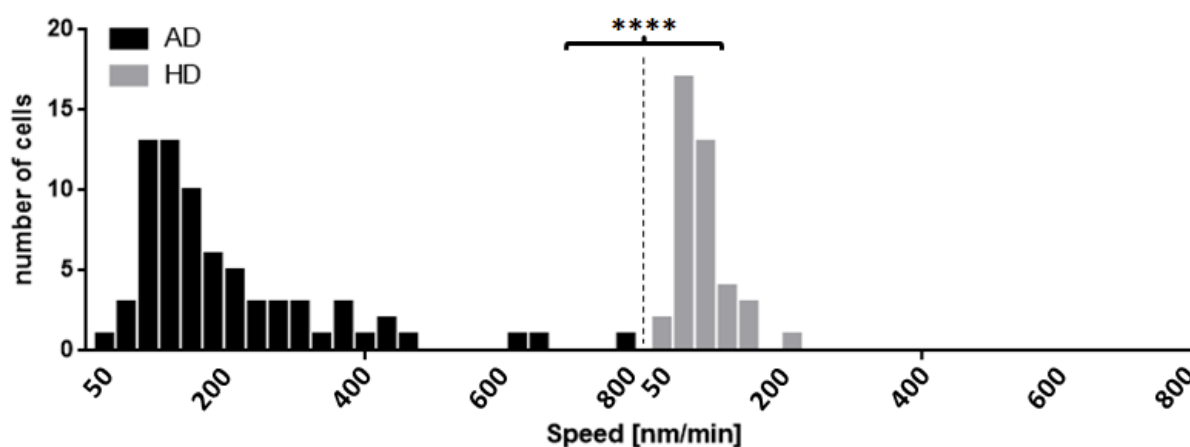


Figure 18: Motility of MGLCs determined by time-lapse microscopy.

The average speed of healthy control MGLCs (HD) was 109.6 nm/min \pm 35.4 nm/min (n = 40). The speed is significantly lower ($p = 1.82E-06$) in comparison to LOAD MGLCs (AD) (221.6 nm/min \pm 133.27 nm/min, n = 71). The maximum velocity values of the LOAD MGLCs revealed 766.02 nm/min.

3.4.2.2 Measurement of Ramification and Activation

As already mentioned, in the context of motility, microglia have an increased degree of plasticity, which undergoes several structural changes depending on their location and activation state. Variations of the processes were analyzed using the convex hull method, while activation and the associated enlargement of the cell bodies were determined using the perimeter method (**Fig. 19**). Both, the measurement of ramification and the polarization showed a change in the direction of activation. The analysis of polarization revealed significant results, but the differences in ramification were not significant.

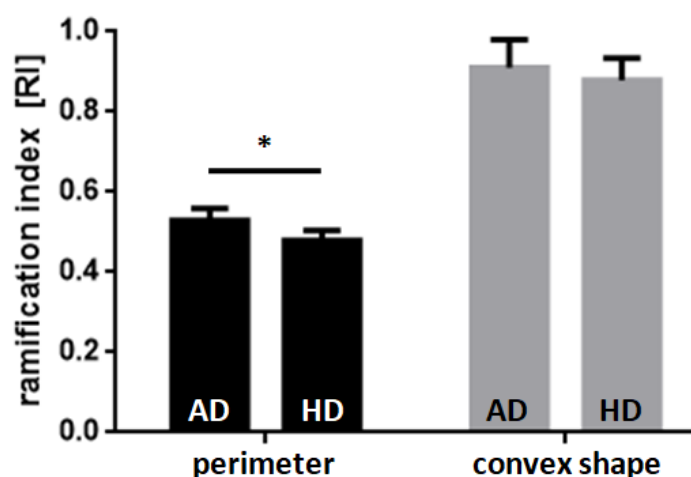


Figure 19: Dynamic processes determined by time-lapse microscopy in MGLCs.

The convex hull method was used to measure the index of ramification. For this purpose, no significant changes in shape were observed, indicating that the number of projections and branches in the healthy control (HD) (mean: 0.88; SV: 0.08; n: 40) were similar to those of the LOAD MGLCs (AD) (mean: 0.91; SV: 0.08; n: 71; $p = 0.11$). When measuring the polarization, LOAD MGLCs (mean: 0.53, SV: 0.013, n: 71; $p < 0.05$) showed a significant difference compared to the HD MGLCs (mean: 0.48, SV: 0.012, n: 40), which was analyzed by the perimeter method.

3.4.2.3 Telomere Length Analysis

To study the effects of replicative aging and telomere shortening in the context of AD, multiplex qRT PCR was used to determine the relative telomere lengths in reference MGLCs compared to healthy control and LOAD MGLCs. Examination of the relative telomere length in LOAD MGLCs showed a significant telomere shortening compared to the reference line and the healthy control MGLCs (**Fig. 20; Supplement 7**). Furthermore, a significant shortening of the telomeres was observed in healthy control MGLCs in comparison to reference MGLCs. Healthy control MGLCs were obtained from old age donors, whereas reference MGLCs were obtained from prenatal and postnatal donors.

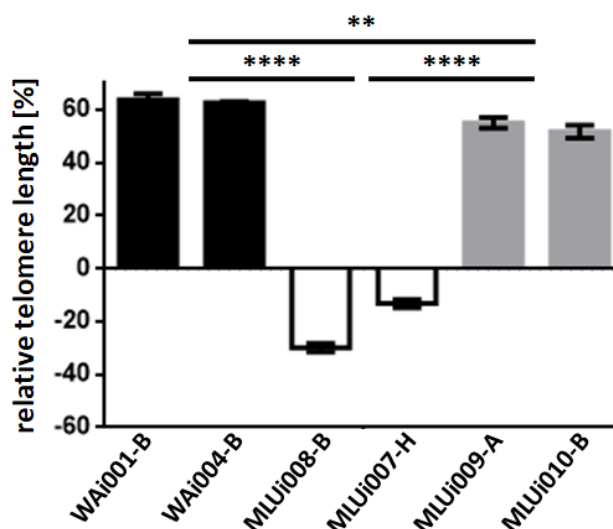


Figure 20: Telomere length analysis in MGLCs.

Relative telomere length is shown by quotient of the T/S ratio of MGLCs divided by the T/S ratio of iPSCs representing the initial telomere length at the beginning of the differentiation. Two biological replicates represented by iPSCs from two different donors are shown for reference MGLCs (black), LOAD MGLCs (white), and healthy control MGLCs (grey). Error bars represent SD (** $p \leq 0.01$; **** $p < 0.0001$).

3.4.2.4 Cytokine Analysis

Bio-Plex Precision Pro™ Human Cytokine Assay was used to detect cytokine and chemokine concentrations in the supernatants of primary and MGLCs using multiplex technology. For the evaluation of the assay, unstimulated and 5.0 μM A β pE3-42-stimulated primary microglia were analyzed in duplets for their immune response. The assay was able to simultaneously detect ten cytokines in very low concentrations and in very small sample volumes of 50.0 μl . The cytokines IL1 β , IL2, IL4, IL5, IL6, IL10, IL12, IL13, INF γ , and TNF α could be detected in very low concentrations in the unstimulated human primary microglia. In the stimulated human primary microglia, increased concentrations of all measured analytes were observed in comparison to unstimulated human primary microglia. For the compounds IL5, IL6, IL10, and INF γ , the highest concentrations were measured by A β pE3-42 treatment (**Fig. 21 A**). A β stimulated the expression of several proinflammatory cytokines such as IL1 β , IL6, TNF α , and INF γ .

In both reference lines (WAI001-B s and WAI004-B s) the cytokines IL1 β , IL6, IL10, and TNF α were increased after stimulation with A β pE3-42 (**Fig. 21 B**). Furthermore, low concentrations of IL2, IL12 and INF γ were detected in stimulated reference line WAI001-B. For the unstimulated reference MGLCs from WAI001-B, low concentrations of IL1 β were detected in addition to IL6 and IL10.

When comparing the healthy control MGLCs against the LOAD MGLCs, IL6 was detected both in the healthy controls and in the LOAD MGLCs from MLUi008-B in stimulated and unstimulated cells. TNF α could solely be analyzed in the two stimulated LOAD patients in low concentrations. For the homozygous APOE4 defined LOAD patient, an immune response could be detected in each of the measured analytes following stimulation with A β pE3-42 (**Fig. 21 C, indicated by a red star**).

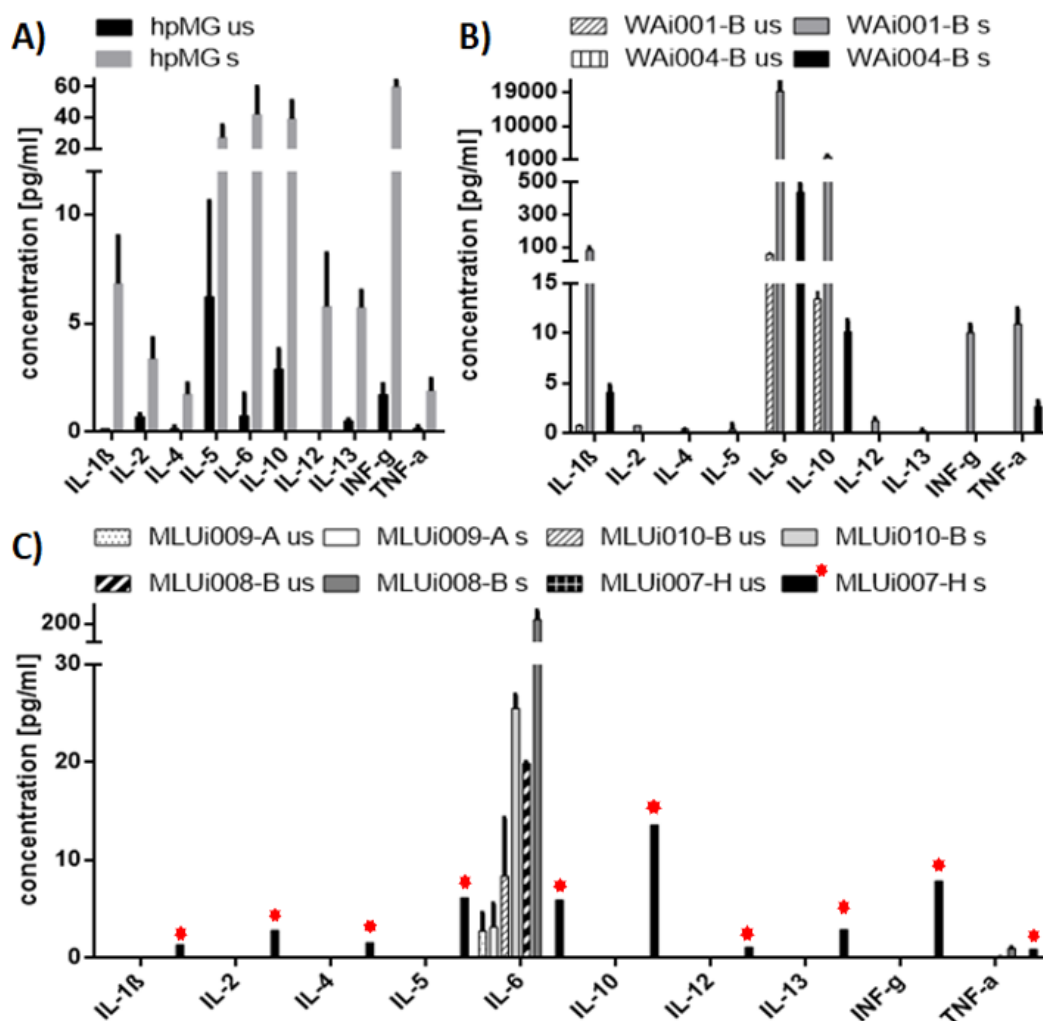


Figure 21: Multiplex cytokine assay analysis of MGLCs.

By Bio-Plex™ Precision Pro™ Human Cytokine Assay ten cytokines (IL1 β , IL2, IL4, IL5, IL6, IL10, IL12 (p70), IL13, INF γ , and TNF α) were measured simultaneously. **(A)** In human primary microglia (hpMG) it was shown that all cytokines were detectable after stimulation (s) with 5.0 μ M A β (pE3-42). Unstimulated (us) hpMG showed lower concentration of cytokines. **(B)** WAI001-B and WAI004-B are the reference cell lines. The references show unstimulated high concentrations of IL6 and IL10. By stimulating the cells, IL1 β , INF γ and TNF α were further increased. **(C)** Both, the healthy controls (MLUi009-A, MLUi010-B) and the two LOAD patients (MLUi007-H, MLUi008-B) exhibited a measurable concentration of IL6 in all cases. Cytokines beside IL6 could exclusively be detected in the stimulated MGLCs of LOAD patient MLUi007-H (labeled with a red star). Both LOAD patients showed an increase in TNF α after A β pE3-42 stimulation.

3.5 Proteome Analysis of MGLCs

Application of mass spectrometry techniques for proteome analysis and profiling of LOAD-specific MGLCs in comparison to healthy control MGLCs was performed to get insights into proteomic changes related to neurodegenerative mechanisms.

3.5.1 Flow cytometry to Verify the Culture Purity

In order to determine the proteome of MGLCs as accurately as possible, the cell population was checked for homogeneity using flow cytometry prior mass spectrometric analysis. CX3CR1 was measured to quantify the amount of mature MGLCs. To confirm the specificity of the CX3CR1 antibody, HEK293T cells and PBMCs were used as negative and positive control. As expected, HEK293T cells were not stained by CX3CR1 events in flow cytometry (**Fig. 22 left**). PBMCs were co-stained using the CD14 antibodies to highlight the monocytic subpopulation. With respect to the isotype controls, staining with the CX3CR1 antibody revealed specific expression of the receptor on all the monocytes as well as on a subpopulation of CD14-negative cells that could represent CD8-positive T cells or natural killer cells (**Fig. 22 middle**). Evaluation of differentiated MGLCs by flow cytometry showed a homogenous expression of CX3CR1 in almost all MGLCs (**Fig. 22 right**).

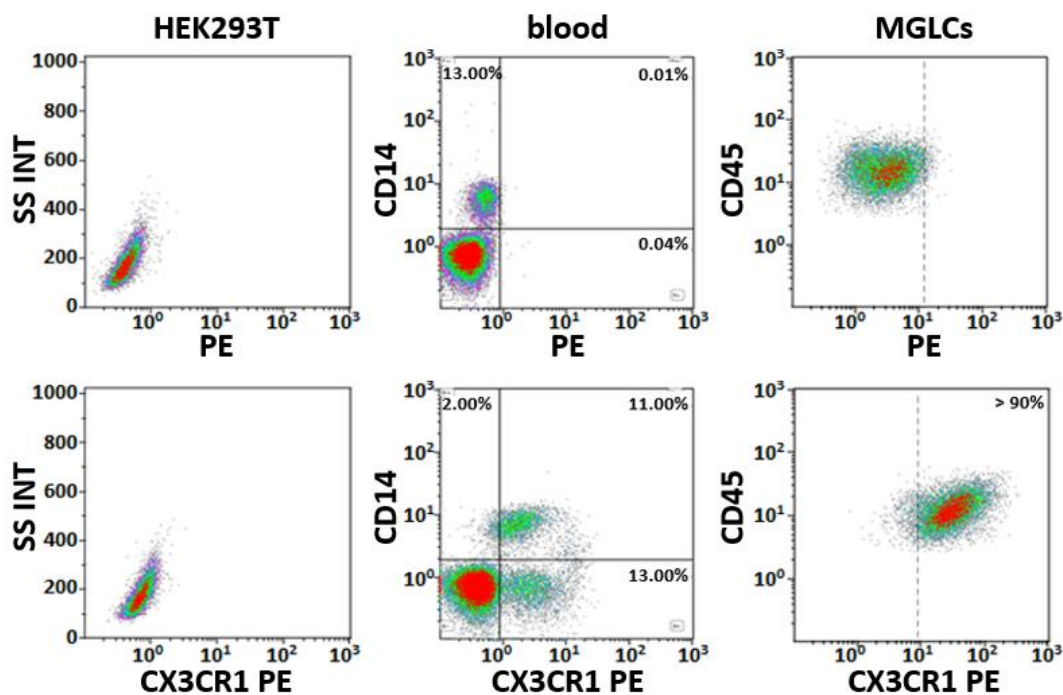


Figure 22: Evaluation of CX3CR1 in MGLCs.

HEK293T cells (left), blood (center) and differentiated MGLCs (right) from MLUi009-A were stained with anti-CX3CR1 antibodies (bottom) or isotype control (top). For the HEK293T cells, as negative control, side scatter intensity (SS INT) was used for the measurement. For blood cells, the CD14 antibody was also used to stain monocytes. MGLCs were co-stained with CD45. Shown are the dot plots from one representative experiment out of $n = 9$.

3.5.2 Raw data Analysis and Hierarchical Clustering

Mass spectrometry analysis revealed the total identification of 4946 proteins and 2014 proteins were obtained after filtering the rows based on valid values, with at least two in one group. First, the two biological replicates were grouped and the changes in protein abundance were detected with a linear regression method using logarithmically transformed protein expression values.

Imputation of missing values were performed with a normal distribution (width = 0.3; shift = 1.8). For multi-sample test comparison of proteins and determination of significant differences in protein abundances, ANOVA with Kruskal Wallis statistics were applied with a threshold p-value of 0.05 and S0 of 0. For the visualization of the hierarchical clustering, the values were normalized by using the Z-Score. In order to determine the degree of relationship, a hierarchical clustering of the 489 proteins identified as significant by ANOVA was carried out. Protein expression patterns were obtained for distinguishing MGLCs from LOAD iPSCs (red dots), healthy control iPSCs (black dots) and reference iPSCs (green dots). The controls branch divides into young (green dots) and old (black dots) donors and the related biological replicates clustered together (**Fig. 23 A**).

A PCA of the data was performed to obtain an overview of the group profiles. The results of both components suggest that the profiles in the two reference MGLCs and healthy control MGLCs were more similar than the profiles of the LOAD MGLCs (**Fig. 23 B**).

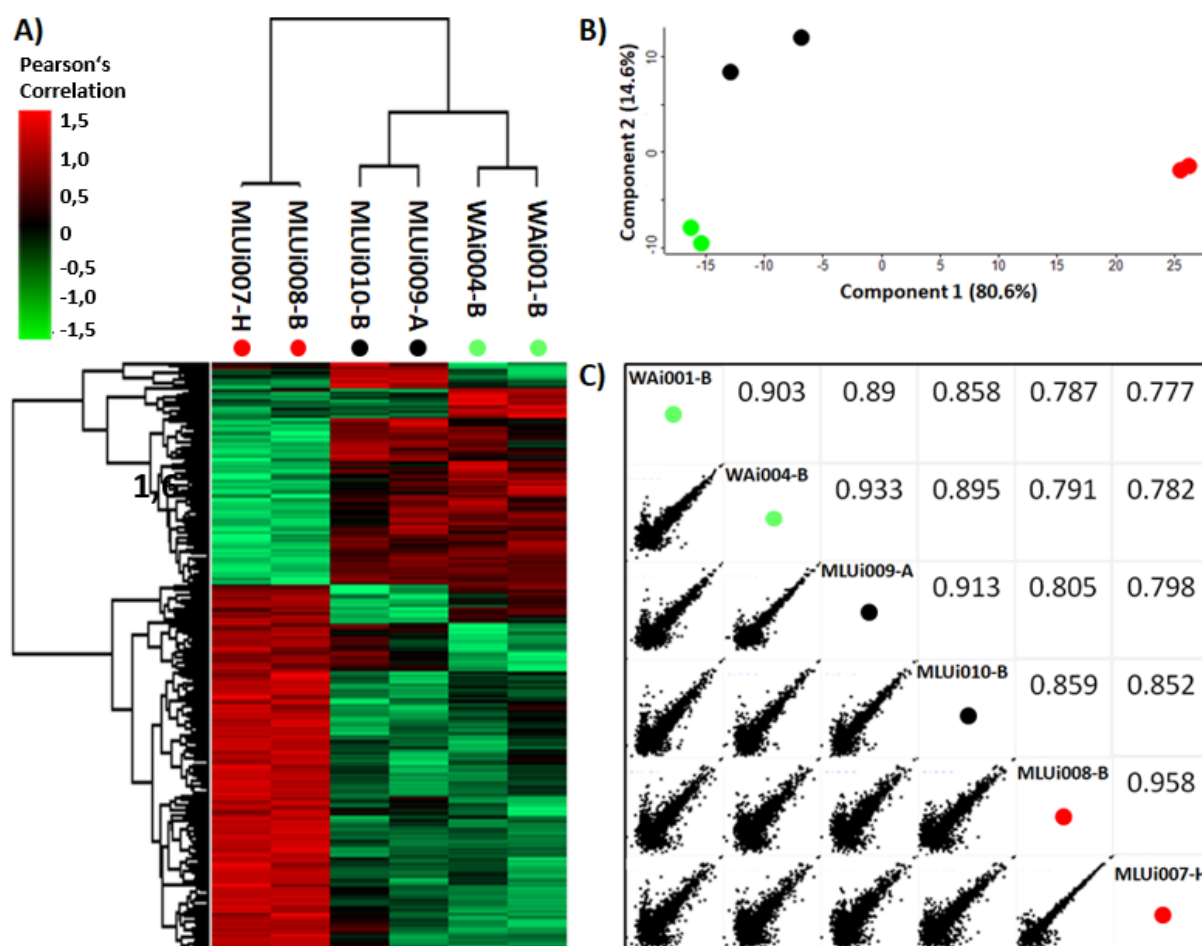


Figure 23: Explorative analysis of proteomic data.

(A) The hierarchical clustering of protein expression data from MGLCs, based on the Pearson correlation coefficients between them, shows a higher similarity between MGLCs from young and old donors compared to LOAD. (B) The greatest variance attributed to principal component analysis is the difference between MGLCs from LOAD (reference green dots), young donors (red dots; component 1; 80.6%). Furthermore, the old group (healthy control, black dots) could be clearly distinguished from the other two groups in its variance. (C) The multiple scattering of averaged profiles between the three groups clearly represents the progression from young to old to LOAD by plotting the correlation using the Pearson coefficient.

Component 1 separates the profiles of the two healthy controls and the two references from the LOAD group. Component 2 mainly separated the healthy control group from the reference group, while the LOAD group remained unchanged. Within each group, the generated MGLCs cluster very well together (**Fig. 23 B**). For the determination of the similarity within and between the groups shown by the multi-scatter diagrams with a Pearson correlation, the lowest correlation between the references and the LOAD MGLCs were determined. The correlation coefficients (R) between the respective groups are $R = 0.93$ for the reference group, $R = 0.913$ for the healthy control group and $R = 0.958$ for the group of LOAD MGLCs. Correlation coefficients between the groups resulted in the mean values and standard deviation: $R = 0.894 \pm 0.03$ (references versus healthy controls), $R = 0.784 \pm 0.006$ (references versus LOAD group) and $R = 0.829 \pm 0.03$ (healthy controls versus LOAD group) (**Fig. 23 C**).

3.5.3 Non-Hypothesis-Driven Analysis

In order to identify a subset of proteins that would significantly differentiate the three groups in a supervised manner, we performed a T-test using the 489 proteins from the hierarchical cluster. In comparison to the LOAD group, 329 proteins were expressed significantly differently for the references and 277 proteins for the healthy controls, with a false discovery rate of less than 0.05. The volcanic plot reveals the $-\text{Log}_{10}$ p-value of each protein compared to the fold change of the groups, which were compared (**Fig. 24 A**). Proteins with a p-value lower than 0.05 and a fold change lower than -1 and higher than 1 were inserted into a Venn diagram. Therefore, the proteins were fed into two Venn diagrams, grouped into up regulated proteins (**Fig. 24 B**) and down regulated proteins (**Fig. 24 C**). A total number of 276 proteins were analyzed. A STRING network of a gene ontology enrichment analysis of biological processes was performed with the proteins of the two Venn diagrams marked in grey.

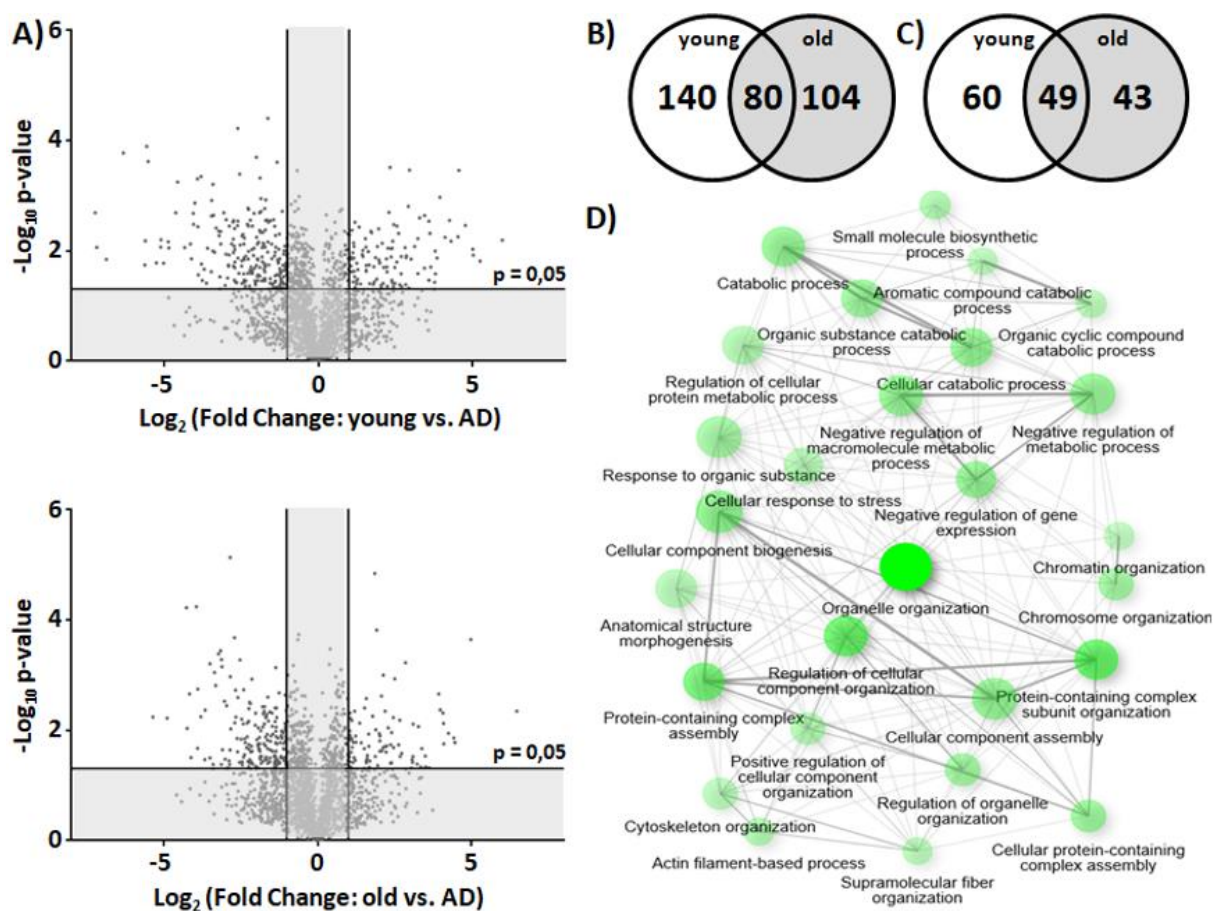


Figure 24: Comparative protein content analysis of microglia-like cells.

(A) The proteomic data were plotted as volcano diagram with $-\log_{10}$ p-values, against \log_2 fold change (reference vs. LOAD (above) and healthy control vs. LOAD (bottom)). The horizontal line represents the T-test threshold with the assigned significance of $p < 0.05$. The vertical lines define the limits for regulated proteins with a fold change lower than -1 or higher than 1. (B, C) The two-way Venn diagrams compares the number of proteins up- and downregulated in MGLCs from young references and the old healthy controls in comparison to LOAD. (D) A Gene Ontology Enrichment analysis of biological processes was performed on the 276 proteins shown in B and C in grey. For the analysis, a p-value cutoff of 0.00005 was set for the false discovery rate. The online tool ShinyGO v0.61 was used to generate the image and the analysis. The size of the points indicates the number of proteins in the set. The strength of the lines corresponds to the percentage of overlapping proteins.

In the enrichment analysis, strongest associations were obtained for the processes of organelle organization ($p = 5.6E-17$, 106 proteins), the organization of complex subunits containing proteins ($p = 4.6E-9$, 65 proteins), and for the regulation of the organization of cellular components ($p = 9.1E-9$, 67 proteins). The cytoskeletal organization ($p = 2.7E-5$, 37 proteins, marked blue) was additionally identified associated as a subbranch of the organelle organization integrated into the network (Fig. 24 D). Regulation of morphogenesis and regulation of endocytosis were related as subordinate biological processes of the associated process of regulation of cellular component organization. Subordinate to the biological process of intermediate filament cytoskeleton organization, the process intermediate filament polymerization or depolymerization is related to the biological process of protein containing complex subunit organization.

3.5.4 Altered Cytoskeleton Organization in LOAD MGLCs

In addition to the enrichment analysis of the STRING network, the proteins from the Venn diagrams of **Figure 24** (marked grey) were assigned to the associated processes. This was accompanied by a general upregulation (black bars) of identified proteins. Mainly down-regulated proteins (grey bars) appear to have a function in transport, protein localization and cell signaling (**Fig. 25 A**). AD-associated proteins have been identified mainly in biological processes that indicate functions in the immune system, signal transduction, developmental biology and in the process of disease, so they have been studied in detail (**Fig. 25 B**). Following a more detailed analysis, the identified proteins show a potential function in axon control, homeobox gene activation and transcriptional regulation of granulopoiesis, which are described as subordinate processes of developmental biology. Furthermore, the associated proteins of the three other biological processes could be associated with subordinate processes. The biological processes subordinate to disease indicates an influence in signal transduction disease, transporter disruption, infectious disease, and neurodegenerative disease.

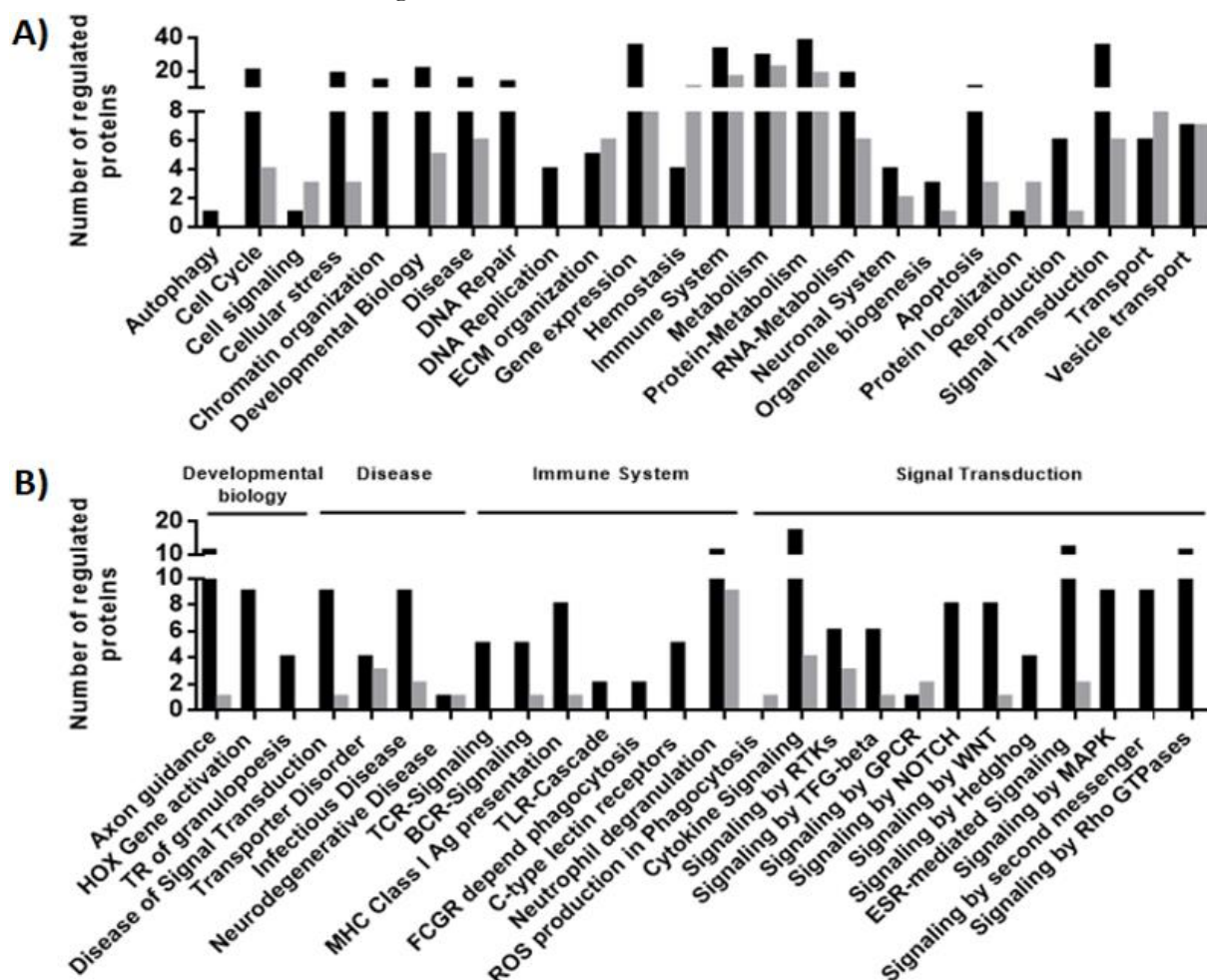


Figure 25: Gene ontology of biological processes.

(A) The number of regulated proteins was shown for the biological processes. Upregulated proteins are displayed in black and downregulated proteins in grey. (B) A closer look was carried out for four of the biological processes in LOAD MGLCs, the subordinate groups were examined more closely. **Abbreviations:** Homeobox, **HOX**; Transcriptional Regulation, **TR**; T-cell Receptor Dependent **TCR**; B-cell Receptors, **BCR**; Receptor Tyrosin Kinases, **RTK**; G Protein-Coupled Receptors, **GPCR**; Estrogen Signaling Receptor, **ESR**.

Proteins associated with the immune system mainly indicate functions in antigen presentation via the MHC system, T cell receptor dependent signaling, neutrophil degranulation and cytokine signaling. In signal transduction, for most associated proteins, involvement in the NOTCH pathway, the MAPK, the rho GTPase signaling pathway, and messenger signaling via enrichment analysis was identified. In addition to the number of proteins in the respective associated biological processes, the individual LOAD-associated proteins (black dots) and non-associated proteins (grey dots) were shown with their respective fold changes in the process. These are shown in **Figure 26** with different medians (black = AD-associated, grey = non-AD-associated significant proteins). A general upregulation of proteins in LOAD MGLCs compared to healthy control MGLCs was observed. The AD association and the respective AD score were determined using an online tool (www.genecards.org) (**Supplement 8**). The calculated medians of AD-associated proteins were mostly similar to the medians of non-AD-associated proteins of the respective associated biological processes. 75 of 276 identified proteins were exclusively analyzed in the healthy controls and were associated with LOAD. The list of the top ten proteins found exclusively in the healthy controls and associated with AD indicates a strong association for the processes of cytoskeletal organization (Cystatin-B, microtubule-associated protein 2, MAP2; cofilin-1, Fermitin family homologue 2), regulation of endocytosis (peptidyl-prolyl cis-trans isomerase NIMA-interacting 1, lactadherin), immune response (alpha-crystalline B chain, 72 kDa type IV collagenase), glucose metabolism (triose phosphate isomerase), cholesterol transport (APOE) and the response to reactive oxygen species (protein/nucleic acid deglycase-DJ-1). Proteins can have multiple functions and therefore be associated with multiple biological processes. An extended string analysis of the top ten proteins most strongly indicated changes in the actin cytoskeleton in LOAD MGLCs.

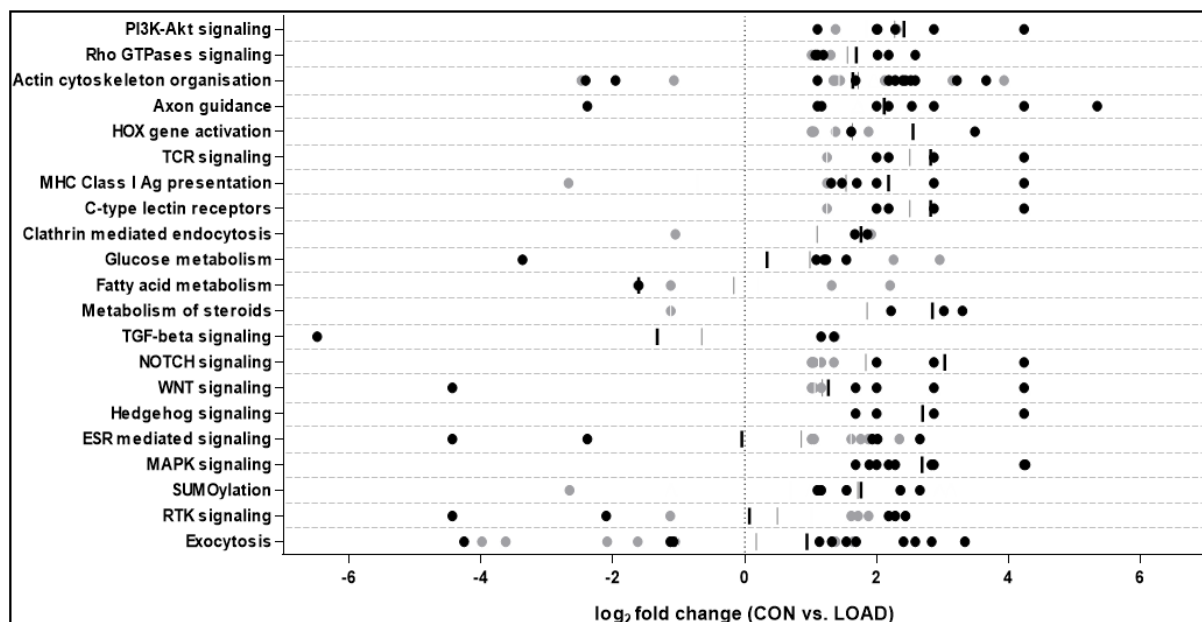


Figure 26: Altered biological processes in LOAD-specific MGLCs.

Significant individual proteins were represented with their associated fold change (healthy control (CON) versus LOAD) for the respective biological processes. Proteins were marked in black when previous data already reported altered expression associated with AD (black dots). Not AD-associated proteins are also shown (grey dots). Medians for LOAD-associated proteins were shown in black and for all proteins of the respective biological process in grey, as a horizontal line.

4 Discussion

AD is the most common form of dementia. The vast majority of patients do not show clinical symptoms until the age of 65 (termed as LOAD), while about 2-10% show an early onset course (termed as EOAD)¹⁸⁶. Both LOAD and EOAD show the two hallmarks of increased A β -plaques and neurofibrillary tangles. Due to an accumulation of extracellular A β -plaques and intracellular neurofibrillary tangles, neurons die with a dramatic loss of cognitive abilities and memory. In addition to other risk factors such as elevated cholesterol levels, environmental factors like aluminium¹⁸⁷, and blood pressure, old age is a key risk factor for AD. APOE4 was the first genetic risk variant discovered in context of AD. In recent years, numerous GWAS have been conducted in large cohorts and different ethnic groups leading to further susceptibility variants associated with AD. Many of the genes carrying risk variants are expressed by microglia and have been identified as being relevant for the immune system including endocytosis or lipid metabolism^{23,26}.

4.1 Genotyping of LOAD-Associated DNA Risk Variants in B-LCLs

Since the nineties, the genetics of AD has been an active field of research. By identifying mutations in the genes APP, PSEN1, and PSEN2, the underlying pathophysiological processes responsible for EOAD could be elucidated. In addition to the risk variants in these three genes, APOE was also identified as a susceptibility gene for both EOAD and LOAD in the 1990s¹⁸⁸. The cholesterol transporter protein APOE is translated into different isoforms. The most relevant isoforms are APOE2, APOE3, and APOE4, which are generated by the presence of two different SNPs rs429358 and rs7412 (**TAB 1**). APOE4 represents the major risk variant for AD^{30,36}. This study used mass spectrometry to proof the APOE status of patients and controls, which was recently determined by colleagues using TaqMan assays. The two healthy controls MLUi009-A and MLUi010-B have a homozygous APOE3 genotype. Genotyping of the two LOAD patients resulted in a heterozygous APOE34 genotype for MLUi008-B and a homozygous APOE44 genotype for MLUi007-H (**TAB 2**). In previous studies it was shown that the clearance of A β and the formation of senile plaques are dependent on the APOE genotype²¹. Due to arginine to cysteine exchange in the N-terminal domain by the two SNPs, functional changes in the respective isoforms occur. The region where the SNPs are located is the APOE lipid binding site. In the case of APOE4, the ability to bind lipids is impaired due to structural changes (**Fig 3**). APOE3 is the most abundant non-AD associated isoform of apolipoprotein. A reduced risk for AD is observed in patients with the isoform APOE2³⁹, while the isoform APOE4 is found more often in AD patients³⁸. The risk variant APOE44 was associated as a risk gene in various ethnic groups, where it was shown that there are differences in OR. Populations of African Americans and Hispanics (OR < 10) show a weaker association with AD than Japanese and Europeans (OR > 10)³⁰. In recent years, numerous GWAS have verified APOE as a risk gene and identified many other susceptibility genes^{19,23,26,29,189}. Most of the genes are related to the three biological processes of immune system and inflammation response, endocytosis/intracellular trafficking, and lipid metabolism²³.

In this thesis, genotyping of SNPs was performed on a mass array system combined with a multiplexed primer extension iPLEX assay using MALDI-TOF mass spectrometry. Twelve SNPs located in CD33, eleven SNPs in TREM2, one SNP in CD2AP, two SNPs in EPHA1, one SNP in MS4A4A, and one SNP in MS4A4E were analyzed for genotyping of 16 LOAD patients and 26 healthy controls (**TAB 1**). In **Figure 5**, the genotyping was visualized based on the SNP rs3826656 in CD33. The selection of LOAD-associated genes and SNPs was based on recent GWAS performed with the participation of our research team headed by Prof. Dan Rujescu's^{23,27}. The CD33 gene encodes a transmembrane receptor that provides mostly mediate inhibitory signaling by sialic acid binding^{23,148}. In the human brain, CD33 is expressed on microglia cells. In previous studies, it was observed that the surface expression of CD33 was increased in AD patients compared to the healthy controls¹⁵². The most often published AD-associated CD33 SNP is rs3865444 with C as a risk allele. For genotyping of MLUi007 and MLUi008 rs3865444 was detected homozygous for C in both cases. In contrast, the allele A was measured homozygous in the healthy controls (**TAB 1**). In total, the SNP rs3865444 was detected ten times homozygous and three times heterozygous for the risk allele C in the 16 analyzing LOAD patients. According to other studies, rs3865444C is associated with AD and leads to an increased expression of the protein, which is further associated with a decreased clearance of A β . SNP rs3865444 is located 373 bp upstream of the first exon of CD33 in the promoter region and is involved in the alternative splicing of exon 2. Exon 2 encodes a Ig V-set domain, which necessary to recognize sialic acid¹⁵². However, compared to the genetic association studies with North Chinese¹⁹⁰ and Caucasian cohorts²³, CD33 is not detected as significant in African American populations¹⁹¹. Another SNP rs3826656 with G as a risk allele is located 1722 bp upstream of the CD33 coding sequence and associated with LOAD recently demonstrated in an East Asian population¹⁵⁸. In the present thesis, the SNP rs3826656 with G as a risk allele was detected homozygous in the B-LCLs and iPSCs obtained from one LOAD patient (LCL007, MLUi007-J). B-LCLs and iPSCs from the second LOAD patient (LCL008, MLUi008-B) and both healthy controls (LCL009, MLUi009-A; LCL010, MLUi010-B) carried homozygous rs3826656 with major non risk allele A (**TAB 1**). In total, the SNP rs3826656 with G as a risk allele was detected 1 time homozygous and five times heterozygous in 16 LOAD patients. The minor allele of rs3826656 encoding G occurs less frequently in the Caucasian population than in the Chinese population¹⁹². The two CD33 SNPs rs3826656 and rs3865444 are complete linkage disequilibrium ($LD = 1$) to each other, which means that both are inherited together. A third SNP rs2455069 is in linkage disequilibrium with rs3865444 ($LD = 1$). SNP rs2455069 is located at 168 bp at a splice site in exon 2 of CD33. The minor allele G causes an amino acid exchange Arg69Gly¹⁵⁷. Furthermore, studies revealed that rs2455069 with the risk allele G is associated with an increased amount of CD33 on the cell surface on immune cells¹⁵⁷ and with altered gene expression of hyaluronan synthase 1 (HAS-1) in the cortex of AD patients¹⁵⁵. HAS1 activity may lead to insoluble N-acetylglucosamine (GlcNAc) oligomers, which activate microglia and release pro-inflammatory cytokines¹⁹³. SNP rs2455069 with risk allele G was detected homozygous in only one of the two used LOAD patient MLUi008. In both healthy controls (LCL009, MLUi009-A; LCL010, MLUi010-B) the major non risk allele A of SNP rs2455069 was

analyzed (**TAB 1**). In total, the SNP rs2455069 with risk allele G was detected four times homozygous and five times heterozygous for the LOAD patients. Furthermore, on CD33 SNP rs138197061 with the risk allele InDel causing a short intronic deletion in the DNA (delTTTCTATAAATGCC) was detected in B-LCLs and iPSCs of one LOAD patient (**TAB 1**). In total, SNP rs138197061 with the InDel allele was detected three times in 16 LOAD patients. European populations reveal the highest allele frequency of 0.0777 next to the populations African American and African in which a deletion with an allele frequency of 0.01 occurs (SNP database of NCBI, 13.04.2020). In summary, the present AD-specific in vitro model includes AD-associated SNP risk alleles in CD33, which may potent regulators of the CD33 gene expression leading to an increased expression of CD33 on the cell to counteract A β clearance.

CD33 expression on immune cells correlates inversely with TREM2 surface expression¹⁹⁴. As shown in **Figure 4**, TREM2 is an activator of phagocytosis and is described via the ITAM signaling pathway as an antagonist of ITIM signaling of the inhibitor CD33. Furthermore, **Figure 4** indicates that the ITIM domain of CD33 blocks the ITAM-mediated signal of TREM2, thus affecting its function. In the brain, TREM2, like CD33, is expressed exclusively in microglia and is involved in several important immune processes, such as reorganization of the cytoskeleton, production of chemokines, and stimulation of phagocytosis. Furthermore, TREM2 controls the production of proinflammatory cytokines and ROS¹⁹⁵. Dan Rujescu's lab first published LOAD-associated a loss-of-function mutation in TREM2 in 2013²⁷. In recent years, additional AD-associated SNPs and mutations were found in TREM2¹⁹⁴. However, genotyping performed in the present study using B-LCLs and iPSCs from 16 LOAD patients and 26 healthy controls did not reveal any risk variant in TREM2 (**TAB 1, Supplement 9**). Importantly, this negative result includes the SNP rs75932628 with the risk allele T responsible for the amino acid exchange R47H.

Nevertheless, it is important to mention that exon sequencing and GWAS analyses verified a strong association for TREM2 with AD recently. Additionally, AD-associated SNPs and mutations in TREM2 are associated with Nasu-Hakola disease, known as Polycystic lipomembranous osteodysplasia with sclerosing leukoencephalopathy, frontotemporal dementia and frontotemporal lobar dementia¹⁹⁴. For example, the amino acid exchange Q33X in TREM2, caused by SNP rs104894002 with the risk allele T, leads to a TAG stop codon, which results in a loss of function of the TREM2 protein. Q33X is associated with LOAD and sclerosing leukoencephalopathy^{194,196}. Another SNP rs201258663 with the risk allele A leading to the amino acid exchange T66M increases TREM2 expression in the endoplasmic reticulum and shows a decreased TREM2 surface localization. Together with another amino acid exchange V126G, T66M leads to impaired protein packing. SNP rs121908402 with the risk allele C is causative for V126G. T66M most probably acts on protein folding to impair the degradation of TREM2. More general, T66M leads to reduced TREM2 RNA and protein expression, which also affects phagocytosis. Another SNP rs142232675 with the risk allele T is causative for the amino acid exchange D87N and shows an impaired ligand binding. Another SNP rs2234256 with the risk allele T leads to the amino acid exchange L211P is located on the intracellular domain of TREM2 suggesting that signal transmission inside the cell may be disturbed by L211P. Further studies have identified an association of this SNP rs2234256

(with risk allele T) with AD, frontotemporal dementia and frontotemporal lobar dementia¹⁹⁴. Another intronic TREM2 SNP rs2234258 with the risk allele G produced a truncated transcript (transcript variant 2) caused by a stop mutation W191X in the African American population¹⁹⁷. Another SNP rs104894001 with risk allele T is located at a splice site and leads to an amino acid exchange W44X causative for a truncated TREM2 protein lacking the transmembrane and cytoplasmic domains. Another SNP rs79011726 with risk allele T leads to an amino acid exchange E151K at the stalk region of TREM2. A mutation in the intracellular domain necessary for binding to DAP12 is caused by SNP rs28937876 with the risk allele T leading to the amino acid exchange K186N¹⁹⁴. Furthermore, there are the two variants SNPs rs200820365 with risk allele T and SNP rs149622783 with risk allele A responsible for the amino acid exchanges S183C¹⁹⁸ and R136Q¹⁹⁹, which are associated with LOAD. In summary, SNPs in TREM2 reduce protein expression, produce truncated TREM2 isoforms, and restrict ligand binding to the adapter protein DAP12.

MS4A4E belongs to the family of 16 MS4A genes located on chromosome 11, which are expressed on cells of the immune system¹⁹. For genotyping of the 16 LOAD patients, the SNP rs4938933 with risk allele C in the MS4A4A gene was analyzed and detected heterozygous in MLUi007, homozygous in MLUi008. For genotyping of the two healthy controls the SNP rs4938933 with the risk allele C in the MS4A4A gene was detected heterozygous in MLUi009. In the second healthy control (MLUi010) the risk allele T was detected homozygous (**TAB 1**). In total, the SNP rs4938933 with the risk allele C was detected six times homozygous and seven times heterozygous for the LOAD patients. SNP rs4938933 with the risk allele C associated with LOAD was recently identified in the EADI1 consortium¹⁹.

In the present study the SNP rs610932 with the risk allele T in the gene MS4A6A, another gene of the MS4A gene family, was investigated for the patients. The risk allele T was detected heterozygous in MLUi007 and homozygous in MLUi008. In the healthy controls, MLUi009 was detected heterozygous with the risk allele T, while MLUi010 was analyzed homozygous with the non-risk allele G (**TAB 1**). In total, the SNP rs610932 with the risk allele G was detected four times homozygous and eight times heterozygous for the LOAD patients. The SNP rs610932 with the risk allele T has already been found to be associated with LOAD in previous studies in Caucasian and Chinese populations²⁰⁰. Furthermore, an association of the MS4A gene family could be associated with increased soluble TREM2²⁰¹. In summary, the underlying effect of SNPs in the genes MS4A6A and MS4A4A is not yet known. However, due to the involvement of the related genes in regulating the immune system, the accumulation of A β in the brain could be enhanced by these SNPs²⁰⁰.

Two SNPs in the gene EPHA1 have been investigated in the present study. EPHA1 belongs to the protein tyrosine kinase family and the ephrin receptor subfamily. These cell surface receptors regulate cell adhesion, migration, and plasticity. EPHA1 is involved in the regulation of cell motility and morphology via cytoskeletal reorganization in a RhoA-ROCK depend manner²⁰². The genotyping of the 16 LOAD patients showed three patients heterozygous for SNP rs11767557 with the risk allele C. For the SNP rs11767557 with risk allele C both LOAD patients MLUi008

and MLUi007 as well as the healthy control MLUi010 were analyzed homozygous for the non-risk allele T. In the second healthy control MLUi009 the SNP rs11767557 with risk allele C was analyzed heterozygous (**TAB 1**). In a second SNP rs11771145 with the risk allele A on the gene EPHA1, the LOAD patient MLUi007 was detected homozygous for A. The second patient MLUi008 and one of the healthy controls (MLUi010) were analyzed heterozygous with the risk allele A for the SNP rs11771145 (**TAB 1**). In 2011, a combined GWAS analysis of four AD consortia (GERAD1, TGEN1, ADNI1, EADI1), with the participation of Dan Rujescu's lab, was able to verify the EPHA1 as a LOAD associated risk gene. EPHA1 carried SNPs rs11767557 with the risk allele C and SNP rs11771145 with the risk allele. They were found to be in linkage disequilibrium of $r^2 = 0.28$, $D' = 0.75^{23}$. In summary, the effect of the two investigated LOAD-associated SNPs in EPHA1 has not yet been clarified.

The present study also includes the analysis of SNPs in the CD2AP gene encoding a scaffold protein that binds to nephrin, actin, and other proteins involved in the remodeling of the actin cytoskeleton. CD2AP probably regulates membrane transport and dynamic actin remodeling required for endocytosis and cytokinesis^{203,204}. The LOAD-associated SNP rs9349407 with the risk allele C was also identified in 2011 by the above mentioned four AD consortia with the participation of the group of Dan Rujescu's lab²³. In case of the SNP rs9349407 with the risk allele C the LOAD patient MLUi007 as well as the two healthy controls MLUi009 and MLUi010 were detected heterozygous with the risk allele. Second LOAD patient showed a homozygous genotype for the non-risk allele G (**TAB 1**). In total, SNP rs9349407 with risk allele C was detected exclusively six times heterozygous in LOAD patients. LOAD association of the SNP rs9349407 with the risk allele C was demonstrated in different ethnic groups, such as Chinese, Japanese, African American, European-American, European, and Canadian populations and is related to an increased A β accumulation²⁰⁵.

In summary, the detected AD-associated risk alleles probably impair the actin cytoskeleton, endocytosis, and cytokinesis, which potentially supports the accumulation of A β for the progression of LOAD.

4.2 CD33-Dependent Phagocytosis

As resident macrophages of the CNS, microglia are an elementary component of the immune system in the CNS. They perform a variety of tasks of the innate and adaptive immune system, such as phagocytosis and receptor-mediated endocytosis or cytokine release. Furthermore, microglia express MHC class I/II proteins and are therefore involved in antigen presentation and lymphocyte activation for the immune response of the CNS²⁰⁶. However, the demands of these specialized tasks require polarization into corresponding phenotypes. Due to this plasticity, microglia enable efficient and specific responses to the registered environmental signals with the adapted phenotype. Microglia are activated in response to a registered signal, resulting in the formation of the corresponding phenotype. Two main polarization states are described. In the case of M2 polarization there is an increased phagocytosis and the release of both anti-inflammatory

cytokines and neurotrophic factors, resulting in increased clearance, CNS remodeling and neuronal repair. Polarization to the M1 state leads to the release of pro-inflammatory cytokines, ROS, and chemokines, causing neuronal dysfunction and chronic neuroinflammation. In AD, microglia with impaired phagocytosis and pro-inflammatory cytokine release are increasingly described in the most recent literature²⁰⁷. GWAS analyses showed that molecular genetics plays a crucial role in the progression of AD, especially in genes related to the immune system. The surface receptor CD33 is one of the risk genes crucial for proper function of the immune system²³. Due to the different AD-associated CD33 SNPs regulating surface localization in the microglia, CD33-dependent phagocytosis is impaired in AD. CD33 is activated via ligand binding to SA, which recruits SHP proteins to the ITIM domain in CD33¹⁴⁹. Activation of the ITIM domain has an inhibitory effect on the activating ITAM domain and the TLR receptors in CD33, which are both related to be involved in the regulation of phagocytosis, cytokinesis, and actin remodeling^{168,208} (**Fig. 4**). Many publications describe activation of microglia via stimulation with LPS, which mainly induces the M1 phenotype²⁰⁷.

For studying basic mechanisms of CD33-dependent phagocytosis, a simple cell culture model with human primary monocytes was used in the present study. In microglia and monocytes, the CD33 expression on cell surfaces and the molecular machinery that regulates phagocytosis are very similar. To investigate the influence of CD33 on phagocytosis, monocytes were analyzed before and after stimulation with sialic acid, LPS, a protein kinase inhibitor and an antibody against CD33. **Figure 6** represents the fold change of phagocytosis for the respective treatments. To simulate the influence of sialic acid in the phagocytosis process, the internalization of beads in monocytes was investigated. In the evaluation of the data, we detected a significantly reduced receptor-mediated phagocytosis of sialic acid treated monocytes. This result could indicate an activation of sialic acid ligands like CD33. To verify the reducing effect of sialylated surface proteins in monocytes on phagocytosis, cells were additionally stimulated with LPS after sialic acid treatment. Evaluation of the phagocytosis of sialic and LPS treated monocytes showed a significant increase in bead internalization compared to untreated controls. Stimulation phagocytosis by LPS was already shown in monocytes. This study showed that single treatment with LPS and combined treatment with sialic acid and LPS lead to no significant differences with a p value of 0.0519 (**Fig. 6**). The experiments in this thesis confirmed that treatment with sialic acid significantly reduces phagocytosis. This result could verify a previous study by Cabral et. al²⁰⁹, who showed that desialylation significantly increases phagocytosis in monocyte mature dendritic cells treated with sialidase. In another study, it was shown in invertebrates that sialic acid has a negative effect on phagocytosis. In a previous study, the treatment of phagocytes with N-acetyl-D-mannosamine (ManNAc), a biological precursor of sialic acid Neu5Ac, showed that both the phagocytosis reaction was inhibited and released superoxide anion and nitric oxide were reduced during phagocytosis²¹⁰.

For the analysis of the effects of the surface receptor CD33 on phagocytosis, CD33 was blocked with an anti-CD33 antibody, and the internalization of the beads were measured. In the evaluation of phagocytosis, no significant change was found by blocking the surface receptor. An additional

stimulation of monocytes with LPS leads to a significant increase in phagocytosis when CD33 signaling is interrupted. A significant increase in phagocytosis by treatment with CD33 antibody and LPS was observed both, in comparison to the untreated control and to LPS stimulation. The increased phagocytosis due to blocking of the surface receptor CD33 verifies the results of other studies, in which an increase in phagocytosis was observed by a knockout of CD33. Based on the results shown in this thesis and previous studies that produced a CD33 knockout, a correlation between CD33 expression and A β -clearance could be obtained^{152,211}. Treatment with an inhibitor of protein kinases regulating CD33-independent phagocytosis, served as a control for the integrity of phagocytosis regulating intercellular machinery. A protein kinase inhibitor greatly reduced phagocytosis (**Fig. 6**). Based on this result, already achieved results could be verified in which protein kinases influence phagocytosis. Makranz and colleagues were able to show in macrophages and microglia that the protein kinase A inhibitor H-89 acts dose dependent and can inhibit myelin phagocytosis²¹². Furthermore, it was shown for protein kinase C that decisive proteins in the machinery of phagocytosis are phosphorylated by protein kinase C and an inhibitor against protein kinase C inhibits phagocytosis²¹³. A further step of the immune system, which should always be investigated in connection with the process of phagocytosis, is the release of cytokines.

Besides the internalization of latex beads by activating the phagocytosis machinery, intracellular specific gene expression patterns are induced regulating the synthesis of pro-inflammatory cytokines. In this study, the cells of the phagocytosis experiment were used to show how both pro-inflammatory cytokines such as IL1 β , IL6 and PTEN are affected by the activation and blocking of CD33. LPS was used to show that monocytes can be stimulated. Treatments with sialic acid and CD33 antibodies induced slightly, but not significantly, the expression of IL1 β , IL6, and PTEN. Ensuing a stimulation with LPS a significantly increased transcription was detected for IL1 β , IL6. Furthermore, a highly increased transcription for PTEN was detected. The combined treatment with LPS and sialic acid also resulted in a significant increase in mRNA levels of IL1 β and IL6 at lower levels than observed in the single treatments (**Fig. 7 A, B**). In contrast to interleukins, mRNA levels of PTEN continued to increase in the combined treatment with LPS and sialic acid (**Fig. 7 C**). Cabral et al.²⁰⁹ showed similar to own results in this thesis (**Fig. 6**) that pro-inflammatory cytokines IL6 and TNF α are increasingly released in desialylated monocytes. This response was further increased using LPS from *Escherichia coli* as a stimulus. The increased release of pro-inflammatory cytokines such as IL1 β by desialylation was described in another study by Lajaunias et al.²¹⁴ They demonstrated that an increased IL1 β production in desialylated monocytes can be reduced by sialic acid treatment. When treated with an antibody against CD33, an increased release of IL1 β from the monocytes was observed. Phospholipid-modifying enzymes such as PI3K regulate Fc-receptor-mediated phagocytosis by binding to the SH2 domain of ITAM motifs and thereby activating them. Lipid phosphatases such as SHIP1 and PTEN counteract this activation²¹⁵. PTEN has effects on reduced receptor-mediated phagocytosis, increased Toll-like receptor signaling, and pro-inflammatory cytokine response. Stimulation by LPS increases PTEN gene expression, which was shown by others²¹⁶. PTEN is involved via its expression in the regulation of the activating ITAM domain containing proteins like TREM2. Phosphorylase is the regulatory

antagonist of the kinase PI3K a downstream target of ITAM signaling. Upregulation of PTEN results in inhibitory phagocytosis²¹⁷. Activation of the ITIM domain in CD33 by sialic acid most probably enhances the stimulation of LPS by inhibiting PI3K to enhance PTEN gene expression (Fig 4).

4.3 Generation of AD-Specific iPSCs

The discovery of a Japanese research group to generate iPSCs from somatic cells provided the opportunity to study human cells that are difficult to access⁴³. Human iPSCs also provide a powerful tool for translational medicine. Especially in clinical trials, many findings from studies in mice did not lead to therapeutic approaches because of the large species-dependent differences²¹⁸.

In the field of neuroscience, this technology offers the possibility to differentiate patient- and disease-specific cells for a better understanding of underlying disease mechanisms. *In vitro* model systems based on iPSCs were established in many labs including the most common neurodegenerative diseases AD and Parkinson's disease⁷⁶. In this work, patient-specific iPSCs for LOAD and matched healthy controls were produced to investigate LOAD-associated susceptibility variants. For the generation of LOAD-specific and control iPSCs, B-LCLs were reprogrammed using a previously published protocol with minor modifications. In order to increase the efficiency of reprogramming, the modified protocol included treatment with histone methyltransferase inhibitor BIX01294 and the DNA methyltransferase inhibitor RG-108. BIX01294 has already been used in various combined reprogramming cocktails and modifies the methylation of histone 3 at lysine 9. Both BIX01294 alone²¹⁹ and RG-108 interfere with the epigenetic modification of the DNA and influence the reprogramming of somatic into stem cells²²⁰. For the analysis of the LOAD two iPSC lines from LOAD patients (MLUi007-H, MLUi008-B) and iPSCs from healthy controls (MLUi009-A, MLUi010-B) was generated, characterized, and subsequently applied for differentiation into MGLCs. Age, sex, ethnicity, and the APOE status were considered in the selection of the donor subjects. One of the LOAD patients also suffered from diabetes mellitus type 2. (TAB 2). Fernanda et. al²²¹ could already show that brains of AD patients with diabetes show an increased release of pro-inflammatory cytokines, such as IL6, compared to non-diabetics and that the blood-brain barrier becomes more permeable through diabetes. Furthermore, insulin signaling disorders have been shown to be associated with protein phosphatase, such as PTEN²²¹.

In this study, modelling of LOAD with iPSCs was chosen because iPSCs enable patient-specific studies of LOAD-associated genetics. In contrast to mouse models, human iPSC-derived MGLCs hold the promise to capture the pathomechanisms of LOAD more completely because the analysis of disease mechanisms is limited by these species-specific differences²²².

4.3.1 Verification of Pluripotency Markers

For the characterization and evaluation of pluripotency, alkaline phosphatase staining was initially performed in LOAD iPSCs and iPSCs from healthy controls (Fig. 8). The generated iPSC colonies

show densely packed cells with sharp edges and a large ratio of nucleus to cytoplasm and thus exhibit a typical morphology for stem cells⁴³. A blue staining of the alkaline phosphatase activity distinguishes iPSCs from the surrounding mouse embryonic fibroblasts. In addition to stem cells, alkaline phosphatase is expressed in other cell types such as bone, liver or placenta. Therefore, this technique serves as a first pluripotency marker, but only together with morphologic analysis²²³. To further characterize the pluripotency of the generated iPSCs, a transcript analysis was performed. As shown in **Figure 9**, the pluripotency-related genes CDH1, DPPA2, KFL4, LIN28A, MYC, NANOG, OCT4, REST, and SOX2 could be detected in MLUi007-H. A frequently published iPSC line WAi001-B²²⁴ served as a positive control and revealed signals in all analyzed pluripotency-related genes. The expression of these genes was also detected in iPSCs generated by other labs and published for example by Congras et al.²²⁵. In another study, the gene expression of REST was strongly detected in ESCs²²⁶. Besides the pluripotency-related genes, three B-LCL marker genes GPR183, FCRLA, and BTLA were examined in the iPSCs to check the remained expression of differentiation markers from the donor also termed somatic memory. According to **Figure 9**, none of the three B-LCL marker genes were expressed in MLUi007-H, indicating absent somatic memory and high quality of reprogramming. Pluripotency related genes are not expressed in B-LCLs shown by previous analyses of the working group.

4.3.2 Proteome Analysis of iPSCs and their Corresponding donors

In a recent article by Kumar et al.²²⁷, transcriptomic analysis was used to study differential gene expression between B-LCLs and their reprogrammed iPSCs. Using hierarchical clustering and principal component analysis, the examined cells could be clustered into two superordinate groups. Within the two subgroups, both B-LCLs and iPSCs showed high similarities. The differentiation of the two cell types suggests a complete reprogramming of the B-LCLs into iPSCs. In the present study, the reprogramming was also verified by proteomic analysis. For this purpose, a proteome analysis of donor B-LCLs (LCL007, LCL008, LCL009, LCL010) and successfully generated iPSC lines (MLUi007, MLUi008, MLUi009, MLUi010) was performed. In a shotgun proteomics approach, we identified 1568 proteins of which 75 proteins differed significantly in protein abundance. In the hierarchical cluster, we could first divide into the two subgroups of B-LCLs, and the iPSC lines generated from them. Moreover, in the respective two subgroups, clustering into healthy controls and LOAD cells could be observed. Reference cell lines clustered together with the healthy controls (**Fig 10 A**). Clustering into two superordinate groups verifies the results revealed in a transcript analysis between B-LCLs and iPSCs by Kumar et al.²²⁷. In addition to the division into the two cell types, a further differentiation into healthy and AD cells was observed in both the group of B-LCLs and the group of iPSCs. The obtained results verify a another transcriptomic analysis performed by Maes et al., which used blood mononuclear cells from LOAD patients and controls to show that both groups cluster differently in a disease-specific manner²²⁸. Compared to the other six of seven iPSCs in the hierarchical clustering, the second reference stem cell line (WAi001-B) is different and forms a separate branch (**Fig 10 A**), which can be explained by different donor material. These results verify a proteome analysis by Kim et al., which shows

remarkably high similarities between ESCs and foreskin-derived iPSCs. Several clones of the generated iPSCs of the study from Kim et. al contained small protein groups in the heat map of the hierarchical cluster, which remained upregulated after reprogramming²²⁹. WAI001-B is also reprogrammed using episomal vectors from foreskin fibroblasts and shows an upregulated protein cluster, resulting in the formation of a separate branch in the dendrogram (**Fig. 10 A**). The donor cell specific transcriptional pattern that can be maintained was also observed by another group²³⁰. The more commonly used reference stem cell line WAI004-B was generated from fetal fibroblasts of the lung via a lentiviral reprogramming strategy and does not appear to have this proteomic profile.

The comparison of four different B-LCL cell lines with the seven iPSC lines confirmed, at the protein level, that the reprogramming process successfully suppressed the expression of somatic genes of the B-LCLs. A principal component analysis of significantly altered proteins from the generated hierarchical cluster visually verifies the division into the two major groups B-LCLs and iPSCs. WAI001-B displays, as in the heat map, small deviations from the other six iPSC lines in component 2 (**Fig 10 B**). The principal component analysis of the B-LCL and iPSC proteome performed in this study verifies the principal component analysis of the group of Kumar et al. Very similar to the transcript analysis, the principal component analysis produced values of 84.5% for component 1 and 3.7% for component 2. Kumar et al. produced values of 84.17 and 85.35 for the microRNAs and mRNAs of component 1 or 3.68 and 3.75 for component 2²²⁷.

In the 75 significantly identified proteins in the analysis, eight of them were found to be upregulated in iPSCs (**Fig. 10 C**). This thesis revealed that seven of the eight proteins were associated with processes for the self-renewal of stem cells. In order to detect differences in the less abundant proteins, such as transcription factors, a labelled proteome analysis would be required. The most highly regulated protein in the iPSC group is the cell growth-regulating nucleolar protein LYAR (Q9NX58). LYAR is a nuclear oncoprotein for the regulation of cell growth. LYAR is highly expressed in undifferentiated ESCs on the mRNA and the protein level counteracting differentiation processes. In addition, LYAR is essential for the maintenance of self-renewal under participation of further nucleolar proteins²³¹. The second highest expressed protein Matrin-3 (P43243) has been identified in neural stem cells and is linked to neurogenesis. Matrin-3 has so far not been described in connection with iPSCs and ESCs. Downregulation of the protein induces differentiation into neuronal cells, suggesting that it is involved in the maintenance of neural stem cells²³². Furthermore, Matrin-3 is involved in the OCT4 network, which controls self-renewal of ESCs²³³. In a global gene expression analysis of ESC lines H9 (WA09), HSF-6 (UC06) and HSF-1 (UC06), the gene NACA was found to be up regulated in the signature of the three ESC lines compared to the inner cell mass. The protein alpha NAC (E9PAV3) translated by the gene NACA was also detected up-regulated in the group of iPSCs in this work, which verifies this result²³⁴. Another protein that was found upregulated in the iPSC group is cathepsin D (P07339) and is described in the literature as being associated with many cancers, such as gastric cancer, melanoma, ovarian cancer, and breast cancer. Cathepsin D was detected in the cancer stem cell subpopulation²³⁵. Importin α 1 (P52292), a protein that was detected in previous studies mainly

expressed in undifferentiated ESCs, was found to be significantly upregulated in the group of iPSCs in this study. Importin $\alpha 1$ is also known to interact with OCT4, which is additionally associated with a nucleocytoplasmic transport of OCT4 in lung cancer²³⁶. Another upregulated protein in iPSCs is otoferlin (Q9HC10), which is known in the literature as calcium sensor and plays a central role in mammalian hearing²³⁷. In a study by Wong et al., mRNA splicing of RNPS1 was investigated demonstrating that RNPS1 together with other factors maintains the self-renewal of ESCs. RNPS1 (Q15287) was also detected up-regulated in the iPSCs and has been shown in the literature to be elevated in ESCs and neural precursor cells²³⁸. Another RNA-binding protein, insulin-like growth factor 2 mRNA-binding protein 3 (O00425), was detected in chicken stem cells in comparison to chicken fibroblasts in a microarray analysis in addition to typical stem cell transcription factors such as NANOG and OCT4²³⁹.

4.3.3 Verification of pluripotency by differentiation into derivatives of three germ layers

In order to further verify pluripotency of iPSCs, their differentiation into derivatives of the three germ layers was demonstrated in this study. Therefore, the spontaneous differentiation of iPSCs using medium supplemented with fetal calf serum was applied. In this study it could be elucidated that MLUi007-H expressed typical markers of the three germ layers in at least one of the measured time points. A transcript analysis was performed to analyze the markers for ectoderm (PAX6, MSI1, SHH), mesoderm (TBXT, PRRX1), and endoderm (CXCR4, FOXA2, SOX17) on day 3, 5, and 10. In MLUi007-H, all markers except of FOXA2 were detected at least for one time point (**Fig 11**). In a study by Torres et al., PAX6 and MSI1 were also used for showing ectodermal differentiation, FOXA2 and SOX17 for endodermal differentiation, and TBXT for mesodermal differentiation²⁴⁰. The three time points were chosen according to the literature²⁴¹ as shown in **Figure 11**. Absent FOXA2 can be explained by the possibility that the spontaneous expression peak may have occurred between the time points. The pluripotency analysis of all five iPSC lines generated in this study showed both the presence of pluripotency-related transcripts and the potential to differentiate into the three germ layers. In accordance with other studies²⁴², we observed no differences between healthy and diseased iPSCs.

4.4 Generation of Human iPSC-Derived MGLCs

Microglia develop during embryonic development from erythromyeloid progenitor cells as well as primitive macrophages of yolk sac prior to peripheral hematopoiesis occurs. Subsequently, the cells enter the CNS and mature into resistant microglia, which are present throughout humans live. In the context of neuroinflammation and especially in LOAD, a migration of peripheral monocytes into the brain has been described^{101,117}. These peripheral monocytes are indistinguishable from resident microglia and elevate the number of immune cells in those brains. Due to their phagocytic properties, microglia are the main cells comprising the immune response in CNS. Thus, they are key regulators in neurodegenerative disorders such as AD. However, isolation techniques are still

elusive since isolation of primary microglia obtained from postmortem tissue of AD patients is very tough and shows an artificial gene expression or phenotypes. Moreover, in order to keep them in culture, serum additives of media developed for primary cell cultures trigger their activation and morphological transformation²⁴³.

Even though animal models are widely used for answering scientific questions, in the context of only a small number of animal models is available including the 5xFAD mouse model²⁴⁴. However, a recent transcript analysis of AD associated genes indicated strong differences between human and mouse microglia⁹⁵. A promising alternative to primary postmortem cultures and animal models represents human iPSCs. iPSCs are obtained from genetically characterized patients with known AD mutations enabling the generation of MGLCs carrying a number of genetic mutations that play a role in AD pathophysiology¹⁷⁶. Regarding that, patient derived MGLCs were generated in this thesis and investigated with respect to AD.

To study microglial processes in LOAD, a robust and reproducible serum-free differentiation protocol was developed to generate MGLCs via monocytes. The factor of serum free differentiation is essential for the functionality of the microglia. Serum can greatly influence the morphology and the way in which cells become activated²⁴⁵. Microglia and monocytes undergo comparable differentiation in early development, which explains a comparable profile of surface markers in mature cells. Both microglia and monocytes develop from hemangioblast cells that are formed from primitive streak cells. Microglia progenitor cells migrate at stage E10.5 into the developing brain and mature into adult microglia, while monocytes progenitor cells differentiate into mature monocytes in the liver and later in the bone marrow and are subsequently released into peripheral blood vessels¹⁰⁵.

In 2010 the first microglia differentiation protocol from mouse ESCs was published. In this article mouse microglia were differentiated according to a five step protocol using embryoid bodies via the neuroectodermal germ layer and required up to 60 days for mature MGLCs²⁴⁶. A further protocol for the differentiation of MGLCs was published in 2016. In this differentiation approach the cells were also first developed in embryoid bodies and subsequently differentiated via the neuroectodermal germ layer to mature MGLCs¹⁷⁶. For the first time, human iPSCs and ESCs were used for differentiation¹⁷⁶. In 2017, three further differentiation approaches appeared to generate MGLCs from iPSCs²⁴⁷⁻²⁴⁹. The three protocols were based on a 2-dimensional differentiation without the generation of embryoid bodies via the mesodermal germ layer. In this thesis the MGLCs were also generated with a 2-dimensional protocol based on the development via the mesodermal germ layer with monocytes as an intermediate stage.

For differentiation of microglia from iPSCs via monocytic progenitor cells, we modified an already published protocol. The group of Yanagimachi et al. differentiated iPSCs into MGLCs via primitive streak-like cells into hematopoietic stem cells and finally into monocytes²⁵⁰. The protocol of Yanagimachi and slightly modified protocols were proven in further studies²⁵¹. For the generation of MGLCs, human iPSCs undergo a five-step differentiation process. For this purpose, iPSCs were first cultivated in several small colonies and grown until a confluence of about 70 to 80%. The

differentiation of iPSCs was induced by BMP4 for the initial differentiation into primitive streak-like cells. Subsequently, cells were developed into hemangioblast-like hematopoietic progenitor cells by the factors VEGFB, FGF2, and KITLG in a second step. In early mesodermal differentiation, KIT and KITLG are of crucial importance in the development of erythroid and myeloid progenitor cells^{104,114}. Myeloid progenitor cells are further differentiated into hematopoietic cells in StemPro™-34 SFM medium with hematopoietic cytokines such as KITLG, FLT3, IL3, MCSF, and TPO. In order to further differentiate myeloid progenitor cells not migrated from yolk sac into the CNS, the two factors TPO and FLT3 are required¹¹⁴. Terminal differentiation to an intermediate stage resembling monocytes was achieved in step four via the factors FLT3, MCSF, and GMCSF. Based on these factors the proliferation into monocyte-like cells was regulated and the differentiation was further advanced^{113,252}. The fourth step includes the generation of monocyte-like cells detaching from the plate and growing in suspension. For the differentiation into MGLCs, the monocyte-like cells in suspension were collected and transferred to a plate coated with 0.1% gelatin. The collection of monocyte-like cells was repeated up to five times every fourth day.

The oxygen supply was important for proper differentiation into MGLCs. The initial treatment under hypoxia for one day accelerated the differentiation induced by IL34, MCSF, and GMCSF in MGDM medium. IL34 has a decisive influence on survival and differentiation into microglia¹¹³.

After differentiation for about 40 days mature MGLCs were generated. For a further differentiation of monocytes into microglia, a medium was used that is supposed to mimic the brain interstitial fluid. This medium was established by Muffat et al., which is suitable to obtain microglia via neuroectodermal progenitors¹⁷⁶. The adaptation of conditions such as coating, oxygen level and time of treatment were adapted by various experiments and are shown in **Figure 12**. At the end of the differentiation, we obtained a good yield of MGLCs from different iPSC lines, which were both comparable and reproducible as well as usable for phenotype detection.

4.4.1 Characterization of Developing Monocyte Lineage MGLCs

To investigate whether the iPSC derived MGLCs are similar to primary microglia, histological, morphological and gene expression analyses were performed. The morphology of differentiating cells undergoes many stages of hematopoietic differentiation. **Figure 13 A** shows the course of differentiation, starting from iPSCs, through primitive hemangioblasts to MGLCs. Furthermore, as shown in the differentiation progression in **Figure 12**, MLCs were differentiated as an intermediate stage to MGLCs and morphologically characterized using a Wright-Giemsa staining. In comparison to primary monocytes, monocyte like cells indicate strong macroscopic similarities in staining (**Fig 13 B**). A characterization of iPSC-derived monocytes via Wright-Giemsa staining has already been used in differentiation protocols of other groups and showed similar results^{247,249}.

To further characterize the differentiated microglia-like cells, a transcript analysis with crucial myeloid markers (AIF1, CD68, and SP1) and markers involved in phagocytosis (TREM2, CD33, and TYROBP) was performed. For the study of gene expression, 40 days old differentiated MGLCs were used. As shown in **Figure 14 B**, all investigated markers were similarly expressed in

MGLCs, control primary monocytes and primary microglia. Previous studies^{176,249,250,253} have shown these markers expressed in both primary and iPSC derived myeloid cells, such as monocytes, macrophages, and microglia, confirming the results. In order to characterize the subgroups of myeloid cells, Butovsky et al. investigated specific cell type signatures using a quantitative mass spectrometry²⁵⁴. In the signatures of monocytes, macrophages, and microglia, six proteins with different expressions were identified and validated by subsequent gene expression. In this study, four of these genes (C1QA, MERTK, PROS1, and GAS6) were analyzed by quantitative transcript analysis to distinguish them from monocytes and to improve microglia differentiation (**Fig. 14 A**). Similar to results of Butovsky et al., the MGLCs differentiated in this study showed great similarities to primary microglia. Compared to primary microglia and MGLCs, the four genes were markedly lower expressed in the primary monocytes. The genes discovered by Butovsky et al. were also used in other microglia differentiation protocols to distinguish microglia from monocytes²⁴⁹.

Two additional methods were used to detect the translation and expression of functional proteins in addition to transcription. On the one hand, immunofluorescence analysis was used to visualize the detection of proteins on the cell surface, in the cytoplasm and in the cell nucleus. Second, the results were quantified using flow cytometry. The visualization of the cellular localization of TUBB3, PTPRC, ITGAM, CD68, CD33, AIF1, and TREM2 as well as the transcription factor PU.1 in the cell nucleus were shown by immunohistochemical staining shown in **Figure 15**. Double staining and the individual channels show that the microglial markers are similarly localized as described in the literature^{246,249,254}. Especially for PU.1, the signal was detected as described very clearly localized exclusively in the cell nucleus¹⁷⁶. Flow cytometry verified the genes expressed in the transcript analysis at the protein level and was demonstrated for the surface molecules CD11b, CD11c, CD14, CD40, CD45, and CD33 in **Figure 16**. By flow cytometric measurement of membrane receptors two subpopulations of the cells were detected. It should be noted that the expression of the surface markers is strongly dependent on the activation condition of the microglia, which enables the formation of these populations^{208,255–257}. This phenomenon is a good example for the high plasticity of the cells.

In addition to the investigation of iPSC derived MGLCs for crucial microglia markers, a physiological characterization was performed. For the purpose of excluding the influence of LOAD and age in the analyses, the reference iPSC line WAI001-B was used to investigate membrane potential and the production of cytokines. In **Figure 17**, a transcript analysis was performed in the iPSCs, and iPSC derived differentiated MGLCs. This study demonstrated that the examined cytokines IL10, IL8, IL6, IL1 β , and TNF α were exclusively expressed in the iPSC derived MGLCs. Furthermore, no differences between pro- and anti-inflammatory cytokines were observed. These results were verified in a previous study²⁵⁸ using iPSC derived monocytes also expressing these cytokines as proteins. In order to investigate the electrophysiological properties of MGLCs, a whole cell patch clamp analysis was performed to measure the membrane potential. The analysis of the MGLCs revealed a resting membrane potential of -49.5 ± 3.7 mV and a depolarization potential of 24.5 ± 1.4 mV of the MGLCs after treatment with KCl. For patch clamp analysis, six independently differentiated MGLC cultures from the iPSC line differentiated from

WAI001-B were used. In the present study, the resting membrane potential of the MGLCs were found to be similar to the resting membrane potential of -40.6 ± 0.6 mV from a study on primary microglia from rats²⁵⁹. Other studies also observed depolarization values similar to the present study using KCl in primary rat microglia. Furthermore, the small variation of the values indicated a homogeneous MGLC population similar to primary cells. The membrane potential of microglia is sensitive and responds immediately to small changes in membrane current. Thus, a release of ATP in case of cell damage can activate the microglia and thus has an influence on the motility and the release of cytokines²⁵⁹.

Functional characterization of MGLCs was performed based on the capacity for phagocytosis and the process of stimulation with LPS. In LOAD, the process of phagocytosis plays a crucial role; therefore, both differentiated MGLCs of healthy control WAI001-B and LOAD-specific MGLCs were used for the phagocytosis assay. **Figure S6 A** showed a higher rate of phagocytosis in the healthy control MGLCs compared with the LOAD MGLCs, both when untreated and as a result of stimulation. A longer stimulation of 24 h showed an increased phagocytosis rate in the LOAD-MGLCs compared to the healthy controls. To verify phagocytosis and to exclude beads that adhered to the cell surface but were not internalized, a second phagocytosis assay was performed. To also exclude nonspecific phagocytosis, MGLCs were treated with a fluorescently labeled *Escherichia coli* K-12 strain BioParticles™ in a second approach to ensure receptor-dependent uptake. In this approach, the results of healthy controls obtained in the first approach were verified **Figure S6 B**. Due to the fact that both phagocytosis assays were performed once, no clear statistically relevant conclusion can be made about altered internalization in the case of LOAD. However, the initially lower phagocytosis in LOAD MGLCs at 4 h stimulation suggests a limited response in LOAD. The verification of this preliminary results would suit to other results obtained in the present thesis. For the characterization of MGLCs the internalization of latex beads as well as *Escherichia coli* K-12 strain BioParticles™ showed the ability of phagocytosis. This method for testing the ability of phagocytosis has already been used by established protocols of phagocytizing cells for the characterization²⁵³ and pathogenesis of AD²⁴⁹.

4.4.2 Functional Analysis of Immune Plasticity in LOAD MGLCs

Functional analysis was performed with live cell imaging. This study used 12 h time-lapse microscopy and revealed a significantly increased speed of the LOAD MGLCs compared to the healthy control MGLCs (**Fig. 18**). In the LOAD cells, velocities of individual cells of up to 766 nm/min could be recorded, while the healthy control cells moved at a maximum speed of about 240 nm/min. Due to their homeostasis, the microglia are in different stages of activation and therefore move at different velocities. Cell activation leads to morphological changes, allowing microglia to migrate immediately to the site of the perceived stimulus. In the primary resting microglia, hardly any movement was observed. For activated primary microglia, velocities of up to 1.5 $\mu\text{m}/\text{min}$ have been described in the literature, whereby the cells were observed to have an amoeboid morphology with fewer processes^{260,261}. In addition to the increased motility to a stimulus and the altered morphology, a previous study could further show that surrounding cells influence

microglia in their velocity as well²⁶¹. In co-cultures with neurons an increased motility was observed compared to single cultures. In a study by Gyoneva et al.¹¹⁹, a significantly increased velocity of the A β surrounding microglia in 5xFAD mice was detected, which verified the significant change in velocity of LOAD iPSC derived MGLCs in this thesis.

Morphological changes described in previous studies could be verified in this thesis^{119,261}. As already mentioned for motility, microglia show an increased degree of plasticity, which can undergo several structural changes depending on their status of activation. In order to investigate the morphology and branching of LOAD MGLCs in comparison to healthy control MGLCs, the degree of ramification of the cells was analyzed using the convex hull method. However, convex hulls exclusively determine the degree of ramification. Therefore, the perimeter method was used for a further calculation in order to further determine the degree of cell activation. In the evaluation of the ramification index, both methods showed increased values in the group of LOAD cells compared to healthy control cells. A tendency for decreased branching of the protrusions was observed in the LOAD cells, but differences were not significant. For the analysis with the perimeter method, a significant enlargement of the cell bodies for LOAD compared to healthy controls was shown indicating an increased activation of the MGLCs in LOAD (**Fig. 19**). In the literature, microglia of LOAD patients have also been described as more activated in an amoeboid morphology with increased motility¹¹⁹. Of crucial importance for the processes of motility and activation is the reorganization of the actin cytoskeleton, which moreover regulates migration²⁶². As introduced earlier in **chapter 4.1**, various genes such as EPHA1 or CD2AP associated with LOAD have also been described as putative functional regulators of actin cytoskeleton remodeling.

In addition to morphological changes and motility, telomere shortening associated with AD has also been described for activated microglia in previous studies. Telomeres are conserved DNA sequences at chromosome ends that shorten with each cell division, thus providing a marker for replicative aging²⁶³. To investigate the effects of replicative aging and telomere shortening on the progression of LOAD, a multiplex quantitative PCR was used to determine the relative telomere lengths in reference MGLCs (WAI001-B, WAI004-B) compared to healthy control MGLCs (MLU009-A, MLU010-B), and MGLCs from LOAD patients (MLU007-H, MLU008-B). Reference iPSCs were obtained from young donors, whereas healthy controls were obtained from old healthy donors. The evaluation of the relative telomere lengths initially showed significantly shortened telomeres of the old healthy control MGLCs compared to the young reference MGLCs. Furthermore, a significant shortening of telomeres was observed in LOAD MGLCs compared to healthy controls and the reference MGLCs (**Fig. 20**). Furthermore, high similarities in telomere length were found within the biological replicates of reference and healthy control MGLCs. In LOAD MGLCs, a discrepancy in telomere length was observed between the two cell lines MLU008-B and MLU007-H. In the case of the patient cell line MLU008-B, the clinical history of the cell line included AD and diabetes mellitus type 2 (**TAB 2**), which is additionally described as a factor for telomere shortening²⁶³. The results presented in this work verify the process of telomere shortening known in ageing. Furthermore, it could be shown that telomere shortening also occurs in AD. In previous studies, in addition to telomere shortening, increased telomerase

activity was detected in AD patients compared to healthy controls. Telomere shortening leads to senescence and progression of LOAD in both microglia and peripheral monocytes, which in turn leads to the release of pro-inflammatory interleukins^{263,264}.

To investigate the release of pro- and anti-inflammatory cytokines, a Bio-Plex Precision Pro™ cytokine assay was performed to analyze cytokine concentrations of cell supernatants. The multiplex method is based on magnetic beads, which allows accurate measurement of low concentrations of ten human cytokines IL1 β , IL2, IL4, IL5, IL6, IL10, IL12 (p70), IL13, INF γ , and TNF α . Primary human microglia were used for validation of the multiplex technology. For the study of cytokines, primary microglia were analyzed for their immune response in duplets, both unstimulated and stimulated with 5.0 μ M A β pE3-42. In the unstimulated human primary microglia low concentrations of IL2, IL4, IL5, IL6, IL10, IL13, and INF γ were detected. IL1 β and IL12 were not detected in unstimulated human primary microglia or were below the detection threshold. As a result of stimulation with A β pE3-42 an increased release of all cytokines was observed. The highest concentrations were found for IL5, IL6, IL10, and INF γ . Furthermore, the interleukins IL1 β and IL12 were detected in the stimulated human primary microglia, which were not measurable in the unstimulated human primary microglia (**Fig. 21 A**). In general, primary microglia served as a control verifying that the cytokines were detectable and that A β pE3-42 stimulates the release of cytokines. The accumulation of A β and intracellular neurofibrillary tangles has been described as the hallmarks of AD causative for loss of synaptic function, neuronal death, and activation of microglia. Furthermore, A β has been associated with the microglial release of pro-inflammatory cytokines in AD. A β accumulation is a neuropathological feature of LOAD and is characterized by a diversity of A β peptides during aggregation. A β 42 has been associated with increased aggregation. Besides the different peptide lengths, posttranslational modifications have a decisive influence on the etiology of AD^{265,266}. In this work, A β pE3-42 was used to stimulate the cells to mimic the physiological conditions of LOAD. This modified form of A β was found very frequently in AD brains and is produced enzymatically during posttranslational peptide maturation by cyclization of N-terminal glutamate residues²⁶⁶.

Multiplex technology was subsequently used to study cytokine release in untreated and stimulated MGLCs. In the two references unstimulated WAi001-B and unstimulated WAi004-B, a signal was detected exclusively for the unstimulated cell line WAi001-B for the interleukins IL6 and IL10. Following stimulation with A β pE3-42, a signal for IL1 β , IL6, and TNF α was analyzed for both stimulated cell lines WAi001-B and WAi004-B. In the stimulated WAi004-B, IL4, IL12, and INF γ were additionally detected as a result of the stimulation. In the stimulated cell line WAi001-B, low concentrations of IL4, IL5, and IL13 were measured due to A β treatment (**Fig. 21 B**). In summary, both reference cell lines (WAi001-B and WAi004-B) showed an increased release of pro-inflammatory cytokines due to A β pE3-42 treatment. Moreover, anti-inflammatory cytokines such as IL10 were also observed following stimulation. The high basal level for IL6 and IL10 of the unstimulated WAi001-B line indicates that the cells have already been previously activated. IL6 is produced dependent on Toll-like receptor 2 signaling and could therefore be the consequence of phagocytosis. Toll-like receptor 2 and 4 are essentially involved in phagocytosis and the anti-

inflammatory IL10 is mostly secreted as a result of the regulation of IL6²⁶⁷. Dying cells probably caused by NaOH in the treatment of both unstimulated and stimulated cells (see 2.5.4.2) would be a possible cause for the activation of phagocytosis and the resulting release of interleukins. NaOH was used to dissolve A β pE3-42 and for standardization of the samples it was also added to the unstimulated MGLCs in the identical concentration.

Figure 21 C displays cytokines concentrations in the media of cell cultures for the two healthy control MGLCs (MLUi009-A, MLUi010-B) and the two LOAD MGLCs (MLUi007-H, MLUi008-B) before and after A β pE3-42 treatment. For the healthy controls, low concentrations of IL6 were detected in the unstimulated cells, which increased after A β pE3-42 treatment for 24 h. Similarly, for the LOAD cell line MLUi008-B, an increased IL6 concentration was detected in unstimulated cells, which increased strongly as a result of stimulation. In MLUi008-B a higher IL6 concentration was measured before and after A β pE3-42 treatment compared to the healthy controls. Additionally, a low concentration of TNF α was observed in the stimulated MLUi008-B. The second LOAD cell line MLUi007-H did not show a signal in the unstimulated cells in any of the investigated parameters. In the stimulated cells, a signal was detected for stimulated MLUi007-H in each of the ten analytes investigated. IL5, IL6, IL10, and INF γ were most strongly released after A β pE3-42 treatment. Compared to reference MGLCs, lower concentrations of cytokines were released in healthy control MGLCs and LOAD MGLCs. In the human primary microglia, similar cytokine concentrations were analyzed in comparison with the MGLCs from the iPSCs generated in the present thesis. Differences between the reference iPSCs and iPSCs generated in the present study most probably are due to the origin of the donor material used for reprogramming. In this study, the most released interleukins IL6 and IL10 were also found to be elevated in LOAD. IL10 has a regulatory effect on IL6 and decreases in concentration during A β stress. Elevated IL1 β levels in blood were also found to be strongly associated with AD in previous studies²⁴⁴. In this work, IL1 β was increased in references and LOAD MGLCs from MLUi007-H as a result of A β treatment. Another analyte associated with LOAD, TNF α was detected in MGLCs from both LOAD iPSCs, whereas no signal was detected in the healthy controls²⁶⁷. In a further study, it was shown that IL1 β , IL6, TNF α , and INF γ is increased secreted by A β treatment as a result of microglia activation²⁶⁸.

In summary, this thesis successfully developed a protocol to generate iPSC derived MGLCs that expressed all investigated markers recently described for the characterization of microglia. A subsequent transcript analysis of four genes differently expressed in the myeloid cells showed higher similarities of MGLCs to primary microglia than to primary monocytes. Furthermore, MGLCs showed the ability to move, release cytokines and chemokines, and were able to phagocytize both latex beads and *Escherichia coli* K-12 strain BioParticlesTM indicating the functionality of MGLCs. Patient-specific generation of MGLCs enabled the identification of differences in LOAD cells compared to healthy controls providing a robust and reproducible tool for modeling LOAD.

4.5 Proteome Analysis of MGLCs

To further investigate underlying mechanisms in LOAD, proteome analysis was performed to profile LOAD MGLCs in comparison to MGLCs of the reference and healthy controls. An investigation of significantly altered proteins will further characterize microglia in the development of neurodegenerative diseases in order to possibly provide new functionally relevant molecular insights. In order to ensure an accurate determination of the proteome, we performed flow cytometry to evaluate the homogeneity of the cells in the cell population prior to mass spectrometric analysis. For verification of the purity of the population, the surface marker CX3CR1 was used and analyzed co-stained with CD45. To confirm the specificity of the CX3CR1 antibody, HEK293T cells and PBMCs were used as negative and positive controls. HEK293T cell line used as negative control was not stained by CX3CR1 events in flow cytometry, both during isotype control (**Fig. 22 top left**) and after measurement of CX3CR1 surface receptor (**Fig. 22 bottom left**). For the PBMCs, staining was performed together with CD14 antibodies to show the monocytic population of 13.0% (**Fig. 22 top middle**). As already shown in a previous study²⁶⁹, the surface receptor CD14 was detected in the analysis of PBMCs exclusively on monocytes at a frequency of 11.0% in the total PBMC population. For staining with the anti-CX3CR1 antibody, specific expression of the receptor was revealed on all monocytes as well as on a subpopulation of CD14-negative cells with respect to isotype control. The subpopulation of CD14-negative CX3CR1-positive cells comprises a population of CD8-positive T cells and natural killer cells (**Fig. 22 bottom middle**). For verifying this, the expression of the fractalkine receptor on the cell surface of CD8-positive T cells and natural killer cells was confirmed by a previous study²⁷⁰. For the analysis of differentiated MGLCs, more than 90.0% positive cells revealed an almost homogeneous expression of CX3CR1 compared to the isotype control (**Fig. 22 right**). In a study on the development of microglia, the course of expression of specific markers in the maturation of cells was described. Progenitor cells matured from yolk sac developed into CD45-positive CX3CR1-negative immature microglia and, after migration in the brain, matured into CD45-positive CX3CR1-positive adult microglia. In the brain, microglia are the most abundant cells expressing CX3CR1¹⁰⁴. In order to obtain an adult homogeneous microglia population, flow cytometric analysis with the markers CD45 and CX3CR1 was used in previous studies²⁴⁹.

To identify differences in microglial signature for LOAD, we performed quantitative mass spectrometry analysis of the nearly homogeneous MGLC population. Based on the statistics subsequently performed, relative protein expression of 489 proteins were identified as significantly different via a multi-sample test. For visualization, the values were normalized with the Z-score and presented as hierarchical clustering. The hierarchical clustering resulted in an initial categorization of cell lines into healthy (green and black dots) and diseased (red dots) MGLCs. In the healthy group, a further subdivision into young references and old healthy controls was observed (**Fig. 23 A**). In the attached principal component analysis, the three groups could be clearly separated, with the strongest difference shown between the healthy controls and LOAD MGLCs. Within each group, a high similarity of the respective biological replicates was identified

(**Fig. 23 B**). The results of hierarchical clustering and principal component analysis indicate the ability of the cells to model both aging and AD. The results of principal component analysis were then verified using a multi-scatter plot with a Pearson correlation. For this, all significantly identified proteins were considered to define differences by the correlation coefficient R (**Fig. 23 C**). Similar differences in microglia signatures have been shown in previous studies using transcript analysis for both aging²⁷¹ and AD²⁷² in mice. Another study also identified altered gene profiles in iPSC derived microglia from AD patients. Furthermore, this study demonstrated that human iPSC derived MGLCs have a similar signature to human primary microglia and provide new insights into AD²⁴⁹. Thus, it was verified that iPSC derived MGLCs are an important tool to better understand the underlying mechanisms of LOAD. In this context, transcriptome and proteome analyses were performed to detect altered signaling pathways or biological processes.

4.5.1 Non-Hypothesis-Driven Analysis

To investigate the significantly identified 489 proteins of the ANOVA between the groups, a T-test of the reference and healthy controls compared to LOAD was performed. In the evaluation, 329 proteins were identified for the references and 277 proteins for the healthy controls compared to LOAD. Identified proteins were plotted in a volcano plot with the respective fold change versus p-value (**Fig. 24 A**). Proteins with a p-value smaller than 0.05 and a fold change smaller than -1 and larger than 1 were transferred to a Venn diagram. Therefore, the proteins were fed into two Venn diagrams, grouped for up- (**Fig. 24 B**) and down (**Fig. 24 C**) regulated proteins. A total of 276 proteins in the healthy controls were analyzed in comparison to LOAD. Aging is one of the major risk factors of LOAD, reflecting a large overlap of proteins between the reference (young donors) and healthy controls (old donors) compared to LOAD. In addition, the Venn diagram presented proteins that are exclusively altered with age compared to LOAD. In the Venn diagrams more upregulated proteins were identified. A greater upregulation of proteins in AD was recently found in a previous study in APP/PSEN1 mice²⁷³. To classify the proteins modified in LOAD compared to the healthy controls, a STRING network of a gene ontology enrichment analysis of biological processes was performed (**Fig. 24 D**). In the analysis of the affected biological processes, the significantly identified proteins were most strongly correlated to the processes of organelle organization (FDR $p = 5.6E-17$, 106 proteins), protein-containing complex subunit organization (FDR $p = 4.6E-9$, 65 proteins) and regulation of the cellular component organization (FDR $p = 9.1E-9$, 67 proteins). An enrichment analysis of biological processes in a previous study also identified the three biological processes associated with neuronal A β treated cells. Hwang et al. further identified the several proteins related to DNA packing, macromolecular complex subunit organization and actin filament-based process in the performed proteome analysis²⁷⁴. In the enrichment analysis network, an accumulation of proteins was identified whose functions are associated with the cytoskeletal organization (p -value of $2.7E-5$), the regulation of morphogenesis and regulation of endocytosis. Protein related pathways identified in this work in LOAD MGLCs compared to the healthy controls MGLCs verified the results of a previous study. In the lab of Orre et al., a transcript analysis of isolated APP was performed in mouse microglia compared to

aged mice, in which up-regulated proteins were particularly related to the processes of defense response, positive regulation of immune response, cytoskeletal function, complement activation and antigen presentation²⁷⁵. In particular, the actin cytoskeleton is considered to play a crucial role in the regulation of LOAD^{274,275}. Finally, cellular response to stress was associated with identified proteins of LOAD MGLCs compared to the healthy control cells.

4.5.2 Focused Analysis Revealed by Cytoskeleton Organization in LOAD

In order to gain insight into the molecular changes underlying LOAD induced microglia reactivity, the identified proteins and their associated biological processes were presented in a diagram (**Fig. 25**). Based on the number of proteins associated with the respective functional protein cluster, the biological processes particularly affected by LOAD were investigated in advance. In general, an upregulation was observed during the investigation. In the enrichment analysis of biological processes, the 276 significantly identified proteins in LOAD were classified into 24 biological processes (**Fig. 25 A**). In six of the protein groups involved in the regulation of cell cycle, cellular stress, chromatin organization, DNA repair, apoptosis and signal transduction, a strong up-regulation without accompanying downregulation was identified. In a previous study, RNA sequencing analysis of hippocampal microglia of a 5xFAD mouse revealed upregulation of the genes encoding proteins that play a role in cell cycle, response to stress, chromatin organization and DNA repair²⁷⁶. In a transcript analysis of human purified microglia, a further study showed that the putative proteins, involved processes mentioned above, are also altered in aging²⁷⁷. In order to examine the identified proteins for their association with AD, they were matched with an online GeneCards database (Weizmann Institute of Science, <http://www.genecards.org/>) for AD²⁷⁸. For four of the biological processes many of the AD-associated proteins were classified. AD-associated proteins have been identified mainly in biological processes indicating functions in the immune system, signal transduction, developmental biology and in the process of disease and are shown in **Figure 25 B** with the number of proteins involved. According to a deeper analysis, the identified proteins indicate a potential function in axon guidance, homeobox gene activation and transcriptional regulation of granulopoiesis, which are described as subordinate processes of developmental biology.

In a previous study, Axon Guidance and genes involved in cell adhesion were shown to be associated with ageing²⁷⁷. Significantly associated proteins may be associated for more than one biological process. In the biological processes, associations were shown for aging, LOAD, and activation of microglia. For axon guidance an association for aging was shown in a previous study as well as for cell adhesion involved genes²⁷⁷. For homeobox gene activation²⁷⁹ as well as granulopoiesis²⁸⁰, microglial activation as a result of inflammation or aging processes has been described. The biological processes associated with the process of the disease suggest an effect in signal transduction disease, transporter disorder, infectious disease, and neurodegenerative disease. Identified proteins associated with immune system functions were identified in both aging^{277,281} and AD^{275,276} studies. For proteins that suggest functions in antigen presentation, actin cytoskeleton remodeling, pro-inflammatory cytokine release and the process of phagocytosis, AD-dependent

upregulation was predominantly observed^{275,282}. Several proteins have been identified to be associated with the processes of signal transduction in an upregulated manner. The analysis mainly identified proteins associated with signaling by receptor tyrosine kinases, TGF- β , G-protein coupled proteins, NOTCH, WNT, Hedghog, MAPK, second messenger, rho-GTPases and estrogen signaling receptor -mediated signaling. As a result of microglia activation and neuroinflammation, the biological processes of Actin Cytoskeleton Organization, Stress Response, and Immune Response have been identified as altered in AD^{274,275}. The subgroups and signaling pathways identified in Signal Transduction are involved in the regulation of biological processes. In LOAD, altered phagocytosis and endocytosis as well as the release of pro-inflammatory cytokines have been described as a consequence of altered signal transduction. Rho-GTPase signaling plays a crucial role in the ramification process of microglia. Furthermore, GTPases have been described to play a role in the regulation of pro-inflammatory cytokines, motility, actin cytoskeletal remodeling and phagocytosis²⁸³. The group of Grandbarbe et al. described a crucial role of NOTCH signaling for the regulation of pro-inflammatory cytokines and phagocytosis using rat microglia. Furthermore, an upregulation of NOTCH after LPS stimulation was observed²⁸⁴. Furthermore, MAPK²⁸⁵ and WNT²⁸⁶ signaling play a crucial role in AD by being involved in phagocytosis and release of pro-inflammatory cytokines. Because AD is closely related to aging, some common phenotypes, and alterations of biological processes with aging microglia have been identified in AD microglia. In recent studies, key processes such as microglia activation and neuroinflammation have been frequently discussed in relation to aging, so that biological processes in AD as well as aging have been described¹²².

In order to further investigate altered biological processes in LOAD, exclusively identified proteins of the healthy controls (old donors) compared to the LOAD group were used for further analysis. The protein cutoffs of the references and healthy controls compared to LOAD (**Fig. 24 B and C**) were excluded from the analysis. A subsequent enrichment analysis of biological processes should only represent modified processes for LOAD. **Figure 26** demonstrated the proteins with their fold change to the corresponding biological process. Of the total protein count of 276, 75 proteins were exclusively in the healthy controls and associated with AD. Top ten list of significant proteins found exclusively in the healthy controls (old donors), have a high p-value, a high fold change and associated with a high AD score, could be indicated to be involved in cytoskeleton organization, regulation of endocytosis, response to reactive oxygen species, immune response, glucose metabolism, and APOE.

In fact, the microglial cytoskeleton is composed of actin, vimentin-containing intermediate filaments, and microtubules. While the vimentin-containing intermediate filaments and microtubules form dense networks that radiate into the periphery, F-actin is diffusely arranged in the cytoplasm. In the case of microglia activation, there are changes in the organization of the components of the cytoskeleton. F-actin reorganizes to thick filamentous bundles below the cell membrane. A reorganization of the cytoskeleton is associated with motility, phagocytosis, morphological changes and antigen presentation²⁸⁷. In this thesis, the proteins cystatin-B (CSTB), fermitin family homolog 2 (FERMT2), cofilin-1 (CFL1), microtubule-associated protein 2 (MAP2)

were identified associated with the cytoskeletal organization, which might indicate a role in progression of LOAD. Cystatin B was identified upregulated and is known from previous studies to interact with several proteins involved in the Cytoskeleton Organization²⁸⁸. Furthermore, an association for A β accumulation in AD has been described for this protein. In a cystatin B knock out in a mouse model a reduced A β load could be verified by Yang et al.²⁸⁹. Based on previous studies, cystatin B appears to have a function in cytoskeletal remodeling and has also been described by associations studies as having a role in A β accumulation in AD. Until now, an exact function of the protein in the cytoskeleton is not known.

In GWAS, FERMT2 has already been identified as associated with AD²⁹⁰. FERMT2 was detected together with TREM2 and APOE exclusively in microglia, but not in monocytes, where it plays a role in actin cytoskeleton organization, WNT signaling and signal transmission via integrin activation²⁶¹. The Yasuda-Yamahara group was able to show that FERMT2 has a crucial function in the reorganization of F-actin into thick filamentous bundles. An upregulation in the MGLCs, as shown in this work, could therefore indicate a reorganization of the actin cytoskeleton in LOAD²⁹¹. Furthermore, cofilin-1 has been identified downregulated in the LOAD MGLCs. Moreover, in contrast to FERMT2, cofilin-1 has a regulatory effect on actin dynamics by accelerating the dissociation rate of actin subunits and cleaving actin filaments²⁹². A downregulation of cofilin-1 indicates a shift in the ratio of G- to F-actin. In a further study, an association with AD was identified for cofilin-1. The protein was found to play an important role in actin cytoskeleton remodeling both in the ageing process and in AD²⁹³. Cofilin-1 is regulated by Rho-GTPases and plays a key role in the regulation of actin dynamics. In microglia, an additional role in activation and migration for the protein has been described²⁹⁴. The alteration of these two proteins is associated with the maintenance of the F-actin network of the cytoskeleton organization, which is related to possible functions in motility, phagocytosis and chemotaxis²⁹⁵. In addition to the actin cytoskeleton, the microtubules play a decisive role in maintaining the stability of the cell. MAP2 plays a pivotal role in this process²⁹⁶. In the LOAD MGLCs, this protein was upregulated which could lead to changes in plasticity. Microtubule-associated protein 2 was identified as the fourth protein for the cytoskeleton organization with a high AD score of 17.39 as earlier described²⁹⁷.

However, the process of cytoskeletal remodeling is also of crucial importance for the regulation of endocytosis. Furthermore, in previous studies as well as in this thesis, an upregulation of rho GTPases could be related to the processes of cytoskeleton organization and endocytosis²⁹⁸. For the process of endocytosis, the proteins peptidyl-prolyl cis-trans isomerase NIMA-interacting 1 (PIN1) and lactadherin were determined in association. PIN1 has been described in connection with protein endocytosis and vesicular trafficking²⁹⁹. Furthermore, PIN1 was reported to be a positive regulator of TLR4 signaling in phagocytosis³⁰⁰. In comparison with AD associated proteins PIN1 is listed with an AD score of 24.63. The protein lactadherin, significantly identified in LOAD MGLCs, is released by activated microglia, binds to neurons and causes subsequent phagocytosis of these neurons³⁰¹.

Reactive oxygen species play a role in phagocytosis as well as in many processes of the immune system. In this work, protein/nucleic acid deglycase DJ1 was identified in the list of the top ten proteins as an associated protein for the process reaction to reactive oxygen species. Dj1 has been described as a sensor for oxidative stress. Moreover, in connection with the regulation of DJ1, altered pro-inflammatory cytokines such as IL1 β and IL6 and an influence on the expression of TREM2 were described³⁰². An AD score of 8.43 was identified for protein DJ1. Regarding the immune response, the two proteins alpha-crystallin B chain and, 72 kDa type IV collagenase were identified as associated proteins. For alpha-crystallin B chain an immunoregulatory response in microglia activation has been described. In fact, an increased release of cytokines such as IL1 β , IL12p40, IL10, IL6, and TNF α was described when the protein was knocked out^{303,304}. Furthermore, one study showed a strong association and involvement of crystallin B for the process of amyloid toxicity³⁰⁴. In the LOAD MGLCs analyzed in this thesis, a down regulation of the protein was observed. A second protein 72 kDa type IV collagenase (alternative name matrix metalloproteinase 2) was downregulated regulating immune response. Previous studies have also shown downregulated levels of metalloproteinase in AD. Furthermore, the protein has been described to play a role in the degradation of A β , secretion of IL1 β and the phagocytosis process³⁰⁵. Moreover, the protein triose phosphate isomerase of the Glucose Metabolism was identified up-regulated in LOAD MGLCs, as it was already shown in a proteome study in post mortem AD brains³⁰⁶. In the fourth associated biological process named Cholesterol Transport, APOE was significantly upregulated in LOAD cells. APOE in 5xFAD mouse microglia has also been shown in previous studies to be up regulated at both RNA and protein level in the aging process and in AD. However, a strong association of APOE with AD was only shown for the genotypes APO34 and 44³⁰⁷. Proteins associated with processes in the immune system, responses to reactive oxygen species and glucose metabolism identified in this work indicate a shift towards pro-inflammatory cytokine release and a role in the degradation of A β . Together, a possible impairment of cytoskeletal remodeling in LOAD suggests a possible role of the immune system in LOAD and provides established MGLCs as a good tool to study the disease.

In addition, compared to the top ten proteins with a high AD score, the three proteins with the highest fold change (ISYNA1, PSME1, RPL29) have a low association with AD. As already identified for the proteins mainly related to AD, alterations in the expression patterns of those Proteins with the highest fold change suggest impairments of cytoskeletal remodeling and the immune system. ISYNA1, inositol-3-phosphate synthase 1 is a key enzyme in the myo-inositol biosynthetic pathway that catalyzes the conversion of glucose-6-phosphate to 1-myo-inositol-1-phosphate NAD-dependent. Furthermore, in a previous study an upregulation of the ISYNA1 gene in response to LPS stimulation in macrophages was demonstrated³⁰⁸. In a recent analysis, an association to ISYNA1 was detected in persons with the APOE4 allele³⁰⁹. ISYNA1 serves to maintain the inositol level and has already been shown to be altered for diseases such as bipolar disorder and AD. Moreover, ISYNA1 has functions in the organization of the cytoskeleton, mitochondrial function, DNA and protein regulation³¹⁰.

PSME1, proteasome activator complex subunit 1, is involved in immunoproteasome assembly and required for efficient antigen processing³¹¹. Moreover, PSME1 is an important factor in cell proliferation, which has already been shown in leukemia cells³¹². In a recent study, the influence of A β on retinal photoreceptor cells was investigated, revealing changes in cytoskeletal organization, oxidative phosphorylation, and the ribosomal machinery in AD. In the case of ribosomal proteins, RPL29, 60S ribosomal protein L29, indicated the strongest effect on A β treatment³¹³. However, changes in the expression of ribosomal proteins due to oxidative damage to the RNA have been well described in AD³¹⁴.

Altogether, the present study established a suitable model for analyzing LOAD-associated DNA variants and their impact on the development and function of microglia using a patient-specific *in vitro* model. In **Figure 27**, the process for the development of the *in vitro* model is illustrated. Human iPSC based *in vitro* models have been established by others as well, but the combined application of LOAD-specific iPSCs carrying LOAD associated risk variants, their differentiation into microglia, and the intensive characterization of microglia represents a unique data set that is unique in the scientific field. Quality of LOAD-specific iPSCs was characterized with state-of-the-art techniques according to the literature. SNP genotyping demonstrated the presence of LOAD-specific risk variants in LOAD-specific iPSCs. Based on an accumulation of LOAD-associated SNPs in a LOAD *in vitro* model it was possible to visualize AD specific phenotypes. Further, an intrinsic LOAD-specific protein profile was shown highlighting the specificity of the model in the context of LOAD. Phenotypes for altered phagocytosis initially observed for dysfunctional CD33 in reporter cell lines were verified in iPSC derived microglia. Microglia are key players in maintaining and restoring main functions of the CNS as innate immune response, phagocytosis, maintenance of biochemical homeostasis, maturation of neuronal circuits during development and remodeling of neuronal circuits in the adult brain. In order to be able to regulate those processes they are characterized by a high plasticity, which makes them able to monitor the brain parenchyma and respond to any change in brain homeostasis. To perform those tasks, they are capable of becoming activated and change their morphology and migrate due to their polarization properties to the area of interest. Based on the protocol for the generation of MGLCs established in this work, we were capable of simulating the high plasticity of the cells *in vitro* and to illustrate the phenotype of LOAD.

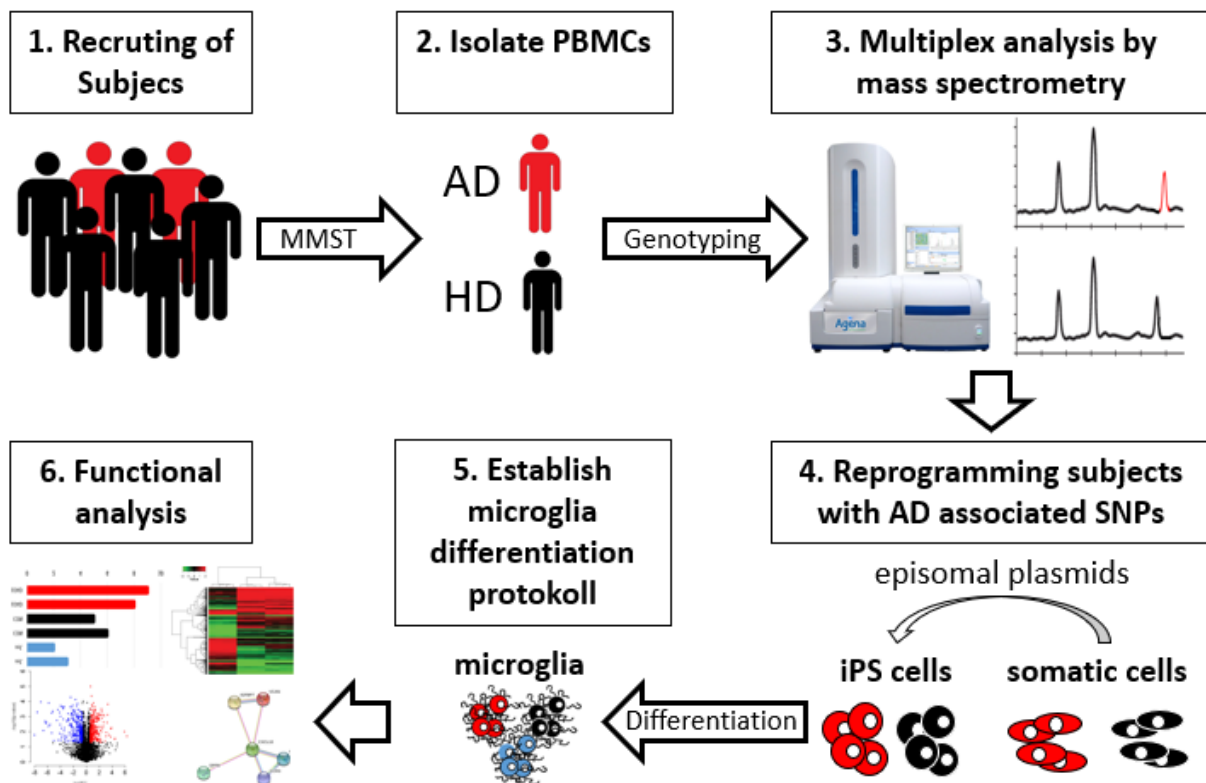


Figure 27: Overview of the thesis work packages.

The work packages are shown, which were passed through in this thesis. Steps 1 and 2 were already performed in the working group before. Provided samples from patients (AD and HD) were selected from a database and first genotyped for LOAD associated SNPs. Subsequently, the patients carrying the risk variants were selected and reprogrammed. A differentiation protocol was established to generate specific iPSCs MGLCs from the obtained patients. The generated LOAD MGLCs were then functionally analyzed in comparison to healthy controls (HD).

The connection between LOAD-associated risk variants and related functional effects is reflected in the detected associated biological processes. LOAD-MGLCs were more strongly activated, more motile and showed altered cytokine release and phagocytosis. This contributes to the pathology that predominates in AD patients.

Differences to the healthy cells could already be observed during the generation of the donor cells. In the course of the reprogramming and differentiation process starting from BLCLs, via iPSCs to generated MGLCs, proteome analyses in each of these cell types revealed a clustering into young, old and LOAD cells. Certainly, the observed LOAD phenotypes can be explained by altered endocytosis processes and cytoskeletal organization in which the investigated SNPs are associated for. A closer examination of the proteome profile of LOAD MGLCs revealed a significant impairment of the cytoskeleton remodeling of the cells. However, the effects of the cytoskeleton in turn play a crucial role in motility, cytokine release of activation and ramification and the endocytosis process.

This protocol produced functional cells of adequate purity and functionality, similar to the published protocols. MGLCs were able to represent the phenotype of LOAD *in vitro*. Finally, it could be shown that LOAD iPSC derived MGLCs exhibit impaired function, which promotes LOAD due to impaired cytoskeletal remodeling.

In the context of the present thesis regarding AD, we have established a completely new protocol for the generation of LOAD-specific MGLCs, which is a unique tool for further research questions. Among others, a closer characterization of this model showed a strong alteration in the organization of the cytoskeleton and phagocytosis. Based on this, future studies could focus more deeply on LOAD-associated SNPs, which are known to be involved in these functions. Furthermore, additional phagocytosis assays are necessary to further characterize the internalization of beads or even A β . A blockade of the membrane proteins CD33 and TREM2, as partly applied in this thesis, could be extended to gain new insights of these proteins into microglia behavior. In addition, further phagocytosis and motility analyses with different sialic acid concentrations should be performed to extend the understanding of siglecs to microglia reactions. Following this, more detailed description of microglia behavior would be achievable by using modified sialic acid. This includes metabolic oligosaccharide engineering, whereby the original N-Acetylmannosamin is replaced by sialic acid precursors like N-Propanoylmannosamin in the ongoing metabolism resulting in altered sialic acid products integrated in the final Sialoglycane. Furthermore, motility and organization of the LOAD cytoskeleton should be analyzed using microscope-base techniques. Using cytochalasine, like cytochalasin D, in combination with this technique, enables characterization of actin polymerisation as well as cell motility processes in LOAD compared with healthy controls. Finally, LOAD associated SNPs could be analyzed more closely using the CRISPR-CAS method to generate specific SNP alterations within one cell line. In this manner, LOAD MGLC as well as isogenic control cell lines could be established to examine functional consequences of those mutations. Summarized, this thesis provides the fundamental basis to study functional alterations and disease progress of LOAD *in vitro*.

5 References

1. Villarejo Galende, A., Eimil Ortiz, M., Llamas Velasco, S., Llanero Luque, M., López de Silanes de Miguel, C. & Prieto Jurczynska, C. *et al.* Report by the Spanish Foundation of the Brain on the social impact of Alzheimer disease and other types of dementia. *Neurología (English Edition)*; 10.1016/j.nrleng.2017.10.004 (2019).
2. Bateman, R. J., Xiong, C., Benzinger, T. L.S., Fagan, A. M., Goate, A., Fox, N. C. & Marcus, D. S. *et al.* Clinical and Biomarker Changes in Dominantly Inherited Alzheimer's Disease. *New England Journal of Medicine* **367**, 795–804; 10.1056/NEJMoa1202753 (2012).
3. Mayeux, R. & Stern, Y. Epidemiology of Alzheimer Disease. *Cold Spring Harb Perspect Med* **2**, a006239; 10.1101/cshperspect.a006239 (2012).
4. Caruso A, Nicoletti F, Mango D, Saidi A, Orlando R, Scaccianoce S. Stress as risk factor for Alzheimer's disease. *Pharmacological Research* **132**, 130–134; 10.1016/j.phrs.2018.04.017 (2018).
5. Michael McLeod, Leigh Breen, D. Lee Hamilton & Andrew Philp. Live strong and prosper: the importance of skeletal muscle strength for healthy ageing. *Biogerontology* **17**, 497–510; 10.1007/s10522-015-9631-7 (2016).
6. Selkoe, D. J. & Hardy, J. The amyloid hypothesis of Alzheimer's disease at 25 years. *EMBO molecular medicine* **8**, 595–608; 10.15252/emmm.201606210 (2016).
7. Christian Ledig, Andreas Schuh, Ricardo Guerrero, Rolf A. Heckemann & Daniel Rueckert. Structural brain imaging in Alzheimer's disease and mild cognitive impairment: biomarker analysis and shared morphometry database. *Sci Rep* **8**, 1–16; 10.1038/s41598-018-29295-9 (2018).
8. Puglielli, L., Tanzi, R. E. & Kovacs, D. M. Alzheimer's disease: the cholesterol connection. *Nat Neurosci* **6**, 345–351; 10.1038/nn0403-345 (2003).
9. Lambert, J.-C., Heath, S., Even, G., Campion, D., Sleegers, K., Hiltunen, M. & Combarros, O. *et al.* Genome-wide association study identifies variants at CLU and CR1 associated with Alzheimer's disease. *Nat Genet* **41**, 1094–1099; 10.1038/ng.439 (2009).
10. Lee, H.-g., Perry, G., Moreira, P. I., Garrett, M. R., Liu, Q., Zhu, X. & Takeda, A. *et al.* Tau phosphorylation in Alzheimer's disease: pathogen or protector? *Trends in molecular medicine* **11**, 164–169; 10.1016/j.molmed.2005.02.008 (2005).
11. Alonso, A. D., Cohen, L. S., Corbo, C., Morozova, V., Elldrissi, A., Phillips, G. & Kleiman, F. E. *et al.* Hyperphosphorylation of Tau Associates With Changes in Its Function Beyond Microtubule Stability. *Front. Cell. Neurosci.* **12**, 338; 10.3389/fncel.2018.00338 (2018).
12. Pagani, L. & Eckert, A. Amyloid-Beta Interaction with Mitochondria. *International Journal of Alzheimer's Disease* **2011**; 10.4061/2011/925050 (2011).
13. Shepherd, C., McCann, H. & Halliday, G. M. Variations in the neuropathology of familial Alzheimer's disease. *Acta Neuropathologica* **118**, 37–52; 10.1007/s00401-009-0521-4 (2009).
14. Braak, H. & Braak, E. Neuropathological staging of Alzheimer-related changes. *Acta Neuropathologica* **82**, 239–259; 10.1007/bf00308809 (1991).
15. Mendez, M. F. Early-onset Alzheimer's Disease: Nonamnesic Subtypes and Type 2 AD. *Archives of Medical Research* **43**, 677–685; 10.1016/j.arcmed.2012.11.009 (2012).
16. Hsu, S., Gordon, B. A., Hornbeck, R., Norton, J. B., Levitch, D., Loudon, A. & Ziegemeier, E. *et al.* Discovery and validation of autosomal dominant Alzheimer's disease mutations. *Alz Res Therapy* **10**, 1–8; 10.1186/s13195-018-0392-9 (2018).
17. Mendez, M. F. Early-onset Alzheimer Disease and Its Variants. *Continuum (Minneapolis, Minn.)* **25**, 34–51; 10.1212/CON.0000000000000687 (2019).
18. Palasí, A., Gutiérrez-Iglesias, B., Alegret, M., Pujadas, F., Olabarrieta, M., Liébana, D. & Quintana, M. *et al.* Differentiated clinical presentation of early and late-onset Alzheimer's disease: is 65 years of age providing a reliable threshold? *J Neurol* **262**, 1238–1246; 10.1007/s00415-015-7698-3 (2015).
19. Naj, A. C., Jun, G., Beecham, G. W., Wang, L.-S., Vardarajan, B. N., Buross, J. & Gallins, P. J. *et al.* Common variants at MS4A4/MS4A6E, CD2AP, CD33 and EPHA1 are associated with late-onset Alzheimer's disease. *Nature genetics* **43**, 436–441; 10.1038/ng.801 (2011).
20. Kamboh, M. I. Molecular Genetics of Late-Onset Alzheimer's Disease. *Annals of Human Genetics* **68**, 381–404; 10.1046/j.1529-8817.2004.00110.x (2004).
21. Kline, A. Apolipoprotein E, amyloid- β clearance and therapeutic opportunities in Alzheimer's disease. *Alz Res Therapy* **4**, 1–6; 10.1186/alzrt135 (2012).
22. Hindorf, L. A., Sethupathy, P., Junkins, H. A., Ramos, E. M., Mehta, J. P., Collins, F. S. & Manolio, T. A. *et al.* Potential etiologic and functional implications of genome-wide association loci for human diseases and traits. *PNAS* **106**, 9362–9367; 10.1073/pnas.0903103106 (2009).

23. Hollingworth, P., Harold, D., Sims, R., Gerrish, A., Lambert, J.-C., Carrasquillo, M. M. & Abraham, R. *et al.* Common variants at ABCA7, MS4A6A/MS4A4E, EPHA1, CD33 and CD2AP are associated with Alzheimer's disease. *Nature genetics* **43**, 429–435; 10.1038/ng.803 (2011).
24. Harold, D., Abraham, R., Hollingworth, P., Sims, R., Gerrish, A., Hamshere, M. L. & Pahwa, J. S. *et al.* Genome-wide association study identifies variants at CLU and PICALM associated with Alzheimer's disease. *Nat Genet* **41**, 1088–1093; 10.1038/ng.440 (2009).
25. Seshadri, S., Fitzpatrick, A. L., Ikram, M. A., DeStefano, A. L., Gudnason, V., Boada, M. & Bis, J. C. *et al.* Genome-wide Analysis of Genetic Loci Associated With Alzheimer Disease. *JAMA* **303**, 1832–1840; 10.1001/jama.2010.574 (2010).
26. Lambert, J. C., Ibrahim-Verbaas, C. A., Harold, D., Naj, A. C., Sims, R., Bellenguez, C. & DeStefano, A. L. *et al.* Meta-analysis of 74,046 individuals identifies 11 new susceptibility loci for Alzheimer's disease. *Nature genetics* **45**, 1452–1458; 10.1038/ng.2802 (2013).
27. Jonsson, T., Stefansson, H., Steinberg, S., Jonsdottir, I., Jonsson, P. V., Snaedal, J. & Bjornsson, S. *et al.* Variant of TREM2 associated with the risk of Alzheimer's disease. *The New England journal of medicine* **368**, 107–116; 10.1056/NEJMoa1211103 (2013).
28. Wetzel-Smith, M. K., Hunkapiller, J., Bhangale, T. R., Srinivasan, K., Maloney, J. A., Atwal, J. K. & Sa, S. M. *et al.* A rare mutation in UNC5C predisposes to late-onset Alzheimer's disease and increases neuronal cell death. *Nat Med* **20**, 1452–1457; 10.1038/nm.3736 (2014).
29. Giri, M., Zhang, M. & Lü, Y. Genes associated with Alzheimer's disease: an overview and current status. *Clinical Interventions in Aging* **11**, 665–681; 10.2147/CIA.S105769 (2016).
30. Farrer, L. A., Cupples, L. A., Haines, J. L., Hyman, B., Kukull, W. A., Mayeux, R. & Myers, R. H. *et al.* Effects of age, sex, and ethnicity on the association between apolipoprotein E genotype and Alzheimer disease. A meta-analysis. APOE and Alzheimer Disease Meta Analysis Consortium. *JAMA* **278**, 1349–1356 (1997).
31. Szumilas, M. Explaining Odds Ratios. *Journal of the Canadian Academy of Child and Adolescent Psychiatry* **19**, 227–229 (2010).
32. Koistinaho, M., Lin, S., Wu, X., Esterman, M., Koger, D., Hanson, J. & Higgs, R. *et al.* Apolipoprotein E promotes astrocyte colocalization and degradation of deposited amyloid- β peptides. *Nat Med* **10**, 719–726; 10.1038/nm1058 (2004).
33. Mahley, R. W., Weisgraber, K. H. & Huang, Y. Apolipoprotein E4: A causative factor and therapeutic target in neuropathology, including Alzheimer's disease. *PNAS* **103**, 5644–5651; 10.1073/pnas.0600549103 (2006).
34. Wang X, Ciralo G, Morris R, Gruenstein E. Identification of a neuronal endocytic pathway activated by an apolipoprotein E (apoE) receptor binding peptide. *Brain research* **778**, 6–15; 10.1016/S0006-8993(97)00877-9 (1997).
35. Nguyen, D., Dhanasekaran, P., Nickel, M., Mizuguchi, C., Watanabe, M., Saito, H. & Phillips, M. C. *et al.* Influence of domain stability on the properties of human apolipoprotein E3 and E4 and mouse apolipoprotein E. *Biochemistry* **53**, 4025–4033; 10.1021/bi500340z (2014).
36. Tejedor, M. T., Garcia-Sobreviela, M. P., Ledesma, M. & Arbones-Mainar, J. M. The Apolipoprotein E Polymorphism rs7412 Associates with Body Fatness Independently of Plasma Lipids in Middle Aged Men. *PLoS one* **9**; 10.1371/journal.pone.0108605 (2014).
37. Liu, C.-C., Kanekiyo, T., Xu, H. & Bu, G. Apolipoprotein E and Alzheimer disease: risk, mechanisms, and therapy. *Nature reviews. Neurology* **9**, 106–118; 10.1038/nrneurol.2012.263 (2013).
38. Frieden, C. & Garai, K. Structural differences between apoE3 and apoE4 may be useful in developing therapeutic agents for Alzheimer's disease. *Proceedings of the National Academy of Sciences of the United States of America* **109**, 8913–8918; 10.1073/pnas.1207022109 (2012).
39. C Conejero-Goldberg, J J Gomar, T Bobes-Bascaran, T M Hyde, J E Kleinman, M M Herman & S Chen *et al.* APOE2 enhances neuroprotection against Alzheimer's disease through multiple molecular mechanisms. *Mol Psychiatry* **19**, 1243–1250; 10.1038/mp.2013.194 (2014).
40. Ellis, R. J., Olichney, J. M., Thal, L. J., Mirra, S. S., Morris, J. C., Beekly, D. & Heyman, A. *et al.* Cerebral amyloid angiopathy in the brains of patients with Alzheimer's disease: the CERAD experience, Part XV. *Neurology* **46**, 1592–1596; 10.1212/wnl.46.6.1592 (1996).
41. Drzezga, A., Grimmer, T., Henriksen, G., Muhlau, M., Perneczky, R., Miederer, I. & Praus, C. *et al.* Effect of APOE genotype on amyloid plaque load and gray matter volume in Alzheimer disease. *Neurology* **72**, 1487–1494; 10.1212/WNL.0b013e3181a2e8d0 (2009).
42. Nelson, P. T., Pious, N. M., Jicha, G. A., Wilcock, D. M., Fardo, D. W., Estus, S. & Rebeck, G. W. *et al.* APOE- ϵ 2 and APOE- ϵ 4 Correlate With Increased Amyloid Accumulation in Cerebral Vasculature. *J Neuropathol Exp Neurol* **72**, 708–715; 10.1097/NEN.0b013e31829a25b9 (2013).

43. Takahashi, K. & Yamanaka, S. Induction of pluripotent stem cells from mouse embryonic and adult fibroblast cultures by defined factors. *Cell* **126**, 663–676; 10.1016/j.cell.2006.07.024 (2006).
44. Yu, J., Vodyanik, M. A., Smuga-Otto, K., Antosiewicz-Bourget, J., Frane, J. L., Tian, S. & Nie, J. *et al.* Induced Pluripotent Stem Cell Lines Derived from Human Somatic Cells. *Science* **318**, 1917–1920; 10.1126/science.1151526 (2007).
45. Pera, M. F. Low-risk reprogramming. *Nature* **458**, 715–716; 10.1038/458715a (2009).
46. Kadari, A., Lu, M., Li, M., Sekaran, T., Thummer, R. P., Guyette, N. & Chu, V. *et al.* Excision of viral reprogramming cassettes by Cre protein transduction enables rapid, robust and efficient derivation of transgene-free human induced pluripotent stem cells. *Stem Cell Research & Therapy* **5**, 47; 10.1186/scrt435 (2014).
47. Lai, M. I., Wendy-Yeo, W. Y., Ramasamy, R., Nordin, N., Rosli, R., Veerakumarasivam, A. & Abdullah, S. *et al.* Advancements in reprogramming strategies for the generation of induced pluripotent stem cells. *J Assist Reprod Genet* **28**, 291–301; 10.1007/s10815-011-9552-6 (2011).
48. Chou, B.-K., Mali, P., Huang, X., Ye, Z., Dowey, S. N., Resar, L. M. S. & Zou, C. *et al.* Efficient human iPS cell derivation by a non-integrating plasmid from blood cells with unique epigenetic and gene expression signatures. *Cell Res* **21**, 518–529; 10.1038/cr.2011.12 (2011).
49. Kang, X., Yu, Q., Huang, Y., Song, B., Chen, Y., Gao, X. & He, W. *et al.* Effects of Integrating and Non-Integrating Reprogramming Methods on Copy Number Variation and Genomic Stability of Human Induced Pluripotent Stem Cells. *PLoS one* **10**; 10.1371/journal.pone.0131128 (2015).
50. Talluri TR, Kumar D, Glage S, Garrels W, Ivics Z, Debowski K, Behr R, Kues WA. Non-viral reprogramming of fibroblasts into induced pluripotent stem cells by Sleeping Beauty and piggyBac transposons. *Biochemical and Biophysical Research Communications* **450**, 581–587; 10.1016/j.bbrc.2014.06.014 (2014).
51. Rao, M. S. & Malik, N. Assessing iPSC reprogramming methods for their suitability in translational medicine. *Journal of Cellular Biochemistry* **113**, 3061–3068; 10.1002/jcb.24183 (2012).
52. Schlaeger, T. M., Daheron, L., Brickler, T. R., Entwisle, S., Chan, K., Cianci, A. & DeVine, A. *et al.* A comparison of non-integrating reprogramming methods. *Nature biotechnology* **33**, 58–63; 10.1038/nbt.3070 (2015).
53. Park, I.-H., Zhao, R., West, J. A., Yabuuchi, A., Huo, H., Ince, T. A. & Lerou, P. H. *et al.* Reprogramming of human somatic cells to pluripotency with defined factors. *Nature* **451**, 141–146; 10.1038/nature06534 (2008).
54. Takahashi, K., Tanabe, K., Ohnuki, M., Narita, M., Ichisaka, T., Tomoda, K. & Yamanaka, S. *et al.* Induction of Pluripotent Stem Cells from Adult Human Fibroblasts by Defined Factors. *Cell* **131**, 861–872; 10.1016/j.cell.2007.11.019 (2007).
55. Staerk, J., Dawlaty, M. M., Gao, Q., Maetzel, D., Hanna, J., Sommer, C. A. & Mostoslavsky, G. *et al.* Reprogramming of peripheral blood cells to induced pluripotent stem cells. *Cell stem cell* **7**, 20–24; 10.1016/j.stem.2010.06.002 (2010).
56. Wang, J., Gu, Q., Hao, J., Bai, D., Liu, L., Zhao, X. & Liu, Z. *et al.* Generation of Induced Pluripotent Stem Cells with High Efficiency from Human Umbilical Cord Blood Mononuclear Cells. *Genomics, Proteomics & Bioinformatics* **11**, 304–311; 10.1016/j.gpb.2013.08.002 (2013).
57. Haase, A., Olmer, R., Schwanke, K., Wunderlich, S., Merkert, S., Hess, C. & Zweigerdt, R. *et al.* Generation of induced pluripotent stem cells from human cord blood. *Cell stem cell* **5**, 434–441; 10.1016/j.stem.2009.08.021 (2009).
58. Kim, J. B., Greber, B., Araúzo-Bravo, M. J., Meyer, J., Park, K. I., Zaehres, H. & Schöler, H. R. *et al.* Direct reprogramming of human neural stem cells by OCT4. *Nature* **461**, 649–653; 10.1038/nature08436 (2009).
59. Tamaoki, N., Takahashi, K., Tanaka, T., Ichisaka, T., Aoki, H., Takeda-Kawaguchi, T. & Iida, K. *et al.* Dental pulp cells for induced pluripotent stem cell banking. *Journal of dental research* **89**, 773–778; 10.1177/0022034510366846 (2010).
60. Ohmine, S., Squillace, K. A., Hartjes, K. A., Deeds, M. C., Armstrong, A. S., Thatava, T. & Sakuma, T. *et al.* Reprogrammed keratinocytes from elderly type 2 diabetes patients suppress senescence genes to acquire induced pluripotency. *Aging (Albany NY)* **4**, 60–73 (2012).
61. Xue, Y., Cai, X., Wang, L., Liao, B., Zhang, H., Shan, Y. & Chen, Q. *et al.* Generating a Non-Integrating Human Induced Pluripotent Stem Cell Bank from Urine-Derived Cells. *PLoS one* **8**; 10.1371/journal.pone.0070573 (2013).
62. Sugii, S., Kida, Y., Berggren, W. T. & Evans, R. M. Feeder-dependent and feeder-independent iPSC cell derivation from human and mouse adipose stem cells. *Nat Protoc* **6**, 346–358; 10.1038/nprot.2010.199 (2011).
63. Panopoulos, A. D., Ruiz, S., Yi, F., Herrerías, A., Batchelder, E. M. & Belmonte, J. C. I. *et al.* Rapid and Highly Efficient Generation of Induced Pluripotent Stem Cells from Human Umbilical Vein Endothelial Cells. *PLoS one* **6**; 10.1371/journal.pone.0019743 (2011).
64. Kunisato, A., Wakatsuki, M., Kodama, Y., Shinba, H., Ishida, I. & Nagao, K. *et al.* Generation of induced pluripotent stem cells by efficient reprogramming of adult bone marrow cells. *Stem cells and development* **19**, 229–238; 10.1089/scd.2009.0149 (2010).
65. Sridharan, R. & Plath, K. Illuminating the Black Box of Reprogramming. *Cell stem cell* **2**, 295–297; 10.1016/j.stem.2008.03.015 (2008).

66. Fujimori, K., Tezuka, T., Ishiura, H., Mitsui, J., Doi, K., Yoshimura, J. & Tada, H. *et al.* Modeling neurological diseases with induced pluripotent cells reprogrammed from immortalized lymphoblastoid cell lines. *Mol Brain* **9**, 1–14; 10.1186/s13041-016-0267-6 (2016).
67. Kolios, G. & Moodley, Y. Introduction to stem cells and regenerative medicine. *Respiration; international review of thoracic diseases* **85**, 3–10; 10.1159/000345615 (2013).
68. Wert, G. de & Mummery, C. Human embryonic stem cells: research, ethics and policy. *Human reproduction (Oxford, England)* **18**, 672–682; 10.1093/humrep/deg143 (2003).
69. Charron, D., Suberbielle-Boissel, C. & Al-Daccak, R. Immunogenicity and Allogenicity: A Challenge of Stem Cell Therapy. *J. of Cardiovasc. Trans. Res.* **2**, 130–138; 10.1007/s12265-008-9062-9 (2009).
70. Lerou, P. H., Yabuuchi, A., Huo, H., Miller, J. D., Boyer, L. F., Schlaeger, T. M. & Daley, G. Q. *et al.* Derivation and maintenance of human embryonic stem cells from poor-quality in vitro fertilization embryos. *Nat Protoc* **3**, 923–933; 10.1038/nprot.2008.60 (2008).
71. Ye, L., Swingen, C. & Zhang, J. Induced Pluripotent Stem Cells and Their Potential for Basic and Clinical Sciences. *Current Cardiology Reviews* **9**, 63–72; 10.2174/157340313805076278 (2013).
72. Farkhondeh, A., Li, R., Gorshkov, K., Chen, K. G., Might, M., Rodems, S. & Lo, D. C. *et al.* Induced pluripotent stem cells for neural drug discovery. *Drug discovery today* **24**, 992–999; 10.1016/j.drudis.2019.01.007 (2019).
73. van Pham, P., Phan, N. L.-C., Vu, N. B., Truong, N. H. & Phan, N. K. New Trends in Clinical Applications of Induced Pluripotent Stem Cells. In *Stem Cell Processing*, edited by P. van Pham (Springer International Publishing, Cham, 2016), pp. 77–98.
74. Mungenast AE, Siegert S, Tsai LH. Modeling Alzheimer's disease with human induced pluripotent stem (iPS) cells. *Molecular and Cellular Neuroscience* **73**, 13–31; 10.1016/j.mcn.2015.11.010 (2016).
75. Calatayud, C., Carola, G., Consiglio, A. & Raya, A. Modeling the genetic complexity of Parkinson's disease by targeted genome edition in iPS cells. *Current Opinion in Genetics & Development* **46**, 123–131; 10.1016/j.gde.2017.06.002 (2017).
76. Imaizumi, Y. & Okano, H. Modeling human neurological disorders with induced pluripotent stem cells. *Journal of neurochemistry* **129**, 388–399; 10.1111/jnc.12625 (2014).
77. Matsui T, Akamatsu W, Nakamura M, Okano H. Regeneration of the damaged central nervous system through reprogramming technology: Basic concepts and potential application for cell replacement therapy. *Experimental neurology* **260**, 12–18; 10.1016/j.expneurol.2012.09.016 (2014).
78. Yang, J., Li, S., He, X.-B., Cheng, C. & Le, W. Induced pluripotent stem cells in Alzheimer's disease: applications for disease modeling and cell-replacement therapy. *Mol Neurodegeneration* **11**, 1–11; 10.1186/s13024-016-0106-3 (2016).
79. VandenDriessche, T., Chai, Y. C., Boon, D. & Chuah, M. K. Pluripotent Stem Cells for Gene Therapy of Hereditary Muscle Disorders. In *Muscle Gene Therapy*, edited by D. Duan & J. R. Mendell. 2nd ed. (Springer International Publishing, Cham, 2019), pp. 81–97.
80. Fatehullah, A., Tan, S. H. & Barker, N. Organoids as an in vitro model of human development and disease. *Nat Cell Biol* **18**, 246–254; 10.1038/ncb3312 (2016).
81. Hynds, R. E. & Giangreco, A. Concise review: the relevance of human stem cell-derived organoid models for epithelial translational medicine. *Stem cells (Dayton, Ohio)* **31**, 417–422; 10.1002/stem.1290 (2013).
82. Yoshida, Y. & Yamanaka, S. Recent stem cell advances: induced pluripotent stem cells for disease modeling and stem cell-based regeneration. *Circulation* **122**, 80–87; 10.1161/CIRCULATIONAHA.109.881433 (2010).
83. Jay Penney, William T. Ralvenius & Li-Huei Tsai. Modeling Alzheimer's disease with iPSC-derived brain cells. *Mol Psychiatry* **25**, 148–167; 10.1038/s41380-019-0468-3 (2020).
84. Charles Arber, Christopher Lovejoy & Selina Wray. Stem cell models of Alzheimer's disease: progress and challenges. *Alz Res Therapy* **9**, 1–17; 10.1186/s13195-017-0268-4 (2017).
85. Studer, L., Vera, E. & Cornacchia, D. Programming and Reprogramming Cellular Age in the Era of Induced Pluripotency. *Cell stem cell* **16**, 591–600; 10.1016/j.stem.2015.05.004 (2015).
86. Miller, J. D., Ganat, Y. M., Kishinevsky, S., Bowman, R. L., Liu, B., Tu, E. Y. & Mandal, P. K. *et al.* Human iPSC-based modeling of late-onset disease via progerin-induced aging. *Cell stem cell* **13**, 691–705; 10.1016/j.stem.2013.11.006 (2013).
87. Soria-Valles, C. & López-Otín, C. iPSCs: On the Road to Reprogramming Aging. *Trends in molecular medicine* **22**, 713–724; 10.1016/j.molmed.2016.05.010 (2016).
88. Sherida de Leeuw & Christian Tackenberg. Alzheimer's in a dish – induced pluripotent stem cell-based disease modeling. *Transl Neurodegener* **8**, 1–13; 10.1186/s40035-019-0161-0 (2019).
89. Helen A. Rowland, Nigel M. Hooper & Katherine A. B. Kellett. Modelling Sporadic Alzheimer's Disease Using Induced Pluripotent Stem Cells. *Neurochem Res* **43**, 2179–2198; 10.1007/s11064-018-2663-z (2018).

90. Trepel, M. *Neuroanatomie. Struktur und Funktion ; mit 23 Tabellen*. 2nd ed. (Urban & Fischer, München, 2001).
91. Salter, M. W. & Stevens, B. Microglia emerge as central players in brain disease. *Nature medicine* **23**, 1018–1027; 10.1038/nm.4397 (2017).
92. Robertson, F. A Microscopic Demonstration of the Normal and Pathological Histology of Mesoglia Cells. *J. ment. sci* **46**, 724; 10.1192/bjp.46.195.724 (1900).
93. Nissl, F. Über einige Beziehungen zwischen Nervenzellerkrankungen und gliösen Erscheinungen bei verschiedenen Psychosen. *Arch Psychiatr* **32**, 1–21 (1899).
94. Alzheimer, A. *Beiträge zur Kenntnis der pathologischen Neuroglia und ihrer Beziehungen zu den Abbauvorgängen im Nervengewebe* (G. Fischer, Jena, 1910).
95. David Gosselin, Dylan Skola, Nicole G. Coufal, Inge R. Holtman, Johannes C. M. Schlachetzki, Eniko Sajti & Baptiste N. Jaeger *et al.* An environment-dependent transcriptional network specifies human microglia identity. *Science* **356**; 10.1126/science.aal3222 (2017).
96. Chen, Z., Jalabi, W., Shpargel, K. B., Farabaugh, K. T., Dutta, R., Yin, X. & Kidd, G. J. *et al.* Lipopolysaccharide-induced microglial activation and neuroprotection against experimental brain injury is independent of hematogenous TLR4. *The Journal of neuroscience : the official journal of the Society for Neuroscience* **32**, 11706–11715; 10.1523/JNEUROSCI.0730-12.2012 (2012).
97. Schettlers, S. T. T., Gomez-Nicola, D., Garcia-Vallejo, J. J. & van Kooyk, Y. Neuroinflammation: Microglia and T Cells Get Ready to Tango. *Frontiers in immunology* **8**, 1905; 10.3389/fimmu.2017.01905 (2017).
98. Paolicelli, R. C., Bolasco, G., Pagani, F., Maggi, L., Scianni, M., Panzanelli, P. & Giustetto, M. *et al.* Synaptic pruning by microglia is necessary for normal brain development. *Science (New York, N.Y.)* **333**, 1456–1458; 10.1126/science.1202529 (2011).
99. Tremblay, M.-È., Stevens, B., Sierra, A., Wake, H., Bessis, A. & Nimmerjahn, A. *et al.* The role of microglia in the healthy brain. *The Journal of neuroscience : the official journal of the Society for Neuroscience* **31**, 16064–16069; 10.1523/JNEUROSCI.4158-11.2011 (2011).
100. Elisa M. York, Louis-Philippe Bernier & Brian A. MacVicar. Microglial modulation of neuronal activity in the healthy brain. *Developmental Neurobiology* **78**, 593–603; 10.1002/dneu.22571 (2018).
101. Kaur, C., Hao, A. J., Wu, C. H. & Ling, E. A. Origin of microglia. *Microscopy research and technique* **54**, 2–9; 10.1002/jemt.1114 (2001).
102. Ginhoux, F., Lim, S., Hoeffel, G., Low, D. & Huber, T. Origin and differentiation of microglia. *Front. Cell. Neurosci.* **7**, 45; 10.3389/fncel.2013.00045 (2013).
103. Joan Stiles & Terry L. Jernigan. The Basics of Brain Development. *Neuropsychol Rev* **20**, 327–348; 10.1007/s11065-010-9148-4 (2010).
104. Katrin Kierdorf, Daniel Erny, Tobias Goldmann, Victor Sander, Christian Schulz, Elisa Gomez Perdiguero & Peter Wieghofer *et al.* Microglia emerge from erythromyeloid precursors via Pu.1- and Irf8-dependent pathways. *Nat Neurosci* **16**, 273–280; 10.1038/nn.3318 (2013).
105. Ginhoux, F., Lim, S., Hoeffel, G., Low, D. & Huber, T. Origin and differentiation of microglia. *Front. Cell. Neurosci.* **7**, 45; 10.3389/fncel.2013.00045 (2013).
106. Gang Huang, Pu Zhang, Hideyo Hirai, Shannon Elf, Xiaomei Yan, Zhao Chen & Steffen Koschmieder *et al.* PU.1 is a major downstream target of AML1 (RUNX1) in adult mouse hematopoiesis. *Nat Genet* **40**, 51–60; 10.1038/ng.2007.7 (2008).
107. Lutterbach, B. & Hiebert, S.W. Role of the transcription factor AML-1 in acute leukemia and hematopoietic differentiation. *Gene* **245**, 223–235; 10.1016/S0378-1119(00)00014-7 (2000).
108. Igor M. Samokhvalov, Natalia I. Samokhvalova & Shin-ichi Nishikawa. Cell tracing shows the contribution of the yolk sac to adult haematopoiesis. *Nature* **446**, 1056–1061; 10.1038/nature05725 (2007).
109. Zusso, M., Methot, L., Lo, R., Greenhalgh, A. D., David, S. & Stifani, S. *et al.* Regulation of postnatal forebrain amoeboid microglial cell proliferation and development by the transcription factor Runx1. *The Journal of neuroscience : the official journal of the Society for Neuroscience* **32**, 11285–11298; 10.1523/JNEUROSCI.6182-11.2012 (2012).
110. Walton, M. R., Gibbons, H., MacGibbon, G. A., Sirimanne, E., Saura, J., Gluckman, P. D. & Dragunow, M. *et al.* PU.1 expression in microglia. *Journal of neuroimmunology* **104**, 109–115; 10.1016/S0165-5728(99)00262-3 (2000).
111. Noushine Mossadegh-Keller, Sandrine Sarrazin, Prashanth K. Kandalla, Leon Espinosa, E. Richard Stanley, Stephen L. Nutt & Jordan Moore *et al.* M-CSF instructs myeloid lineage fate in single haematopoietic stem cells. *Nature* **497**, 239–243; 10.1038/nature12026 (2013).
112. Berclaz, P.-Y., Shibata, Y., Whitsett, J. A. & Trapnell, B. C. GM-CSF, via PU.1, regulates alveolar macrophage FcγR-mediated phagocytosis and the IL-18/IFN-γ-mediated molecular connection between innate and adaptive immunity in the lung. *Blood* **100**, 4193–4200; 10.1182/blood-2002-04-1102 (2002).
113. Ginhoux, F. & Prinz, M. Origin of microglia: current concepts and past controversies. *Cold Spring Harbor perspectives in biology* **7**, a020537; 10.1101/cshperspect.a020537 (2015).

114. Böiers, C., Buza-Vidas, N., Jensen, C. T., Pronk, C. J. H., Kharazi, S., Wittmann, L. & Sitnicka, E. *et al.* Expression and role of FLT3 in regulation of the earliest stage of normal granulocyte-monocyte progenitor development. *Blood* **115**, 5061–5068; 10.1182/blood-2009-12-258756 (2010).
115. Florent Ginhoux, Melanie Greter, Marylene Leboeuf, Sayan Nandi, Peter See, Solen Gokhan & Mark F. Mehler *et al.* Fate Mapping Analysis Reveals That Adult Microglia Derive from Primitive Macrophages. *Science* **330**, 841–845; 10.1126/science.1194637 (2010).
116. Tay, T. L., Savage, J. C., Hui, C. W., Bisht, K. & Tremblay, M.-È. Microglia across the lifespan: from origin to function in brain development, plasticity and cognition. *The Journal of physiology* **595**, 1929–1945; 10.1113/JP272134 (2017).
117. Mildner, A., Schlevogt, B., Kierdorf, K., Böttcher, C., Erny, D., Kummer, M. P. & Quinn, M. *et al.* Distinct and Non-Redundant Roles of Microglia and Myeloid Subsets in Mouse Models of Alzheimer's Disease. *The Journal of Neuroscience* **31**, 11159–11171; 10.1523/JNEUROSCI.6209-10.2011 (2011).
118. Cameron, B. & Landreth, G. E. Inflammation, microglia, and Alzheimer's disease. *Neurobiology of disease* **37**, 503–509; 10.1016/j.nbd.2009.10.006 (2010).
119. Gyoneva, S., Swanger, S. A., Zhang, J., Weinshenker, D. & Traynelis, S. F. Altered motility of plaque-associated microglia in a model of Alzheimer's disease. *Neuroscience* **330**, 410–420; 10.1016/j.neuroscience.2016.05.061 (2016).
120. Rogers, J. & Lue, L.-F. Microglial chemotaxis, activation, and phagocytosis of amyloid β -peptide as linked phenomena in Alzheimer's disease. *Neurochemistry International* **39**, 333–340; 10.1016/S0197-0186(01)00040-7 (2001).
121. Jean-Vianney Haure-Mirande, Minghui Wang, Mickael Audrain, Tomas Fanutza, Soong Ho Kim, Szilvia Heja & Ben Readhead *et al.* Integrative approach to sporadic Alzheimer's disease: deficiency of TYROBP in cerebral A β amyloidosis mouse normalizes clinical phenotype and complement subnetwork molecular pathology without reducing A β burden. *Mol Psychiatry* **24**, 431–446; 10.1038/s41380-018-0255-6 (2019).
122. Mosher, K. I. & Wyss-Coray, T. Microglial dysfunction in brain aging and Alzheimer's disease. *Biochemical pharmacology* **88**, 594–604; 10.1016/j.bcp.2014.01.008 (2014).
123. Dijkstra, S., Geisert, E.E., Dijkstra, C.D., Bär, P.R. & Joosten, E.A.J. CD81 and microglial activation in vitro: proliferation, phagocytosis and nitric oxide production. *Journal of neuroimmunology* **114**, 151–159; 10.1016/S0165-5728(01)00240-5 (2001).
124. Dana Kurpius, Nicholas Wilson, Leah Fuller, Amara Hoffman & Michael E. Dailey. Early activation, motility, and homing of neonatal microglia to injured neurons does not require protein synthesis. *Glia* **54**, 58–70; 10.1002/glia.20355 (2006).
125. Wolfgang J. Streit, Sean D. Hurley, Tanya S. McGraw & Susan L. Semple-Rowland. Comparative evaluation of cytokine profiles and reactive gliosis supports a critical role for interleukin-6 in neuron-glia signaling during regeneration. *Journal of neuroscience research* **61**, 10–20; 10.1002/1097-4547(20000701)61:1<10::AID-JNR2>3.0.CO;2-E (2000).
126. Sunhee C. Lee, Wei Liu, Celia F. Brosnan & Dennis W. Dickson. GM-CSF promotes proliferation of human fetal and adult microglia in primary cultures. *Glia* **12**, 309–318; 10.1002/glia.440120407 (1994).
127. Willard, S. S. & Koochekpour, S. Glutamate, glutamate receptors, and downstream signaling pathways. *International journal of biological sciences* **9**, 948–959; 10.7150/ijbs.6426 (2013).
128. Liang, J., Takeuchi, H., Jin, S., Noda, M., Li, H., Doi, Y. & Kawanokuchi, J. *et al.* Glutamate induces neurotrophic factor production from microglia via protein kinase C pathway. *Brain research* **1322**, 8–23; 10.1016/j.brainres.2010.01.083 (2010).
129. Irino, Y., Nakamura, Y., Inoue, K., Kohsaka, S. & Ohsawa, K. Akt activation is involved in P2Y₁₂ receptor-mediated chemotaxis of microglia. *Journal of neuroscience research* **86**, 1511–1519; 10.1002/jnr.21610 (2008).
130. Klein, K., Aeschlimann, A., Jordan, S., Gay, R., Gay, S. & Sprott, H. *et al.* ATP induced brain-derived neurotrophic factor expression and release from osteoarthritis synovial fibroblasts is mediated by purinergic receptor P2X₄. *PLoS one* **7**, e36693; 10.1371/journal.pone.0036693 (2012).
131. Pradillo, J. M., Hurtado, O., Romera, C., Cárdenas, A., Fernández-Tomé, P., Alonso-Escolano, D. & Lorenzo, P. *et al.* TNFR1 mediates increased neuronal membrane EAAT3 expression after in vivo cerebral ischemic preconditioning. *Neuroscience* **138**, 1171–1178; 10.1016/j.neuroscience.2005.12.010 (2006).
132. Zheng, H., Zhu, W., Zhao, H., Wang, X., Wang, W. & Li, Z. *et al.* Kainic acid-activated microglia mediate increased excitability of rat hippocampal neurons in vitro and in vivo: crucial role of interleukin-1 β . *Neuroimmunomodulation* **17**, 31–38; 10.1159/000243083 (2010).
133. Petersen, M. A. & Dailey, M. E. Diverse microglial motility behaviors during clearance of dead cells in hippocampal slices. *Glia* **46**, 195–206; 10.1002/glia.10362 (2004).
134. Eder, C. Regulation of microglial behavior by ion channel activity. *Journal of neuroscience research* **81**, 314–321; 10.1002/jnr.20476 (2005).

135. Suzuki, T., Kohyama, K., Moriyama, K., Ozaki, M., Hasegawa, S., Ueno, T. & Saitoe, M. *et al.* Extracellular ADP augments microglial inflammasome and NF- κ B activation via the P2Y12 receptor. *European journal of immunology* **50**, 205–219; 10.1002/eji.201848013 (2020).
136. Deborah Doens & Patricia L Fernández. Microglia receptors and their implications in the response to amyloid β for Alzheimer's disease pathogenesis. *J Neuroinflammation* **11**, 1–14; 10.1186/1742-2094-11-48 (2014).
137. Kathryn J. Moore, Vidya V. Kunjathoor, Stephanie L. Koehn, Jennifer J. Manning, Anita A. Tseng, Jessica M. Silver & Mary McKee *et al.* Loss of receptor-mediated lipid uptake via scavenger receptor A or CD36 pathways does not ameliorate atherosclerosis in hyperlipidemic mice. *J Clin Invest* **115**, 2192–2201; 10.1172/JCI24061 (2005).
138. Cameron R Stewart, Lynda M Stuart, Kim Wilkinson, Janine M van Gils, Jiusheng Deng, Annett Halle & Katey J Rayner *et al.* CD36 ligands promote sterile inflammation through assembly of a Toll-like receptor 4 and 6 heterodimer. *Nat Immunol* **11**, 155–161; 10.1038/ni.1836 (2010).
139. Thais Minett, John Classey, Fiona E. Matthews, Marie Fahrenhold, Mariko Taga, Carol Brayne & Paul G. Ince *et al.* Microglial immunophenotype in dementia with Alzheimer's pathology. *J Neuroinflammation* **13**, 1–10; 10.1186/s12974-016-0601-z (2016).
140. Kober, D. L. & Brett, T. J. TREM2-ligand interactions in health and disease. *Journal of molecular biology* **429**, 1607–1629; 10.1016/j.jmb.2017.04.004 (2017).
141. Kim, Y. K., Shin, J.-S. & Nahm, M. H. NOD-Like Receptors in Infection, Immunity, and Diseases. *Yonsei Medical Journal* **57**, 5–14; 10.3349/ymj.2016.57.1.5 (2016).
142. Lee, S., Varvel, N. H., Konerth, M. E., Xu, G., Cardona, A. E., Ransohoff, R. M. & Lamb, B. T. *et al.* CX3CR1 Deficiency Alters Microglial Activation and Reduces Beta-Amyloid Deposition in Two Alzheimer's Disease Mouse Models. *The American Journal of Pathology* **177**, 2549–2562; 10.2353/ajpath.2010.100265 (2010).
143. Chi-Ho Lee, Se Jin Jeon, Kyu Suk Cho, Eunjung Moon, Arjun Sapkota, Hee Sook Jun & Jong Hoon Ryu *et al.* Activation of Glucagon-Like Peptide-1 Receptor Promotes Neuroprotection in Experimental Autoimmune Encephalomyelitis by Reducing Neuroinflammatory Responses. *Mol Neurobiol* **55**, 3007–3020; 10.1007/s12035-017-0550-2 (2018).
144. Caitriona M. Long-Smith, Sean Manning, Paula L. McClean, Meghan F. Coakley, Domhnall J. O'Halloran, Christian Holscher & Cora O'Neill *et al.* The Diabetes Drug Liraglutide Ameliorates Aberrant Insulin Receptor Localisation and Signalling in Parallel with Decreasing Both Amyloid- β Plaque and Glial Pathology in a Mouse Model of Alzheimer's Disease. *Neuromol Med* **15**, 102–114; 10.1007/s12017-012-8199-5 (2013).
145. Paul D. Wes, Faten A. Sayed, Frédérique Bard & Li Gan. Targeting microglia for the treatment of Alzheimer's Disease. *Glia* **64**, 1710–1732; 10.1002/glia.22988 (2016).
146. Paul R. Crocker, James C. Paulson & Ajit Varki. Siglecs and their roles in the immune system. *Nat Rev Immunol* **7**, 255–266; 10.1038/nri2056 (2007).
147. Vanessa C. Taylor, Christopher D. Buckley, Michael Douglas, Alison J. Cody, David L. Simmons & Sylvie D. Freeman *et al.* The Myeloid-specific Sialic Acid-binding Receptor, CD33, Associates with the Protein-tyrosine Phosphatases, SHP-1 and SHP-2. *J. Biol. Chem.* **274**, 11505–11512; 10.1074/jbc.274.17.11505 (1999).
148. Huan Cao & Paul R. Crocker. Evolution of CD33-related siglecs: regulating host immune functions and escaping pathogen exploitation? *Immunology* **132**, 18–26; 10.1111/j.1365-2567.2010.03368.x (2011).
149. Lingzhi Zhao. CD33 in Alzheimer's Disease – Biology, Pathogenesis, and Therapeutics: A Mini-Review. *GER* **65**, 323–331; 10.1159/000492596 (2019).
150. Efthymiou, A. G. & Goate, A. M. Late onset Alzheimer's disease genetics implicates microglial pathways in disease risk. *Molecular neurodegeneration* **12**, 43; 10.1186/s13024-017-0184-x (2017).
151. Sims, R., van der Lee, S. J., Naj, A. C., Bellenguez, C., Badarinarayan, N., Jakobsdottir, J. & Kunkle, B. W. *et al.* Rare coding variants in PLCG2, ABI3, and TREM2 implicate microglial-mediated innate immunity in Alzheimer's disease. *Nature genetics*; 10.1038/ng.3916 (2017).
152. Raj, T., Ryan, K. J., Replogle, J. M., Chibnik, L. B., Rosenkrantz, L., Tang, A. & Rothamel, K. *et al.* CD33: increased inclusion of exon 2 implicates the Ig V-set domain in Alzheimer's disease susceptibility. *Hum Mol Genet* **23**, 2729–2736; 10.1093/hmg/ddt666 (2014).
153. Bradshaw, E. M., Chibnik, L. B., Keenan, B. T., Ottoboni, L., Raj, T., Tang, A. & Rosenkrantz, L. L. *et al.* CD33 Alzheimer's disease locus: altered monocyte function and amyloid biology. *neuro* **16**, 848–850; 10.1038/nn.3435 (2013).
154. Crocker, P. R. & Varki, A. Siglecs, sialic acids and innate immunity. *Trends in immunology* **22**, 337–342; 10.1016/S1471-4906(01)01930-5 (2001).
155. Jasmine Nettiksimmons, Gregory Tranah, Daniel S. Evans, Jennifer S. Yokoyama & Kristine Yaffe. Gene-based aggregate SNP associations between candidate AD genes and cognitive decline. *AGE* **38**, 1–10; 10.1007/s11357-016-9885-2 (2016).

156. Malik, M., Simpson, J. F., Parikh, I., Wilfred, B. R., Fardo, D. W., Nelson, P. T. & Estus, S. *et al.* CD33 Alzheimer's risk-altering polymorphism, CD33 expression, and exon 2 splicing. *The Journal of neuroscience : the official journal of the Society for Neuroscience* **33**, 13320–13325; 10.1523/JNEUROSCI.1224-13.2013 (2013).
157. Leslie Mortland, Todd A. Alonzo, Roland B. Walter, Robert B. Gerbing, Amit K. Mitra, Jessica A. Pollard & Michael R. Loken *et al.* Clinical Significance of CD33 Nonsynonymous Single-Nucleotide Polymorphisms in Pediatric Patients with Acute Myeloid Leukemia Treated with Gemtuzumab-Ozogamicin-Containing Chemotherapy. *Clin Cancer Res* **19**, 1620–1627; 10.1158/1078-0432.CCR-12-3115 (2013).
158. Mao, Y.-F., Guo, Z.-Y., Pu, J.-L., Chen, Y.-X. & Zhang, B.-R. Association of CD33 and MS4A cluster variants with Alzheimer's disease in East Asian populations. *Neuroscience letters* **609**, 235–239; 10.1016/j.neulet.2015.10.007 (2015).
159. Lin, E., Tsai, S.-J., Kuo, P.-H., Liu, Y.-L., Yang, A. C. & Kao, C.-F. *et al.* Association and interaction effects of Alzheimer's disease-associated genes and lifestyle on cognitive aging in older adults in a Taiwanese population. *Oncotarget* **8**, 24077–24087; 10.18632/oncotarget.15269 (2017).
160. Wen-Ying Wang, Ying Liu, Hui-Fu Wang, Lin Tan, Fu-Rong Sun, Meng-Shan Tan & Chen-Chen Tan *et al.* Impacts of CD33 Genetic Variations on the Atrophy Rates of Hippocampus and Parahippocampal Gyrus in Normal Aging and Mild Cognitive Impairment. *Mol Neurobiol* **54**, 1111–1118; 10.1007/s12035-016-9718-4 (2017).
161. Cukier, H. N., Kunkle, B. K., Hamilton, K. L., Rolati, S., Kohli, M. A., Whitehead, P. L. & Jaworski, J. *et al.* Exome Sequencing of Extended Families with Alzheimer's Disease Identifies Novel Genes Implicated in Cell Immunity and Neuronal Function. *Journal of Alzheimer's disease & Parkinsonism* **7**; 10.4172/2161-0460.1000355 (2017).
162. Medway, C. & Morgan, K. Sialic Acid Binding Immunoglobulin-Like Lectin-3 (CD33). In *Genetic Variants in Alzheimer's Disease*, edited by K. Morgan & M. M. Carrasquillo (Springer New York, New York, NY, 2013), pp. 181–190.
163. Jiang, Y.-T., Li, H.-Y., Cao, X.-P. & Tan, L. Meta-analysis of the association between CD33 and Alzheimer's disease. *Annals of translational medicine* **6**; 10.21037/atm.2018.04.21 (2018).
164. Hendrik Poeck & Jürgen Ruland. SYK kinase signaling and the NLRP3 inflammasome in antifungal immunity. *J Mol Med* **88**, 745–752; 10.1007/s00109-010-0631-4 (2010).
165. Linnartz, B., Wang, Y. & Neumann, H. Microglial immunoreceptor tyrosine-based activation and inhibition motif signaling in neuroinflammation. *International journal of Alzheimer's disease* **2010**; 10.4061/2010/587463 (2010).
166. Marco Colonna. TREMs in the immune system and beyond. *Nat Rev Immunol* **3**, 445–453; 10.1038/nri1106 (2003).
167. Jessica A. Hamerman, Minjian Ni, Justin R. Killebrew, Ching-Liang Chu & Clifford A. Lowell. The expanding roles of ITAM adapters FcRγ and DAP12 in myeloid cells. *Immunological reviews* **232**, 42–58; 10.1111/j.1600-065X.2009.00841.x (2009).
168. Bettina Linnartz & Harald Neumann. Microglial activatory (immunoreceptor tyrosine-based activation motif)- and inhibitory (immunoreceptor tyrosine-based inhibition motif)-signaling receptors for recognition of the neuronal glycocalyx. *Glia* **61**, 37–46; 10.1002/glia.22359 (2013).
169. Fischer, K.-D., Kong, Y.-Y., Nishina, H., Tedford, K., Marengère, L.E.M., Kozieradzki, I. & Sasaki, T. *et al.* Vav is a regulator of cytoskeletal reorganization mediated by the T-cell receptor. *Current Biology* **8**, 554-S3; 10.1016/S0960-9822(98)70224-6 (1998).
170. Zhou, Y., Su, J., Shi, L., Liao, Q. & Su, Q. DADS downregulates the Rac1-ROCK1/PAK1-LIMK1-ADF/cofilin signaling pathway, inhibiting cell migration and invasion. *Oncology reports* **29**, 605–612; 10.3892/or.2012.2168 (2013).
171. Hirsch, I., Janovec, V., Stranska, R. & Bendriss-Vermare, N. Cross Talk between Inhibitory Immunoreceptor Tyrosine-Based Activation Motif-Signaling and Toll-Like Receptor Pathways in Macrophages and Dendritic Cells. *Frontiers in immunology* **8**, 394; 10.3389/fimmu.2017.00394 (2017).
172. Salminen, A. & Kaarniranta, K. Siglec receptors and hiding plaques in Alzheimer's disease. *Journal of molecular medicine (Berlin, Germany)* **87**, 697–701; 10.1007/s00109-009-0472-1 (2009).
173. Vivier, E. & Daëron, M. Immunoreceptor tyrosine-based inhibition motifs. *Immunology Today* **18**, 286–291; 10.1016/S0167-5699(97)80025-4 (1997).
174. Daniel D. Billadeau & Paul J. Leibson. ITAMs versus ITIMs: striking a balance during cell regulation. *J Clin Invest* **109**, 161–168; 10.1172/JCI14843 (2002).
175. Barrett, R., Ornelas, L., Yeager, N., Mandefro, B., Sahabian, A., Lenaeus, L. & Targan, S. R. *et al.* Reliable generation of induced pluripotent stem cells from human lymphoblastoid cell lines. *Stem cells translational medicine* **3**, 1429–1434; 10.5966/sctm.2014-0121 (2014).
176. Muffat, J., Li, Y., Yuan, B., Mitalipova, M., Omer, A., Corcoran, S. & Bakiasi, G. *et al.* Efficient derivation of microglia-like cells from human pluripotent stem cells. *Nature medicine* **22**, 1358–1367; 10.1038/nm.4189 (2016).
177. Massa, C. & Seliger, B. Fast dendritic cells stimulated with alternative maturation mixtures induce polyfunctional and long-lasting activation of innate and adaptive effector cells with tumor-killing capabilities. *The Journal of Immunology* **190**, 3328–3337; 10.4049/jimmunol.1202024 (2013).

178. Cawthon, R. M. Telomere measurement by quantitative PCR. *Nucleic acids research* **30**, e47 (2002).
179. Klemenz, A., Wolgast, S., Hanitzsch, R., Markwardt, F. & Peschke, E. Effects of insulin on norepinephrine- and acetylcholine-induced membrane currents of pinealocytes from healthy Wistar and type 2 diabetic GK rats. *Cell and Tissue Research* **355**, 437–446; 10.1007/s00441-013-1748-x (2014).
180. Hohmann, T., Grabiec, U., Ghadban, C., Feese, K. & Dehghani, F. The influence of biomechanical properties and cannabinoids on tumor invasion. *Cell adhesion & migration* **11**, 54–67; 10.1080/19336918.2016.1183867 (2017).
181. Heppner, F. L., Roth, K., Nitsch, R. & Hailer, N. P. Vitamin E induces ramification and downregulation of adhesion molecules in cultured microglial cells. *Glia* **22**, 180–188; 10.1002/(SICI)1098-1136(199802)22:2<180::AID-GLIA9>3.0.CO;2-B (1998).
182. Distler, U., Kuharev, J., Navarro, P. & Tenzer, S. Label-free quantification in ion mobility-enhanced data-independent acquisition proteomics. *Nature protocols* **11**, 795–812; 10.1038/nprot.2016.042 (2016).
183. Distler, U., Kuharev, J., Navarro, P., Levin, Y., Schild, H. & Tenzer, S. *et al.* Drift time-specific collision energies enable deep-coverage data-independent acquisition proteomics. *nmeth* **11**, 167–170; 10.1038/nmeth.2767 (2014).
184. Sacramento, E. K., Kirkpatrick, J. M., Mazzetto, M., Di Sanzo, S., Caterino, C., Sanguanini, M. & Papaevgeniou, N. *et al.* Reduced proteasome activity in the aging brain results in ribosome stoichiometry loss and aggregation (2019).
185. Schwanhäusser, B., Busse, D., Li, N., Dittmar, G., Schuchhardt, J., Wolf, J. & Chen, W. *et al.* Global quantification of mammalian gene expression control. *Nature* **473**, 337–342; 10.1038/nature10098 (2011).
186. Caroline Van Cauwenberghe, Christine Van Broeckhoven & Kristel Sleegers. The genetic landscape of Alzheimer disease: clinical implications and perspectives. *Genet Med* **18**, 421–430; 10.1038/gim.2015.117 (2016).
187. Mirza, A., King, A., Troakes, C. & Exley, C. Aluminium in brain tissue in familial Alzheimer's disease. *Journal of trace elements in medicine and biology : organ of the Society for Minerals and Trace Elements (GMS)* **40**, 30–36; 10.1016/j.jtemb.2016.12.001 (2017).
188. Ekaterina Rogaeva. The solved and unsolved mysteries of the genetics of early-onset Alzheimer's disease. *Neuromol Med* **2**, 1–10; 10.1385/NMM:2:1:01 (2002).
189. Giri, M., Zhang, M. & Lü, Y. Genes associated with Alzheimer's disease: an overview and current status. *Clinical Interventions in Aging* **11**, 665–681; 10.2147/CIA.S105769 (2016).
190. Tan, L., Yu, J.-T., Zhang, W., Wu, Z.-C., Zhang, Q., Liu, Q.-Y. & Wang, W. *et al.* Association of GWAS-linked loci with late-onset Alzheimer's disease in a northern Han Chinese population. *Alzheimer's & dementia : the journal of the Alzheimer's Association* **9**, 546–553; 10.1016/j.jalz.2012.08.007 (2013).
191. Logue, M. W., Schu, M., Vardarajan, B. N., Burros, J., Green, R. C., Go, R. C. P. & Griffith, P. *et al.* A comprehensive genetic association study of Alzheimer disease in African Americans. *Archives of neurology* **68**, 1569–1579; 10.1001/archneurol.2011.646 (2011).
192. Jiang, T., Yu, J.-T., Hu, N., Tan, M.-S., Zhu, X.-C. & Tan, L. *et al.* CD33 in Alzheimer's disease. *Molecular neurobiology* **49**, 529–535; 10.1007/s12035-013-8536-1 (2014).
193. Turano, E., Busetto, G., Marconi, S., Guzzo, F., Farinazzo, A., Comisso, M. & Bistaffa, E. *et al.* Neurotoxicity and synaptic plasticity impairment of N-acetylglucosamine polymers: implications for Alzheimer's disease. *Neurobiology of aging* **36**, 1780–1791; 10.1016/j.neurobiolaging.2014.12.033 (2015).
194. Jay, T. R., Saucken, V. E. von & Landreth, G. E. TREM2 in Neurodegenerative Diseases. *Molecular neurodegeneration* **12**, 56; 10.1186/s13024-017-0197-5 (2017).
195. ElAli, A. & Rivest, S. Microglia Ontology and Signaling. *Frontiers in cell and developmental biology* **4**, 72; 10.3389/fcell.2016.00072 (2016).
196. Borroni, B., Ferrari, F., Galimberti, D., Nacmias, B., Barone, C., Bagnoli, S. & Fenoglio, C. *et al.* Heterozygous TREM2 mutations in frontotemporal dementia. *Neurobiology of aging* **35**, 934.e7-10 (2014).
197. Sheng Chih Jin, Minerva M Carrasquillo, Bruno A Benitez, Tara Skorupa, David Carrell, Dwani Patel & Sarah Lincoln *et al.* TREM2 is associated with increased risk for Alzheimer's disease in African Americans. *Mol Neurodegeneration* **10**, 1–7; 10.1186/s13024-015-0016-9 (2015).
198. Jiang, T., Tan, L., Chen, Q., Tan, M.-S., Zhou, J.-S., Zhu, X.-C. & Lu, H. *et al.* A rare coding variant in TREM2 increases risk for Alzheimer's disease in Han Chinese. *Neurobiology of aging* **42**, 217.e1-3; 10.1016/j.neurobiolaging.2016.02.023 (2016).
199. Maud Gratuze, Cheryl E. G. Leyns & David M. Holtzman. New insights into the role of TREM2 in Alzheimer's disease. *Mol Neurodegeneration* **13**, 1–16; 10.1186/s13024-018-0298-9 (2018).
200. Yu-Lei Deng, Li-Hua Liu, Ying Wang, Hui-Dong Tang, Ru-Jing Ren, Wei Xu & Jian-Fang Ma *et al.* The prevalence of CD33 and MS4A6A variant in Chinese Han population with Alzheimer's disease. *Hum Genet* **131**, 1245–1249; 10.1007/s00439-012-1154-6 (2012).
201. Deming, Y., Filipello, F., Cignarella, F., Cantoni, C., Hsu, S., Mikesell, R. & Li, Z. *et al.* The MS4A gene cluster is a key regulator of soluble TREM2 and Alzheimer disease risk. *bioRxiv*, 352179; 10.1101/352179 (2018).

202. Yamazaki, T., Masuda, J., Omori, T., Usui, R., Akiyama, H. & Maru, Y. *et al.* EphA1 interacts with integrin-linked kinase and regulates cell morphology and motility. *Journal of cell science* **122**, 243–255; 10.1242/jcs.036467 (2009).
203. Lehtonen, S., Zhao, F. & Lehtonen, E. CD2-associated protein directly interacts with the actin cytoskeleton. *American journal of physiology. Renal physiology* **283**, F734–43; 10.1152/ajprenal.00312.2001 (2002).
204. Tao, Q.-Q., Chen, Y.-C. & Wu, Z.-Y. The role of CD2AP in the Pathogenesis of Alzheimer's Disease. *Aging and disease* **10**, 901–907; 10.14336/AD.2018.1025 (2019).
205. Hongyuan Chen, Guihua Wu, Yongshuai Jiang, Rennan Feng, Mingzhi Liao, Liangcai Zhang & Guoda Ma *et al.* Analyzing 54,936 Samples Supports the Association Between CD2AP rs9349407 Polymorphism and Alzheimer's Disease Susceptibility. *Mol Neurobiol* **52**, 1–7; 10.1007/s12035-014-8834-2 (2015).
206. Kettenmann, H., Hanisch, U.-K., Noda, M. & Verkhratsky, A. Physiology of microglia. *Physiological Reviews* **91**, 461–553; 10.1152/physrev.00011.2010 (2011).
207. Loane, D. J. & Kumar, A. Microglia in the TBI brain. The good, the bad, and the dysregulated. *Experimental neurology* **275 Pt 3**, 316–327; 10.1016/j.expneurol.2015.08.018 (2016).
208. Estus, S., Shaw, B. C., Devanney, N., Katsumata, Y., Press, E. E. & Fardo, D. W. *et al.* Evaluation of CD33 as a genetic risk factor for Alzheimer's disease. *Acta Neuropathologica* **138**, 187–199; 10.1007/s00401-019-02000-4 (2019).
209. M. Guadalupe Cabral, Zélia Silva, Dário Ligeiro, Elsa Seixas, Hélio Crespo, Mylène A. Carrascal & Mariana Silva *et al.* The phagocytic capacity and immunological potency of human dendritic cells is improved by α 2,6-sialic acid deficiency. *Immunology* **138**, 235–245; 10.1111/imm.12025 (2013).
210. Raman, T., Arumugam, M. & Mullainadhan, P. Agglutinin-mediated phagocytosis-associated generation of superoxide anion and nitric oxide by the hemocytes of the giant freshwater prawn *Macrobrachium rosenbergii*. *Fish & shellfish immunology* **24**, 337–345; 10.1016/j.fsi.2007.12.005 (2008).
211. Griciuc, A., Serrano-Pozo, A., Parrado, A. R., Lesinski, A. N., Asselin, C. N., Mullin, K. & Hooli, B. *et al.* Alzheimer's disease risk gene CD33 inhibits microglial uptake of amyloid beta. *Neuron* **78**, 631–643; 10.1016/j.neuron.2013.04.014 (2013).
212. Makranz, C., Cohen, G., Reichert, F., Kodama, T. & Rotshenker, S. cAMP cascade (PKA, Epac, adenylyl cyclase, Gi, and phosphodiesterases) regulates myelin phagocytosis mediated by complement receptor-3 and scavenger receptor-AI/II in microglia and macrophages. *Glia* **53**, 441–448; 10.1002/glia.20303 (2006).
213. Larsen, E. C., Ueyama, T., Brannock, P. M., Shirai, Y., Saito, N., Larsson, C. & Loegering, D. *et al.* A role for PKC- ϵ in Fc γ R-mediated phagocytosis by RAW 264.7 cells. *J Cell Biol* **159**, 939–944; 10.1083/jcb.200205140 (2002).
214. Lajaunias, F., Dayer, J.-M. & Chizzolini, C. Constitutive repressor activity of CD33 on human monocytes requires sialic acid recognition and phosphoinositide 3-kinase-mediated intracellular signaling. *European journal of immunology* **35**, 243–251; 10.1002/eji.200425273 (2005).
215. Kamen, L. A., Levinsohn, J. & Swanson, J. A. Differential association of phosphatidylinositol 3-kinase, SHIP-1, and PTEN with forming phagosomes. *Molecular biology of the cell* **18**, 2463–2472; 10.1091/mbc.e07-01-0061 (2007).
216. Okamura, H., Yoshida, K., Sasaki, E., Qiu, L., Amorim, B. R., Morimoto, H. & Haneji, T. *et al.* Expression of PTEN and Akt phosphorylation in lipopolysaccharide-treated NIH3T3 cells. *Cell biology international* **31**, 119–125; 10.1016/j.cellbi.2006.09.014 (2007).
217. Kim, J. S., Peng, X., De, P. K., Geahlen, R. L. & Durden, D. L. PTEN controls immunoreceptor (immunoreceptor tyrosine-based activation motif) signaling and the activation of Rac. *Blood* **99**, 694–697; 10.1182/blood.v99.2.694 (2002).
218. Appelt-Menzel, A., Oerter, S., Mathew, S., Haferkamp, U., Hartmann, C., Jung, M. & Neuhaus, W. *et al.* Human iPSC-Derived Blood-Brain Barrier Models: Valuable Tools for Preclinical Drug Discovery and Development? *Current protocols in stem cell biology* **55**, e122; 10.1002/cpsc.122 (2020).
219. Yanqi Chang, Xing Zhang, John R Horton, Anup K Upadhyay, Astrid Spannhoff, Jin Liu & James P Snyder *et al.* Structural basis for G9a-like protein lysine methyltransferase inhibition by BIX-01294. *Nat Struct Mol Biol* **16**, 312–317; 10.1038/nsmb.1560 (2009).
220. Asadi, S., Dehghan, S., Hajikaram, M., Mowla, S. J., Ahmadiani, A. A. & Javan, M. *et al.* Comparing The Effects of Small Molecules BIX-01294, Bay K8644, RG-108 and Valproic Acid, and Their Different Combinations on Induction of Pluripotency Marker-Genes by Oct4 in The Mouse Brain. *Cell journal* **16**, 416–425; 10.22074/cellj.2015.488 (2015).
221. Felice, F. G. de & Ferreira, S. T. Inflammation, defective insulin signaling, and mitochondrial dysfunction as common molecular denominators connecting type 2 diabetes to Alzheimer disease. *Diabetes* **63**, 2262–2272; 10.2337/db13-1954 (2014).
222. Jung, M. & Rujescu, D. Translational medicine. From disease- and patient-specific stem cell research to clinical trials and back again. *European archives of psychiatry and clinical neuroscience* **266**, 679–680; 10.1007/s00406-016-0742-1 (2016).

223. José Luis Millán & Michael P. Whyte. Alkaline Phosphatase and Hypophosphatasia. *Calcif Tissue Int* **98**, 398–416; 10.1007/s00223-015-0079-1 (2016).
224. Yu, J., Hu, K., Smuga-Otto, K., Tian, S., Stewart, R., Slukvin, I. I. & Thomson, J. A. *et al.* Human induced pluripotent stem cells free of vector and transgene sequences. *Science (New York, N.Y.)* **324**, 797–801; 10.1126/science.1172482 (2009).
225. Annabelle Congras, Harmonie Barasc, Kamila Canale-Tabet, Florence Plisson-Petit, Chantal Delcros, Olivier Feraud & Noufissa Oudrhiri *et al.* Non integrative strategy decreases chromosome instability and improves endogenous pluripotency genes reactivation in porcine induced pluripotent-like stem cells. *Sci Rep* **6**, 1–17; 10.1038/srep27059 (2016).
226. Thomas F. Westbrook, Guang Hu, Xiaolu L. Ang, Peter Mulligan, Natalya N. Pavlova, Anthony Liang & Yumei Leng *et al.* SCF β -TRCP controls oncogenic transformation and neural differentiation through REST degradation. *Nature* **452**, 370–374; 10.1038/nature06780 (2008).
227. Kumar, S., Espinosa, E. C., Leandro, A. C., Curran, J. E. & Blangero, J. microRNA and mRNA interactions in induced pluripotent stem cell reprogramming of lymphoblastoid cell lines. *American Journal of Stem Cells* **8**, 28–37 (2019).
228. Maes, O. C., Xu, S., Yu, B., Chertkow, H. M., Wang, E. & Schipper, H. M. *et al.* Transcriptional profiling of Alzheimer blood mononuclear cells by microarray. *Neurobiology of aging* **28**, 1795–1809; 10.1016/j.neurobiolaging.2006.08.004 (2007).
229. Kim, S. Y., Kim, M.-J., Jung, H., Kim, W. K., Kwon, S. O., Son, M. J. & Jang, I.-S. *et al.* Comparative proteomic analysis of human somatic cells, induced pluripotent stem cells, and embryonic stem cells. *Stem cells and development* **21**, 1272–1286; 10.1089/scd.2011.0243 (2012).
230. Ghosh, Z., Wilson, K. D., Wu, Y., Hu, S., Quertermous, T. & Wu, J. C. *et al.* Persistent donor cell gene expression among human induced pluripotent stem cells contributes to differences with human embryonic stem cells. *PLoS one* **5**, e8975; 10.1371/journal.pone.0008975 (2010).
231. Li, H., Wang, B., Yang, A., Lu, R., Wang, W., Zhou, Y. & Shi, G. *et al.* Ly-1 antibody reactive clone is an important nucleolar protein for control of self-renewal and differentiation in embryonic stem cells. *Stem cells (Dayton, Ohio)* **27**, 1244–1254; 10.1002/stem.55 (2009).
232. Kanako Niimori-Kita, Nobuaki Tamamaki, Daikai Koizumi & Daisuke Niimori. Matrin-3 is essential for fibroblast growth factor 2-dependent maintenance of neural stem cells. *Sci Rep* **8**, 1–10; 10.1038/s41598-018-31597-x (2018).
233. Pardo, M., Lang, B., Yu, L., Prosser, H., Bradley, A., Babu, M. M. & Choudhary, J. *et al.* An expanded Oct4 interaction network: implications for stem cell biology, development, and disease. *Cell stem cell* **6**, 382–395; 10.1016/j.stem.2010.03.004 (2010).
234. Reijo Pera, R. A., DeJonge, C., Bossert, N., Yao, M., Hwa Yang, J. Y., Asadi, N. B. & Wong, W. *et al.* Gene expression profiles of human inner cell mass cells and embryonic stem cells. *Differentiation; research in biological diversity* **78**, 18–23; 10.1016/j.diff.2009.03.004 (2009).
235. Mehrotra, S., Wickremesekera, S. K., Brasch, H. D., van Schaijik, B., Marsh, R. W., Tan, S. T. & Itinteang, T. *et al.* Expression and Localization of Cathepsins B, D and G in Cancer Stem Cells in Liver Metastasis From Colon Adenocarcinoma. *Front. Surg.* **5**, 40; 10.3389/fsurg.2018.00040 (2018).
236. Xiao-Lei Li, Lan-Ling Jia, Mu-Mu Shi, Xin Li, Zhong-Hua Li, Hui-Feng Li & En-Hua Wang *et al.* Downregulation of KPNA2 in non-small-cell lung cancer is associated with Oct4 expression. *J Transl Med* **11**, 1–11; 10.1186/1479-5876-11-232 (2013).
237. Johnson, C. P. & Chapman, E. R. Otoferlin is a calcium sensor that directly regulates SNARE-mediated membrane fusion. *J Cell Biol* **191**, 187–197; 10.1083/jcb.201002089 (2010).
238. Wong, Q. W.-L., Vaz, C., Lee, Q. Y., Zhao, T. Y., Luo, R., Archer, S. K. & Preiss, T. *et al.* Embryonic Stem Cells Exhibit mRNA Isoform Specific Translational Regulation. *PLoS one* **11**, e0143235; 10.1371/journal.pone.0143235 (2016).
239. Jean, C., Oliveira, N. M. M., Intarapat, S., Fuet, A., Mazoyer, C., Almeida, I. de & Trevers, K. *et al.* Transcriptome analysis of chicken ES, blastodermal and germ cells reveals that chick ES cells are equivalent to mouse ES cells rather than EpiSC. *Stem cell research* **14**, 54–67; 10.1016/j.scr.2014.11.005 (2015).
240. Morales Torres, C., Laugesen, A. & Helin, K. Utx is required for proper induction of ectoderm and mesoderm during differentiation of embryonic stem cells. *PLoS one* **8**, e60020; 10.1371/journal.pone.0060020 (2013).
241. Berger, C., Bjørlykke, Y., Hahn, L., Mühlemann, M., Kress, S., Walles, H. & Luxenhofer, R. *et al.* Matrix decoded – A pancreatic extracellular matrix with organ specific cues guiding human iPSC differentiation. *Biomaterials* **244**, 119766; 10.1016/j.biomaterials.2020.119766 (2020).
242. Park, I.-H., Arora, N., Huo, H., Maherali, N., Ahfeldt, T., Shimamura, A. & Lensch, M. W. *et al.* Disease-specific induced pluripotent stem (iPS) cells. *Cell* **134**, 877–886; 10.1016/j.cell.2008.07.041 (2008).

243. Guttenplan, K. A. & Liddelow, S. A. Astrocytes and microglia: Models and tools. *The Journal of experimental medicine* **216**, 71–83; 10.1084/jem.20180200 (2019).
244. Boza-Serrano, A., Yang, Y., Paulus, A. & Deierborg, T. Innate immune alterations are elicited in microglial cells before plaque deposition in the Alzheimer's disease mouse model 5xFAD. *Scientific reports* **8**, 1550; 10.1038/s41598-018-19699-y (2018).
245. Bohlen, C. J., Bennett, F. C., Tucker, A. F., Collins, H. Y., Mulinyawe, S. B. & Barres, B. A. *et al.* Diverse Requirements for Microglial Survival, Specification, and Function Revealed by Defined-Medium Cultures. *Neuron* **94**, 759–773.e8; 10.1016/j.neuron.2017.04.043 (2017).
246. Beutner, C., Roy, K., Linnartz, B., Napoli, I. & Neumann, H. Generation of microglial cells from mouse embryonic stem cells. *Nature protocols* **5**, 1481–1494; 10.1038/nprot.2010.90 (2010).
247. Takata, K., Kozaki, T., Lee, C. Z. W., Thion, M. S., Otsuka, M., Lim, S. & Utami, K. H. *et al.* Induced-Pluripotent-Stem-Cell-Derived Primitive Macrophages Provide a Platform for Modeling Tissue-Resident Macrophage Differentiation and Function. *Immunity* **47**, 183–198.e6; 10.1016/j.immuni.2017.06.017 (2017).
248. Douvaras, P., Sun, B., Wang, M., Kruglikov, I., Lallo, G., Zimmer, M. & Terrenoire, C. *et al.* Directed Differentiation of Human Pluripotent Stem Cells to Microglia. *Stem cell reports*; 10.1016/j.stemcr.2017.04.023 (2017).
249. Abud, E. M., Ramirez, R. N., Martinez, E. S., Healy, L. M., Nguyen, C. H. H., Newman, S. A. & Yeromin, A. V. *et al.* iPSC-Derived Human Microglia-like Cells to Study Neurological Diseases. *Neuron* **94**, 278–293.e9; 10.1016/j.neuron.2017.03.042 (2017).
250. Yanagimachi, M. D., Niwa, A., Tanaka, T., Honda-Ozaki, F., Nishimoto, S., Murata, Y. & Yasumi, T. *et al.* Robust and highly-efficient differentiation of functional monocytic cells from human pluripotent stem cells under serum- and feeder cell-free conditions. *PLoS one* **8**, e59243; 10.1371/journal.pone.0059243 (2013).
251. Sontag, S., Forster, M., Qin, J., Wanek, P., Mitzka, S., Schuler, H. M. & Koschmieder, S. *et al.* Modelling IRF8 Deficient Human Hematopoiesis and Dendritic Cell Development with Engineered iPSC Cells. *Stem cells (Dayton, Ohio)*; 10.1002/stem.2565 (2017).
252. Christine Servet-Delprat, Sylvie Arnaud, Pierre Jurdic, Serge Nataf, Marie-France Grasset, Caroline Soulas & Chantal Domenget *et al.* Flt3 + macrophage precursors commit sequentially to osteoclasts, dendritic cells and microglia. *BMC Immunol* **3**, 1–11; 10.1186/1471-2172-3-15 (2002).
253. Karlsson, K. R., Cowley, S., Martinez, F. O., Shaw, M., Minger, S. L. & James, W. *et al.* Homogeneous monocytes and macrophages from human embryonic stem cells following coculture-free differentiation in M-CSF and IL-3. *Experimental hematology* **36**, 1167–1175; 10.1016/j.exphem.2008.04.009 (2008).
254. Butovsky, O., Jedrychowski, M. P., Moore, C. S., Cialic, R., Lanser, A. J., Gabriely, G. & Koeglperger, T. *et al.* Identification of a unique TGF- β -dependent molecular and functional signature in microglia. *Nature neuroscience* **17**, 131–143; 10.1038/nn.3599 (2014).
255. Kavon Rezai-Zadeh, Jared Ehrhart, Yun Bai, Paul R Sanberg, Paula Bickford, Jun Tan & R Douglas Shytle *et al.* Apigenin and luteolin modulate microglial activation via inhibition of STAT1-induced CD40 expression. *J Neuroinflammation* **5**, 1–10; 10.1186/1742-2094-5-41 (2008).
256. Ben J. Gu, Xin Huang, Amber Ou, Alan Rembach, Christopher Fowler, Pavan K. Avula & Adam Horton *et al.* Innate phagocytosis by peripheral blood monocytes is altered in Alzheimer's disease. *Acta Neuropathol* **132**, 377–389; 10.1007/s00401-016-1596-3 (2016).
257. Remington, L. T., Babcock, A. A., Zehntner, S. P. & Owens, T. Microglial Recruitment, Activation, and Proliferation in Response to Primary Demyelination. *The American Journal of Pathology* **170**, 1713–1724; 10.2353/ajpath.2007.060783 (2007).
258. Lachmann, N., Ackermann, M., Frenzel, E., Liebhaber, S., Brenning, S., Happle, C. & Hoffmann, D. *et al.* Large-scale hematopoietic differentiation of human induced pluripotent stem cells provides granulocytes or macrophages for cell replacement therapies. *Stem cell reports* **4**, 282–296; 10.1016/j.stemcr.2015.01.005 (2015).
259. Madry, C., Kyrargyri, V., Arancibia-Cárcamo, I. L., Jolivet, R., Kohsaka, S., Bryan, R. M. & Attwell, D. *et al.* Microglial Ramification, Surveillance, and Interleukin-1 β Release Are Regulated by the Two-Pore Domain K⁺ Channel THIK-1. *Neuron* **97**, 299–312.e6; 10.1016/j.neuron.2017.12.002 (2018).
260. Raivich, G. Like cops on the beat: the active role of resting microglia. *Trends in neurosciences* **28**, 571–573; 10.1016/j.tins.2005.09.001 (2005).
261. Haenseler, W., Sansom, S. N., Buchrieser, J., Newey, S. E., Moore, C. S., Nicholls, F. J. & Chintawar, S. *et al.* A Highly Efficient Human Pluripotent Stem Cell Microglia Model Displays a Neuronal-Co-culture-Specific Expression Profile and Inflammatory Response. *Stem cell reports* **8**, 1727–1742; 10.1016/j.stemcr.2017.05.017 (2017).
262. Scheiblich, H., Roloff, F., Singh, V., Stangel, M., Stern, M. & Bicker, G. *et al.* Nitric oxide/cyclic GMP signaling regulates motility of a microglial cell line and primary microglia in vitro. *Brain research* **1564**, 9–21; 10.1016/j.brainres.2014.03.048 (2014).

263. Hochstrasser, T., Marksteiner, J. & Humpel, C. Telomere length is age-dependent and reduced in monocytes of Alzheimer patients. *Experimental Gerontology* **47**, 160–163; 10.1016/j.exger.2011.11.012 (2012).
264. Boccardi, V., Pelini, L., Ercolani, S., Ruggiero, C. & Mecocci, P. From cellular senescence to Alzheimer's disease. The role of telomere shortening. *Ageing research reviews* **22**, 1–8; 10.1016/j.arr.2015.04.003 (2015).
265. Rampe, D., Wang, L. & Ringheim, G. E. P2X7 receptor modulation of beta-amyloid- and LPS-induced cytokine secretion from human macrophages and microglia. *Journal of neuroimmunology* **147**, 56–61; 10.1016/j.jneuroim.2003.10.014 (2004).
266. Alexandru, A., Jagla, W., Graubner, S., Becker, A., Bäuscher, C., Kohlmann, S. & Sedlmeier, R. *et al.* Selective hippocampal neurodegeneration in transgenic mice expressing small amounts of truncated A β is induced by pyroglutamate-A β formation. *The Journal of neuroscience : the official journal of the Society for Neuroscience* **31**, 12790–12801; 10.1523/JNEUROSCI.1794-11.2011 (2011).
267. Wang, W.-Y., Tan, M.-S., Yu, J.-T. & Tan, L. Role of pro-inflammatory cytokines released from microglia in Alzheimer's disease. *Annals of translational medicine* **3**, 136; 10.3978/j.issn.2305-5839.2015.03.49 (2015).
268. Bhaskar, K., Maphis, N., Xu, G., Varvel, N. H., Kokiko-Cochran, O. N., Weick, J. P. & Staugaitis, S. M. *et al.* Microglial derived tumor necrosis factor- α drives Alzheimer's disease-related neuronal cell cycle events. *Neurobiology of disease* **62**, 273–285; 10.1016/j.nbd.2013.10.007 (2014).
269. Grunin, M., Burstyn-Cohen, T., Hagbi-Levi, S., Peled, A. & Chowers, I. Chemokine receptor expression in peripheral blood monocytes from patients with neovascular age-related macular degeneration. *Investigative ophthalmology & visual science* **53**, 5292–5300; 10.1167/iovs.11-9165 (2012).
270. Bolovan-Fritts, C. A. & Spector, S. A. Endothelial damage from cytomegalovirus-specific host immune response can be prevented by targeted disruption of fractalkine-CX3CR1 interaction. *Blood* **111**, 175–182; 10.1182/blood-2007-08-107730 (2008).
271. Suzanne E Hickman, Nathan D Kingery, Toshiro K Ohsumi, Mark L Borowsky, Li-chong Wang, Terry K Means & Joseph El Khoury *et al.* The microglial sensome revealed by direct RNA sequencing. *Nat Neurosci* **16**, 1896–1905; 10.1038/nn.3554 (2013).
272. Wang, Y., Cella, M., Mallinson, K., Ulrich, J. D., Young, K. L., Robinette, M. L. & Gilfillan, S. *et al.* TREM2 lipid sensing sustains the microglial response in an Alzheimer's disease model. *Cell* **160**, 1061–1071; 10.1016/j.cell.2015.01.049 (2015).
273. Lv, J., Ma, S., Zhang, X., Zheng, L., Ma, Y., Zhao, X. & Lai, W. *et al.* Quantitative proteomics reveals that PEA15 regulates astroglial A β phagocytosis in an Alzheimer's disease mouse model. *Journal of proteomics* **110**, 45–58; 10.1016/j.jprot.2014.07.028 (2014).
274. Hwang, J. Y., Shim, J. S., Song, M.-Y., Yim, S.-V., Lee, S. E. & Park, K.-S. *et al.* Proteomic analysis reveals that the protective effects of ginsenoside Rb1 are associated with the actin cytoskeleton in β -amyloid-treated neuronal cells. *Journal of ginseng research* **40**, 278–284; 10.1016/j.jgr.2015.09.004 (2016).
275. Orre, M., Kamphuis, W., Osborn, L. M., Jansen, A. H. P., Kooijman, L., Bossers, K. & Hol, E. M. *et al.* Isolation of glia from Alzheimer's mice reveals inflammation and dysfunction. *Neurobiology of aging* **35**, 2746–2760; 10.1016/j.neurobiolaging.2014.06.004 (2014).
276. Mathys, H., Adai, C., Gao, F., Young, J. Z., Manet, E., Hemberg, M. & Jager, P. L. de *et al.* Temporal Tracking of Microglia Activation in Neurodegeneration at Single-Cell Resolution. *Cell reports* **21**, 366–380; 10.1016/j.celrep.2017.09.039 (2017).
277. Galatro, T. F., Holtman, I. R., Lerario, A. M., Vainchtein, I. D., Brouwer, N., Sola, P. R. & Veras, M. M. *et al.* Transcriptomic analysis of purified human cortical microglia reveals age-associated changes. *Nature neuroscience* **20**, 1162–1171; 10.1038/nn.4597 (2017).
278. Augustin, R., Lichtenthaler, S. F., Greeff, M., Hansen, J., Wurst, W. & Trümbach, D. *et al.* Bioinformatics identification of modules of transcription factor binding sites in Alzheimer's disease-related genes by in silico promoter analysis and microarrays. *International journal of Alzheimer's disease* **2011**, 154325; 10.4061/2011/154325 (2011).
279. Kamphuis, W., Kooijman, L., Orre, M., Stassen, O., Pekny, M. & Hol, E. M. *et al.* GFAP and vimentin deficiency alters gene expression in astrocytes and microglia in wild-type mice and changes the transcriptional response of reactive glia in mouse model for Alzheimer's disease. *Glia* **63**, 1036–1056; 10.1002/glia.22800 (2015).
280. Markus G. Manz & Steffen Boettcher. Emergency granulopoiesis. *Nat Rev Immunol* **14**, 302–314; 10.1038/nri3660 (2014).
281. Orre, M., Kamphuis, W., Osborn, L. M., Melief, J., Kooijman, L., Huitinga, I. & Klooster, J. *et al.* Acute isolation and transcriptome characterization of cortical astrocytes and microglia from young and aged mice. *Neurobiology of aging* **35**, 1–14; 10.1016/j.neurobiolaging.2013.07.008 (2014).
282. Yin, Z., Raj, D., Saiepour, N., van Dam, D., Brouwer, N., Holtman, I. R. & Eggen, B. J. L. *et al.* Immune hyperreactivity of A β plaque-associated microglia in Alzheimer's disease. *Neurobiology of aging* **55**, 115–122; 10.1016/j.neurobiolaging.2017.03.021 (2017).

283. Neubrand, V. E., Pedreño, M., Caro, M., Forte-Lago, I., Delgado, M. & Gonzalez-Rey, E. *et al.* Mesenchymal stem cells induce the ramification of microglia via the small RhoGTPases Cdc42 and Rac1. *Glia* **62**, 1932–1942; 10.1002/glia.22714 (2014).
284. Grandbarbe, L., Michelucci, A., Heurtaux, T., Hemmer, K., Morga, E. & Heuschling, P. *et al.* Notch signaling modulates the activation of microglial cells. *Glia* **55**, 1519–1530; 10.1002/glia.20553 (2007).
285. Reed-Geaghan, E. G., Savage, J. C., Hise, A. G. & Landreth, G. E. CD14 and toll-like receptors 2 and 4 are required for fibrillar A β -stimulated microglial activation. *The Journal of neuroscience : the official journal of the Society for Neuroscience* **29**, 11982–11992; 10.1523/JNEUROSCI.3158-09.2009 (2009).
286. Halleskog, C., Mulder, J., Dahlström, J., Mackie, K., Hortobágyi, T., Tanila, H. & Kumar Puli, L. *et al.* WNT signaling in activated microglia is proinflammatory. *Glia* **59**, 119–131; 10.1002/glia.21081 (2011).
287. Abd-el-Basset, E. & Fedoroff, S. Effect of bacterial wall lipopolysaccharide (LPS) on morphology, motility, and cytoskeletal organization of microglia in cultures. *Journal of neuroscience research* **41**, 222–237; 10.1002/jnr.490410210 (1995).
288. Lisa Ulbrich, Mauro Cozzolino, Elettra Sara Marini, Ilaria Amori, Antonella De Jaco, Maria Teresa Carri & Gabriella Augusti-Tocco *et al.* Cystatin B and SOD1: Protein–Protein Interaction and Possible Relation to Neurodegeneration. *Cell Mol Neurobiol* **34**, 205–213; 10.1007/s10571-013-0004-y (2014).
289. Yang, D.-S., Stavrides, P., Mohan, P. S., Kaushik, S., Kumar, A., Ohno, M. & Schmidt, S. D. *et al.* Reversal of autophagy dysfunction in the TgCRND8 mouse model of Alzheimer's disease ameliorates amyloid pathologies and memory deficits. *Brain : a journal of neurology* **134**, 258–277; 10.1093/brain/awq341 (2011).
290. Medway, C. & Morgan, K. Review: The genetics of Alzheimer's disease; putting flesh on the bones. *Neuropathology and applied neurobiology* **40**, 97–105; 10.1111/nan.12101 (2014).
291. Yasuda-Yamahara, M., Rogg, M., Frimmel, J., Trachte, P., Helmstaedter, M., Schroder, P. & Schiffer, M. *et al.* FERMT2 links cortical actin structures, plasma membrane tension and focal adhesion function to stabilize podocyte morphology. *Matrix Biology* **68–69**, 263–279; 10.1016/j.matbio.2018.01.003 (2018).
292. Katharina Rehkla, Lena Hoffmann, Christine B Gurniak, Martin Ott, Walter Witke, Luca Scorrano & Carsten Culmsee *et al.* Cofilin1-dependent actin dynamics control DRP1-mediated mitochondrial fission. *Cell Death Dis* **8**, e3063–e3063; 10.1038/cddis.2017.448 (2017).
293. Barone, E., Mosser, S. & Fraering, P. C. Inactivation of brain Cofilin-1 by age, Alzheimer's disease and γ -secretase. *Biochimica et biophysica acta* **1842**, 2500–2509; 10.1016/j.bbadis.2014.10.004 (2014).
294. Agnieszka Popow-Woźniak, Antonina Joanna Mazur, Hans Georg Mannherz, Maria Malicka-Błaszkiwicz & Dorota Nowak. Cofilin overexpression affects actin cytoskeleton organization and migration of human colon adenocarcinoma cells. *Histochem Cell Biol* **138**, 725–736; 10.1007/s00418-012-0988-2 (2012).
295. Faff, L. & Nolte, C. Extracellular acidification decreases the basal motility of cultured mouse microglia via the rearrangement of the actin cytoskeleton. *Brain research* **853**, 22–31; 10.1016/S0006-8993(99)02221-0 (2000).
296. Sánchez, C., Díaz-Nido, J. & Avila, J. Phosphorylation of microtubule-associated protein 2 (MAP2) and its relevance for the regulation of the neuronal cytoskeleton function. *Progress in neurobiology* **61**, 133–168; 10.1016/S0301-0082(99)00046-5 (2000).
297. Coumans, J. V. F., Palanisamy, S. K. A., McFarlane, J. & Moens, P. D. J. Proteomic and Microscopic Strategies towards the Analysis of the Cytoskeletal Networks in Major Neuropsychiatric Disorders. *International journal of molecular sciences* **17**; 10.3390/ijms17040581 (2016).
298. Qualmann, B., Kessels, M. M. & Kelly, R. B. Molecular links between endocytosis and the actin cytoskeleton. *J Cell Biol* **150**, F111–6; 10.1083/jcb.150.5.f111 (2000).
299. Kurochkina, N., Bhaskar, M., Yadav, S. P. & Pant, H. C. Phosphorylation, Dephosphorylation, and Multiprotein Assemblies Regulate Dynamic Behavior of Neuronal Cytoskeleton: A Mini-Review. *Front. Mol. Neurosci.* **11**, 373; 10.3389/fnmol.2018.00373 (2018).
300. Wei-Shan Hung, Pin Ling, Ju-Chien Cheng, Shy-Shin Chang & Ching-Ping Tseng. Disabled-2 is a negative immune regulator of lipopolysaccharide-stimulated Toll-like receptor 4 internalization and signaling. *Sci Rep* **6**, 1–14; 10.1038/srep35343 (2016).
301. Neniskyte, U. & Brown, G. C. Lactadherin/MFG-E8 is essential for microglia-mediated neuronal loss and phagoptosis induced by amyloid β . *Journal of neurochemistry* **126**, 312–317; 10.1111/jnc.12288 (2013).
302. Trudler, D., Weinreb, O., Mandel, S. A., Youdim, M. B. H. & Frenkel, D. DJ-1 deficiency triggers microglia sensitivity to dopamine toward a pro-inflammatory phenotype that is attenuated by rasagiline. *Journal of neurochemistry* **129**, 434–447; 10.1111/jnc.12633 (2014).
303. Shalina S. Ousman, Beren H. Tomooka, Johannes M. van Noort, Eric F. Wawrousek, Kevin O'Conner, David A. Hafler & Raymond A. Sobel *et al.* Protective and therapeutic role for α B-crystallin in autoimmune demyelination. *Nature* **448**, 474–479; 10.1038/nature05935 (2007).

304. Yoo, B. C., Kim, S. H., Cairns, N., Fountoulakis, M. & Lubec, G. Deranged expression of molecular chaperones in brains of patients with Alzheimer's disease. *Biochemical and Biophysical Research Communications* **280**, 249–258; 10.1006/bbrc.2000.4109 (2001).
305. Mairuae, N., Connor, J. R. & Cheepsunthorn, P. Increased cellular iron levels affect matrix metalloproteinase expression and phagocytosis in activated microglia. *Neuroscience letters* **500**, 36–40; 10.1016/j.neulet.2011.06.001 (2011).
306. Castegna, A., Thongboonkerd, V., Klein, J. B., Lynn, B., Markesbery, W. R. & Butterfield, D. A. *et al.* Proteomic identification of nitrated proteins in Alzheimer's disease brain. *Journal of neurochemistry* **85**, 1394–1401; 10.1046/j.1471-4159.2003.01786.x (2003).
307. Srikant Rangaraju, Eric B. Dammer, Syed Ali Raza, Tianwen Gao, Hailian Xiao, Ranjita Betarbet & Duc M. Duong *et al.* Quantitative proteomics of acutely-isolated mouse microglia identifies novel immune Alzheimer's disease-related proteins. *Mol Neurodegeneration* **13**, 1–19; 10.1186/s13024-018-0266-4 (2018).
308. Abu Hena M. Kamal, Michael B. Fessler & Saiful M. Chowdhury. Comparative and network-based proteomic analysis of low dose ethanol- and lipopolysaccharide-induced macrophages. *PLOS ONE* **13**, e0193104; 10.1371/journal.pone.0193104 (2018).
309. Ma, Y., Jun, G. R., Zhang, X., Chung, J., Naj, A. C., Chen, Y. & Bellenguez, C. *et al.* Analysis of Whole-Exome Sequencing Data for Alzheimer Disease Stratified by APOE Genotype. *JAMA neurology*; 10.1001/jamaneurol.2019.1456 (2019).
310. Frej, A. D., Clark, J., Le Roy, C. I., Lilla, S., Thomason, P. A., Otto, G. P. & Churchill, G. *et al.* The Inositol-3-Phosphate Synthase Biosynthetic Enzyme Has Distinct Catalytic and Metabolic Roles. *Molecular and cellular biology* **36**, 1464–1479; 10.1128/MCB.00039-16 (2016).
311. Galassie, A. C., Goll, J. B., Samir, P., Jensen, T. L., Hoek, K. L., Howard, L. M. & Allos, T. M. *et al.* Proteomics show antigen presentation processes in human immune cells after AS03-H5N1 vaccination. *Proteomics* **17**; 10.1002/pmic.201600453 (2017).
312. Hou, H., Li, D., Gao, J., Gao, L., Lu, Q., Hu, Y. & Wu, S. *et al.* Proteomic profiling and bioinformatics analysis identify key regulators during the process from fanconi anemia to acute myeloid leukemia. *American Journal of Translational Research* **12**, 1415–1427 (2020).
313. Deng, L., Pushpitha, K., Joseph, C., Gupta, V., Rajput, R., Chitranshi, N. & Dheer, Y. *et al.* Amyloid β Induces Early Changes in the Ribosomal Machinery, Cytoskeletal Organization and Oxidative Phosphorylation in Retinal Photoreceptor Cells. *Front. Mol. Neurosci.* **12**, 24; 10.3389/fnmol.2019.00024 (2019).
314. Hernández-Ortega, K., García-Esparcia, P., Gil, L., Lucas, J. J. & Ferrer, I. Altered Machinery of Protein Synthesis in Alzheimer's: From the Nucleolus to the Ribosome. *Brain pathology (Zurich, Switzerland)* **26**, 593–605; 10.1111/bpa.12335 (2016).
315. Glasow, A., Prodromou, N., Xu, K., Lindern, M. von & Zelent, A. Retinoids and myelomonocytic growth factors cooperatively activate RARA and induce human myeloid leukemia cell differentiation via MAP kinase pathways. *Blood* **105**, 341–349; 10.1182/blood-2004-03-1074 (2005).
316. Chanput, W., Mes, J., Vreeburg, R. A. M., Savelkoul, H. F. J. & Wichers, H. J. Transcription profiles of LPS-stimulated THP-1 monocytes and macrophages. A tool to study inflammation modulating effects of food-derived compounds. *Food & function* **1**, 254–261; 10.1039/c0fo00113a (2010).
317. Forero, A., Moore, P. S. & Sarkar, S. N. Role of IRF4 in IFN-stimulated gene induction and maintenance of Kaposi sarcoma-associated herpesvirus latency in primary effusion lymphoma cells. *Journal of immunology (Baltimore, Md. : 1950)* **191**, 1476–1485; 10.4049/jimmunol.1202514 (2013).
318. Chen, D.-Y., Yao, L., Chen, Y.-M., Lin, C.-C., Huang, K.-C., Chen, S.-T. & Lan, J.-L. *et al.* A potential role of myeloid DAP12-associating lectin (MDL)-1 in the regulation of inflammation in rheumatoid arthritis patients. *PLoS one* **9**, e86105; 10.1371/journal.pone.0086105 (2014).
319. Ishikawa, M., Sonobe, M., Nakayama, E., Kobayashi, M., Kikuchi, R., Kitamura, J. & Imamura, N. *et al.* Higher Expression of Receptor Tyrosine Kinase Axl, and Differential Expression of its Ligand, Gas6, Predict Poor Survival in Lung Adenocarcinoma Patients. *Annals of Surgical Oncology* **20**, 467–476; 10.1245/s10434-012-2795-3 (2013).
320. Ng, C.-T., Dheen, S. T., Yip, W.-C. G., Ong, C.-N., Bay, B.-H. & Lanry Yung, L.-Y. *et al.* The induction of epigenetic regulation of PROS1 gene in lung fibroblasts by gold nanoparticles and implications for potential lung injury. *Biomaterials* **32**, 7609–7615; 10.1016/j.biomaterials.2011.06.038 (2011).
321. Santer, D. M., Wiedeman, A. E., Teal, T. H., Ghosh, P. & Elkon, K. B. Plasmacytoid dendritic cells and C1q differentially regulate inflammatory gene induction by lupus immune complexes. *Journal of immunology (Baltimore, Md. : 1950)* **188**, 902–915; 10.4049/jimmunol.1102797 (2012).

6 APPENDIX

Supplement 1: List of Primers for MassArray PCR

Displayed are single nucleotide polymorphism with her expected length, mass (Dalton) and the corresponding gene.

SNP_ID	2nd-PCR	1st-PCR	Length	Da	Gene
rs201060968	ACGTTGGATGAGAAAGCGCTTGAGAAGCAG	ACGTTGGATGAGAGACTGACCAGGGCTCTG	119	4320.8	ABCA7
rs121908402	ACGTTGGATGCAAAACATGAGGCCTGGAAC	ACGTTGGATGAGGCTGACACCCTCAGGAAG	118	4433.9	TREM2
rs3745842	ACGTTGGATGTGGACCCAGAGTCCATC	ACGTTGGATGACCAGCTGCAGCCGGCAGT	107	4528.9	ABCA7
rs113809142	ACGTTGGATGTTGCTGTGACAGGACGCCA	ACGTTGGATGCGTGTCTGAAAAACCTCAC	120	4739.1	ABCA7
rs117187003	ACGTTGGATGCATATGCCCTCTGCTGGAAG	ACGTTGGATGTGTAACACTTGGTGCCAGC	87	4948.3	ABCA7
rs2234256	ACGTTGGATGACAGAAGCCAGGGACACATC	ACGTTGGATGCAGAGTTGGAGCTGATACC	93	5108.4	TREM2
rs149622783	ACGTTGGATGTCTCGAAGCTCTCAGACTC	ACGTTGGATGATGGCTGTGCTCCCATAGA	103	5139.4	TREM2
rs199517248	ACGTTGGATGCACCGTCTCCCACTATTCT	ACGTTGGATGAAGAGAGGCCACAGCAATT	82	5315.5	ABCA7
rs142232675	ACGTTGGATGTAATGGTGAGAGTGCCACCC	ACGTTGGATGTGGTACGACGCACAACCTG	119	5524.6	TREM2
rs28937876	ACGTTGGATGTCTCTGGCCTGCATCTTT	ACGTTGGATGATGTGCCCTGGCTTCTGTC	109	5673.7	TREM2
rs200538373	ACGTTGGATGGACACATTGGCCAGCAGGG	ACGTTGGATGACAAGGACGTGAGGGCCAAC	119	5813.8	ABCA7
rs201665195	ACGTTGGATGCGCCTGAGCAACTCAACG	ACGTTGGATGTGCAGCCCCGAGTTTGAG	94	5926.9	ABCA7
rs4147918	ACGTTGGATGAGAAGCTGCAGGAGGTGAG	ACGTTGGATGTTCCGCACCATGTCAATGAG	114	6157.0	ABCA7
rs2234258	ACGTTGGATGAAAAGCCAGGAGAAGTCCC	ACGTTGGATGTCTCTTGGCAGCAGAACA	111	6292.1	TREM2
rs104894001	ACGTTGGATGTGGCATGGGCCCTTCTCTC	ACGTTGGATGTGTCTTGGCCCTATGACTCC	102	6368.1	TREM2
rs3752232	ACGTTGGATGTTTCATGAAGGTGAAGATCCG	ACGTTGGATGAGGTGAACCGGACCTTCGAG	111	6481.2	ABCA7
rs78117248	ACGTTGGATGTAACCTGAACTGACCCC	ACGTTGGATGGACCTAGTGTGGAGGTCAG	103	6489.2	ABCA7
rs2242437	ACGTTGGATGTGGCTCAAGGACACACATGC	ACGTTGGATGTGGTGCCTGGAGAAAATA	100	4496.9	ABCA7
rs201258663	ACGTTGGATGTGATGGCTGTGCTCCCATTC	ACGTTGGATGAGAGAAGGGCCATGCCAG	109	4577.0	TREM2
rs3752246	ACGTTGGATGTGCAGGGTAGGACATGCAG	ACGTTGGATGAACCAACCCCTGAACTCAC	101	4915.2	ABCA7
rs376824416	ACGTTGGATGACAGCAGCGTAGCACTGA	ACGTTGGATGAGAGCCCTGGTCAGTCTCT	89	5002.3	ABCA7
rs79011726	ACGTTGGATGTTAGGAAAGCCATCGCTG	ACGTTGGATGATGCTGGAGATCTCTGGTTC	116	5106.3	TREM2
rs200820365	ACGTTGGATGAAAAGCCAGGAGAAGTCCC	ACGTTGGATGCAGAACAAGGAGTCTGGTG	98	5390.5	TREM2
rs2234253	ACGTTGGATGACTGGTAGAGACCCGCATCA	ACGTTGGATGACAGCCATCACAGACGATAC	105	5530.6	TREM2
rs104894002	ACGTTGGATGCTTCATGGAGTCATAGG	ACGTTGGATGCCCAACACCCACAGTGTTT	97	5895.9	TREM2
rs10948363	ACGTTGGATGAAGTCTAACTTCTTAGGG	ACGTTGGATGCCACAGGTCAATTTTCTAAC	105	6479.2	CD2AP
rs11273989	ACGTTGGATGTTCTCTATAGCAAGCCAAG	ACGTTGGATGTGGCTGATAAACCTTTGGC	103	7978.3	CD33
rs113464261	ACGTTGGATGAGGTTGGTTGGATTCTCTG	ACGTTGGATGTTTGACGCTCCATCTCCCA	118	4857.2	CD33
rs11767557	ACGTTGGATGCCATCTTCTTGTGGCTCC	ACGTTGGATGATGATGTCTTAGGGCATCTC	103	5241.4	EPHA1
rs11771145	ACGTTGGATGACTCGACACCAAGAATGC	ACGTTGGATGAACACCCAGGAGTGATTG	98	6082.0	EPHA1
rs201074739	ACGTTGGATGCTACTAGACTTGACCCACAG	ACGTTGGATGCAGAGCAGGTGAGTTTTTG	102	6360.2	CD33
rs201473304	ACGTTGGATGGGAAATCCTCTCTCTCTCTC	ACGTTGGATGTCTTCTACCTGAGCCATC	102	5756.8	CD33
rs35112940	ACGTTGGATGAAGACCCACAGGAGGAAAGC	ACGTTGGATGAGGATGCCCATCACTCAC	117	4410.9	CD33
rs3764650	ACGTTGGATGAGGCTCTGTTGGGAACCTTC	ACGTTGGATGTGCAGCAGGTGACGTGGAGT	96	6679.4	ABCA7
rs3826656	ACGTTGGATGCAAAATGAGGATGCAGCTAC	ACGTTGGATGCTTCCACCATACTTTGTCT	118	6292.1	CD33
rs386834140	ACGTTGGATGAATGGGACACAGCCATCAC	ACGTTGGATGTCATGGGGTTGTAGATTCCG	97	4875.2	TREM2
rs386834142	ACGTTGGATGATGCTCAAAGTGAAGGAGAG	ACGTTGGATGTCTCCGGCTGCTCATCTTAC	103	5036.3	TREM2
rs4938933	ACGTTGGATGGCAGGACTGGAATAATCTGA	ACGTTGGATGGGCCAGTACCAATTTTGGAG	120	6238.1	MS4A
rs58413603	ACGTTGGATGTCAGGCTCAGTCTTAAATG	ACGTTGGATGTCACTCTTCCCTCAATATC	120	7601.9	CD33
rs58847341	ACGTTGGATGGCAGAAAGGAAACAACCAAC	ACGTTGGATGTCACTTGTGATGAATAGC	107	5863.9	CD33
rs73932888	ACGTTGGATGACTAAGACTTCCCGTATGCC	ACGTTGGATGAAATGTACCACTCTGATGGG	99	6927.5	CD33
rs769449	ACGTTGGATGATCCTCACCTCAACCTCTG	ACGTTGGATGTCAAATCGCTGTTGAGAGCC	115	5067.3	APOE
rs7748513	ACGTTGGATGTCTATCTAAACTGTCAAGC	ACGTTGGATGTGAACTCCCTTAGCCACCTC	108	5434.5	TREM2
rs781150115	ACGTTGGATGTAGCATGTGGCACGTAATAG	ACGTTGGATGCAACAAGCAAGACCTGTCT	93	7079.6	CD33
rs8112072	ACGTTGGATGCTTACTTGGGACTAAGTCTG	ACGTTGGATGCCAGAATAGAAGATACACAG	86	6470.2	CD33
rs9349407	ACGTTGGATGCAGTGAGTGGTGAGCAAATG	ACGTTGGATGGTTAGCTTTAGTGTATGGTG	104	7210.7	CD2AP
rs9381040	ACGTTGGATGAATCTGCAGCTGACTCTGTG	ACGTTGGATGGTACAGGCGATTGACAGTT	119	4490.9	TREML2
rs1354106	ACGTTGGATGTGTCTGGGTCTAAGAAGGTC	ACGTTGGATGACTTAGGGTCAAAGTGGTCT	114	5392.5	CD33
rs138197061	ACGTTGGATGTGAGGTGCAGACGTTTCTTC	ACGTTGGATGACCATATGATCCAGCAACCC	102	6610.3	CD33
rs1399839	ACGTTGGATGAAAGGATCCAGCTGGTAGTG	ACGTTGGATGGACTTGACATAAAGTGCACC	92	5864.8	CD33
rs148284870	ACGTTGGATGTCACTTGTGATGAATAGC	ACGTTGGATGGCAGAAAGGAAACAACCAAC	107	6080.0	CD33
rs1803254	ACGTTGGATGTTTGAAGCAGAGAGTCTGTG	ACGTTGGATGGGTTAAGGAGCTTGTGTGAC	99	5759.8	CD33
rs2234258	ACGTTGGATGCCAGAGCAGAACAAGGAGTC	ACGTTGGATGGGAAAAGCCAGGAGAAGTC	106	5251.4	TREM2
rs2455069	ACGTTGGATGTAGCTTGTGTGGCCACTG	ACGTTGGATGTACTACGACAAGAAGTCCCC	110	4538.0	CD33
rs34813869	ACGTTGGATGAGATGGAGCTGCAAGGCC	ACGTTGGATGAGTAGTGTAGTGCAGCAAGG	115	4824.1	CD33
rs3865444	ACGTTGGATGTTTACACAGGGCTGATCAC	ACGTTGGATGAATCTATATCTGCTGGAC	109	6894.5	CD33
rs386834141	ACGTTGGATGTGGAGGCTCTGGCACTGGTA	ACGTTGGATGACAGCATCACAGACGATAC	118	5195.4	TREM2
rs56662071	ACGTTGGATGTGGCTGATAAAACCTTTGGC	ACGTTGGATGTTCTCTATAGCAAGCCAAG	103	7043.6	CD33
rs610932	ACGTTGGATGCCAGAAACAAGGCAGAATG	ACGTTGGATGTGCTTCACTGTGATCCATTG	120	6398.2	MS4A6A
rs75932628	ACGTTGGATGACAAGTTGTGCGTGTGACC	ACGTTGGATGCCTATGACTCCATGAAGCAC	119	6184.0	TREM2
rs778496474	ACGTTGGATGACTTCCCCTCTATTGTCTT	ACGTTGGATGGCCATACACAAAGAAGAAAG	120	4645.0	CD33

Supplement 2: List of Extension Primers for MassArray PCR

Displayed are the sequence (EXT1_SEQ, EXT2_SEQ) of the extension primer with the corresponding mass (EXT1_Da, EXT2_Da) for the analyzed SNPs. EXT_1 and EXT_2 represent the possible variations of the SNP.

SNP_ID	EXT_1	EXT1_Da	EXT1_SEQ	EXT_2	EXT2_Da	EXT2_SEQ
rs201060968	G	4568.0	GGCGGGTCAGTGCCC	A	4647.9	GGCGGGTCAGTGCCCT
rs121908402	C	4681.1	CCTGCCAGCACCTCCC	A	4705.1	CCTGCCAGCACCTCCA
rs3745842	A	4800.2	CCTGCCAGGTAGCCA	G	4816.2	CCTGCCAGGTAGCCG
rs113809142	G	4986.3	GGCCCCCAGTTCCCC	T	5010.3	GGCCCCCAGTTCCCA
rs117187003	G	5195.4	GCCAGAAAGATGAGCAC	A	5275.3	GCCAGAAAGATGAGCAT
rs2234256	G	5355.5	ACATCCACCAGTGAACC	A	5435.4	ACATCCACCAGTGAACCT
rs149622783	C	5386.5	AGAGATCTCCAGCATCCC	T	5466.5	AGAGATCTCCAGCATCCT
rs199517248	A	5586.7	GCCACCTATTCTCCCCAA	G	5602.7	GCCACCTATTCTCCCCAG
rs142232675	C	5771.8	GAGTGCCACCAGGGTATC	T	5851.7	GAGTGCCACCAGGGTATT
rs28937876	C	5960.9	CCTGCATCTTTCTCATCAAG	A	6000.8	CCTGCATCTTTCTCATCAAT
rs200538373	C	6061.0	CCTTGACGGCCACAGGTGAC	G	6101.0	CCTTGACGGCCACAGGTGAG
rs201665195	G	6214.1	CCCCAACTTCAACGACTCCCG	T	6254.0	CCCCAACTTCAACGACTCCCT
rs4147918	A	6428.2	TGTGAGCCGGATCTTGAAACA	G	6444.2	TGTGAGCCGGATCTTGAAACG
rs2234258	T	6563.3	CATCCTGCATACTTGCCACTTA	C	6579.3	CATCCTGCATACTTGCCACTTG
rs104894001	C	6615.3	GGAACAGGCCTTGCGCTCCCC	T	6695.2	GGAACAGGCCTTGCGCTCCCT
rs3752232	G	6728.4	GGAGGACATCCCTCAGCAGGGC	A	6808.3	GGAGGACATCCCTCAGCAGGGT
rs78117248	A	6760.4	GAGGTCTGAGCCAGAGACAAA	G	6776.4	GAGGTCTGAGCCAGAGACAAAG
rs2242437	G	4744.1	CACACGGTTTACCAC	C	4784.2	CACACGGTTTACCAG
rs201258663	A	4848.2	AGCCACAAGTTGTGCA	G	4864.2	AGCCACAAGTTGTGCG
rs3752246	G	5162.4	AGGGACTCACAGTGAC	T	5186.4	AGGGACTCACAGTGCAA
rs376824416	C	5249.4	GCCCTCTATCCCTCACC	A	5273.5	GCCCTCTATCCCTCACA
rs79011726	C	5353.5	CTCCACATGGGCATCCTC	T	5433.4	CTCCACATGGGCATCCTT
rs200820365	T	5661.7	CCCGTCCCACCAGGGACCA	A	5717.6	CCCGTCCCACCAGGGACCT
rs2234253	C	5777.8	GGTTGTAGATTCGCGAGCC	A	5801.8	GGTTGTAGATTCGCGAGCA
rs104894002	A	6167.1	GAAGAGGGGCAAGACACCTA	G	6183.1	GAAGAGGGGCAAGACACCTG
rs10948363	A	6750.4	GGGAACTTCTTAGGGCAAAAACA	G	6766.4	GGGAACTTCTTAGGGCAAAAACG
rs11273989	INS	8225.4	AAAGAATGAACATAACATAATTTTAC	DEL	8249.5	AAAGAATGAACATAACATAATTTTAA
rs113464261	C	5104.4	CCTGTCTCTGGGACAA	A	5128.4	CCTGTCTCTGGGACAAA
rs11767557	C	5488.6	TTCGATGCTGGGCAGTAC	T	5568.5	TTCGATGCTGGGCAGTAT
rs11771145	G	6329.2	CATATCAGATGATTCGGTTTT	A	6409.1	CATATCAGATGATTCGGTTTT
rs201074739	DEL	6631.4	AGCACTGGCACTCTAGAACC	INS	6647.4	AGCACTGGCACTCTAGAACC
rs201473304	INS	6004.0	CTAGATGTTCCACAGAACC	DEL	6028.0	CTAGATGTTCCACAGAACC
rs35112940	A	4682.1	ACCCACCTACCACAA	G	4698.1	ACCCACCTACCACAG
rs3764650	G	6966.6	AACATGCTGCGAACTTTGCACCG	T	7006.5	AACATGCTGCGAACTTTGCACCT
rs3826656	A	6563.3	CCTGCAGCTACCTCTCTATTAA	G	6579.3	CCTGCAGCTACCTCTCTATTAG
rs386834140	C	5162.4	ACAGACGATACCTGGG	DEL	5202.3	ACAGACGATACCTGGT
rs386834142	INS	5283.5	AGGGCACGGAGGGGATC	DEL	5307.5	AGGGCACGGAGGGGATA
rs4938933	T	6509.3	ATGGAAAAATCTGAGGAGTAA	C	6525.3	ATGGAAAAATCTGAGGAGTAG
rs58413603	INS	7873.2	CCGGATCAGTCTTAAATGTACCCCGA	DEL	7929.0	CCGGATCAGTCTTAAATGTACCCCGT
rs58847341	INS	6135.1	ACAGAGTGAAAAGGCAACCA	DEL	6190.9	ACAGAGTGAAAAGGCAACCT
rs73932888	C	7174.7	ATGACCTTACCCTTACACATAGC	T	7254.6	ATGACCTTACCCTTACACATAGT
rs769449	A	5338.5	CCCCTGGCCCCATTGACA	G	5354.5	CCCCTGGCCCCATTGACG
rs7748513	A	5705.8	CACGTCAAGCTGTCTACA	G	5721.8	CACGTCAAGCTGTCTACG
rs781150115	INS	7350.9	TGGCACGTAATAGAAAATTCATA	DEL	7406.7	TGGCACGTAATAGAAAATTCAACT
rs8112072	G	6717.4	GGACTAAGTCTGAGTCAGTCAC	A	6797.3	GGACTAAGTCTGAGTCAGTCAT
rs9349407	G	7457.9	GGAGAAAATGTGAAGGCTAGGAC	C	7497.9	GGAGAAAATGTGAAGGCTAGGAG
rs9381040	T	4762.2	AACCTGCAGCACCACA	C	4778.2	AACCTGCAGCACCACG
rs1354106	G	5679.7	CTGCTTCCAGGCCCTTTT	T	5719.6	CTGCTTCCAGGCCCTTTTT
rs138197061	DEL	6857.5	TCAATATACTGATTTCCCTTTCCC	INS	6937.4	TCAATATACTGATTTCCCTTTCCCT
rs1399839	C	6112.0	GTTAGATTGACTGGTTTGCC	A	6136.0	GTTAGATTGACTGGTTTGCA
rs148284870	DEL	6327.1	TTCTCTATTCTGTAGGTTGC	INS	6367.2	TTCTCTATTCTGTAGGTTGG
rs1803254	C	6006.9	GTGCTTTTCATTTGCTAAC	G	6047.0	GTGCTTTTCATTTGCTAAG
rs2234258	C	5498.6	CAAGGAGTCTGGTGGCC	T	5578.5	CAAGGAGTCTGGTGGCT
rs2455069	G	4785.1	CCACTGGAGAGTCCCC	A	4865.1	CCACTGGAGAGTCCCT
rs34813869	A	5095.3	GCCTCTGGGTTTCCAA	G	5111.3	GCCTCTGGGTTTCCAG
rs3865444	C	7181.7	TTCTCAGCCTCACCTAGATCCATG	A	7221.6	TTCTCAGCCTCACCTAGATCCATT
rs386834141	C	5442.6	TCACTGGTAGAGACCCGC	DEL	5466.6	TCACTGGTAGAGACCCGA
rs56662071	INS	7330.8	GGCTACCTTTTTAAAATATTGTGG	DEL	7370.7	GGCTACCTTTTTAAAATATTGTGT
rs610932	G	6645.4	TTTTCCAGAAAACCTAGACAGC	T	6669.4	TTTTCCAGAAAACCTAGACAGA
rs75932628	C	6431.2	GAGGGCGGCACCAGGCTTGC	A	6455.2	GAGGGCGGCACCAGGCTTGA
rs778496474	INS	4932.2	TTGTGGTTGGCTGATG	DEL	4972.1	TTGTGGTTGGCTGATT

Supplement 3: List of primers for standard PCR and qRT PCR

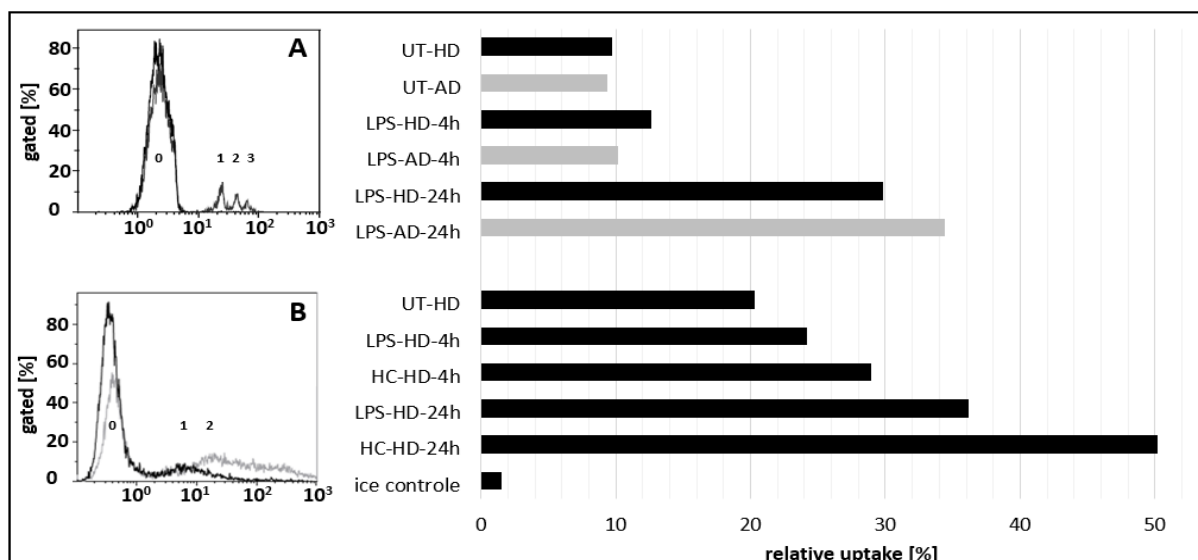
Gene & alias	Forward	Reverse	Comments
B2M	TGACTTTGTCACAGCCCAAGATA	AATCCAAATGCGGCATCTTC	PCR ³¹⁵
CD14	GCTGGACGATGAAGATTTCC	ATTGTGACAGAGGTCTAGGC	PCR, QPCR ³¹⁶
CD33	GCTGTGGGACAGGGCCCT	TGGCTCCTCCCGGAACAGT	PCR
CD33	ATTATGCCGCTGCTGACTGCT	ATTTCACTGGGCTCTGACCTCTG	QPCR ³¹⁶
CD68	TGACACCCACGGTTACAGAG	CGTCTCCGGATGATGCAGAA	PCR
GAS6	CAGGACCTGCCAAGACATAGAC	CAGAGAATTGTCTGCCACATGCC	PCR
IBA1	CTCCAGCTTGAGGAAAAGC	TCTTTGCCAGCATCATCC	PCR
IL1 β	GTGGCAATGAGGATGACTTGTTT	TAGTGGTGGTGGGAGATTCGTA	PCR, QPCR ³¹⁶
IL6	AGCCACTCACCTTTCAGAAC	GCCTTTTGTCTGTTTCACAC	PCR, QPCR ³¹⁶
IL8	CTGATTTCTGCAGCTCTGTG	GGGTGGAAGGTTTGGAGTATG	PCR, QPCR ³¹⁶
IL10	GTGATGCCCCAAGCTGAGA	CACGGCCTTGTCTTGTGTTT	PCR, QPCR ³¹⁶
GAPDH	CAAGGTCATCCATGACAACCTTG	GTCACCACCCTGTGCTGTAG	PCR
PROS1	CAGAGGCAAACCTTTTGTCAAAGC	GGGATGTTCTTGACACAGC	PCR
RPL32	CAACATTGGTTATGGAAGCAACA	TGACGTTGGTGGACCAGGAAC	PCR ³¹⁷
SPI1, PU.1	GCGACCATTACTGGGACTTCC	GGGTATCGAGGACGTGCAT	PCR ³¹⁸
TNF α	CTGCTCACTTTGGAGTGAT	AGATGATCTGACTGCCTGGG	PCR, QPCR ³¹⁶
TREM2	CCTGGTTTCTCCCATTTCC	AGGAGAAGCAGTGTTCAGGC	PCR
TYROBP, DAP12	AGCGATTGCAAGTTGCTCTAC	GTGATACGCTGTTCCGGGT	PCR ³¹²
GAS6	ACATCTTGCCGTGCGTGCCCTTCA	ATTCGCGCCAGCTCTCAACAGA	QPCR ³¹⁹
Pros1	CCTAGTGCTTCCCGTCTCAG	TTCCGGGTCATTTTCAAAG	QPCR ³²⁰
MERTK	GGGTCCAGAACCATGAGATG	GCAGCCTCAATACTGAAAAGG	QPCR ³²¹
C1QA	ACAGGAGGCAGAGGCATCA	CACAAGTCCTCGGTACCAT	QPCR
PTEN	GGACCAGAGACAAAAGGGAGTA	TCGTGTGGGCTCTGAATTGG	QPCR
PAX6	ACCCATTATCCAGATGTGTTTCCCGAG	ATGGTGAAGCTGGGCATAGGCGGCAG	PCR
MSI1	AGGAGTGCTGGTGATGCG	GCGGAGGCTGTATAACTCC	PCR
SHH	CGAAGATGGCCACCACTCAG	GCTTTCACCGAGCAGTGGAT	PCR
TBXT	AATTGGTCCAGCCTTGAAT	TACTGGCTGTCCACGATGTC	PCR
PRRX1	GACCATGACCTCCAGCTACG	GAGCAGGACGAGGTACGATG	PCR
MEOX1	GCAGCGTACCCTGACTTCTC	CGGTTCTGGAACCACTTT	PCR
CXCR4	GCCTGTTGGCTGCCTTACTA	CAGGAAAAACGTTCCACGGG	PCR
FOXA2	TGGGAGCGGTGAAGATGGAAGGCAC	TCATGCCAGCGCCACGTACGACGAC	PCR
SOX17	TAGTTGGGGTGGTCTGCAT	CGCTTTCATGGTGTGGGCTA	PCR

Supplement 4: List of antibodies for immunofluorescence analysis

Name	Host	Target cell type	Dilution	Supplier, catalog number	
primary antibody					
CD68	mouse	microglia, macrophages, monocytes	1:1000	Bio-Techne, NBP2-37265	
SPI1, PU.1	rabbit	microglia, macrophages, monocytes	1:500	BioCat, AP14850b-ev-AB	
TUBB3	mouse	neurons	1:1000	Merk, MAB1637	
AIF1, Iba1	goat	microglia, macrophages, monocytes	1:200	Bio-Techne, NB100-1028	
PTPRC, CD45	rat	microglia, macrophages, monocytes	1:500	Bio-Techne, NB100-77417	
ITGAM, CD11b	rat	microglia, macrophages, monocytes	1:500	Bio-Techne, NB600-1327	
CD33	mouse	microglia, macrophages, monocytes	1:500	BioCat, AM2149b-AB	
TREM2	goat	microglia, macrophages, monocytes	1:1000	Bio-Techne, AF1828-SP	
secondary antibody					
Target	Host	Conjugate	Isotype	Dilution	Supplier, catalog number
goat	donkey	Alexa Fluor 488	IgG	1:400	ThermoFisher Scientific, A11055
goat	rabbit	Cy3	IgG	1:400	Jackson Immuno Research, 305-165-003
mouse	goat	Alexa Fluor 488	IgG	1:400	ThermoFisher Scientific, A11001
mouse	rabbit	FITC	IgG	1:400	Jackson Immuno Research, 315-095-003
rat	rabbit	Alexa Fluor 488	IgG	1:400	ThermoFisher Scientific, A21210
rabbit	goat	Cy3	IgG	1:400	Jackson Immuno Research, 111-165-003
rabbit	goat	Alexa Fluor 488	IgG	1:400	ThermoFisher Scientific, A11034
rat	donkey	Cy3	IgG	1:400	Jackson Immuno Research, 712-165-153

Supplement 5: List of antibodies for flow cytometry analysis

Name	Host	Conjugate	Isotype	Supplier, catalog number
CD11b	mouse	FITC	IgG1	Beckman coulter, IM0530
CD11c	mouse	FITC	IgG1	Biolegend, 337215
CD33	mouse	PECy7	IgG1	Biolegend, 366618
CD45	mouse	PECy7	IgG1	Biolegend, 304006
CD14	mouse	FITC	IgG2	Beckman coulter, im0645
CD40	mouse	PerCP-1Flour™710	IgG1	ThermoFischer, 46-0409-42



Supplement 6: Phagocytosis assay

MGLCs differentiated from two different donors (HD: healthy controls; AD: LOAD patients) were stimulated with both LPS and hydrocortisone (HC) and incubated with fluorescent latex beads (cell bead ratio 1:100). Flow cytometry was used to count latex beads. Differentiated MGLCs were analyzed according to LPS or HC stimulation or measured untreated (UT). The numbers 0 to 3 mark the gates with the corresponding number of phagocytized beads. Gate 0 shows cells that do not internalize any beads per cell. In gate 1, one bead per cell was internalized. In gate 2, two beads per cell were internalized. In gate 3, three beads per cell were internalized. (A) Displayed is a representative data set for the relative uptake of beads into MGLCs from one out of $n = 3$ experiments. After a stimulation of 4 h and 24 h with 100 $\mu\text{g}/\text{ml}$ LPS at 37°C, the cells were incubated with fluorescent microspheres for phagocytosis. Unstimulated approaches were incubated in parallel. Flow cytometry was used to count fluorescent microspheres. Shown are the percentages of cells that engulfed fluorescence-labelled beads. (B) Displayed is a representative data set for receptor depend internalized particles into MGLCs from one out of $n = 2$ experiments. After a stimulation of 4 h and 24 h with 100 $\mu\text{g}/\text{ml}$ LPS or 3.0 μM HC at 37°C or on ice, the cells were incubated with *Escherichia coli* K-12 strain BioParticles™ conjugated with Alexa Fluor™ 488 for phagocytosis. Unstimulated approaches were incubated in parallel. Flow cytometry was used to count Alexa Fluor 488 conjugated *E. coli* particles. Shown are the percentages of cells that engulfed fluorescence-labelled particles. Analyzed samples are shown in black; unquenched control is shown in gray line. The numbers 0 to 3 mark the gates with the corresponding number of phagocytized particles. Gate 0 shows cells that do not internalize any particles per cell. In gate 1, one particle per cell was internalized. In gate 2, two particles per cell were internalized. In gate 3, three particles per cell were internalized. **Abbreviations:** LPS, lipopolysaccharides; HC, hydrocortisone; UT, untreated; AD, Alzheimer's disease; HD, healthy controls.

Supplement 7: Statistical telomere analysis

1way ANOVA multiple comparison test was done with GraphPad, Prism version 7.1.

Turkey's multiple comparison test	Mean Diff	95% CI of diff	Significant	Summary	p-value
WAI001-B vs. MLUi009-A	9	3,98 to 14,02	Yes	***	0,0007
WAI001-B vs. WAI004-B	1	-4,02 to 6,02	No	ns.	0,9822
WAI001-B vs. MLUi010-B	12	6,98 to 17,02	Yes	****	<0,0001
WAI001-B vs. MLUi008-B	94	88,98 to 99,02	Yes	****	<0,0001
WAI001-B vs. MLUi007-H	77	71,98 to 82,02	Yes	****	<0,0001
WAI004-B vs. MLUi009-A	8	2,98 to 13,02	Yes	**	0,0018
WAI004-B vs. MLUi010-B	11	5,98 to 16,02	Yes	****	<0,0001
WAI004-B vs. MLUi008-B	93	87,98 to 98,02	Yes	****	<0,0001
WAI004-B vs. MLUi007-H	76	70,98 to 81,02	Yes	****	<0,0001
MLUi009-A vs. MLUi010-B	3	-2,02 to 8,02	No	ns	0,3918
MLUi009-A vs. MLUi008-B	85	79,98 to 90,02	Yes	****	<0,0001
MLUi009-A vs. MLUi007-H	68	62,98 to 73,02	Yes	****	<0,0001
MLUi010-B vs. MLUi008-B	82	76,98 to 87,02	Yes	****	<0,0001
MLUi010-B vs. MLUi007-H	65	59,98 to 70,02	Yes	****	<0,0001
MLUi008-B vs. MLUi007-H	-17	-22,02 to -11,98	Yes	****	<0,0001

Supplement 8: Summary statistic

Shown are significantly regulated proteins and the fold change of protein expression between LOAD MGLCs / healthy control MGLCs and reference MGLCs. AD association and scores were determined online (<https://www.genecards.org/Search/Keyword?startPage=0&queryString=alzheimer&pageSize=-1>).

log2 p-value	fold change	Protein ID	Gene names	AD Score	log2 p-value	fold change	Protein ID	Gene names	AD Score
significantly changed proteins in LOAD which were exclusively analysed comparatively in old CONS					significantly changed proteins in LOAD which were analysed both in comparison to young references and old CONS				
2.239	5.349	P47914	RPL29	0.13	2.341	6.486	P05121	SERPINE1	3.69
2.031	4.237	Q06323	PSME1	0.49	3.639	4.987	O00622	CYR61	-
2.658	4.155	Q9NPH2	ISYNA1	0.63	2.218	4.887	P49888	SULT1E1	-
2.738	3.89	P11137	MAP2	17.39	1.774	4.474	P11166	SLC2A1	0.18
1.332	3.516	P21589	NT5E	0.76	1.855	4.436	Q03135	CAV1	2.45
1.528	3.511	Q76M96	CCDC80	-	4.216	4.262	P07196	NEFL	16.61
1.382	3.392	Q96K17	BTF3L4	-	1.943	4.258	P16070	CD44	1.2

2.064	3.29	O14773	TPP1	0.13	1.504	4.115	O75368	SH3BGRL	-
1.382	3.243	O00592	PODXL	1.83	1.748	4.106	Q14126	DSG2	0.63
3.38	3.217	P21291	CSRP1	0.55	2.122	4.104	P35613	BSG	2.65
1.378	3.127	Q02880	TOP2B	-	2.307	4.08	O95084	PRSS23	0.49
3.278	3.12	P00492	HPRT1	1.42	2.365	3.987	P15924	DSP	-
1.415	3.095	Q08431	MFGE8	1.38	2.658	3.943	Q08257	CRYZ	-
1.311	3.052	O94919	ENDOD1	-	4.231	3.936	Q5T7N3	KANK4	-
1.476	2.999	P41567	EIF1	0.49	1.668	3.896	Q9NR99	MXRA5	-
1.311	2.906	O14737	PDCD5	-	2.241	3.79	P32455	GBP1	-
3.674	2.696	P18615	NELFE	-	1.467	3.663	Q9H3Q1	CDC42EP4	0.49
2.18	2.674	P61619	SEC61A1	-	2.362	3.65	Q96RW7	HMCN1	0.76
1.848	2.617	Q13228	SELENBP1	1.83	1.315	3.627	P11169	SLC2A3	-
2.587	2.586	Q13576	IQGAP2	0.63	3.199	3.492	O00470	MEIS1	0.13
2.928	2.516	Q6UB35	MTHFD1L	2.88	1.497	3.491	Q15059	BRD3	0.49
1.835	2.487	O43765	SGTA	-	1.666	3.395	Q7Z434	MAVS	-
2.201	2.457	Q9UUK9	NUDT5	-	1.33	3.37	Q16822	PCK2	0.49
1.371	2.444	P54821	PRRX1	-	3.04	3.342	Q13442	PDAP1	0.49
1.408	2.411	Q6KF10	GDF6	-	2.806	3.304	Q01581	HMGCS1	-
2.11	2.411	O60784	TOM1	1.23	3.435	3.15	P13796	LCP1	-
1.512	2.402	Q9COC2	TNKS1BP1	-	2.109	3.114	Q9Y3E5	PTRH2	-
2.734	2.399	Q9UEY8	ADD3	1.05	1.524	3.106	P27144	AK4	0.49
1.733	2.386	P08253	MMMP2	2.9	3.146	3.104	Q9H425	C1oldrf198	-
1.399	2.379	P02511	CRYAB	3.77	1.645	3.092	Q5KU26	COLEC12	5.83
1.555	2.368	O00170	AIP	-	1.466	3.081	Q9Y570	PPME1	0.39
1.841	2.361	P63165	SUMO1	1.4	2.523	3.022	P14324	FDP5	0.99
1.561	2.345	Q99873	PRMT1	-	2.441	2.958	P49790	NUP153	-
1.767	2.344	Q9P2K5	MYEF2	-	1.443	2.868	Q9UL46	PSME2	0.49
1.683	2.307	Q13330	MTA1	-	3.218	2.865	Q9P0I2	EMC3	-
2.127	2.282	P09619	PDGFRB	3.32	1.377	2.858	P78347	GTF2I	-
1.435	2.256	P46926	GNPDA1	-	1.641	2.845	Q96A83	COL26A1	-
1.712	2.253	P13497	BMP1	-	5.124	2.834	P13798	APEH	0.28
1.333	2.233	Q92785	DPF2	-	2.967	2.831	P06493	CDK1	1.23
1.604	2.232	P17302	GJA1	0.39	2.022	2.823	Q8WXX5	DNAJC9	-
1.661	2.227	P05114	HMGNI	-	1.576	2.734	Q9Y394	DHRS7	-
1.462	2.199	P40123	CAP2	-	1.522	2.691	Q70UQ0	IKBIP	0.49
1.441	2.183	Q13153	PAK1	1.38	2.129	2.689	Q92896	GLG1	-
1.606	2.175	P00352	ALDH1A1	0.13	2.723	2.66	Q9BPU6	DPYSL5	-
2.993	2.145	Q10471	GALNT2	1.03	2.238	2.658	Q14683	SMC1A	0.13
1.709	2.145	Q96KP1	EXOC2	-	1.73	2.641	O94925	GLS	2.77
1.409	2.132	Q13564	NAE1	16.31	1.605	2.593	P48739	PITPNB	-
1.615	2.121	O43395	PRPF3	-	1.419	2.534	O43602	DCX	0.49
1.625	2.103	P02649	APOE	98.01	3.27	2.522	P13797	PLS3	0.49
1.617	2.034	Q8WUP2	FBLIM1	-	1.686	2.477	Q69YQ0	SPECC1L	-
1.936	2.013	Q9H9Z2	LIN28A	-	2.224	2.464	Q9UKD2	MRTO4	0.63
2.305	2.013	Q96CT7	CCDC124	-	1.426	2.439	P16949	STMN1	1.88
1.825	1.965	Q8IWS0	PHF6	-	1.955	2.412	Q9NZN4	EHD2	0.63
1.356	1.962	Q14517	FAT1	0.63	2.041	2.298	O00541	PES1	0.13
1.321	1.938	O43491	EPB41L2	0.66	1.879	2.284	A1X283	SH3PXD2B	-
1.714	1.934	Q13451	FKBP5	1.29	2.16	2.232	Q96I25	RBM17	1.05
1.745	1.931	Q96KG9	SCYL1	0.49	1.735	2.224	O60828	PQBP1	0.49
3.81	1.929	P05026	ATP1B1	0.18	2.386	2.22	P23511	NFYA	1.12
1.651	1.903	Q9NRR5	UBQLN4	0.13	1.402	2.213	P08579	SNRPB2	-
2.005	1.898	Q9Y241	HIGD1A	0.13	2.339	2.205	Q13277	STX3	0.18
1.524	1.883	Q4L180	FILIP1L	-	2.504	2.204	Q96CM8	ACSF2	-
1.862	1.88	P30876	POLR2B	-	1.701	2.202	Q9UM54	MYO6	-
1.752	1.878	P49321	NASP	0.13	2.479	2.183	O43768	ENSA	-
1.512	1.859	P52594	AGFG1	0.52	1.685	2.129	P05783	KRT18	0.18
1.987	1.844	P09382	LGALS1	-	2.922	2.125	P11171	EPB41	-
1.399	1.833	O60885	BRD4	-	1.384	2.108	Q9H2P0	ADNP	2.59
1.522	1.819	Q96AC1	FERMT2	2.59	2.618	2.088	Q13217	DNAJC3	-
2.421	1.781	P12694	BCKDHA	-	1.896	2.035	O43837	IDH3B	-
2.422	1.72	P20908	COL5A1	-	1.802	2.029	O75431	MTX2	-
1.469	1.699	P61086	UBE2K	1.12	2.088	2.016	O60341	KDM1A	0.56
1.326	1.688	Q9Y2S7	PoldIP2	0.52	1.345	2.002	Q92530	PSMF1	-
1.716	1.688	P04080	CSTB	3.01	2.04	1.919	Q5TON5	FNBP1L	-
1.515	1.672	Q9H9Q2	COPS7B	0.49	1.661	1.891	P30086	PEBP1	2.57
2.234	1.669	Q9NPO8	RIC8A	0.63	1.619	1.871	Q92522	H1FX	-
2.283	1.645	O15347	HMGB3	-	4.835	1.868	P43304	GPD2	-
1.676	1.631	Q9UMY4	SNX12	0.39	1.473	1.861	P35249	RFC4	-
1.54	1.623	P09110	ACAA1	-	1.529	1.841	Q15631	TSN	-
1.664	1.617	P61964	WDR5	0.52	2.251	1.798	Q15006	EMC2	-
1.482	1.615	Q9P032	NDUFAF4	-	1.433	1.775	O15294	OGT	15.55

2.6	1.61	Q02952	AKAP12	0.63	2.054	1.775	Q7Z3K3	POGZ	0.49
1.401	1.598	P55081	MFAP1	-	2.294	1.759	O60216	RAD21	-
2.166	1.597	Q9H910	HN1L	-	1.752	1.742	P16403	HIST1H1C	4.05
1.411	1.592	Q13637	RAB32	-	2.338	1.733	Q8IXM2	BAP18	-
1.446	1.591	Q8NEY1	NAV1	0.49	2.11	1.723	P21810	BGN	0.99
2.569	1.587	P56182	RRP1	0.99	1.441	1.708	Q9UII2	ATPIF1	-
1.498	1.544	Q99497	PARK7	8.43	1.876	1.687	Q8TD19	NEK9	-
1.428	1.542	P06744	GPI	0.6	2.23	1.68	Q13618	CUL3	0.55
1.491	1.541	Q9BY32	ITPA	-	1.706	1.674	P02545	LMNA	2.87
1.799	1.528	Q5T5P2	KIAA1217	-	1.925	1.667	Q9NR30	DDX21	1.05
1.306	1.527	Q15397	KIAA0020	-	1.461	1.649	P09429	HMGB1	-
1.891	1.51	Q9Y4G6	TLN2	1.72	1.923	1.635	O43488	AKR7A2	0.39
1.767	1.422	O00469	PLOD2	-	1.816	1.626	P26583	HMGB2	0.63
1.314	1.405	Q9BRJ6	C7oldrf50	0.52	1.396	1.615	P52434	POLR2H	-
1.405	1.396	Q9HB40	SCPEP1	-	1.452	1.608	Q15165	PON2	3.25
1.543	1.387	Q9UGV2	NDRG3	0.13	2.326	1.551	A5YKK6	CNOT1	-
1.368	1.378	Q9C0B1	FTO	1.48	2.401	1.536	Q8N5M9	JAGN1	0.49
2.398	1.377	Q16576	RBBP7	-	1.642	1.53	Q14839	CHD4	0.13
2.127	1.374	P11117	ACP2	0.63	1.662	1.524	Q9UHQ9	CYB5R1	-
1.523	1.369	P62942	FKBP1A	1.51	2.309	1.475	Q13867	BLMH	16.22
1.321	1.359	Q96QD9	FYTDD1	-	2.07	1.469	P16401	HIST1H1B	1.56
3.13	1.358	Q00688	FKBP3	-	1.614	1.461	P32119	PRDX2	3.43
1.979	1.35	Q13573	SNW1	-	1.927	1.45	P35611	ADD1	-
1.618	1.346	P29536	LMOD1	-	1.517	1.41	O95347	SMC2	-
1.882	1.34	O75347	TBCA	-	1.445	1.377	Q9UJU6	DBNL	-
2.055	1.339	Q9BV38	WDR18	0.63	2.154	1.375	P42166	TMPO	-
1.471	1.321	P62937	PPIA	0.52	1.769	1.364	Q9UHV9	PFND2	-
1.751	1.318	P09960	LTA4H	-	2.4	1.337	Q8IWU6	SULF1	1.23
1.375	1.311	P68036	UBE2L3	1.2	2.229	1.326	Q9HD42	CHMP1A	-
1.421	1.304	Q9P258	RCC2	-	1.781	1.251	P04181	OAT	-
1.853	1.291	Q969G3	SMARCE1	-	1.424	1.245	P51610	HCFC1	-
2.676	1.247	P61088	UBE2N	-	1.4	1.229	O75506	HSBP1	-
1.895	1.241	O76024	WFS1	0.27	1.454	1.228	P84157	MXRA7	-
1.396	1.235	P40925	MDH1	1.12	2.338	1.208	P46087	NOP2	-
1.77	1.204	P60174	TPI1	2.28	1.993	1.166	Q16555	DPYSL2	19.34
1.502	1.193	Q13526	PIN1	24.63	1.983	1.165	P52209	PGD	1.23
1.5	1.189	Q92692	PVRL2	-	1.876	1.163	P58876	HIST1H2BD	-
1.523	1.189	P48723	HSPA13	0.13	1.85	1.16	P09874	PARP1	2.77
1.897	1.185	Q92541	RTF1	0.52	1.416	1.154	Q13586	STIM1	1.41
1.779	1.155	Q0ZGT2	NEXN	-	1.687	1.129	Q93050	ATP6VOA1	-
1.492	1.153	Q15056	EIF4H	-	1.95	1.105	Q99496	RNF2	0.13
1.964	1.134	Q86VP6	CAND1	1.15	1.825	1.08	P61106	RAB14	0.49
1.306	1.124	Q13162	PRDX4	0.49	1.325	1.073	Q13045	FLII	-
1.496	1.124	P07195	LDHB	0.99	1.907	1.059	Q00765	REEP5	-
1.839	1.122	P22307	SCP2	-	1.99	1.055	Q14315	FLNC	-
2.175	1.113	Q92621	NUP205	-	2.635	1.05	Q93077	HIST1H2AC	-
1.667	1.104	P23528	CFS1	2.09	1.516	1.042	Q9NVJ2	ARL8B	0.49
1.759	1.1	O15212	PFND6	-	2.003	1.036	Q8IUD2	ERC1	0.49
1.598	1.097	Q969H8	MYDGF	-	2.352	1.016	P62805	HIST1H4A	-
1.855	1.094	Q9Y673	ALG5	-	1.569	1	Q07021	C1QBP	0.73
1.654	1.086	P06733	ENO1	3.64	2.341	6.486	P05121	SERPINE1	3.69
1.442	1.078	Q7Z739	YTHDF3	-					
2.22	1.071	Q15155	NOMO1	-					
1.336	1.069	Q14690	PDCD11	-					
1.501	1.069	P31150	GDI1	1.41					
2.306	1.057	P00387	CYB5R3	-					
1.424	1.051	O14656	TOR1A	-					
2.121	1.051	P07305	H1FO	0.49					
1.497	1.046	O60664	PLIN3	0.49					
2.048	1.043	P82979	SARNP	0.63					
1.803	1.04	Q14011	CIRBP	1.38					
1.878	1.029	O95777	LSM8	-					
1.384	1.027	Q71UI9	H2AFV	-					
1.436	1.021	Q92922	SMARCC1	-					
1.373	1.019	Q96E15	TCEAL4	-					
1.512	1.018	P23142	FBLN1	1.05					
2.082	1.013	Q01995	TAGLN	0.49					
1.83	1.009	Q9HDC9	APMAP	0.39					

Supplement 9: TREM2 SNP list

The table shows LOAD-associated SNPs in TREM2 with susceptible locus and associated risk alleles for LOAD iPSCs (MLUi007-H, MLUi008-B; in red), healthy control iPSCs (MLUi009-A, MLUi010-B; in green) and reference iPSCs (WAI001-B, WAI004-B; in grey).

SNP	A1/A2	Frequency A2	Gene	AA Change	WAI001-B	WAI004-B	MLUi010-B	MLUi009-A	MLUi008-B	MLUi007-H
rs104894001	C/A	n.d	TREM2	W44X	C	C	C	C	C	C
rs121908402	A/G	0.00001	TREM2	V126G	A	A	A	A	A	A
rs142232675	C/T	0.1	TREM2	D87N	C	C	C	C	C	C
rs149622783	C/T	0,01	TREM2	R136Q	C	C	C	C	C	C
rs2234256	A/G	0.81	TREM2	L211P	A	A	A	A	A	A
rs2234258	C/T	0.012	TREM2	W191X	C	C	C	C	C	C
rs28937876	C/A	n.d	TREM2	K186N	C	C	C	C	C	C
rs104894002	G/A	0.01	TREM2	Q33X	G	G	G	G	G	G
rs200820365	T/A	0.61	TREM2	E151K	T	T	T	T	T	T
rs79011726	C/T	0.16	TREM2	E151K	C	C	C	C	C	C
rs201258663	G/A	0.01	TREM2	T66M	G	G	G	G	G	G
rs75932628	C/T	0.002	TREM2	R47H	n.d	n.d	n.d	n.d	C	C

7 CURRICULUM VITAE

Personal Data

Name	Ehrhardt, Toni
Sex	male
Nationality	German
Date and place of Birth	21 st of October 1987 in Ilmenau

Work Experience

09/2021 – now	Junior Team Leader at BioSpring GmbH, Frankfurt am Main, Department Fill and Finish
08/2020 – 09/2021	Project leader Biontech, Cell Manufacturing
05/2019 – 04/2020	Research Assistant at the Hannover Medical School (MHH), Department of Neuroanatomy
05/2010 - 08/2010	Futurelab Munich, Department Immunology

Education

2016 - 2022	PhD student at the Martin Luther University (MLU) Halle-Wittenberg, Medical Faculty, Department of Psychiatry, Psychotherapy and Psychosomatic medicine headed by Prof. Dr. Dan Rujescu
2014 - 2016	M.Sc. Biochemistry at the Martin Luther University (MLU) Halle-Wittenberg
2010 - 2014	B.Sc. Bioanalytic at the University for applied Science (HS) Coburg
2008 - 2010	Bachelor of medical engineering University of Applied Sciences Jena
2007 - 2008	One-year technical school
2004 - 2007	Vocational school for health and social, Meiningen

Publication

Ehrhardt T, Jung M, Hartmann C, Massa C, Hohmann T, Kozerka S, Klemenz A, Bezold V, Hartmann A, Giegling I, Dehghani F, Seliger B, Hoffmann K, Bork K, Rujescu D. (2021). In vitro modeling of Alzheimer's disease in functional monocyte lineage microglia-like cells reveals altered immune plasticity. In preparation for Blood Journal

Pfeifer J., Jung J. S., Hartmann C., **Ehrhardt T.**, Puls A., Hartmann A., Riemann D., Navarrete Santos A, Rujescu D, Jung M. (2021). Neuronal Stem Cells from Alzheimer Patients show Disturbed Stem Cell Plasticity and Altered Regulation of Sirtuin 1 Depending on Apolipoprotein E. Submitted in Molecular Neurobiology.

Xavier G., Jung M., Hartmann C., Santoro M. L., Flegel N., Rosa S. G., Reinsch J., Majer A., **Ehrhardt T.**, Pfeifer J., Appelt-Menzel A., Martins-De-Souza D., Simm A, Belangero S, Navarrete Santo A, Hartmann A. M., Rujescu D. (2021). Exosome profile comparison among induced pluripotent stem cell-derived brain cells. Submitted in Stem Cells.

Derlig, K., **Ehrhardt, T.**, Gießl, A., Brandstätter, J. H., Enz, R., and Dahlhaus, R. (2014). Simiate is an Actin binding protein involved in filopodia dynamics and arborization of neurons. *Frontiers in cellular neuroscience*, 8, 99.

Place, Date

Signature

EIDESSTATTLICHE ERKLÄRUNG

Hiermit erkläre ich, Toni Ehrhardt, dass diese Arbeit von mir bisher weder der Naturwissenschaftlichen Fakultät I der Martin-Luther-Universität Halle-Wittenberg noch einer anderen wissenschaftlichen Einrichtung zum Zweck der Promotion vorgelegt wurde und ich noch keine vergeblichen Promotionsversuche unternommen habe. Ich versichere hiermit, dass ich diese Arbeit selbstständig, ohne fremde Hilfe und nur unter zur Zuhilfenahme der angegebenen Hilfsmittel und Literatur angefertigt und weiterhin keine anderen als die von mir angegebenen Quellen und Hilfsmittel benutzt wurden.

.....
Ort, Datum

.....
(Unterschrift)